UAB
Universitat Autònoma de Barcelona

Theoretical modelling of the high-energy emission of pulsars

Daniel Íñiguez Pascual

ADVERTIMENT. L'accés als continguts d'aquesta tesi queda condicionat a l'acceptació de les condicions d'ús establertes per la següent llicència Creative Commons: https://creativecommons.org/licenses/?lang=ca

ADVERTENCIA. El acceso a los contenidos de esta tesis queda condicionado a la aceptación de las condiciones de uso establecidas por la siguiente licencia Creative Commons: https://creativecommons.org/licenses/?lang=es

WARNING. The access to the contents of this doctoral thesis it is limited to the acceptance of the use conditions set by the following Creative Commons license: https://creativecommons.org/licenses/?lang=en

INSTITUT DE CIÈNCIES DE L'ESPAI
CSIC IEEC
Universitat Autònoma de Barcelona

DOCTORAL THESIS

Theoretical modelling of the high-energy emission of pulsars

by

Daniel Íñiguez Pascual

Supervisors:
Diego F. Torres
Daniele Viganò

Tutor:
Lluís Font Guiteras

A thesis submitted for the degree of
Doctor of Philosophy in Physics

Barcelona, October 2026

Abstract

Pulsars are among the most fascinating objects in the Universe, holding several records: they are the fastest-spinning stellar objects, possess the strongest magnetic fields, and have some of the highest densities known. Mainly detected by their radio emission, a fraction of these objects have also been observed at high-energies, in X-rays and γ rays. This high-energy emission is produced in the magnetosphere of pulsars and after decades of research, several details of its origin are still not fully understood, such as the exact production sites or the radiation mechanism involved.

This thesis is dedicated to this topic, the modelling of the high-energy emission of pulsars. We develop effective models that rely on few free parameters and compare them with observational data. In this way, we assess the capacity of the models to explain the production of high-energy emission and, at the same time, extract conclusions. The work gathered in this thesis represents the first concurrent fitting of spectra and light curves of the whole population of high-energy pulsars.

We present a radiative model which solves the dynamics of magnetospheric charged particles and computes their emission via synchro-curvature radiation. In this way, by varying only three of the model parameters we generate high-energy spectra that are compared with observational ones. The model succesfully reproduces the γ-ray spectra of the whole population of pulsars, and the whole high-energy spectra, from X-rays to γ-rays, of those pulsars observed in both bands. This achievement reinforces the idea that synchro-curvature radiation is the mechanism responsible of the high-energy emission of pulsars. Complementary to the radiative model, we present a spectro-geometrical model that addresses the spatial distribution of the high-energy emission of pulsars. Together with the dynamics and radiation of the particles, we also calculate the geometry of their trajectories. With this and a realistic prescription of the shape of the emission region, we produce emission maps, which contain geometrical and spectral information. From these maps we extract light curves, which ultimately depend on two geometrical parameters, and we compare these synthetic light curves with observational ones. We are able to match the global structure of many light curves, reproducing their most relevant features. However, the model is not able to capture small scale features and struggles to resemble very complex or asymmetric light curves. The relative success in this fitting suggests that some of the assumptions taken in the model, such as the location of the emission region and its shape, may broadly reflect the true geometry of the magnetosphere, but indicates that further modelling is required to reproduce all the complexity the observational light curves have. Finally, we explore the origin of the dispersion seen in the observational γ-ray efficiency of pulsars, which we use to estimate the distribution of the intrinsic efficiency of the mechanism producing the γ-ray emission.

List of publications related to this thesis

- D. Íñiguez-Pascual, D. Viganò, and D. F. Torres. Synchro-curvature emitting regions in high-energy pulsar models. MNRAS, 516(2):2475–2485, Oct. 2022. doi: 10.1093/mnras/stac2275.
- D. Íñiguez-Pascual, D. F. Torres, and D. Viganò. Synchro-curvature description of γ-ray light curves and spectra of pulsars: global properties. MNRAS, 530(2):1550–1562, May 2024. doi: 10.1093/mnras/stae933.
- D. Íñiguez-Pascual, D. F. Torres, and D. Viganò. Synchro-curvature description of γ-ray light curves and spectra of pulsars: concurrent fitting. MNRAS, 541(2):806–820, Aug. 2025a. doi: 10.1093/mnras/staf1044.
- D. Íñiguez-Pascual, D. Viganò, and D. F. Torres. The dispersion in pulsar γ-ray efficiency. A&A, 704:L14, Dec. 2025b. doi: 10.1051/0004-6361/202557622.

Acknowledgements

Primer de tot, vull donar les gràcies als meus supervisors, Diego i Daniele, per tota l'ajuda i suport rebuts durant el doctorat. En els últims anys he vist com és d'important tenir un bon supervisor en un doctorat, i puc dir sense exagerar que he tingut molta sort. He après moltíssim de vosaltres, m'heu fet sentir molt còmode treballant i sempre heu procurat que millorés com a investigador.

He de continuar pels amics de la carrera de Física, amb els quals va començar aquest viatge fa més d'una dècada: Adri, Alex, Bernat, Jota, Linde, Roger i Uri. Aquesta serà la quarta tesi amb agraïments d'aquest grup, així que ja no queden gaires coses més a dir. Així que no diré gaires coses, simplement gràcies i que seguim molts més anys com estem (potser veient-nos una mica més sovint). No poden faltar unes paraules per als amics del cole, Néstor, Gil, Arnau i Serén, per haver mantingut l'amistat després de tants anys i per haver-me ofert una via d'escapament de la ciència, molt necessària de vegades. Vull agrair especialment a tota la gent que he conegut a l'ICE, que han fet aquest viatge molt més interessant i entretingut. En particular a totes les persones amb qui he tingut el plaer de compartir molts dinars i molt bons moments: Pedro, Antía, Luis, Simone, Carline, Pau, Rebeca, Elena, Guille, Maider, Víctor, Gisela, Giosué i Jose. I al futbolín, per les (moltes) hores de diversió i desestrès (en teoria), i per haver contribuït a fer que aquest grup de companys de feina s'hagi acabat convertint en un grup d'amics. I per descomptat al Charlie, pel suport mutu en molts moments del doctorat, les interminables converses i els viatges per diversos continents. També a la resta de persones que han estat presents durant aquests anys: Michele, Celsa, Clara, Abu, Arianna, Albert, Clàudia, Simran, Jorge, Pablo, i més.

Vull donar les gràcies a tota la meva família, als que hi són i als que ja no, per fer cert el tòpic de què no hauria arribat on soc sense vosaltres: Anna, Susi, Luis, Asun, Víctor, Óscar, Esther i Gerardo. També he d'agrair als Oriol que m'hagin adoptat com un més de la seva família. I sobretot a la Laura, per ser la millor germana que podria desitjar. I molt especialment als meus pares. Gràcies per tot el suport innegociable, per l'amor i la comprensió. Gràcies per inculcar-me la curiositat i el desig de voler entendre el món en què visc. I per acabar, moltes gràcies Mariona. Per estar sempre al meu costat, per fer-me aquest camí molt més fàcil i per ajudar-me a ser millor persona cada dia. En resum, per tot. No sé què m'oferirà el futur, però tinc clar que vull que tu en formis part.

I will not say: do not weep; for not all tears are an evil.
Gandalf, The Lord of the Rings

Contents

1 Pulsars **1**

1.1 What is a pulsar? . . . 1

1.1.1 Pulsar population . . . 1

1.2 Multiwavelength emission of pulsars . . . 4

1.2.1 Radio emission . . . 5

1.2.2 Infrared, optical and ultraviolet emission . . . 7

1.2.3 X-rays . . . 7

1.2.4 γ-rays . . . 8

1.2.5 Very-high-energy emission . . . 12

1.2.6 The neutron star zoo . . . 15

1.3 Neutron star physics . . . 16

1.3.1 Formation . . . 17

1.3.2 Interior . . . 19

2 Magnetospheric models of pulsars **21**

2.1 Spin-down properties of pulsars . . . 21

2.1.1 Energy radiation by magnetic moments . . . 22

2.1.2 Electromagnetic torque and pulsar spin-down . . . 22

2.2 Global Magnetosphere Models . . . 25

2.2.1 Pulsar magnetosphere . . . 25

2.2.2 Vacuum magnetospheres . . . 25

2.2.3 Force-Free Electrodynamics . . . 27

2.2.4 Dissipative force-free simulations . . . 30

2.2.5 Kinetic models with Particle-In-Cell simulations . . . 31

2.3 Radiative models . . . 34

2.3.1 Polar Cap models . . . 34

2.3.2 Slot Gap models . . . 38

2.3.3 Outer Gap models . . . 39

2.3.4 Theoretical ideas from gap models still present nowadays . . . 41

2.3.5 Striped wind models . . . 41

2.4 Geometrical models . . . 43

2.5 Motivation of the model presented in this thesis . . . 46

3 Radiative model **49**
3.1 Particles' trajectories . . . 50
3.1.1 Equation of motion . . . 50
3.2 Synchro-curvature spectra . . . 51
3.2.1 Synchro-curvature radiation . . . 51
3.2.2 Single-particle spectrum . . . 55
3.2.3 Effective weight functions . . . 58
3.2.4 Integrated spectrum . . . 59
3.2.5 Initial conditions of the emitting particles . . . 60

4 Spectro-geometrical model **63**
4.1 Radiative and geometrical modelling . . . 64
4.1.1 Trajectories . . . 64
4.1.2 Emission directions of the travelling particles . . . 64
4.1.3 Location in the magnetosphere and shape of the emission region . . . 65
4.1.4 Radiation emitted from the emission region . . . 68
4.1.5 Emission skymap . . . 68
4.2 Synthetic skymaps and light curves of selected pulsars . . . 69
4.2.1 Effects of the geometry on the skymaps and light curves . . . 69
4.2.2 Effects of the spectral parameters on the skymaps and light curves . . . 72
4.2.3 Spectra seen by different observers . . . 73
4.2.4 Set of geometries and sample of pulsars . . . 74
4.3 Light curves features and comparison with observations . . . 75
4.3.1 Details of the peak recognition algorithm . . . 76
4.4 Comparing the distribution of features of different pulsars . . . 79
4.5 Impact of the geometrical parameters on the distribution of features . . . 79
4.6 Concluding remarks . . . 80

5 Concurrent fitting of spectra and light curves **83**
5.1 Spectral fitting . . . 85
5.1.1 Minimization algorithm . . . 85
5.1.2 Sample selection . . . 87
5.1.3 Results . . . 88
5.2 Light curves fitting . . . 93
5.2.1 Important considerations prior to fitting . . . 93
5.2.2 Fitting procedures . . . 94
5.2.3 Results . . . 98
5.3 Searching for correlations between model parameters . . . 102
5.3.1 Searching for correlations between spectral parameters . . . 102
5.3.2 Searching for correlations between geometrical parameters . . . 105
5.4 Concluding remarks . . . 105

6 The dispersion in pulsar γ-ray efficiency **109**
6.1 Introduction . . . 109
6.2 Ingredients contributing to the dispersion of the observational γ-ray efficiency 110
6.2.1 Beaming factor, f_Ω. . . . 110
6.2.2 Uncertainty on the moment of inertia, $\epsilon_{\rm I}$. . . . 111
6.2.3 Uncertainty on the distance, $\epsilon_{\rm d}$ 112
6.3 Distribution of the mechanism efficiency 113
6.4 Additional sources of $\eta_{\rm obs}$ dispersion 115
6.5 Concluding remarks 116

7 Conclusions **119**

A Injection of particles **125**

B Details on the Nelder-Mead method **129**

C Observed γ-ray spectra in the Second and Third Fermi Pulsar Catalogues **133**

D Timing and best-fitting spectral and geometrical parameters of the whole sample of pulsars studied **141**

E Spectral fits of the whole sample of pulsars studied **151**

F Light curve fits of the whole sample of pulsars studied **167**

Bibliography **196**

1

Pulsars

1.1 What is a pulsar?

Pulsars are rapidly rotating neutron stars with very short spin periods and strong magnetic fields. Pulsars are the fastest rotating stellar objects in the Universe, with spin periods P spanning from a few milliseconds up to several seconds, i.e. spin frequencies from ~ 0.1 Hz to hundreds of Hz. The spin periods are extremely stable and increase very slowly in time, at a pace given by the time derivative of the spin period $\dot{P}$, of around $\sim 10^{-11} - 10^{-22}$. A particular pulsar is defined by both P and $\dot{P}$, which are measured with an extreme precision, a unique case in astronomy. The stability of the rotation of pulsars makes these objects very precise astronomical clocks, competing with the most advanced atomic and quantum optical clocks. Magnetic fields of pulsars are also the highest in the Universe, with inferred values in the range 10^{8-14} G. Historically, the defining observational signature of pulsars has been their radio emission, which is beamed along their magnetic axis. This axis is misaligned with respect to the rotational one, producing the characteristic lighthouse effect: radio emission is detected from Earth when the radio beam sweeps across it, producing a pulsed detection. Pulsars can also emit at other wavelengths, from the optical up to γ-rays, and their emission is powered by the loss of rotational energy due to an electromagnetic torque. For this reason they are usually referred to as rotation-powered pulsars (RPPs), and they account for the majority of the population of neutron stars.

1.1.1 Pulsar population

The first detection of a pulsar occurred in 1967[1], when the PhD student Jocelyn Bell Burnell noticed an unexpected radio signal repeating every 1.337 seconds on her interplanetary

[1]Even though this is the first public discovery, months before a US military officer, Charles Schisler, most probably detected radio signals from the Crab pulsar with a military radar, which was intended for detecting possible Soviet attacks during the Cold War. The classified nature of Schisler's job prevented a communication with the scientific community which could have been very fruitful.

scintillation data, which she used to study quasars at the Mullard Radio Astronomy Observatory (Hewish et al., 1968). The discovery led to the award of the Nobel Prize in Physics to Antony Hewish, Jocelyn Bell Burnell's supervisor. Jokingly nicknamed *Little Green Men* 1, the discovery aroused active speculation in the academic world, until Gold (1968) and Pacini (1968) suggested a fast-rotating, highly magnetised neutron star with a strong magnetic field rotating very fast as the origin of the radio signal. The pulsed nature of the emission of these objects earned them the name of *pulsars*. Many more detections followed the serendipitous discovery, confirming its origin and as of the year 2026 more than 4000 pulsars have been detected, catalogued in the Australian Telescope National Facility (ATNF) Pulsar Catalog[2] (Manchester et al., 2005).

Among the population of pulsars, we can distinguish standard pulsars and millisecond pulsars (MSPs). Standard pulsars have ages in the range $1 - 10^4$ kyr, spin periods above ~ 10 milliseconds and period derivatives $\sim 10^{-11} - 10^{-16}$ [s/s]. MSPs are older, with spin periods below ~ 10 milliseconds and period derivatives $\sim 10^{-18} - 10^{-22}$. Their magnetic field is typically lower than that of standard pulsars. These two classes are clearly separated in the $P - \dot{P}$ diagram, see Figure 1.1, which displays the timing parameters P and $\dot{P}$ of the whole population of pulsars (see García et al. 2022 for an alternative way to visualize the pulsar population).

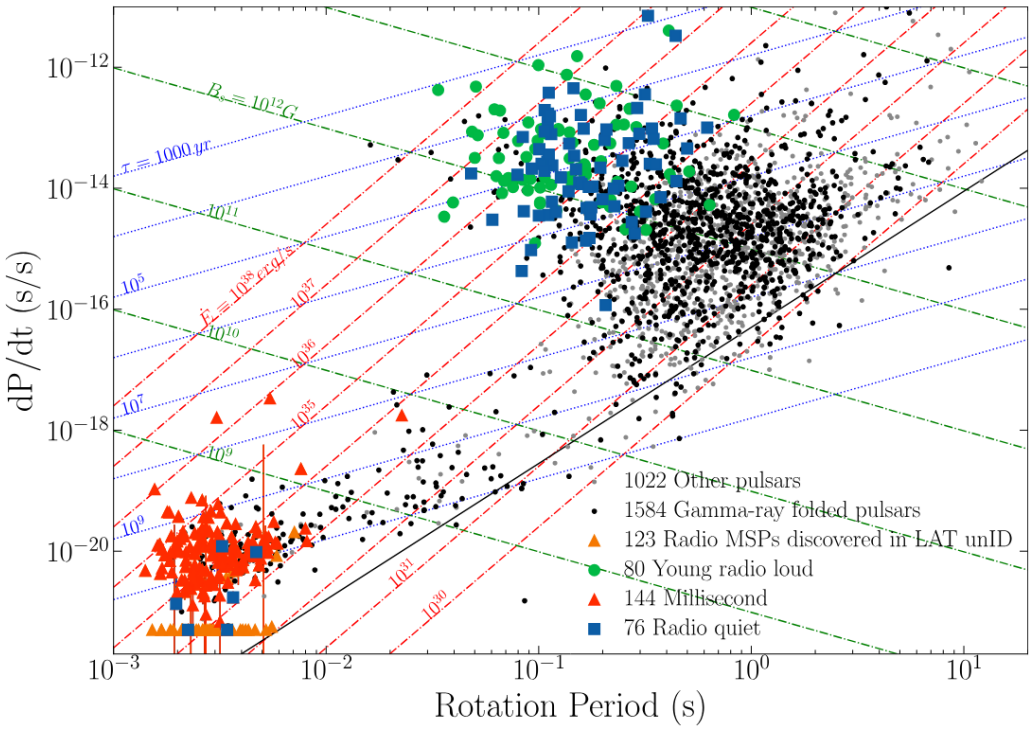


Figure 1.1: P-$\dot{P}$ diagram (figure taken from Smith et al. 2023). Green (blue) dot-dashed lines show P-$\dot{P}$ positions of equal B_s (τ_c) under the vacuum dipole approximation. Red dot-dashed lines show P-$\dot{P}$ positions of equal spin-down power $\dot{E}$.

The formation channel of MSPs is different from that of standard pulsars and is known as the recycling scenario (Tauris and van den Heuvel, 2023). In binary systems with a slow-rotating neutron star (we will see how neutron stars are born in subsection 1.3.1) and a low

[2]See https://www.atnf.csiro.au/research/pulsar/psrcat/ for the updated catalog.

or intermediate mass star, the companion may fill its Roche lobe and start transferring mass to the neutron star, which accretes this matter with a large angular momentum and spins up. At this stage the system is observed as an X-ray binary, with emission dominated by thermal X-rays from the accretion disk. When accretion stops, the neutron star can switch on rotation-powered emission: a MSP is born. Due to its formation history, most MSPs are in a binary system (Harding, 2022) with a companion star, but there are also isolated MSPs, which are thought to have lost the companion star, e.g. due to its complete ablation by the pulsar winds. A fraction of binary MSPs, called spider pulsars, have tight orbits with orbital periods of a few hours, and a low-mass star companion which suffers severe ablation, i.e. evaporation by the pulsar winds. Spider pulsars are divided into black widows and redbacks, with the former having a lighter, more ablated companion. The recycling scenario is backed by the observation in the recent years of binary MSPs switching from rotation-powered to accretion-powered emission, the so-called transitional MSPs (Papitto and de Martino, 2022). A particular subclass of RPPs are rotating radio transients (RRATs), objects for which sporadic radio pulses are detected. Even though no continuous radio signal is observed for the more than 300 RRATs known nowadays (Agarwal et al., 2026), searches for individual, bright pulses hint at a periodicity similar to that of pulsars and at pulsar-like spin-down rates, which allows one to classify them as pulsars (Kaspi and Kramer, 2016).

Part of the rotational energy lost by pulsars is injected into the surrounding medium in the form of a relativistic wind of particles. These winds are terminated by the pressure of the surrounding supernova remnant at the termination shock, forming the so-called pulsar wind nebula (PWNe) (Kennel and Coroniti, 1984). PWNe are bubbles of relativistic particles and magnetic field that emit synchrotron radiation from radio to X-rays and inverse Compton emission up to TeV energies. They are among the brightest X-ray sources in the sky and have been detected around several tens of pulsars (Gaensler and Slane, 2006).

Located all along the Milky Way, most pulsars live in the Galactic plane, see Figure 1.2, reflecting the distribution of massive stars, their progenitors. However, the abundance of pulsars at high latitudes is larger than that of massive stars. The reason is the kick that neutron stars receive at their birth which displaces them from the centre of the supernova and propels them at high velocity, from a few tens of km/s up to more than 1000 km/s, averaging at several hundreds of km/s (Hobbs et al., 2005). Due to observational biases, we observe mostly pulsars located nearby the Solar System, see Figure 1.2, but the pulsar population is expected to be distributed throughout the Galaxy. The real pulsar population in the Milky Way is also expected to be much larger than the currently known population. The sensitivity of the current telescopes in radio and other wavelengths is a limiting factor for the detectability of pulsars. Besides the observational limits, physical reasons limit the number of detectable pulsars: absorption by the interstellar medium, low intrinsic luminosity and narrow emission beams which cross the line of sight of the Earth only in a minority of them.Taking into account the age of the Milky Way, the typical lifetimes of massive stars and supernovae rate in our Galaxy considered to be 1 to 3 per century (Diehl et al., 2006) (more recent studies have found a rate of ~ 2, Pardo-Araujo et al. 2025), it is reasonable to believe that the Milky Way contains millions of pulsars (Gullón et al., 2014; Graber et al., 2024).

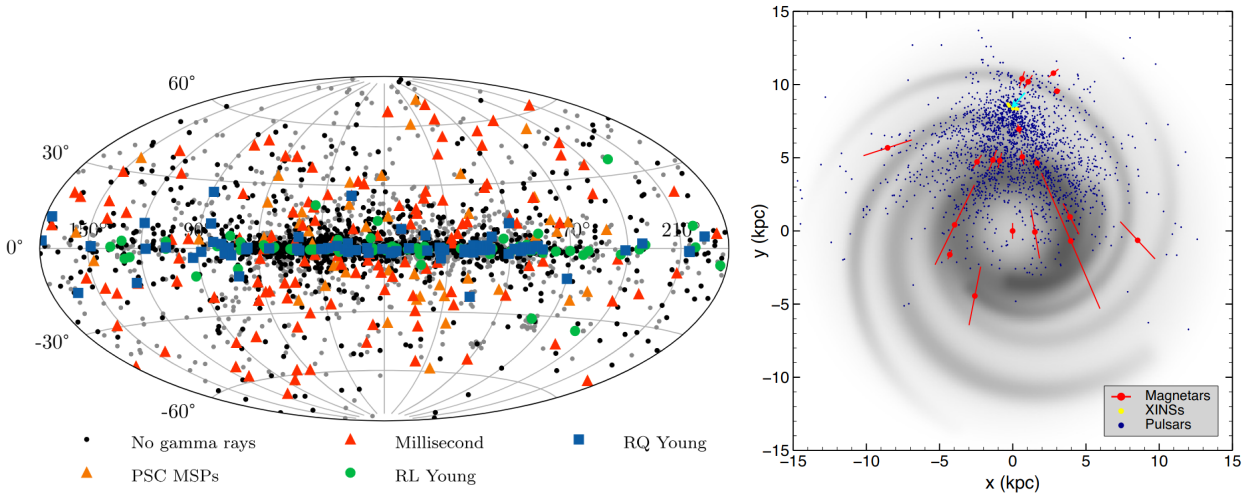


Figure 1.2: Left: Distribution of pulsars in the Milky Way. Black dots represent radio pulsars for which no γ-ray pulsations have been detected so far (figure taken from Smith et al. 2023). Right: Distribution of pulsars in the Milky Way from an azimuthal view. Cyan arrow indicates the Sun position (figure taken from Olausen and Kaspi 2014).

1.2 Multiwavelength emission of pulsars

Pulsar studies rely on certain observables of these objects in order to understand their structure, emission and the rest of their characteristics. In addition, pulsars emit across almost the entire electromagnetic spectrum, from radio to very-high-energies (up to TeVs), and observables can be obtained for all the energy ranges in which they emit: radio, infrared, optical, ultraviolet, X-rays, γ-rays, and TeV energies.

One of the main observables used to study pulsars and their emission are pulse profiles, which are obtained by folding light curves – the detected flux as a function of time – at the spin period of the pulsar, and represents the intensity of the emission as a function of rotational phase, averaged over a given energy range It can provide information about the geometry of the pulsar, such as the angle between the rotational and magnetic axes or the viewing angle from Earth, as well as about the sites of production of radiation. Spectral energy distributions (spectra for brevity) of the detected photons are another useful observable used in pulsar studies. They help us understand better the physics underlying the high-energy emission, such as the dynamics of the emitting particles and the emission mechanisms at work, among others. These spectra can be phase-averaged, meaning that the flux is integrated over a whole spin period, or phase-resolved, integrating the flux over a certain rotational phase range. As we have said, both pulse profiles and spectra can be obtained at different wavelengths: pulse profiles by integrating over selected energy ranges, and spectra by considering separate energy bands. This provides a more complete picture of the geometry of the pulsar and the physical processes occurring there. Additional information can be obtained by studying the degree and properties of the linear and circular polarization of the detected flux. Particularly relevant in the radio and X-ray domains, these are good tools to understand the magnetic fields, since their structure and strength leave a characteristic imprint on polarization data.

1.2.1 Radio emission

The vast majority of pulsars known nowadays are detected in the radio band. The stable radio pulses that reach the Earth at a given period due to the lighthouse effect are the most characteristic phenomenological expression of pulsars. In order to have enough signal-to-noise and smooth out the pulse-to-pulse stochastic variability, folding over hundreds or thousands of cycles is usually done to obtain the radio pulse profile of a pulsar and find the value of its spin period. Figure 1.3 shows some examples of radio pulse profiles radio. The spin period time derivative can be measured by performing many observations distributed over a long period of time and is known for a great portion of pulsars. Timing noise makes the measurement of higher time derivatives of the spin period more difficult, although the second time derivative has been measured for several hundreds of pulsars (Parthasarathy et al., 2019).

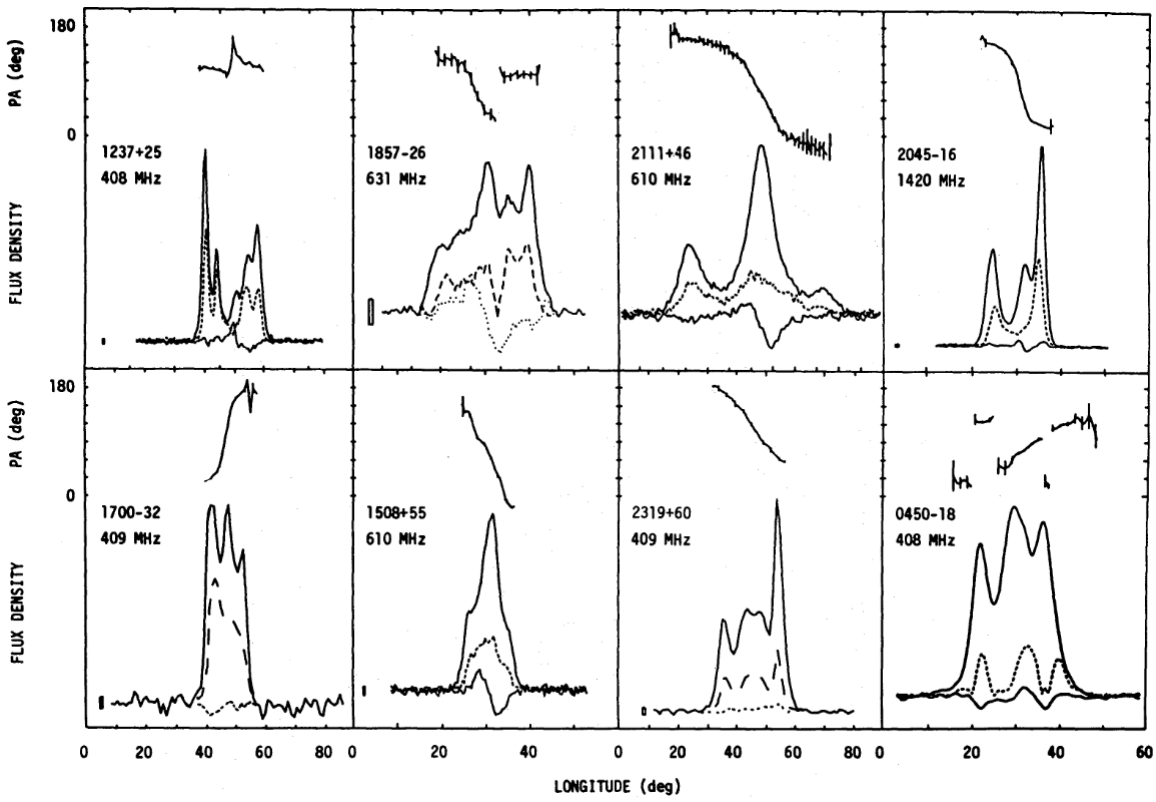


Figure 1.3: Radio pulse profiles of different pulsars and at different frequencies (indicated within each subpanel). Figure taken from Lyne and Manchester (1988).

Radio emission is emitted in the form of hollow, cone-shaped beams, with an opening demarcated by the region with open magnetic field lines and defined by the half-opening angle, $\rho_{\rm b}$, which depends on the emission height above the neutron star surface, r_{em}, and the pulsar period, as $\rho_{\rm b} \sim r_{em}^{1/2} P^{-1/2}$ (Lorimer and Kramer, 2004). In the first models of radio emission, the conal beam is considered empty and the position at which Earth's line of sight crosses it would determine the number (and shape) of peaks we observe: one peak if crossing the rim of the cone and two peaks if the line of sight crosses the interior of the cone. Even though most pulse profiles have one peak, radio pulse profiles present a great diversity of shapes. There are also profiles with several peaks, up to five, and these multi-

peaked profiles can have or not a so-called bridge emission between peaks. The radio pulse profiles of Figure 1.3 show these different features. To explain this diversity several other beam models have been proposed: an extension of the initial hollow-cone beam with an inner cone and an outer cone (Rankin, 1993), a patchy beam with subregions of emission inside the cone (Lyne and Manchester, 1988) or a fan-shaped beam formed by several sub-beams (Wang et al., 2014). Figure 1.4 shows sketches of the different beam models. Pulse profiles also present differences in the width of the peak(s) and in the steepness of each side of a peak, as well as in the asymmetry of the steepness. The width of each peak can be expressed as $W \sim r_{em}^{1/2} P^{-1/2} / \sin \Psi_\Omega$, where $\sin \Psi_\Omega$ is the angle between the rotational and magnetic axes (Tauris and Manchester, 1998).

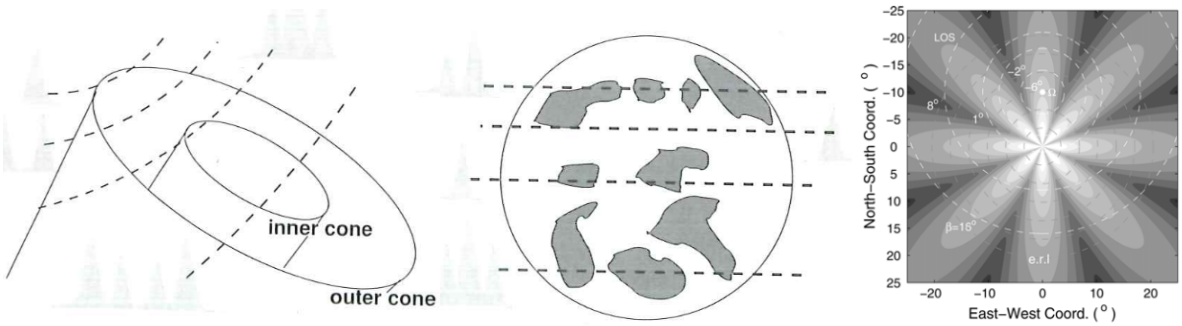


Figure 1.4: Sketches of the radio beam structure proposed by different models. From left to right: double cone beam from Rankin (1993), patchy beam from Lyne and Manchester (1988) (figures taken from Lorimer and Kramer 2004), and fan beam from Wang et al. (2014).

Radio emission is produced by coherent processes of charged particles above the magnetic poles in the region of open field magnetic field lines. The exact mechanism at work is not fully understood yet, and several different mechanisms are proposed and studied, such as antenna mechanisms, in which a bunch of particles oscillate in phase and emit curvature radiation, and relativistic plasma emission mechanisms, in which a plasma instability leads to the release of energy in the form of radio waves (Lorimer and Kramer, 2004). Radio emission is highly linearly polarized, and the Rotating Vector Model (Radhakrishnan and Cooke, 1969) gives a way to use radio polarization data to obtain information about the geometry of a pulsar.

Many facilities around the world carry out observing campaigns devoted to the discovery and characterization of pulsars. Two main kinds of instruments are used for this task. On the one hand, single dish telescopes with very large radii which can reach up to several hundred meters, offer a large collecting area and thus a good sensitivity. Examples of this type of radio telescopes are the (now-deceased) Arecibo Observatory, the Effelsberg 100-m radio telescope, Murriyang in the Parkes Observatory, the Lovell telescope, the Green Bank Telescope (GBT), and the relatively new Five-hundred-meter Aperture Spherical Telescope (FAST). On the other hand, radio interferometer arrays, i.e. arrays of antennas that observe simultaneously, like the Very Large Array (VLA), the LOw Frequency ARray (LOFAR), the Australian SKA Pathfinder (ASKAP), Murchison Widefield Array (MWA) and MeerKAT, provide a high spatial resolution. A large number of antennas could also lead to large collecting areas, as will have the future Square Kilometre Array (SKA), which is expected

to enlarge the known population of pulsars by an order of magnitude.

1.2.2 Infrared, optical and ultraviolet emission

Infrared, optical and ultraviolet emission is the least commonly observed wavelength in pulsars due to its intrinsic faintness. Pulsated data in these energy ranges is only available for less than 30 pulsars. Nevertheless, the few data allow one to argue that the mechanisms producing the infrared, optical and ultraviolet emission are different from that producing the radio emission. Two origins, which may coexist together, are proposed for emission in these energy ranges: synchrotron radiation from charged magnetospheric particles with low energy and thermal emission from the neutron star cooling (Mignani et al., 2000). Based on the spectroscopic data and on phenomenological reasons, the infrared through the optical to the ultraviolet emission is dominated by a non-thermal component in young and bright pulsars, while thermal emission may dominate for old pulsars, and both components contribute in middle-aged and fainter pulsars (Mignani, 2011). Recall that these conclusions are drawn from a very limited sample of detected objects and remain tentative.

1.2.3 X-rays

More than a hundred pulsars have been observed to emit X-ray radiation, in an energy range spanning from 0.1 keV to tens of keV (Becker, 2009; Xu et al., 2025). The origin of this emission can be thermal or non-thermal and is produced at different places of the pulsar. Here we focus only on the emission of isolated pulsars, not on those in binary systems in which there is a relevant component of the X-ray emission coming from the accretion of mass from the companion star onto the pulsar.

As we will see below, neutron stars are born with high temperatures and cool down due to neutrino and photon emission. Pulsars with ages $\sim 10^{1-3}$ kyr usually have surface temperatures of $\sim 10^6$ K and thus emit thermal emission in the soft X-ray band ($0.1 - 1$ keV). Neutron star cooling is related to the internal composition of these objects, and thus studying the thermal emission in X-rays can give valuable information regarding e.g. the EoS (Potekhin et al., 2015). Non-thermal emission is produced by the acceleration of charged particles, most probably via synchrotron radiation. The production site of this radiation still remains unclear, but it is very likely to occur in the magnetosphere, further away from the neutron star surface and even outside the light cylinder. More than 40 pulsars with non-thermal X-ray emission have also been detected in the γ-ray range (Coti Zelati et al., 2020). The modelling presented in this thesis also addresses the non-thermal X-ray emission of these objects, as we will see later on.

Usually the detected X-ray emission is a mixture of thermal and non-thermal components, but it is not always easy to distinguish between them in the observational data (Becker, 2009). The prominence of each component varies with the age of the object: despite the high surface temperatures of young pulsars with ages ~ 1 kyr, the non-thermal component dominates their X-ray emission, while both components are required to understand the X-ray emission in middle-aged pulsars with ages $\sim 10^{2-3}$ kyr (Becker, 2009). Old (non-recycled) pulsars with ages $\gtrsim 10^{3-5}$ kyr have already cooled down to a point at which their surface

temperatures are too low to emit thermal radiation that can be detected (Haensel et al., 2007), and the non-thermal component dominates again. However, MSPs (i.e. old recycled pulsars) still emit significant thermal radiation, usually dominating their X-ray emission. It is produced in the so-called hot spots, small regions in the neutron star surface that have high temperatures of up to $\sim 10^6$ K due to the bombardment by particles accelerated in the magnetosphere and returning to the star. This component is pulsed and can be used to understand e.g. the magnetic field topology thanks to the magnetospheric origin of the hot spots heating (Carrasco et al., 2023).

Thermal and non-thermal components show notable differences in the observables, energy spectra and light curves. While the spectrum of the thermal component is usually modelled as a black-body, the non-thermal one resembles a power-law. Left panel of Figure 1.5 shows some examples of energy spectra in the X-ray band with both thermal and non-thermal components. In the case of pulse profiles, the non-thermal part is usually more modulated and the pulses are narrower than in the thermal one, indicating that the former is more beamed than the latter. The pulse profiles at different energy ranges on the right panel of Figure 1.5 show the differences on the pulse profiles of both components.

X-rays do not penetrate the Earth's atmosphere and they are detected with balloon flights at high altitudes or with telescopes in space, the first ones having been e.g. Uhuru, ROSAT or RXTE (not operating any more). At the present time, the most relevant instruments observing the X-ray emission from pulsars are space-borne: XMM-Newton ($0.15 - 12$ keV), Chandra ($0.1 - 10$ keV), NICER ($0.2 - 12$ keV) and NuStar ($3 - 79$ keV). In the future, *NewAthena* is expected to provide new and better X-ray data of pulsars.

1.2.4 γ-rays

γ-ray emission from 100 MeV up to several tens of GeV is the second most commonly detected wavelength range in pulsars after radio, and most of the rotational energy lost into pulsated emission is radiated in this energy band. Pulsars for which γ-ray pulsated emission is detected are often called γ-ray pulsars, and they form a rather diverse population in terms of timing properties and phenomenology (Smith et al., 2023). Both young and millisecond γ-ray pulsars exist. In this thesis the term *high-energy pulsars* will also be used to define pulsars with γ-rays and/or X-rays detected. Most of them also emit in the radio band, but a non-negligible proportion (about a quarter of the total population) do not. These radio-quiet γ-ray pulsars surprised the community when they were discovered, and contribute to the actual understanding that radio and γ-ray emission are developed separately (though not independently, as we will see in the next chapter). In our current understanding, the radio beam of a radio-quiet γ-ray pulsar simply does not cross the Earth, while its γ-ray beam does because it is wider than the radio one and can point at a different direction.

A few years after the first radio pulsar was discovered, the instrument SAS-2 observed γ-ray pulsations from the Crab (Kniffen et al., 1974) and Vela (Thompson et al., 1975) pulsars, which were confirmed by the COS-B instrument. A great push in γ-ray astronomy came with the Energetic Gamma-Ray Experiment Telescope (EGRET) instrument onboard the Compton Gamma-Ray Observatory, which confirmed the Crab and Vela detections,

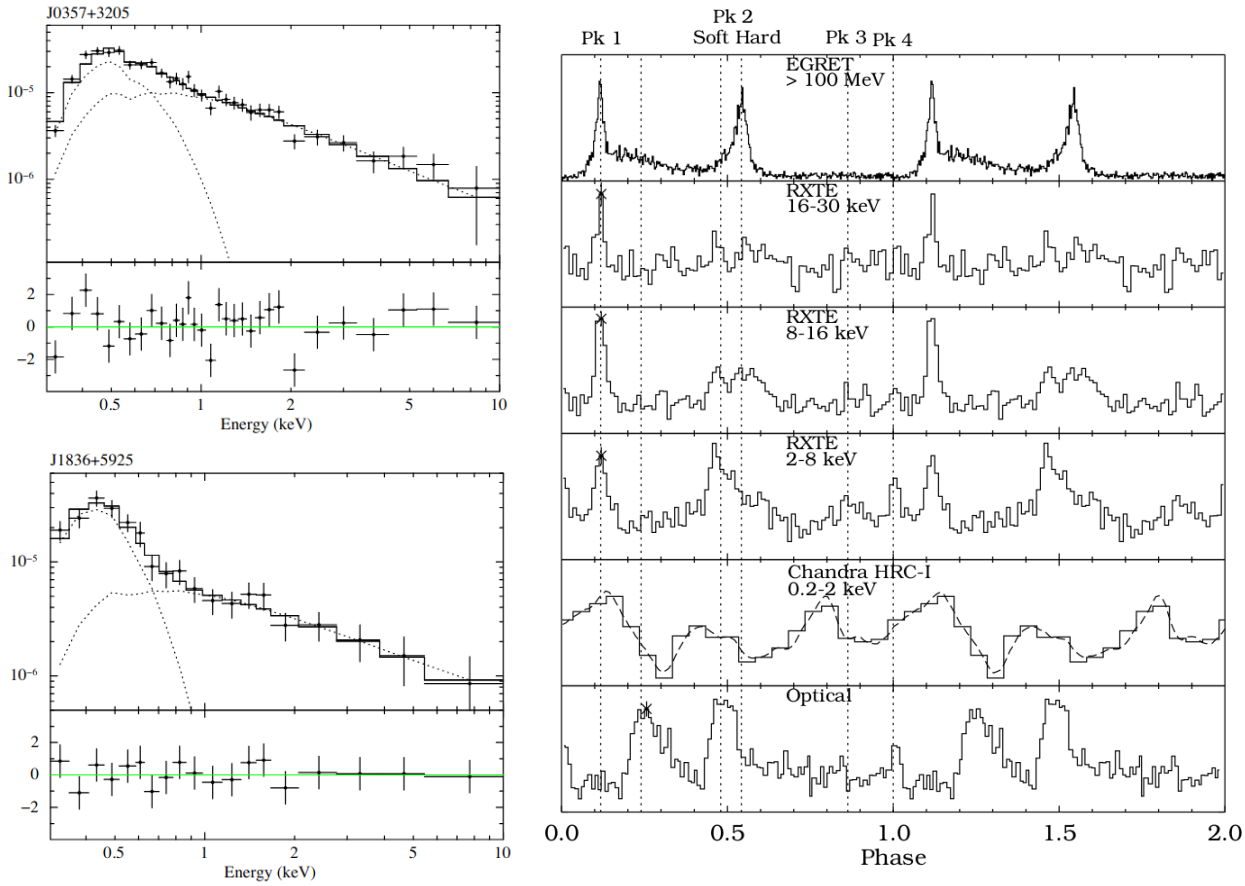


Figure 1.5: Left: Energy spectra in the 0.1−10 keV (soft X-ray) range of pulsars J0357+3205 (top) and J1836+5925 (bottom). Dotted line correspond to the best-fitting models. Bottom subpanels show the post-fit residuals (figures taken from Coti Zelati et al. 2020). Right: Multiwavelength pulse profiles of Vela from optical to γ-ray band (figure taken from Kaspi et al. 2006). The 0.2-2 keV range is purely thermal emission, while the range 16-30 keV is non-thermal.

detected pulsations above 100 MeV from five more pulsars and set upper limits for many more pulsars. One of the confirmed pulsars was Geminga, the first radio-quiet pulsar known. These 7 pulsars, Crab, Vela and the five discovered by EGRET, constituted the very first population of γ-ray pulsars worthy of that name (Thompson, 2004), and were used for testing emission models. After several additional objects discovered by the Astro-Rivelatore Gamma a Immagini Leggero (AGILE) instrument, γ-ray pulsar astronomy was highly boosted in 2008 by the launch of the *Fermi* space telescope with the Large Area Telescope (LAT, Atwood et al. 2009) instrument onboard. See Figure 1.6 for a visual representation of the impact of *Fermi* observations on the number of γ-ray pulsars discovered. After 6-months of operation, the *Fermi*-LAT had already detected 46 pulsars with γ-ray pulsations, gathered in the First Fermi Pulsar Catalog (1PC, Abdo et al. 2010a). The barrier of the hundred objects was broken after four more years of operations, and the γ-ray pulsar population was enlarged in the Second Fermi pulsar Catalog (2PC, Abdo et al. 2013), which presented 117 of these objects. The latest release of observational data of γ-ray pulsars is the Third Fermi Pulsar Catalog (3PC, Smith et al. 2023), which presents 297 pulsars with detected pulsations in the

γ-ray energy band, based on twelve years of data collecting. The 3PC is the most complete catalogue of the γ-ray pulsar population to date.

The almost 300 γ-ray pulsars known nowadays, represent about 10% of the observed pulsar population. This imbalance can be understood with energetics and the age of the pulsars. If the pulsar is old, its spin period P may have reached a value at which the rotational losses, Equation (2.5) (see below), are not very strong. This old pulsar may be capable of emitting γ-rays, but since the number of photons emitted in radio is much larger than in γ-rays, it may occur that the pulsar is only detected with enough significance by radio telescopes but not by the *Fermi*-LAT. The detected γ-ray pulsars are those with a smaller P and larger $\dot{P}$ among standard pulsars (see the $P-\dot{P}$ diagram on Figure 1.1), which indicates a rather large spin-down power (as we will see in subsection 2.1.2). Although many more photons are produced with energies in the radio range than in the γ-ray range, the latter are several orders of magnitude more energetic than the former, and thus most of a pulsar's energy budget is emitted in the γ-ray band. This observational bias is particularly relevant in standard pulsars, which present a wide range of spin-down power values, of $\sim 10^{27-38}$ erg/s. On the contrary, MSPs, which have spin-down powers of $\sim 10^{31-36}$ erg/s, are less affected by this bias because even the less energetic MSPs have spin-down powers large enough to make them detectable in the γ-ray band (provided they are close enough and their emission beam crosses the Earth, condition also applicable to standard pulsars). This explains why standard and millisecond γ-ray pulsars are almost equal in number, while in the radio population the number of detected standard pulsars is around five times higher than that of MSPs.

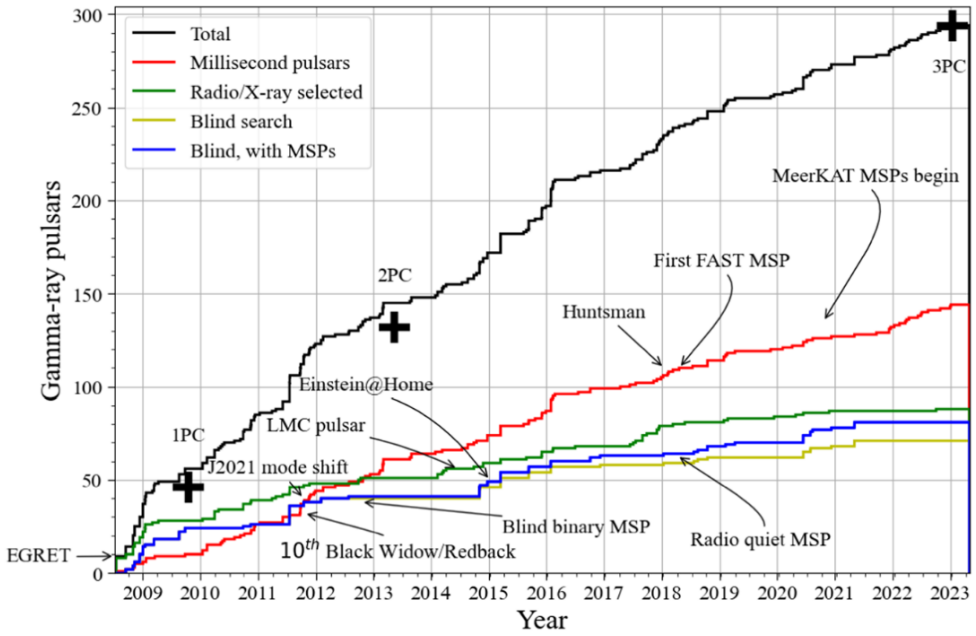


Figure 1.6: Cumulative distributions of γ-ray pulsars and their types as a function of time. Black crosses show the publications of the 1PC, 2PC and 3PC (figure taken from Smith et al. 2023).

Nowadays the *Fermi*-LAT instrument is still the main facility observing γ-ray pulsars. It observes in the energy range from 20 MeV to 300 GeV, and with its field-of-view covering 2.4 steradians scans the whole sky every $\sim$ 3 hours in survey mode. The time resolution is

1μ-second and the energy resolution is less than 10% above 100 MeV. The LAT instrument is a pair-production telescope, i.e. detects a γ-ray photon when it produces an electron-positron pair inside the instrument. The occurrence of pair-production and its reconstruction mainly depends on the energy of the incoming particle and the size of the detector, imposing constraints on the detectable photon energies and the minimum size of the instrument. The LAT is structured as a grid of two-system towers, each system formed by a tracker and a calorimeter. The tracker consists of a stack of tungsten foils that convert the γ-ray photon into an electron-positron pair, interspersed with silicon strip detectors which track the electron and positron charges, and allows to reconstruct the pair creation event. The caesium-iodide calorimeter absorbs the electron-positron pair and measures their energies, thus obtaining the energy of the incoming γ-ray photon. The instrument is coated with an anticoincidence detector aimed at rejecting background emission. Even though a handful of γ-ray pulsars have been discovered in *Fermi*-LAT blind searches, normally the detection of γ-ray pulsations from pulsars requires a previous radio detection. Once a pulsar has been detected and characterized in the radio band, its radio ephemerides are used to phase fold the γ-ray photons from that pulsar. With this folding one obtains pulse profiles from which the existence of pulsations can be assessed, enabling further characterization of the pulsar in the γ-ray band. See Figure 1.7 for an example of a photon phase folding and the resulting pulse profile. The Pulsar Timing Consortium (Smith et al., 2008) organizes observing campaigns with important radio facilities to supply *Fermi* with radio ephemerides. This technique is the most fruitful in γ-ray pulsar discovery, but radio and X-ray searches of unidentified *Fermi* γ-ray sources have also led to many discoveries. Energy spectra of pulsars have a very particular shape, it resembles a power law with a sub-exponential cut-off, a characteristic which is usually used to appoint *Fermi* unidentified sources as possible pulsar candidates. Figure 1.8 shows examples of γ-ray spectra from the 3PC. However, these spectra show a wide variety of shapes, with differences in the spectral indexes at $\sim$ 100 MeV, the widths and positions of the peaks and the steepness of the cut-off at $\gtrsim$ 10 GeV.

γ-ray emission has a non-thermal origin, it is produced by charged particles, electrons and positrons, $e^{\pm}$, being accelerated in the pulsar magnetosphere. Typical energies for $e^{\pm}$ emitting γ-rays are of the order of $\sim$ TeV, i.e. with a Lorentz factor $\Gamma \sim 10^7$. Synchrotron radiation or curvature radiation are usually proposed as the emission mechanism generating γ-rays from pulsars. Synchrotron radiation is emitted by a relativistic charged particle gyrating around a straight magnetic field line, thus describing a spiral motion around it, while curvature radiation is emitted by a relativistic charged particle travelling in a curved magnetic field line. These two mechanisms can be generalized into a single mechanism synchro-curvature radiation, in such a way that synchrotron and curvature radiations are just particular limits of a more general formulation. Synchro-curvature radiation is the framework upon which this thesis has been built. More information about these emission mechanisms will be given in Chapter 3.

For a few pulsars pulsations are detected in the soft γ-ray regime, 20 keV - 30 MeV (see Kuiper and Hermsen (2015) for a catalog of these objects). This emission also has a non-thermal origin and is produced in the magnetosphere, very likely linked to the X-ray and γ-ray emission. The lack of an instrument performing dedicated observations on this

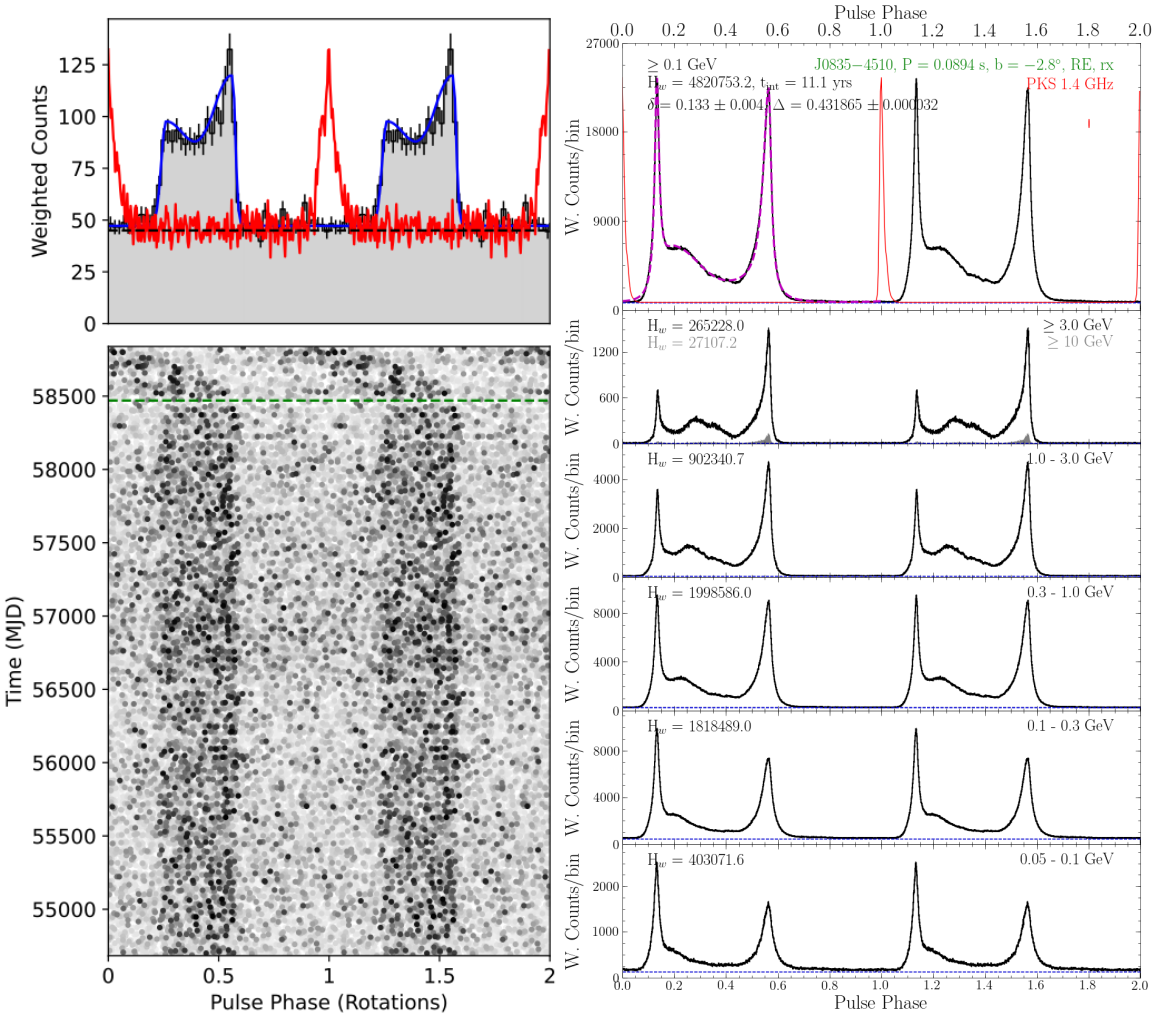


Figure 1.7: Left: Phase histogram in γ-rays of PSR J1648-4611, where the blue line is a fit to the histogram, the red line is the radio pulse profile of that pulsar and the dashed green line indicates when the radio ephemerides is no longer valid. Dots are the photons collected at a given time and pulse phase, with the color scale indicating the photon weight as explained in Smith et al. (2023). Right: Pulse profiles at different energy ranges of PSR J0835-4510 (the Vela pulsar). Top subpanel shows the pulse profile integrated over the entire *Fermi* γ-ray range, and the rest of subpanels show pulse profiles in energy subranges. Figures taken from Smith et al. (2023).

energy band limits our understanding of this emission. Several instruments of this type have been proposed in the last years, like the All-sky Medium-Energy Gamma-ray Observatory eXplorer (AMEGO-X) or newASTROGAM, but none have seen the light yet. Possessing this kind of observational data will greatly boost the modelling of the high-energy emission of pulsars, because it will bring continuous energy spectra across almost eight orders of magnitude in energy.

1.2.5 Very-high-energy emission

Very-high-energy emission from pulsars, above 20 GeV and up to several tens of TeV, has been detected for the first time recently, and at the moment of the writing of this thesis there are only 5 pulsars with pulsations detected at such high energies (MAGIC Collaboration, 2008; H. E. S. S. Collaboration et al., 2023). As in the case of γ-rays, very-high-energy photons

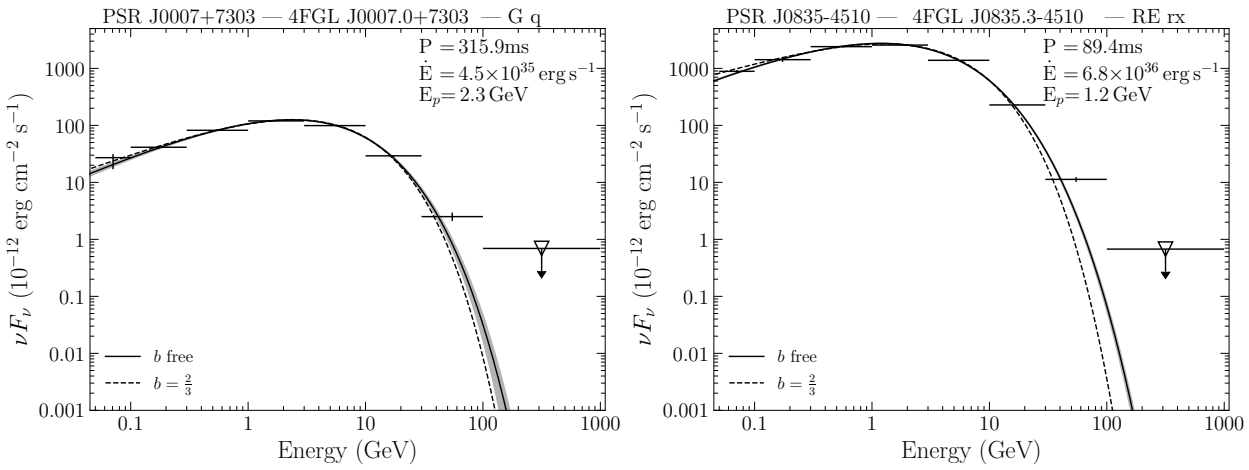


Figure 1.8: Energy spectra in the *Fermi* γ-ray band of PSR J0007+7303 (left) and J0835-4510 (right). Solid and dashed black lines are the fits to the observational data of the phenomenological function PLEC4 presented in Abdollahi et al. (2022). Inverted crosses represent upper limits.

are detected by their pair production. However, the huge energy of the incoming photons results in a production of particles so abundant that a very large detector would be required to reconstruct the event as is done in the *Fermi*-LAT instrument. Building such a huge detector is not feasible, and thus Earth's atmosphere is used for this purpose: the products of the collisions of the very-high-energy photons in the atmosphere are detected from ground and then reconstructed. When the energetic photon collides with an atmospheric particle or molecule it ignites a chain reaction in which particles (hadrons, muons, electrons) are created in several generations until the created particles are not energetic enough to produce more particles or the ground is reached. The subproducts of these extensive air showers can be detected by Imaging Atmospheric Cherenkov Telescopes (IACTs), antennas that detect the Cherenkov radiation of the particles that reach the surface of the Earth.

The Crab pulsar was the first to exhibit emission above tens of GeVs, with pulsations detected by the Major Atmospheric Gamma Imaging Cherenkov Telescopes (MAGIC) above 25 GeV (MAGIC Collaboration, 2008), with the detection confirmed by the Very Energetic Radiation Imaging Telescope Array System (VERITAS) (VERITAS Collaboration, 2011). Again with MAGIC, the TeV frontier in pulsars was broken, and pulsations up to 1.5 TeV from the Crab pulsar were detected (Ansoldi et al., 2016). The Crab energy spectrum has been enlarged recently by the Large Size Telescope - 1 (LST-1), which is part of the future Cherenkov Telescope Array Observatory (CTAO), with pulsations detected at tens of TeV (Abe et al., 2024). The TeV band of the energy spectra smoothly connects with the GeV spectra from *Fermi*-LAT. An energy spectrum with one connected component extending from the Fermi band up to $\sim$ 80 GeV is also observed for the Geminga pulsar (MAGIC Collaboration, 2020), the first middle-aged pulsar detected at this energy range. The situation is very similar for PSR B1706-44, detected below 100 GeV but so far with a 4.7σ significance (Spir-Jacob et al., 2019). The situation is different in the other two pulsars with very-high-energy emission detected, Vela and PSR J1509-5850. Instead of a connected component across several decades in energy, this emission is disconnected from the γ-ray GeV one, forming an energy spectrum with two clearly separated components. This can be seen

in Figure 1.9, together with the light curves at different energy ranges. The reason behind these two different types of spectra remain unclear. Vela's spectrum was found by the High Energy Stereoscopic System (H.E.S.S.) to extend up to 20 TeV (H. E. S. S. Collaboration et al., 2023). At these very-high-energies only the second peak of the light curve clearly remains, while it is not clear whether the first one does or not. J1509-5850 also has detected TeV pulsations with two separated components.

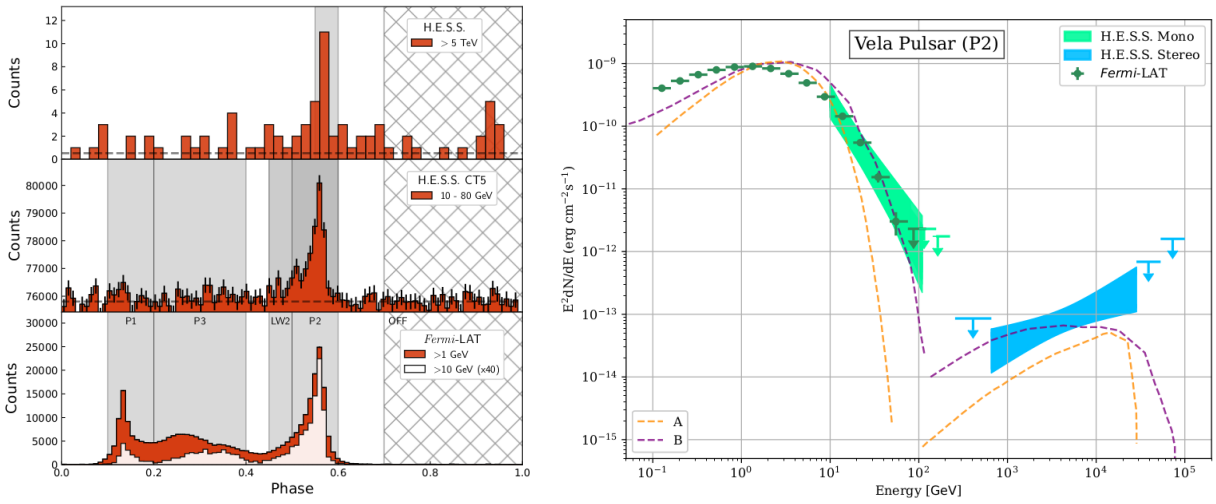


Figure 1.9: Left: Light curves of the Vela pulsar at different energy ranges from H.E.S.S. and *Fermi*-LAT. Right: Phase-resolved high-energy spectrum of the second peak (P2, the one at a phase ~ 0.57) of the Vela pulsar. Figures taken from H. E. S. S. Collaboration et al. (2023).

Within standard synchro-curvature, synchrotron, or curvature radiation scenarios, reproducing both the γ-ray component in the GeV range and the very high-energy component above 20 GeV with a single particle population is difficult under commonly assumed magnetospheric acceleration conditions. An additional emission mechanism should be at work in the magnetosphere. The main candidate is Inverse Compton scattering of low-energy photons by magnetospheric charged particles. The accelerated particles that produce the high-energy emission around GeVs, electrons or positrons, would up-scatter photons surrounding the pulsar and bump their energies up to the TeV range. However, this modelling is still in the first stages and there are many open questions (Harding et al., 2021; H. E. S. S. Collaboration et al., 2023; Cerutti et al., 2025). For instance, the detected pulsations at several tens of TeVs require that the charged emitting particles have very large energies, challenging current particle acceleration mechanisms. Probably the main unknown in this modelling is the target photons that are upscattered. CMB photons, Optical to Near-Infrared photons from the neutron star or soft X-ray photons are candidate target photon fields. The density and distribution of this photon field have only been assumed so far and still require a proper modelling. Synchrotron Self-Compton scattering, i.e. the upscattering of synchrotron photons by the particles emitting them, is also sometimes proposed as the mechanism behind this emission, even though Harding et al. (2018) found it to provide a flux too low for the actual observations.

Apart from the IACTs already mentioned, MAGIC, HESS, VERITAS and LST-1, which are still observing, some new facilities are under construction and will be on duty in the

next few years. Two stand out particularly, the complete CTAO with the North and South Arrays, and the Large Array of imaging atmospheric Cherenkov Telescopes (LACT), which will operate together with the Large High Altitude Air Shower Observatory (LHAASO). Once these new instruments are fully operational, it is expected that the number of pulsars with detected pulsations in this very high-energy band will greatly increase. This may represent a revolution comparable to the *Fermi* one in the GeV range, offering multiple opportunities in the modelling of pulsar emission, which will highly boost this particular field.

1.2.6 The neutron star zoo

RPPs are the most common type of isolated neutron star, but several other classes exist, exhibiting a very diverse phenomenology. Magnetars are objects with an extremely high inferred magnetic field, the highest in the neutron star zoo and the Universe, of $\sim 10^{14-15}$ G, they have large spin periods $P \sim 1 - 10$ seconds and are young, with estimated ages of a few kyr (Kaspi and Beloborodov, 2017). The approximately 30 magnetars currently known are powered by magnetic energy, not by rotational losses, and exhibit powerful flares and bursts of energy in the form of X-rays and soft γ-rays. Even though some of these objects are detected in radio, this emission is extremely variable and strongly differs from the usually stable radio emission of RPPs (Rea and De Grandis, 2026). A few magnetars have inferred dipolar magnetic fields in the range of RPPs and higher estimated ages than the bulk of the population. In parallel, there is a subset of RPPs, the high-B pulsars which have inferred magnetic fields larger than the rest of RPPs, of $\sim 10^{13-14}$ G, and occasionally exhibit magnetar-like outbursts (Gavriil et al., 2008; Archibald et al., 2016b). Therefore, it is plausible to believe in a physical connection between magnetars and RPPs. X-ray dim isolated neutron stars (XDINs) are thermally emitting neutron stars powered by magnetic energy, observed in the X-ray regime but not emitting in radio. Also called the magnificent seven, they are counted among the closest neutron stars to the Earth, have large periods of $P \sim 3 - 11$ seconds and estimated ages of $\sim 10^3$ kyr (Turolla, 2009). Central Compact Objects (CCOs) are detected in X-rays, with no counterparts at other wavelengths, and their emission is of thermal origin (Harding, 2013). CCOs are located at the center of kyr old supernova remnants and for three of them spin periods have been measured, in the range $0.1 - 0.4$ seconds (Borghese and Coti Zelati, 2026). These two last classes have presented phenomenology that connects them with the rest of the neutron star zoo: strong magnetic structures similar to those seen in magnetars have been observed in two XDINs (Borghese et al., 2017) and one CCO has shown magnetar-like activity (Rea et al., 2016). This reinforces the idea that all classes of neutron star (RPPs, magnetars, XDINs, CCOs) are indeed a unique type of object governed by the same fundamental principles but with different properties at birth (e.g. different initial magnetic field) or in different evolutionary stages (Viganò et al., 2013).

Neutron stars can also live in binary systems with a main-sequence star, a white dwarf or another neutron star as companion. Binary systems containing a neutron star and a main-sequence star are often classified based on their phenomenology. Due to the similarity of this phenomenology with binary systems containing a black hole and a star, they are grouped in

joint classes, and dedicated radio timing observations looking for pulsations are required to decipher the nature of the compact object. X-ray binaries contain either a neutron star or a black hole and are divided into high-mass X-ray binaries (Fornasini et al., 2023) or low-mass X-ray binaries (Bahramian and Degenaar, 2023) depending on the mass of the companion star. In these systems, the compact object accretes mass from the companion, forming an accretion disk which thermally emits in X-rays and dominates the total emission from the system. A fraction of LMXBs are proposed as progenitors of MSPs, being the intermediate stage between the binary system with a slow neutron star and the recycled MSP. γ-ray binaries are also binary systems of a neutron star or a black hole, but whose spectra peak in the GeV-TeV energy range (Chernyakova and Malyshev, 2020). The companion stars, of O or Be type, are typically more massive and younger than those of X-ray binaries, and their dominant emission, in the GeV-TeV range, is thought to be produced in the interaction between the stellar winds and the relativistic winds of the compact object. Their emission presents orbital variability at all wavelengths, from radio to TeV. Binary systems formed by two neutron stars, known as double neutron star (DNS) systems, have also been observed, being the endpoint of two massive main-sequence stars in a binary system (Tauris et al., 2017). A few years after the discovery of pulsars, a DNS system in which one of the neutron stars was emitting as a pulsar was observed (Hulse and Taylor, 1975), dubbed the Hulse-Taylor pulsar. The high compactness of the objects forming this system allowed to perform gravitational studies and to test General Relativity with unprecedented accuracy, and its orbital decay was the first (indirect) evidence of gravitational waves emission (Taylor and Weisberg, 1982). The discovery merited a Nobel Prize in Physics, the second and last so far given to studies related to pulsars. Currently, many more DNS systems harbouring a pulsar are known, and are still used as laboratories to test and study General Relativity, for example with precise measurements of timing properties of pulsars in binary systems (Taylor et al., 1979; Kaspi et al., 2000), and gravitational waves from binary neutron star mergers (Abbott et al., 2017). Nowadays the Double Pulsar (Lyne et al., 2004) is the only known DNS system with both neutron stars detected as pulsars.

1.3 Neutron star physics

Having seen the general phenomenology of pulsars, in this section we discuss the physical properties of neutron stars. Neutron stars are the ultra-compact remnants of core-collapse supernovae and were theoretically proposed in 1934 (Baade and Zwicky, 1934), many years prior to the pulsar discovery. Only two years before neutrons had been discovered (Chadwick, 1932) and five years later, independently, Oppenheimer and Volkoff (Oppenheimer and Volkoff, 1939) and Tolman (Tolman, 1939) proposed what is now known as the Tolman-Oppenheimer-Volkoff equation to solve the structure of a neutron star for a given equation of state (EoS).

1.3.1 Formation

Stars are powered by thermonuclear reactions occurring in their interior in which hydrogen is fused into helium. An equilibrium between the thermonuclear pressure and the gravity of the star itself maintains these objects stable during the main-sequence stage, in which stars remain most of their lifetimes. The duration of this stage depends (inversely) on the mass of the star, lasting $\sim 10^{2-3}$ Gyr for red dwarfs, the most common and least massive, $M \sim 0.08-0.6$ $M_\odot$, type of main-sequence star, ~ 10 Gyr for stars like the Sun and $\sim 1-10$ Myr for massive stars, $M \gtrsim 10$ $M_\odot$, the progenitors of neutron stars (Kippenhahn et al., 2013). When the hydrogen budget in the core is exhausted, the star enters the last stage of its life. Since gravity is no longer counteracted, the internal regions begin to contract, which heats up the core and helium fusion into carbon and oxygen is triggered. The thermal pressure of this fusion can counteract gravity in the interior of the star while the outer parts expand and the star converts into a red giant. Density increases in the interior, up to a point in which electrons become degenerate and the electron degeneracy pressure becomes relevant.

In stars with masses $\lesssim 10 M_\odot$, where $M_\odot$ is the Sun's mass, electron degeneracy pressure is able to counteract gravity and prevents further contraction of the core. The subsequent evolution depends on the stellar mass, but in all cases, the outer layers are expelled leaving behind the degenerate core, a remnant called white dwarf, which has a mass in the range $\sim 0.2-1.3$ $M_\odot$ (peaking at ~ 0.6 $M_\odot$), and a size similar to the Earth (Althaus et al., 2010). Stars with masses $\lesssim 0.6$ $M_\odot$ do not reach the temperatures required to ignite helium fusion and the remnant is a Helium white dwarf. Stars with masses in the range $\sim 0.6 - 8 M_\odot$ are able to ignite Helium but not Carbon, and after expelling their outer layers leave behind a white dwarf composed mainly of Carbon and Oxygen, with residues of lighter elements. More massive stars, with masses ~ 10 $M_\odot$, are able to fuse Carbon into Neon and leave behind an Oxygen-Neon white dwarf.

In massive stars with masses in the range $\sim 10 - 20$ $M_\odot$, electron degeneracy pressure cannot counteract gravity and the fusion chain proceeds. After helium is exhausted the core contracts again, igniting the successive burnings of Carbon, Oxygen, Neon and Silicon, each one being triggered by core contraction and increase of temperature once the previous element is exhausted in the core. The repeated burning of different elements creates an onion-like shape with different layers containing the residues of the previous burnings with the newest elements in the core. Each of these processes is faster than the previous one, and proceeds until Iron is produced. Iron has the highest binding energy per nucleon and thus its thermonuclear burning is not energetically favourable and the fusion chain stops. Once further fusion no longer provides sufficient pressure support, gravity overcomes the pressure gradients and the core collapses. This contraction shrinks the core up to a point in which the degenerate pressure of neutrons becomes large enough to counteract gravity. Density reaches very high values, approaching the nuclear density, and the core becomes very rich in neutrons. After the contraction, part of the surrounding envelope of the progenitor falls onto the very dense core and bounces back, resulting in a violent, powerful explosion, the supernova, made possible by the copious neutrino production, and aided by convection, instabilities,

and possibly magnetic fields, which collectively energize the shock (Burrows, 2013). Core-collapse supernovae release a huge amount of energy, able to outshine the entire host galaxy for some weeks or even a few months, and matter, which will enrich the metallicity of the interstellar medium with heavy elements: those up to Iron created in the fusion chain, and even heavier ones produced by endothermic reactions during the supernova due to the extreme energies at play. Normally, the remnant of the supernova is a proto-neutron star, around four orders of magnitude hotter and ten times bigger than the final neutron star. The high temperature and density of the proto-neutron star, $T \sim 10^{11}$ K and $\rho \gtrsim 10^{14}$ g/cm^3, respectively, makes it opaque to neutrinos while these are massively produced and interact with matter producing a thermal pressure that contributes to counteract gravity. As it cools down due to radiation from the surface, it becomes transparent to neutrinos, so they escape and drain energy from the proto-neutron star (Yakovlev et al., 2001), taking out the thermal support and leaving only the degenerate pressure from neutrons to counteract gravity. Due to the emission of neutrinos, the star cools down and shrinks to the final conditions, a neutron star with a temperature below 10^9 K, a radius of $\sim 10 - 15$ km and a mass of $1 - 2$ M$_\odot$. Neutrino cooling is dominant for the first $10 - 100$ kyr of the life of a neutron star, until temperature drops below $\sim 10^8$ K and the cooling is governed by photons emitted from the surface (Potekhin et al., 2015).

The high mass and small size of neutron stars makes them extremely compact objects. Their compactness $\mathcal{C}$, which is defined as the ratio of the Schwarzschild radius, $R_S = 2GM/c^2$ with M the mass, G the gravitational constant and c the speed of light, to the real radius, is $\mathcal{C} \sim \mathcal{O}(0.1)$, while it is 1 for black holes and $\sim 10^{-9}$ for the Earth. This implies that general relativistic effects are important in neutron stars and their surroundings.

Knowing the exact mass and radius of a neutron star is not trivial. So far precise radii measurements remain elusive, because only indirect methods can be used (neutron stars are too small to be resolved from Earth), which rely on strong assumption or models. Masses have been inferred only in some cases. The majority of these calculations have been done for neutron stars in binary systems, measuring post-Keplerian effects, such as the Shapiro delay or the rate of advance of the periastron, to estimate the mass[3]. Measured values range from 1.174 ± 0.004 M$_\odot$ (Martinez et al., 2015) to 2.350 ± 0.170 M$_\odot$ (Romani et al., 2022), and follow a skew normal distribution peaking at $\sim 1.4 M_\odot$ with a long tail at high masses (Özel and Freire, 2016).

Taking into account that neutron stars are the endpoints of massive stars, which typically have spin periods of a few days and surface dipolar magnetic fields on the order of kG (Wade et al., 2016), the rapid rotation and huge magnetic fields of neutron stars can be explained in part with conservation of angular momentum and magnetic flux. During the progenitor collapse, magnetic flux, $\propto BR^2$, and angular momentum $L = I\Omega$ where Ω is the angular velocity and I is the moment of inertia of the neutron star, which depends on the mass and radius of the object, are expected to be roughly conserved. Therefore, the tiny size of a neutron star, ~ 10 km, compared to the size of the progenitor star, $\sim 10^6$ km, implies an increase of both the spin frequency, from $\sim 1 - 100$ μHz to $\sim 0.1 - 1000$ Hz, and the

[3]See www3.mpifr-bonn.mpg.de/staff/pfreire/NS_masses.html for an updated catalogue of neutron star masses.

magnetic field, from $\sim 1-1000$ G to 10^{8-14} G. However, conservation laws neglect important three-dimensional magnetohydrodynamic effects which can be relevant. In particular, the magnetic field of the progenitor can be amplified due to convection and differential rotation during the neutron star formation (Thompson and Duncan, 1993).

1.3.2 Interior

The EoS is a relation between pressure and thermodynamic variables: density and temperature. In the interior of neutron stars, densities exceed the nuclear saturation density ($\rho_0 \approx 2.8 \times 10^{14}$ g/cm^3). We do not know how matter behaves under such huge densities, i.e. we do not know which EoS governs neutron stars. The matter in a neutron star's interior is effectively cold, since its temperature ($T \lesssim 10^8$ K) is orders of magnitude below the Fermi temperature of the degenerate neutrons ($T_F \sim 10^{12}$), which means that the thermal contribution to the pressure is negligible compared to the neutron degeneracy pressure. Neutron degeneracy pressure is exerted by neutrons that have become degenerate by being subjected to high densities and extremely compressed. It is a result of the increase of kinetic energy of the neutrons due to the Pauli exclusion principle. The same concept exists for electrons. As a result, the pressure is a function of density alone and does not depend on temperature. Therefore, the problem reduces to determining the pressure-density function. This is rather uncertain, because at densities $\sim \rho_0$ the behaviour of matter is ruled by the strong nuclear force in a regime not fully understood yet. Many EoSs have been proposed since Oppenheimer, Volkoff and Tolman introduced an EoS for an ideal relativistic gas of degenerate neutrons, mainly differing in the pressure-density relation (see Özel and Freire (2016) for a summary of several EoSs). The composition of the matter inside a neutron star is also different in the many proposed EoSs, since at a given density there is a certain equilibrium composition, which is set very early after the neutron star birth, regardless of the progenitor composition, via fast pycnonuclear reactions. Each EoS predicts a different mass-radius relation for neutron stars, and mass measurements thus provide a way to test and constrain EoSs, since those that predict a maximum mass below the highest reliably measured values can be ruled out. Since physical systems subject to high densities of the order of ρ_0 cannot be replicated in any laboratory on Earth, understanding the EoS of neutron stars will in turn improve our knowledge of the behaviour of matter under extreme conditions.

The most exterior layer of a neutron star is a gaseous atmosphere of density ~ 1 g/cm^3 and a thickness of a few cm. Right below there is the envelope, with a depth of around 100 m and a negligible proportion of the mass of the neutron star. It has a relatively low density of $\lesssim 10^9$ g/cm^3 and is formed by nuclei and electrons. Going inside the neutron star we find the crust, a region of approximately 1 km in depth containing $\sim 1\%$ of the mass of the neutron star, where the density reaches values of $\sim 10^{14}$ g/cm^3, close to the nuclear density. Due to the high density, matter in this layer is in the form of an elastic solid lattice of heavily packed nuclei with the presence of a gas of free degenerate electrons and free neutrons. Free neutrons are only present when the dripping point is reached, at $\rho_d \sim 2-4 \times 10^{11}$ g/cm^3. This point indicates a separation between an inner ($\rho > \rho_d$) and an outer ($\rho < \rho_d$) crust. As we go down the star and approach the core, degenerate neutrons

are more prevalent and matter takes complex shapes with tube-like structures and voids, in what is known as pasta phases. The innermost region is the core and accounts for $\sim 99\%$ of the total mass of the neutron star and typically represents $\sim 70 - 90\%$ of the star's volume, with a radius of ~ 10 km. Here the nuclear saturation density values of $\sim 10^{14-15}$ g/cm^3 are achieved and nuclei dissolve into an ocean of free, degenerate neutrons which coexist with protons, electrons, muons and even exotic forms of matter, such as hyperons. However, the exact composition of the core is not well understood yet, and deconfined quark matter has also been proposed to fill the interior of neutron stars instead of the particles mentioned above. Not only astrophysics would be benefited from a better understanding of the neutron star interior, but also nuclear and particle physics, since it gives a perfect scenario to study matter in conditions so extreme that cannot be studied in the laboratory.

Finally, it is worth mentioning that superfluidity is expected to play a relevant role in the interior of neutron stars, for instance in the form of an important deviation from the remarkably stable rotation of pulsars: glitches. Glitches are sudden spin-up events in which the angular velocity increases suddenly by a fractional amount $\Delta\Omega/\Omega \sim 10^{-11} - 10^{-5}$, followed by a relaxation towards the spin-down rate previous to the glitch on timescales of days to months (Espinoza et al., 2011; Antonopoulou et al., 2022). Glitches have been observed in more than 200 pulsars, with young pulsars such as Vela being the ones in which glitches are more common. It is usually proposed that glitches may be the result of the transfer of angular momentum from a superfluid component in the neutron star core to the crust. Thus, glitches are unique observational probes of the neutron star internal structure (Andersson et al., 2012; Haskell and Melatos, 2015).

2

Magnetospheric models of pulsars

The origin of the high-energy emission of pulsars has been widely studied since the discovery of these objects, being clear since the very beginning that emission should be produced in the region surrounding the neutron star, the so-called magnetosphere. The production of the high-energy emission thus strongly depends on the structure of the magnetosphere, as well as on the electromagnetic fields within it. Therefore, understanding this structure and the configuration of the magnetic and electric fields is crucial to understand the emission of a pulsar, in particular in the high-energy range. In addition, high-energy emission is produced by accelerated charged particles, and thus it is also important to study the dynamics of the emitting particles and the emission mechanisms at work.

Models studying the high-energy emission of pulsars can be divided mainly into three groups: global magnetosphere models, radiative models and geometrical models. Global magnetosphere models attempt to describe the overall configuration of charge currents, particle distributions and electromagnetic fields in the surroundings of the pulsar, while the latter two assume a certain configuration of the electromagnetic fields and try to describe pulsar observations, with more focus on the particle dynamics and energetics (radiative models) or on the geometry of the emission (geometrical models).

2.1 Spin-down properties of pulsars

In the previous chapter we have seen that the emission of pulsars is powered by losses of rotational energy. Therefore, before entering into the details of the magnetospheric models, it is interesting to examine the global energetics of pulsars, mainly governed by an electromagnetic torque exerted on the pulsar, and its relation with the emission.

2.1.1 Energy radiation by magnetic moments

The energy radiated by a misaligned magnetic moment $\mathbf{m}$ in vacuum varying in time is given by classical electrodynamics (Jackson, 1998). The total power radiated by $\mathbf{m}$ integrated over the solid angle is

$$\dot{E}_{\mathbf{m}} = \frac{2}{3c^3}\left|\frac{d^2\mathbf{m}}{dt^2}\right|^2 \ . \tag{2.1}$$

where c is the speed of light and t is the time. For a magnetic dipole rotating in vacuum and misaligned an angle Ψ_Ω with respect to the rotational axis, the magnetic moment is $\mathbf{m} = |\mathbf{m}| \sin\Psi_\Omega e^{i\Omega t}$. The dipolar magnetic field strength at the surface magnetic pole can be expressed in terms of this magnetic moment as $B_{\rm s} = 2|\mathbf{m}|/R_\star^3$, where $R_\star$ is the neutron star radius (at the equator, the surface dipolar magnetic field is half of this value). The electromagnetic energy loss is then

$$\dot{E}_{\mathbf{m}} = \frac{2|\mathbf{m}|^2\Omega^4}{3c^3}\sin^2\Psi_\Omega \ . \tag{2.2}$$

If the dipole is not in vacuum but instead is surrounded by plasma, the energy radiated is enhanced and, as inferred from numerical simulations (e.g. Spitkovsky 2006), can be expressed as

$$\dot{E}_{\mathbf{m}} \simeq \frac{|\mathbf{m}|^2\Omega^4}{c^3}(1+\sin^2\Psi_\Omega) \ , \tag{2.3}$$

which implies that even aligned rotators slow down.

Apart from a rotating dipole, there exists a particularly interesting magnetic configuration, the split-monopole model of Michel (1973), which we will see in subsection 2.2.3. In this idealized case, the magnetic field configuration is formed by two magnetic monopoles with opposite polarities, and the rotational losses do not depend on the inclination angle (Bogovalov, 1999) and are

$$\dot{E}_{\mathbf{m}} = \frac{2|\mathbf{m}|^2\Omega^4}{3c^3} \ . \tag{2.4}$$

2.1.2 Electromagnetic torque and pulsar spin-down

Pulsars slow down with time, i.e. their spin periods increase. This slow-down is caused by an electromagnetic torque exerted on the pulsar, which results in a loss of rotational kinetic energy that can be expressed as (Lorimer and Kramer, 2004)

$$\dot{E} = -\frac{d}{dt}\left(\frac{1}{2}I\Omega^2\right) = -I\Omega\dot{\Omega} = 3.95\times10^{45}\frac{\dot{P}}{P^3}\text{erg/s} \ , \tag{2.5}$$

where the moment of inertia I is usually set to a conventional value of 10^{45} g/cm^2 (see Chapter 6 for more details on this value), $\Omega = 2\pi/P$ and $\dot{\Omega} = -2\pi\dot{P}/P^2$ is the angular velocity derivative. $\dot{E}$, also called spin-down power, is the energy budget of a pulsar, i.e. it is the total power available for the pulsar to be ultimately converted into radiation. It plays a crucial role in the study of pulsar physics.

The origin of the electromagnetic torque is similar if the pulsar is in vacuum or surrounded by plasma. In both cases, energy and angular momentum from the pulsar is carried away by the Poynting flux of an electromagnetic wave propagating at a frequency equal to the spin

frequency of the pulsar. However, in the plasma case part of this Poynting flux is dissipated into acceleration of particles that radiate high-energy emission, as we will see later on. The Poynting flux represents the electromagnetic energy flow and is defined by the electric and magnetic fields as $\mathbf{S} = c\mathbf{E}\times\mathbf{B}/4\pi$. Integrating the Poynting flux over a closed surface of area $\mathbf{A}$ around the neutron star determines the electromagnetic torque, which is the dominant contributor to the spin-down of the pulsar:

$$\dot{E} = \int \mathbf{S}\cdot d\mathbf{A} \tag{2.6}$$

In both cases, the energy radiated by the pulsar's magnetic moment comes at the expense of its rotational energy. Therefore, assuming that the energy losses of pulsars are dominated by magnetic dipole radiation, we can equate Equations (2.2) and (2.5) and obtain:

$$-I\Omega\dot{\Omega} = \frac{2|\mathbf{m}|^2}{3c^3}\Omega^4 f_\Psi \ , \tag{2.7}$$

which can be used to estimate several pulsar quantities given the timing properties of the pulsar, P and $\dot{P}$. f_Ψ is a factor that contains the different magnetic configurations. $f_\Psi = \sin^2\Psi_\Omega$ for a dipole in vacuum, $f_\Psi = 1.5(1+\sin^2\Psi_\Omega)$ for a dipole surrounded by plasma and $f_\Psi = 1$ for a split monopole. Considering only dipolar losses is a reasonable approximation, given that, far away from the surface, the dipolar component ($l = 1$) dominates over multipolar components of order $l > 1$, whose magnetic fields decay as $r^{-(l+2)}$.

The magnetic field strength at the surface of a neutron star can be inferred from Equation (2.7). Substituting in this Equation the expression of the magnetic moment of a dipole presented above, we obtain (using the spin period P instead of the angular velocity Ω):

$$P\dot{P} = \frac{2\pi^2 R_\star^6 f_\Psi}{3c^3 I} B_{\rm s}^2 \ , \tag{2.8}$$

which leads to an expression for the surface magnetic field strength at the magnetic pole of a neutron star:

$$B_{\rm s} = \sqrt{\frac{3c^3 I}{3\pi^2 R_\star^6 f_\Psi} P\dot{P}} \ . \tag{2.9}$$

Using the conventional value of $I = 10^{45}$ g/cm^2, the canonical star radius of $R_\star = 10$ km $= 10^6$ cm and arbitrarily considering an orthogonal rotator in vacuum, i.e. $\Psi_\Omega = 90°$ and $f_\Psi = 1$, we obtain

$$B_{\rm s} = 6.41\times10^{19}\sqrt{P[s]\dot{P}}\ G \ , \tag{2.10}$$

This value is an estimation in which a dipolar magnetic field in vacuum is assumed, i.e. it is an idealized and not totally realistic scenario, and overestimates by a factor $1.5(1+\sin^2\alpha)$ the more realistic plasma-fill case. Moreover, I and $R_\star$ can differ from the fiducial values, introducing further uncertainty on the inferred $B_{\rm s}$.

Equation (2.7) offers an additional interesting output. It can be rearranged to give an expression for the time evolution of the angular velocity:

$$\dot{\Omega} = -\left(\frac{2|\mathbf{m}|^2\sin^2\Psi_\Omega}{3c^3 I}\right)\Omega^3 \ , \tag{2.11}$$

which can be generalized to account for different magnetic field geometries and additional torques apart from the electromagnetic one (e.g. caused by the emission of gravitational waves), following Lorimer and Kramer (2004), as:

$$\dot{\Omega} = -K\Omega^n \ , \tag{2.12}$$

where $K = (2|\mathbf{m}|^2 \sin^2 \Psi_\Omega)/(3c^3 I)$, and n is the so-called braking index, a relevant parameter in the study of pulsar physics. Differentiating Equation (2.12) we obtain an expression for the second time derivative of the angular velocity:

$$\ddot{\Omega} = -nK\Omega\dot{\Omega} \ . \tag{2.13}$$

This expression holds as long as the elements inside the factor K, i.e. the modulus of the magnetic moment $|\mathbf{m}|$ (i.e. the magnetic field strength), the inclination angle Ψ_Ω and the moment of inertia I, do not vary with time. If they do, the calculations complicates and extra terms appear in these expressions. If we combine Equations (2.12) and (2.13), we obtain an expression for the braking index:

$$n = \frac{\Omega\ddot{\Omega}}{\dot{\Omega}} \ . \tag{2.14}$$

For a pure dipolar magnetic field in which $|\mathbf{m}|$, Ψ_Ω and I are constant in time, $n = 3$. However, this is a highly idealized case, and in a real scenario the magnetic field strength and the inclination angle are expected to vary with time (Philippov and Spitkovsky, 2014). Thus, for real pulsars the braking index n can have very different values. Estimating n is not an easy task, since it requires the measurement of the second time derivative of the angular velocity, which is influenced by timing noise. n has been measured for several hundreds of pulsars, even though with large errors in some cases, and values has high as 10^5, both negative and positive, have been found (Pons et al., 2012; Parthasarathy et al., 2019). So far, stable, reliable values of n have been estimated only for a few, young pulsars whose time derivatives of Ω have been measured with low errors, going from $n = 0.9$ (Espinoza et al., 2011) up to $n = 3.15$ (Archibald et al., 2016a).

The age of a pulsar can also be estimated considering its spin-down properties, with the so-called characteristic age:

$$\tau_\mathrm{c} = \frac{P}{2\dot{P}} \ . \tag{2.15}$$

Similarly to B_s, τ_c is only an estimate of a pulsar's age under certain conditions: dipolar magnetic braking as the only source of rotational energy loss, period at birth much smaller than the observed period and no time evolution of inclination angle or magnetic field strength. Thus, the real age of a pulsar may considerably differ from τ_c. This is particularly true in MSPs, which have an evolution different to regular pulsars, undergoing a recycling process that spun them up and decreases their spin period, as we have seen in Chapter 1.

2.2 Global Magnetosphere Models

2.2.1 Pulsar magnetosphere

Maxwell equations describe electromagnetic fields and their evolution, and in global magnetosphere models are solved (in Gaussian units) in order to obtain the structure of the magnetosphere

$$\boldsymbol{\nabla} \cdot \mathbf{E} = 4\pi\rho_e \tag{2.15a}$$

$$\boldsymbol{\nabla} \times \mathbf{E} = -\frac{1}{c}\frac{\partial \mathbf{B}}{\partial t} \tag{2.15b}$$

$$\boldsymbol{\nabla} \cdot \mathbf{B} = 0 \tag{2.15c}$$

$$\boldsymbol{\nabla} \times \mathbf{B} = \frac{4\pi}{c}\mathbf{j} + \frac{1}{c}\frac{\partial \mathbf{E}}{\partial t} \tag{2.15d}$$

where ρ_e and $\mathbf{j}$ are the electric charge and current densities, respectively. For simplicity we consider a flat metric. Corrections of order $10-20\%$ appear if General relativity is considered instead.

A very relevant lengthscale for the study of magnetospheres is the light cylinder radius, defined as

$$R_{LC} = \frac{cP}{2\pi} \ . \tag{2.16}$$

The light cylinder is the surface at which the velocity of corotation with the star becomes equal to the speed of light, and divides the magnetosphere into two regions: inside it, a corotating zone, and outside it, a wind zone. In the corotating zone magnetic field lines are closed and the plasma can corotate with the star. In the wind zone the corotation velocity is higher than the speed of light and thus plasma cannot corotate with the neutron star. This forces a differential rotation of the plasma in this region that sweeps back the lines in the azimuthal direction and stretches them, causing these field lines (that cross the light cylinder) to open up. Open magnetic field lines extend far from the neutron star and carry plasma away from it, forming a relativistic pulsar wind. See Figure 2.1 for a schematic picture.

2.2.2 Vacuum magnetospheres

Initial global magnetosphere models assumed vacuum around the neutron star (Pacini, 1967; Ostriker and Gunn, 1969). These models considered a dipole magnetic field, which under rotation in vacuum emits an electromagnetic wave at the pulsar spin frequency[1] that transports energy and angular momentum away from the neutron star, spinning down the pulsar. Equation (2.2) shows the spin-down power of a vacuum magnetosphere, and implies that an

[1]For regular pulsars ($P \sim 10^{-3} - 1$ s) this implies a frequency of the wave in the range $10^{-3} - 1$ kHz. This frequency is below the plasma frequency of the surrounding nebula (and the interstellar medium) and thus the wave will be absorbed and undetectable. Note that this applies for the electromagnetic wave coming from the rotating dipole, whereas the emission we detected comes from the acceleration of particles and has higher frequencies.

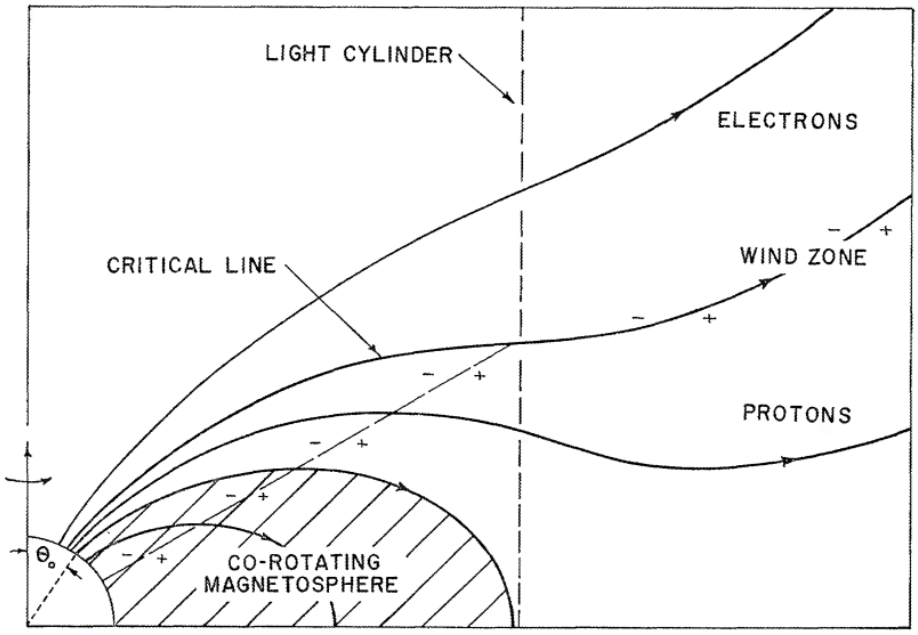


Figure 2.1: Representation of the plasma-filled magnetosphere of Goldreich and Julian (1969), consisting of a corotating region where magnetic field lines are closed and a wind zone with open field lines.

aligned rotator in vacuum does not lose rotational energy and thus does not emit radiation (Pacini, 1968; Ostriker and Gunn, 1969).

The first analytical solution, and so far the only one, for the electromagnetic fields in the magnetosphere was found by Deutsch (1955), who assumed a conducting star in vacuum, the retarded vacuum dipole model. It is relevant to notice that the model was not specifically intended for neutron stars, which had not yet been discovered at the time, but rather for an idealized star. In the scenario of a perfectly conducting, magnetised sphere, the unipolar induction effect creates an electric field in the interior of the neutron star to balance the magnetic force. Taking into account boundary conditions on the neutron star surface, the electric potential outside, Φ, can be found solving Poisson's equation in vacuum $\nabla^2\Phi = 0$. Then, the expression $\mathbf{E} = -\nabla\Phi$ gives the electric field outside the neutron star, which is capable to accelerate particles up to high energies. The radial component of $\mathbf{E}$ is discontinuous at the surface, which implies a surface charge (Mestel, 1971). The exact solution can be found in section 7 of Michel and Li (1999). Notice that in this solution, the electric field outside the neutron star has a quadrupolar structure, $\sim r^{-4}$, while the magnetic field takes the form of a modified magnetic dipole, $\sim r^{-3}$. Near the light cylinder the magnetic field is swept back opposite to the direction of rotation, and beyond the solution takes the form of an electromagnetic wave with the shape of an Archimedean spiral (Harding, 2022).

For reference, it is interesting to show here the electromagnetic structure in the observer frame of a rotating magnetic dipole in vacuum (Cerutti and Beloborodov, 2017),

$$(B_{\rm r}, B_\theta, B_\phi) = B_{\rm s}\left(\frac{R_\star}{r}\right)^3 (2\cos\theta, \sin\theta, 0) \ , \tag{2.17}$$

$$(E_{\rm r}, E_\theta, E_\phi) = B_{\rm s}\frac{R_\star}{R_{LC}}\left(\frac{R_\star}{r}\right)^4 (1-3\cos^2\theta, -\sin 2\theta, 0) \ . \tag{2.18}$$

2.2.3 Force-Free Electrodynamics

Despite the great impact in the history of pulsar emission modelling of the vacuum retarded dipole model, soon after the discovery of pulsars it was found that the model was not physically realistic. Goldreich and Julian (1969) demonstrated that neutron stars cannot be surrounded by vacuum, because the induced electric field outside the neutron star is so strong that it can overcome the gravitational force of the star and strip off charged particles from the surface. See Figure 2.1 for a schematic representation of the magnetosphere. These particles are accelerated by the electric field component parallel to the magnetic field, $E_{||}$, and initiate a pair cascade that fills the magnetosphere. Under this scenario, the magnetosphere is supplied with enough plasma to screen the parallel electric field $E_{||}$, and the electric field is the one of a moving perfect conductor:

$$\mathbf{E} = -\frac{\mathbf{v}_c \times \mathbf{B}}{c} \ , \tag{2.19}$$

where $\mathbf{v}_c = (\Omega \times \mathbf{r})$ is the corotation velocity, with $\mathbf{r}$ the position vector from the centre of the neutron star. This determines a charge density in the magnetosphere, $\rho = \boldsymbol{\nabla} \cdot \mathbf{E}/4\pi$, equal to:

$$\rho_{GJ} \approx \frac{-\boldsymbol{\Omega} \cdot \mathbf{B}}{2\pi c} \ , \tag{2.20}$$

the so-called Goldreich-Julian charge density. In this situation, the Lorentz force on the charged particles vanishes, which leads to the so-called force-free condition,

$$\rho\mathbf{E} + \frac{\mathbf{j} \times \mathbf{B}}{c} = 0 \ , \tag{2.21}$$

where ρ is the charge density and $\mathbf{j}$ is the current density, and implies that $\mathbf{E} \cdot \mathbf{B} = 0$ in the whole magnetosphere.

The most general expression for a current density in the magnetosphere that satisfies the force-free condition is (Pétri, 2016b)

$$\mathbf{j} = c\rho\frac{\mathbf{E} \times \mathbf{B}}{B^2} + j_{||}\frac{\mathbf{B}}{B} \ , \tag{2.22}$$

where $j_{||}$ is a generic field-aligned current density (Philippov and Kramer, 2022).

Magnetic energy density is larger than kinetic energy density, meaning that plasma pressure and inertia terms can be safely neglected, and plasma dynamics in the magnetosphere is solely governed by Equation (2.21). The scenario in which this assumption is considered is the so-called Force-Free Electrodynamics (FFE), which can be also regarded as a low-inertia limit of Magnetohydrodynamics (MHD) with the $\mathbf{E} \cdot \mathbf{B} = 0$ condition. In FFE the magnetospheric plasma is treated as a fluid. The very same nature of FFE magnetospheres implies that emission is not possible, because the parallel component of the electric field always vanishes and thus charged particles are not accelerated along the magnetic field lines and do not emit relevant radiation. They simply follow magnetic field lines (spiralling around them) and corotate with the neutron star with a drift velocity,

$$\mathbf{v}_D = \frac{\mathbf{E} \times \mathbf{B}}{B^2} \tag{2.23}$$

Their corotation velocity would become larger than the speed of light at the light cylinder, and thus further away the charged particles no longer corotate. This imposes a subluminal drift velocity and implies that $E < B$. In this situation, field lines are bent and a toroidal component of the magnetic field is induced.

From the force-free condition, Equation (2.21), we can derive an expression that describes the electromagnetic fields and currents in an axisymmetric FFE magnetosphere, the pulsar equation (Michel, 1973; Scharlemann and Wagoner, 1973). In cylindrical coordinates (R, z) it has the form:

$$\left(1 - \frac{R^2}{R_{LC}^2}\right) \nabla^2 \Psi - \frac{2}{R}\frac{\partial \Psi}{\partial R} + \frac{16\pi^2}{c^2} I(\Psi) \frac{\partial I}{\partial \Psi} = 0 \ , \tag{2.24}$$

where $\Psi(R, z)$ is the magnetic flux function, which describes the poloidal component of the magnetic field, and $I(\Psi)$ is the current function, which describes the amount of current flowing in the magnetosphere along the meridional direction, related to the toroidal component of the magnetic field (Philippov and Kramer, 2022). The pulsar equation, which is a FFE extension of the Grad-Shafranov equation used in MHD, requires the definition of the angular frequency, the magnetic field at the surface and the current function. Michel (1973) found an analytical solution to the pulsar equation assuming a monopole at each hemisphere with opposite polarity of the electromagnetic fields. The solution is

$$(B_{\rm r}, B_\theta, B_\phi) = B_{\rm s} \left(\frac{R_\star}{r}\right) \left(\pm \frac{R_\star}{r}, 0, -\frac{R_\star}{R_{LC}} \sin\theta\right) \ , \tag{2.25}$$

$$(E_{\rm r}, E_\theta, E_\phi) = (0, B_\phi, 0) \ . \tag{2.26}$$

In this model, magnetic field lines do not close and become radial outside the light cylinder and far away from the pulsar, and the toroidal component dominates. Michel's split monopole was generalized to oblique rotators in Bogovalov (1999).

Apart from this particular case, in general the force-free magnetosphere does not have an analytical solution, and thus numerical methods are needed to obtain a solution of the magnetosphere for more realistic magnetic field configurations. The increase in computational capabilities allowed to develop these numerical simulations, and Contopoulos et al. (1999) found the first numerical solution for an axisymmetric FFE magnetosphere with a dipole magnetic field at the neutron star surface (see left panel of Figure 2.2). The approach taken was to solve the pulsar equation inside and outside the light cylinder separately and ensuring smoothness of the solution across the light cylinder. In this solution, magnetic field lines close inside the light cylinder and open up outside, in a picture similar to that proposed in Goldreich and Julian (1969), and far away from the light cylinder lines become almost radial, resembling the split monopole of Michel (1973). The authors found a closed current system in which current flows away from the neutron star along open field lines and returns at the equator, forming an equatorial current sheet (ECS), and at the separatrix, which is the boundary between the closed and open field lines regions (Harding, 2022). The ECS and the separatrix join at the so-called Y-point, located at the light cylinder radius. Magnetic field reverses polarity across the ECS and therefore magnetic reconnection is likely to occur, being usually proposed as a way to accelerate the charged particles responsible for the high-energy emission (Lyubarskii, 1996; Mestel and Shibata, 1994). This is a conceptually similar picture to the one proposed by striped wind models (see below, Section 2.3.5), but modelling

the structure of the whole magnetosphere, from the neutron star surface, and not limiting to the wind zone outside the light cylinder, as striped wind models do. See Pétri (2012a) for a study connecting the striped wind with a FFE magnetosphere. The Contopoulos et al. (1999) solution was reproduced by e.g. Gruzinov (2005) and later by Timokhin (2006), who also found that solutions could be found with the Y-point located at any position within the light cylinder, i.e. the magnetospheric solution was not unique. These solution also have a dipole magnetic field at the surface of the neutron star.

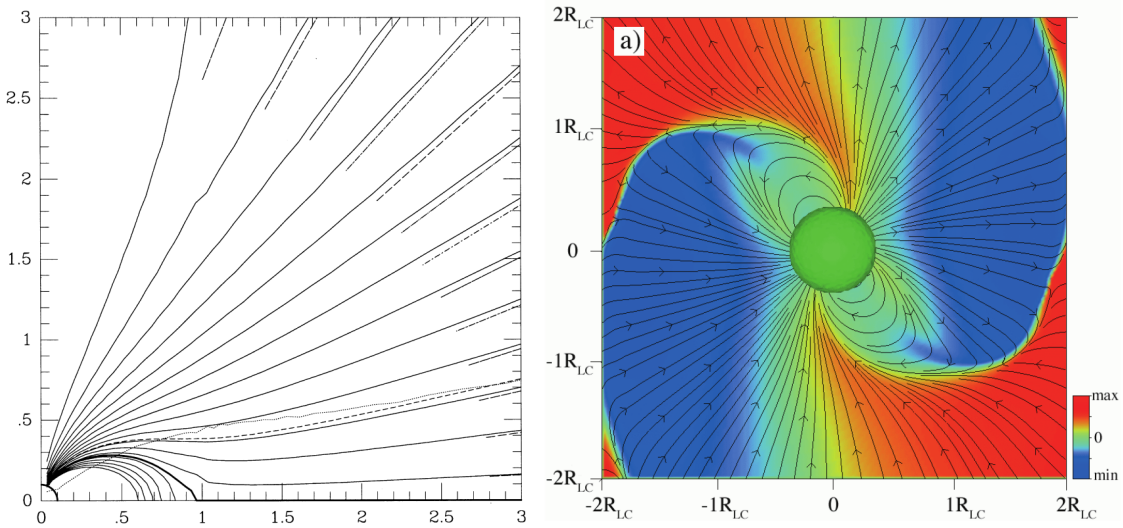


Figure 2.2: Left: solution from Contopoulos et al. (1999) of an axisymmetric FFE magnetosphere, with magnetic field lines closing inside the light cylinder and becoming almost radial far from the neutron star. Right: magnetosphere of an oblique rotator with $\Psi_\Omega = 60°$ from Spitkovsky (2006), where the black lines are the magnetic field lines and the colour scale is the magnetic field strength perpendicular to the plane of the image.

The extension to oblique FFE magnetospheres was given in Spitkovsky (2006), who numerically solved the time-dependent Maxwell equations in three dimensions, in particular Faraday's law (Equation 2.15b) and Ampère's law (Equation 2.15d), for arbitrary inclination angles. Starting from a dipole magnetic field, Maxwell's equations are solved assuming the full FFE current density, Equation (2.22), with the additional condition $\partial(\mathbf{E}\cdot\mathbf{B})/\partial t = 0$, which allows one to express the field-aligned current in terms of the electromagnetic fields. Then, the prescription of the current density fulfilling the force-free condition is (Gruzinov, 1999; Blandford, 2002)

$$\mathbf{j} = c\rho\frac{\mathbf{E}\times\mathbf{B}}{B^2} + \frac{c}{4\pi}\frac{(\boldsymbol{\nabla}\times\mathbf{B})\cdot\mathbf{B} - (\boldsymbol{\nabla}\times\mathbf{E})\cdot\mathbf{E}}{B^2}\mathbf{B} \ . \tag{2.27}$$

The solution found resembled that of Contopoulos et al. (1999), with closed and open field lines regions, and a wind zone outside the light cylinder with a dominant toroidal component of the magnetic field and field lines becoming radial far away from the light cylinder. A closed current system is found, and the Y-point is located at around $1R_{LC}$. The previous degeneracy on its location is resolved, because the time-dependent equations used in this study are not singular at the light cylinder, unlike the pulsar equation, and the current distribution found is unique (Philippov and Kramer, 2022). An ECS is also formed but oscillating around

the rotational equator with amplitude Ψ_Ω and wavelength $2\pi R_{LC}$, resembling the shape of a ballerina skirt (Cerutti and Beloborodov, 2017). See right panel of Figure 2.2 for the structure of this magnetospheric solution.

The solution of Spitkovsky (2006) was replicated by e.g. Kalapotharakos and Contopoulos (2009); Pétri (2012a) and its spatial domain was enlarged in Kalapotharakos et al. (2012a). The effects of General Relativity on a FFE magnetosphere were studied in e.g. Pétri (2016a) and Carrasco et al. (2018), both finding that the spin-down luminosity increases up to a factor ~ 2 when general relativistic effects are taken into account.

A common feature of FFE magnetospheres, as we have seen, is the formation of ECS, across which the magnetic field switches signs. This implies that the radial component of B can approach to 0 at some point, and thus the low-inertia assumption no longer holds and the force-free condition is broken. To overcome this drawback, FFE simulations subtract the generated $E_{||}$ from the electric field $\mathbf{E}$ at each time step (Pétri, 2012a), mimicking dissipation of the magnetic field (Komissarov, 2004). Acting in this way, force-free condition is restored. This marks regions where the magnetic field is dissipated, a feature that does not arise naturally from FFE, i.e. regions where particle acceleration and radiation emission can occur. In addition, it is interesting to note that, since FFE requires abundant plasma supply to hold, the force-free condition can be broken if the charge density in a given place of the magnetosphere departs from ρ_{GJ} by some kind of plasma instabilities.

A caveat of FFE simulations is that no information about particle dynamics can be obtained directly, because they only treat the electromagnetic fields. Therefore, plasma creation, which plays a relevant role in the configuration of the magnetosphere, is not self-consistently addressed and it is simply assumed that there is enough plasma around the neutron star. Efforts have been made in order to understand how the FFE magnetosphere is filled with plasma, such as those in Timokhin (2010); Timokhin and Arons (2013). In addition, FFE simulations are limited by their computational cost, typically amounting to hundreds of thousands of CPU hours. This limits the spatial domain of these simulations to several light cylinder radii, which are in turn just a few neutron star radii. Therefore, the simulated pulsars are typically MSPs and the conclusions obtained are extrapolated to the whole population of pulsars.

2.2.4 Dissipative force-free simulations

FFE simulations do not allow one to study particle acceleration and the associated radiation, for which relaxing the force-free condition is required. Dissipative (or resistive) force-free simulations try to overcome this limitation by imposing artificial dissipation of the magnetic field, which is interpreted to be channelled into particle acceleration and high-energy emission (Li et al., 2012; Kalapotharakos et al., 2012b). In this way, a global magnetosphere solution is found in which the force-free condition is not fulfilled in the entire magnetosphere, allowing the appearance of regions where a parallel electric field can develop. This is done by including a resistive term corresponding to the electrical resistivity, which physically dissipates currents and hence, magnetic fields. The resistive term introduces the electrical conductivity σ. The computational cost does not allow one to reach the microscopical resistive spatial scales

corresponding to realistic values of conductivity, and thus one uses σ as a free, homogeneous parameter. The limit of $\sigma \to 0$ corresponds to a vacuum magnetosphere, while the opposite limit of $\sigma \to \infty$ is the force-free regime, and the spectrum of finite values of σ is explored to investigate different degrees of resistivity. The current density for the case of a resistive force-free magnetosphere was proposed by Gruzinov (2008) and later reformulated by Li et al. (2012) considering Ohm's law in the fluid rest frame which has electric fields parallel to magnetic fields as

$$\mathbf{j} = c\rho \frac{\mathbf{E}\times\mathbf{B} + \sqrt{\frac{B^2+E_0^2}{B_0^2+E_0^2}}\sigma E_0 (B_0\mathbf{B} + E_0\mathbf{E})}{B^2 + E_0^2} \ , \tag{2.28}$$

where B_0 and E_0 are the strength of the magnetic and electric field, respectively, in the frame where they are parallel, as defined by Gruzinov (2008). Notice that the denominator has a term E_0^2 not present in the FFE current density, Equation (2.27). This term prevents the drift velocity from becoming superluminal, which eases the computation of the magnetosphere structure near the ECS. Resistive force-free simulations produce distributions of parallel electric field, thus giving the possibility to trace the locations where particles are accelerated and emit. Therefore, these simulations can generate light curves and spectra that can be compared with observational data. In this way different magnetospheric configurations can be tested and data-driven conclusions can be obtained.

A special case of resistive force-free simulations was introduced in Kalapotharakos et al. (2014), who proposed a force-free magnetosphere inside the light cylinder and a dissipative magnetosphere outside, i.e. the light cylinder divides regions of infinite and finite conductivity. This is called Force-Free Inside Dissipative Outside (FIDO) model and the prescribed current density $\mathbf{j}$ used is

$$\mathbf{j} = c\rho \frac{\mathbf{E}\times\mathbf{B}}{B^2 + E_0^2} + \sigma \mathbf{E}_{\parallel} \ , \tag{2.29}$$

where the second term is the resistive term and regulates the strength of the parallel electric field through the conductivity σ, which is set to infinite inside the light cylinder and high and finite outside. This model was successful in generating light curves with features compatible with the Fermi observational ones, and so was a later extension in which the dynamics of the emitting particles in the dissipative zones was self-consistently calculated (Brambilla et al., 2015).

2.2.5 Kinetic models with Particle-In-Cell simulations

We have seen the difficulty of FFE simulations to create regions of particle acceleration and emission in a self-consistent way. Global kinetic plasma models are a way to overcome this caveat, since they give a way to calculate and track the feedback between the particles and the electromagnetic fields. These models use Particle-In-Cell (PIC) simulations, in which the time-dependent Maxwell's equations are simultaneously solved with the equation of motion of the particles, in alternating time steps. PIC simulations consider macro-particles that represent a large number of charged particles with assumed similar trajectories. In the last decade many PIC simulations have been published, in all of them appearing ECSs like the ones in FFE simulations, and these are indeed the places where the high-energy emission is

produced. The main differences among these simulations lie on the treatment of the plasma supply, which we have already seen that it is a sensitive aspect in pulsar magnetosphere modelling which FFE could not properly address. A relevant parameter in PIC simulations is the plasma magnetization σ_M. The maximum Lorentz factor Γ that magnetospheric particles can be accelerated to is assumed to be a few times σ_M.

The first kinetic models with PIC simulations considered aligned rotators. Philippov and Spitkovsky (2014) used a 3D code with a Cartesian grid in which electron-positron pairs were injected all along the computational domain. Their magnetospheric solution was similar to those of FFE simulations and showed the presence of magnetic reconnection in the ECS. A more physically motivated pair production was introduced in Chen and Beloborodov (2014), in whose simulation pairs were produced if particle energies reached an arbitrary threshold. With this simple plasma supply approach, the authors found that pair creation should occur in the return current layer as well as in the ECS. This conclusion was replicated in Philippov et al. (2015b) for the more general case of oblique rotators. Pair creation in the polar cap for near aligned rotators required the implementation in the simulation of General Relativity effects, in particular frame-dragging, as found by Philippov et al. (2015a).

At that time, other works focused on the Poynting flux dissipation into particle acceleration of aligned rotators, such as Cerutti et al. (2015) with a constant plasma injection from the neutron star surface and Belyaev (2015) injecting particles in regions where $\mathbf{E} \cdot \mathbf{B} \neq 0$. They found qualitatively similar results, with several ten percents of the magnetic energy being dissipated within a few light cylinder radii. Consistent numbers were found in Cerutti et al. (2020), who used a PIC simulation to study the magnetic field dissipation at several tens of light cylinder radii assuming a striped pulsar wind model.

The first kinetic plasma model that treated in depth the acceleration of particles and their emission in the magnetosphere was by Cerutti et al. (2016), who considered radiation-reaction on the accelerated particles. With a magnetosphere where plasma was supplied through surface emission in an oblique rotator, the authors were able to generate spectra and light curves from the PIC simulations, which presented features also seen in observational data. These observables were also obtained by Philippov and Spitkovsky (2018), which considered pair creation by particles reaching arbitrary energy thresholds together with frame-dragging effects in an oblique rotator, and emission being produced via synchrotron radiation by the created electron-positron pairs with the positron emission dominating at higher energies. These authors further improved their PIC simulations in Hakobyan et al. (2019) and Hakobyan et al. (2023), where the plasma dynamics was studied in detail, as well as the impact of magnetic reconnection in the acceleration of particles in the ECS. They also focused on the formation of plasmoids: tearing instabilities lead to the break of the ECS into regions of plasma (the plasmoids) separated by void regions in which the magnetic field annihilates (called X-points). When plasmoids are formed, magnetic field energy is released, powering acceleration of particles in the X-points. See Figure 2.3 to visualize the magnetospheric structure from these authors' PIC simulations, which are one of the most advanced magnetospheric simulations up to date.

Particle acceleration via magnetic reconnection is not the only mechanism proposed in kinetic plasma models. In parallel to the works seen so far, another group of authors suggested

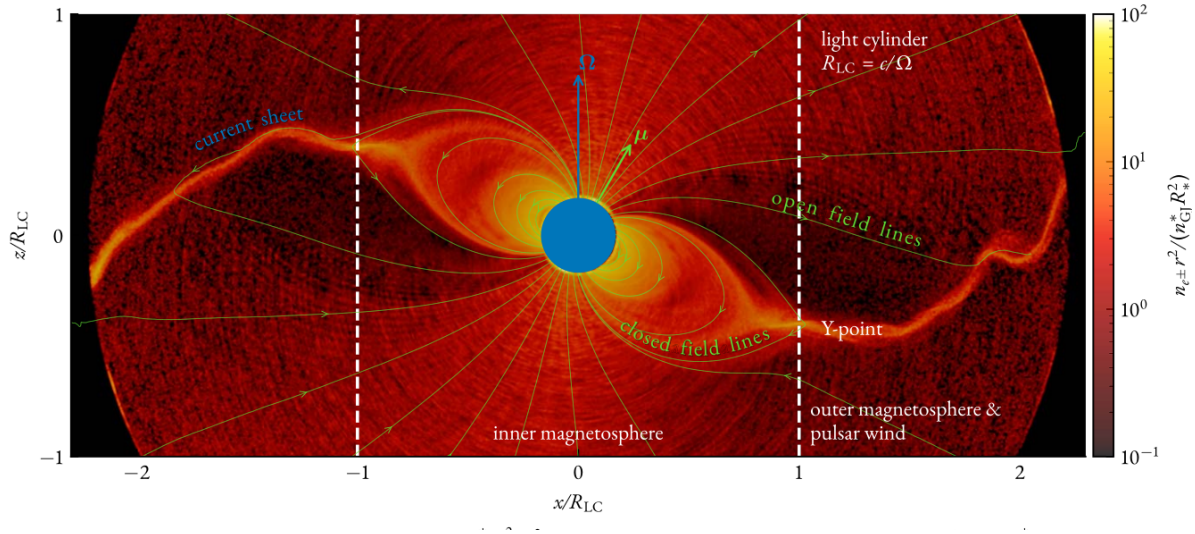


Figure 2.3: Plasma density in the magnetospheric solution of Hakobyan et al. (2023) obtained with a PIC simulation.

that charged particles are accelerated by the component of the electric field parallel to the magnetic field in regions of the magnetosphere where $\mathbf{E} \cdot \mathbf{B} \neq 0$, in a scenario similar to the one in gap models, seen in section 2. The first work of these authors was Kalapotharakos et al. (2018), who considered pair injection in the whole magnetosphere up to a large distance from the neutron star, for oblique rotators. This plasma supply was based on a global particle injection rate, without describing in detail the microphysics. The solutions found ranged from the one of the vacuum retarded dipole model for low injection rates up to a near force-free one for high injection rates. High-energy emission from the magnetospheric solutions found is computed and their properties compared with observational γ-ray data from *Fermi*, finding a relevant correlation between injection rate and spin-down power. In addition, the parallel electric field was found to be more restricted to the ECS for an increasing injection rate. The authors further developed their kinetic plasma model in Brambilla et al. (2018); Kalapotharakos et al. (2023) with emphasis on the generation of observables and their comparison with *Fermi* data.

One of the most recent PIC simulations is Cerutti et al. (2025), where the synthetic light curves generated from the kinetic plasma model were systematically fit to the observational γ-ray light curves from the 3PC.

Despite their self-consistent treatment of the electromagnetic fields and particles, PIC simulations are not free of a number of caveats and rely on some simplifications. Their major downside is the huge computational resources they demand, because solving Maxwell's equations together with the equations of motion of the particles is computationally very demanding. For this same reason, PIC simulations are often limited in the type of magnetospheres they can generate, typically with a spin period of a few milliseconds, similarly to FFE simulations. In addition, the computational domain usually does not extend more than a few light cylinder radii, because otherwise the spatial resolution would not be enough to capture the plasma dynamics. A very relevant issue of kinetic models is how to treat together the macrophysics of the global structure of the magnetosphere with the microphysics

of pair creation and acceleration. The typical lengthscales of these two problems differ by many orders of magnitudes, and this huge difference of scales poses a severe limit on the capabilities of PIC simulations. This is overcome by using unrealistically low values of some physical parameters, such as the magnetic field strength, with the aim of decreasing the scale separation (Cao et al., 2024). Acting in this way, particles can only reach low energies, with Lorentz factors of $\Gamma \sim 10^3$, which are then rescaled up to realistic pulsar values of $\Gamma \sim 10^7$, necessary to generate γ-ray emission. Soudais et al. (2024) addressed some of these caveats by proposing a hybrid FFE-PIC simulation in which ingredients of both types of numerical simulations are combined to provide a realistic pulsar magnetosphere numerical solution in a smaller computational time. The scale problem of PIC simulations was treated, becoming a very promising way to overcome the caveats of PIC simulations while keeping its benefits.

2.3 Radiative models

Radiative models drove during several decades the study of the high-energy emission of pulsars. These do not focus on solving the structure of the magnetosphere and its electromagnetic fields. Instead they assume a given configuration of the magnetic field, usually one of those obtained with the global magnetosphere models seen in Section 2.2 such as the retarded vacuum dipole model of Deutsch (1955). Then, radiative models consider the existence of charge-depleted regions, the so-called gaps, where the high-energy radiation is produced. These gaps develop in open magnetic field lines and their location and extent vary in the different radiative models. Figure 2.4 shows the location in the magnetosphere of the gaps in each of the different gap models. These models typically try to generate spectra and light curves that could be compared with the observational data available at that time. Much focus is put on the acceleration of particles and on their emission and energetics, usually using phenomenological expressions.

2.3.1 Polar Cap models

Polar Cap (PC) models were the first models trying to understand radiation emission from pulsars, which was assumed to be produced by charged particles being accelerated by an electric field parallel to the magnetic field in vacuum gaps. In PC models, gaps are located close to the neutron star surface and at a given height above the magnetic poles, in the so-called PCs, which are limited in area by the region with open magnetic field lines. In these models, the production of γ and radio emission was intertwined and both radiations were considered to be produced closely. Sturrock (1971) proposed that primary electrons and positrons accelerated in the PCs could produce curvature radiation photons at high-energies. These photons then undergo pair production with the huge magnetic field and create pairs of secondary electrons and positrons, which again are accelerated and emit high-energy photons. This process is repeated, creating a pair cascade in the gap, until the energy of the photons is below the pair-production threshold. Pair cascades eventually fill the gap above a pair formation front (PFF), screening the electric field so that particles above the PFF are no longer accelerated. Below the PFF the gap is still maintained, with the

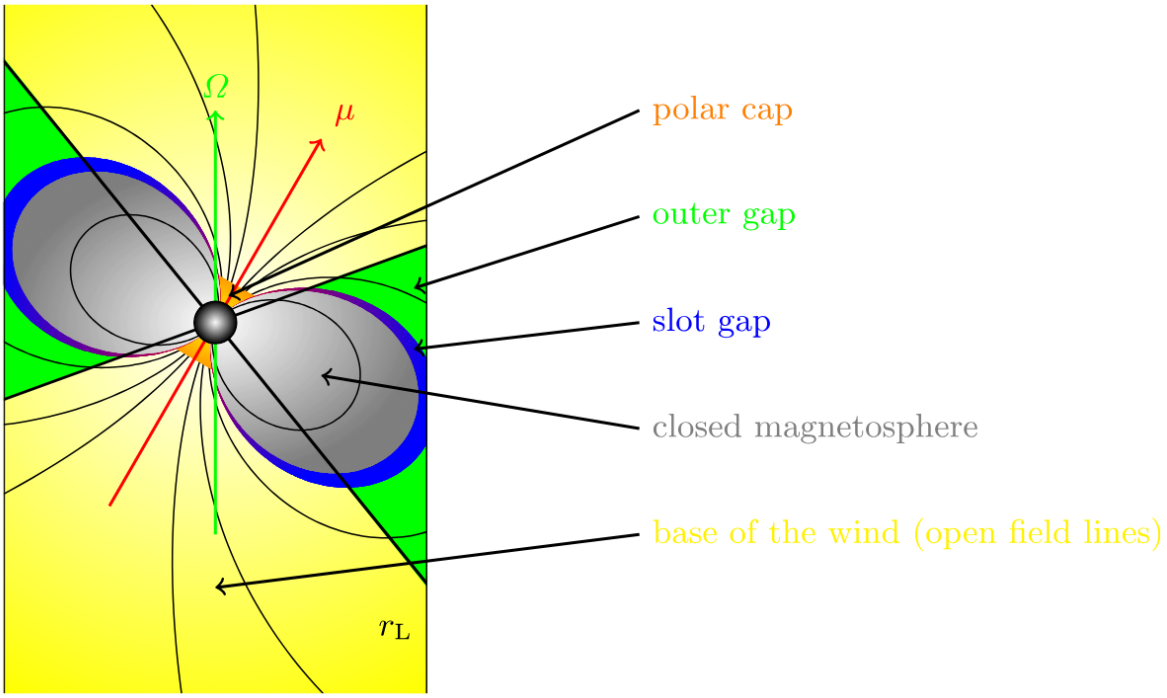


Figure 2.4: Location in a pulsar magnetosphere of the different proposed vacuum gaps (figure taken from Pétri 2016b).

electric field accelerating particles and pair cascades going on. Figure 2.5 shows a schematic representation of a pair cascade. Photons emitted in this process can escape the PC and be detectable from Earth as γ or radio radiation. Ruderman and Sutherland (1975) instead proposed a recurring process in which the vacuum gap collapses due to pair cascades that partially screen the electric field followed by an escaping of the pairs from the gap that leads to a re-emergence of the electric field and particle acceleration, if $\mathbf{\Omega} \cdot \mathbf{B} < 0$, so that the Goldreich-Julian charge density is positive above the PCs. This occurs in timescales of a few microseconds, much shorter than the typical spin period of a pulsar, meaning that this cycle occurs many times per rotation. Hardee (1977) showed that photons with energies above 1 GeV could be produced by particles accelerated in PCs.

Daugherty and Harding (1982) introduced the idea that secondary particles emit photons via synchrotron radiation and found a total cascade multiplicity, i.e. the number of pairs generated per primary charged particle, of 10^{3-4}. In this work the photons with not enough energy to pair produce are identified as those detected on Earth, while electron-positron pairs are suggested to be the inputs to coherent processes that lead to radio emission. They generated energy spectra (see left panel of Figure 2.6) and compared them with the Crab and Vela γ-ray observational spectra available at that time. Other PC models were developed in parallel, focusing on the particle energetics rather than on their acceleration, such as Salvati and Massaro (1978); Harding et al. (1978); Harding (1981). The latter proposed the γ-ray luminosity to scale with the pulsar spin-down power as $L_\gamma \propto \dot{E}^{1/2}$, a correlation which is still arguably seen observationally, with a rather high dispersion (see Chapter 6 for more details). General relativistic effects in PC models were introduced by Muslimov and Tsygan (1992), leading to an enhanced parallel electric field due to frame-dragging.

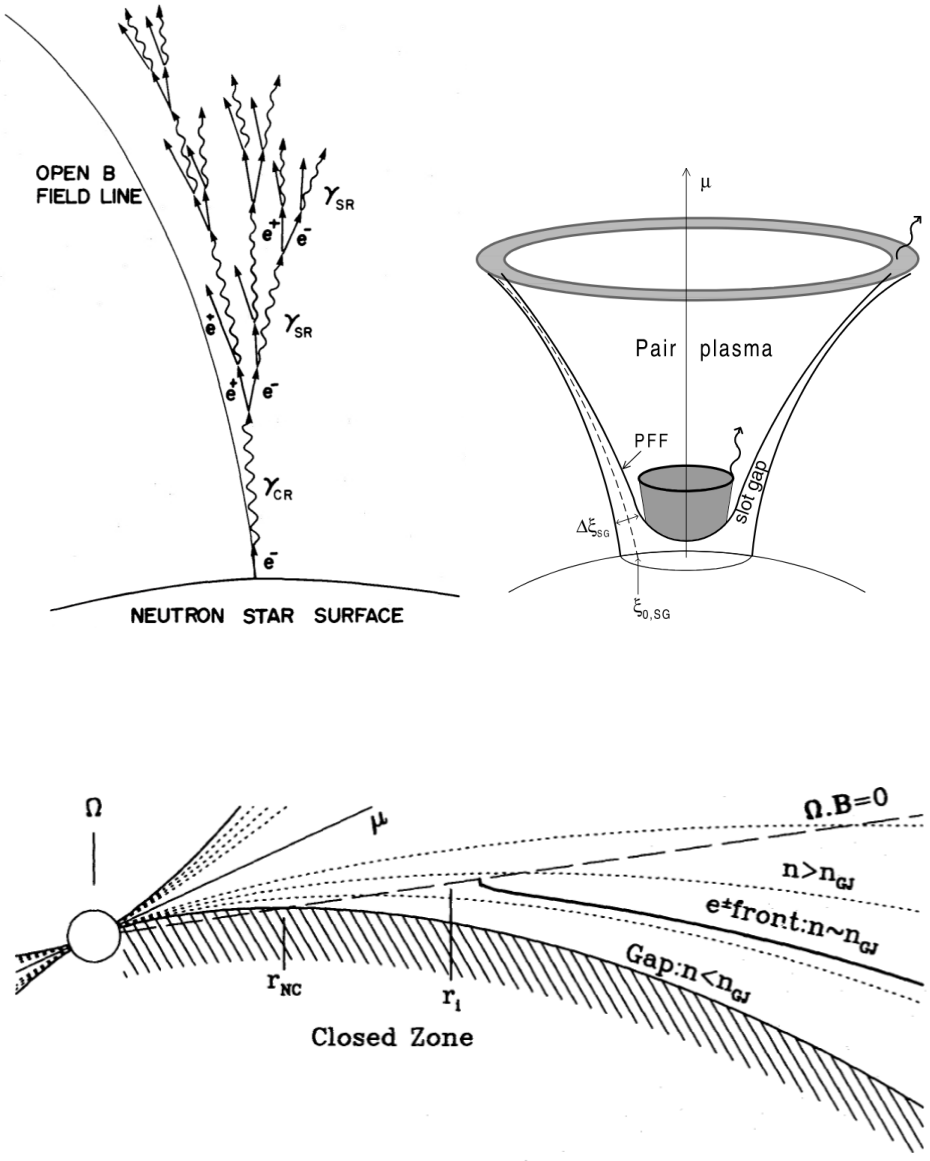


Figure 2.5: Top left: schematic representation of a pair cascade along an open magnetic field line in a PC (figure taken from Daugherty and Harding 1982). Top right: picture of a SG located at a magnetic colatitude $\xi_{0,\mathrm{SG}}$ and a width $\Delta\xi_{\mathrm{SG}}$, with the location of the PFF indicated (figure taken from Muslimov and Harding 2003). Bottom: representation of an OG with a dashed line indicating the null charge surface $\mathbf{\Omega} \cdot \mathbf{B} = 0$ and a striped band marking the beginning of the closed zone (figure taken from Romani 1996).

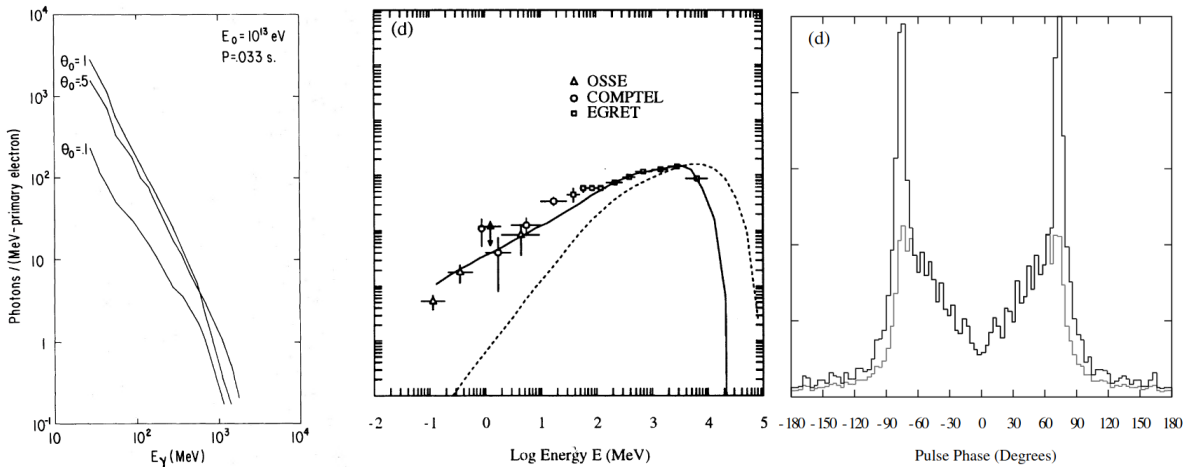


Figure 2.6: Left: γ-ray spectra from the PC model of Daugherty and Harding (1982) for a pulsar with $P = 33$ ms, $B_s = 10^{12}$ G, with cascades initiated at different magnetic colatitudes θ_0 with an initial energy of 10^{13} eV. Middle: Spectra for the Vela pulsar parameters from the PC model of Daugherty and Harding (1996) with observational data available at that time. Solid line shows the spectrum produced by photons emitted by secondary particles created in the pair cascade while dashed line shows the spectrum produced solely by curvature radiation from primary particles. Right: synthetic γ-ray light curves for the Vela pulsar from the PC model of Daugherty and Harding (1996), with the same model parameters used to generate the spectra in the middle panel and an inclination angle of $\Psi_\Omega = 16°$. The gray line corresponds to a model in which the currents in the PC are uniform, i.e. without a major acceleration in the rims, as is the case in the black line.

Morini (1983) considered a PC model but took a different approach from the other PC models on the market at that time and considered that the γ-ray emission was produced by Inverse Compton scattering of thermal photons from the star's surface by primary and secondary particles in the PCs, as well as by Inverse Compton scattering of synchrotron optical photons by charged particles around the light cylinder. The existence of caustics generating the γ-ray light curves observed was proposed: clustering of radiation into a narrow phase range would be produced by the cancelling of the phase differences that are caused by the curvature of the magnetic field lines due to relativistic aberration and time delays of emission beamed along the last open field line of a magnetic dipole. Even though the concept of caustics prevailed and is still used nowadays, the model of Morini (1983) was questioned by Smith et al. (1988) using optical polarization data. Smith et al. (1988) also proposed the formation of caustics, but assuming an OG model with two gaps near the light cylinder and a symmetrical location.

The γ-ray pulsar data gathered by the EGRET instrument unveiled a variety of light curve shapes, which challenged the PC models. Daugherty and Harding (1994, 1996), explained this variety with the differential particle acceleration along the PC, being more relevant in the rims. Right panel of Figure 2.6 shows an example of the light curves produced with this model for the Vela pulsar. In these works the description of the particle acceleration in the PC models was refined. Middle panel of Figure 2.6 shows an example of spectra generated with this model for the Vela pulsar. Using observability arguments, it was suggested that the acceleration of electrons and positrons occurred well above the neutron star surface,

finding that peak energies were achieved at several neutron star radii above the surface. In an independent work, which considered pair cascades to be initiated by Comptonization of primary particles by soft photons coming from the neutron star surface instead of curvature radiation, Sturner and Dermer (1994) reached the same conclusion regarding the variety of light curve shapes. Also independently, Daugherty and Harding (1996) and Sturner et al. (1995) found the spectral index to vary with phase, becoming harder in the interpulse phases, being consistent with EGRET observations of Vela.

PC models were able to successfully reproduce energy spectra in the EGRET era. However, the data obtained by the *Fermi*-LAT instrument revealed that energy spectra resembled a power-law with a sub-exponential cut-off. This challenged PC models, that predict spectra with a super-exponential cut-off. In addition, their difficulty to satisfactorily explain the misalignment usually seen between γ-ray light curves and radio ones and the presence of an interpulse bridge emission in the former questioned even more the capacity of these models to explain the production of high-energy radiation, and favoured others, as we will see below.

2.3.2 Slot Gap models

The slot gap (SG) model is a variation of the PC model, in which the vacuum gap starts at the PCs but extends all along the last closed magnetic field line, and particles are accelerated by an electric field parallel to the magnetic field developing in the gap, where a pair cascade occurs.

The SG model was first proposed by Arons and Scharlemann (1979), who examined the case of a magnetosphere in which $\mathbf{\Omega} \cdot \mathbf{B} > 0$, i.e. with a negative Goldreich-Julian charge density above the PCs (opposed scenario to Ruderman and Sutherland 1975, as we have seen). In this picture electrons are lifted from the star surface and initiate pair cascades as those of the PC models. The main difference comes with the PFF, above which the electric field is screened out: while in the PC models it is located at the same altitude in the entire PC, Arons and Scharlemann (1979) found it to occur at different altitudes depending on the distance from the magnetic axis. In particular, the PFF develops at higher altitudes the closer to the edges of the open field lines region we look at. This leads to the formation of a gap in the PC rim that extends at high altitudes, the SG. Figure 2.5 shows a drawing of a SG above the neutron star surface. Arons (1983) developed further this idea, in which a parallel electric field accelerates particles in the SG up to high altitudes and γ-rays can escape due to a small optical depth in the gap. His model was only applicable to nearly orthogonal rotators, and the structure of the SG was not azimuthally symmetric, instead depending on the curvature of the magnetic field lines, and only developing in those lines curved towards the rotational axis.

The SG model was revived in Muslimov and Harding (2003), with a geometrical model, commented in the next subsection. Radiation from the SG was introduced in Harding et al. (2008), modelling the emission from the optical up to γ-rays. Energy spectra, together with light curves, were produced and compared to observational data from the Crab pulsar, see Figure 2.7.

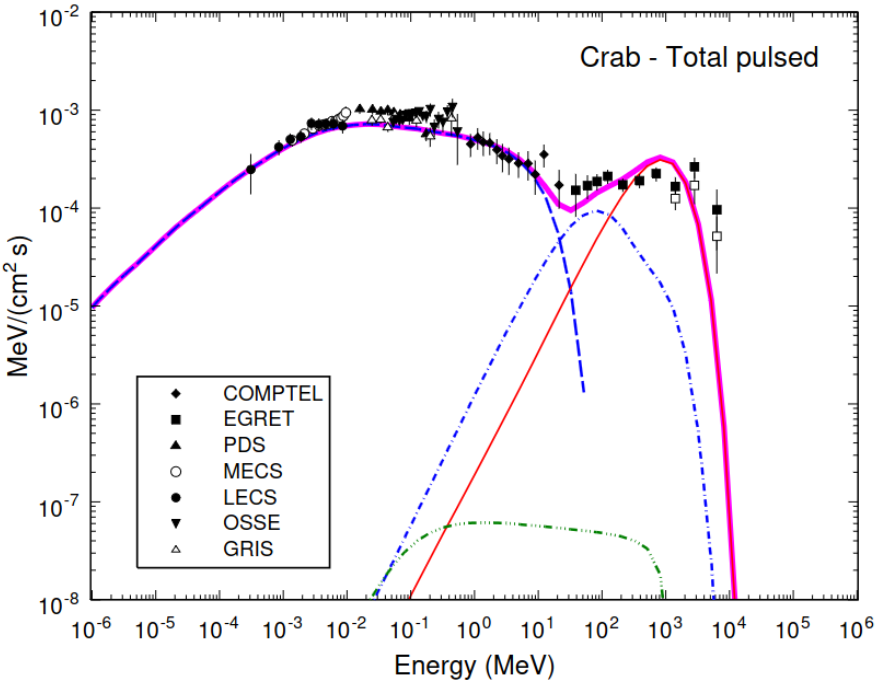


Figure 2.7: Multiwavelength spectra of the Crab pulsar from the SG model of Harding et al. (2008) with observational data available at that time ranging from the optical band up to γ-ray energies. Solid magenta line corresponds to the total spectra, solid red, blue dashed-dot and green dashed-dot-dot lines correspond to curvature, synchrotron and inverse Compton radiation of primary particles, respectively, while blue dashed line corresponds to the synchrotron emission from secondary pairs.

2.3.3 Outer Gap models

In parallel to the models that placed the gaps in the inner part of the magnetosphere, other groups proposed the outer magnetosphere as the location of these gaps, the so-called outer gap (OG) models. Figure 2.5 shows a scheme of this type of gaps. See Viganò et al. (2015b) and Viganò et al. (2015c) for an assessment of OG models. Holloway (1973) was the first to propose the existence of vacuum gaps at large distances from the neutron star, starting at the null charge surface, the imaginary line where $\mathbf{\Omega} \cdot \mathbf{B} = 0$, i.e. where the Goldreich-Julian charge density ρ_{GJ} in the magnetosphere switches its sign. The idea of an OG was further explored by Cheng et al. (1976), who proposed a current flowing out of the null charge surface and particles being accelerated in the potential drop developed in the gap.

The first study in which high-energy emission from OGs was considered is by Cheng et al. (1986a), followed by Cheng et al. (1986b). Two pairs of antipodal gaps were proposed, one per magnetic pole, with a certain azimuthal extent around the $\mathbf{\Omega} \cdot \mathbf{B}$ plane and a small thickness. The gaps start where the null charge surface crosses the last closed field line, above which the gap would develop, and do not finish inside the light cylinder. The pair cascade scheme was similar to that in PC models, but photon-photon pair production is considered in addition to photon-magnetic field pair production. It was considered emission directed outwards and inwards to the star, with the former dominating, and an expression for the parallel electric field $E_{||}$ was given, being dependent on the spin period, curvature radius and strength of the

magnetic field lines and the size of the gap. Energy spectra in the γ-ray band are produced by the model, acceptably resembling observational data of the Vela and Crab pulsars. In posterior works by the authors, the size of the OG was studied in depth and the pair of gaps from each magnetic pole were not separated and with an azimuthal extent restricted to the surrounding of the $\mathbf{\Omega} \cdot \mathbf{B}$ plane, but instead were topologically connected. Zhang and Cheng (1997) introduced a thick OG with a transversal size self-consistently estimated from pair production, and γ-ray luminosities were quantitatively predicted. Cheng et al. (2000) addressed the geometry of the OG in three dimensions and introduced relativistic effects such as aberration and time-of-flight delays, successfully reproducing double-peaked γ-ray light curves. Figure 2.8 shows as an example the spectrum and light curve of the Crab pulsar produced with this model.

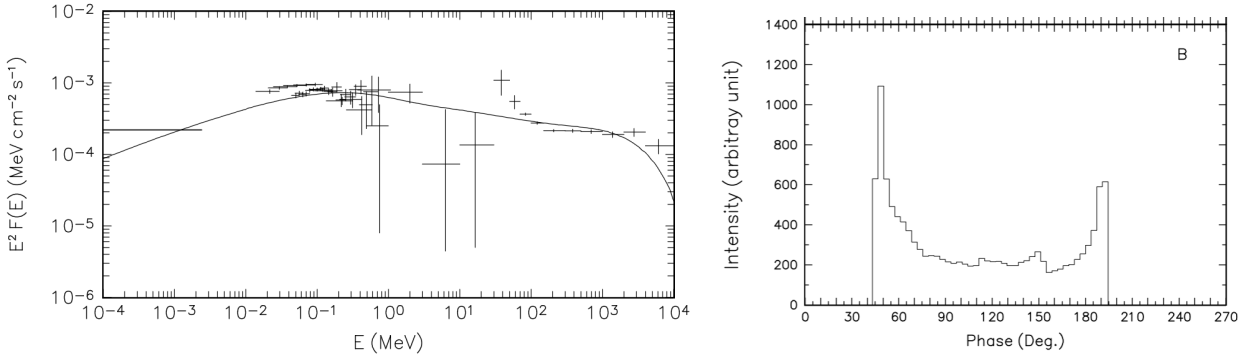


Figure 2.8: Left: γ-ray spectrum generated with the OG model of Cheng et al. (2000) assuming Crab pulsar parameters, together with observational data available at that time. Right: synthetic γ-ray light curve of the Crab pulsar from the OG model of Cheng et al. (2000) with inclination angle $\Psi_\Omega = 65°$ and viewing angle $\theta_{obs} = 82°$.

Another OG model was presented by Chiang and Romani (1992) and Chiang and Romani (1994), extending the gap to all field lines above the closed lines region, i.e. not limiting to the $\mathbf{\Omega} \cdot \mathbf{B}$ plane. The model was refined in Romani (1996), considering a single connected gap, and properly describing the gap closure produced by pair-production on thermal photons from the star surface. Phase-resolved spectra were analysed and a change in spectral index was found throughout the pulse profiles. The authors were able to properly reproduce the phase-averaged and phase-resolved spectra of the Vela pulsar available at that time, see Figure 2.9, as well as to give estimates of some relevant emission properties of the γ-ray pulsars observed at that time compatible with the observations.

The two series of works here explained laid the foundation of OG models, but had an analytical approach in which many parameters were kept constant or remained unexplored. Hirotani, Shibata and Takata published a series of papers along several years, being Hirotani and Shibata (1999) and Hirotani (2006) the most relevant ones, with numerical methods trying to overcome some of the difficulties of previous OG models. The authors evaluated the magnetic field geometry numerically, obtaining consistent values of magnetic field strength and curvature radius all along the gap. In addition, they solved the Poisson equation to describe the parallel electric field in the gap and the Boltzmann equation to follow the dynamics of the emitting particles, including photon-photon pair production. These works found that the inner boundary of the gap depends on the geometry of the magnetic field

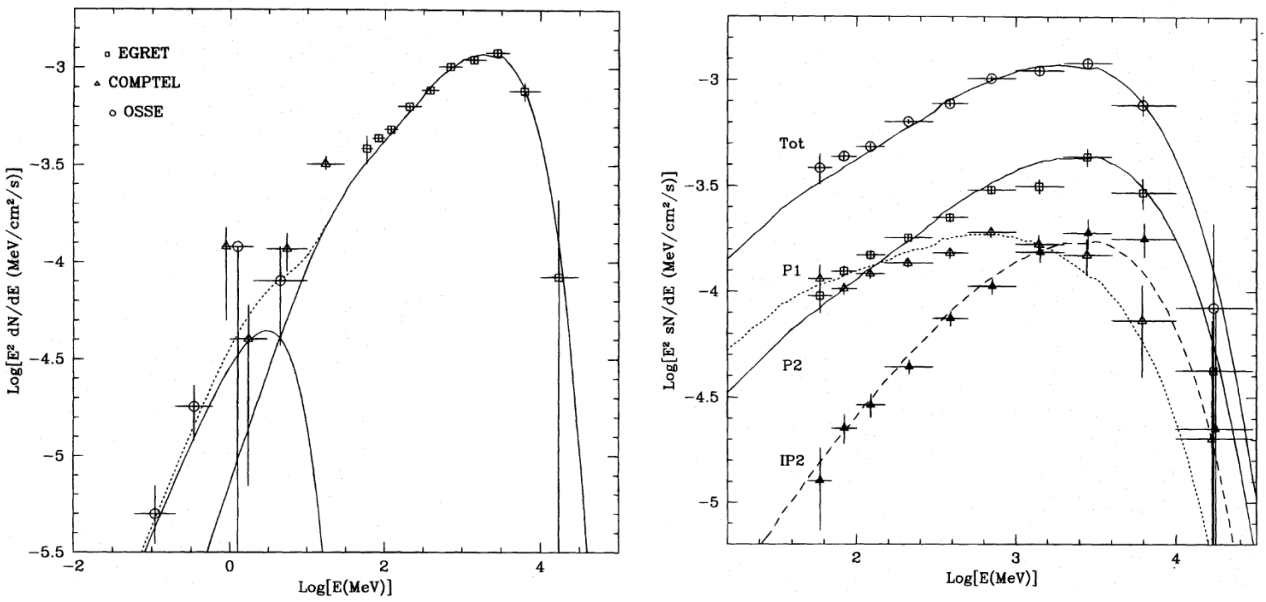


Figure 2.9: Spectra for the Vela pulsar parameters from the OG models of Romani (1996) with observational data available at that time. Left: phase-averaged spectra, with the dashed line the sum of the two solid lines, which correspond to spectra produced by curvature (higher energy peak) and synchrotron (lower energy peak) emissions. Right: phase-resolved spectra of the first peak (P1), second peak (P2), interpulse (IP2) and total emission (Tot).

lines, and that it can be located inside the null charge surface, i.e. closer to the neutron star than in previous OG models.

2.3.4 Theoretical ideas from gap models still present nowadays

The enlarging of the observed γ-ray pulsar population, the wide phenomenological diversity it entailed, and the advent of numerical magnetospheric simulations (see Section 2.2) challenged the traditional gap models presented above. However, their importance is capital, not only because they gave the first steps in the study of the pulsar magnetosphere and its high-energy emission and laid the foundations of these studies, but also because of their impact on modern modelling. Many of the ideas proposed along the decades are still assumed and form the framework upon which studies carried out nowadays are based. The most relevant ones are: the replenishment of the magnetosphere via photon-photon and magnetic field-photon pair production, with most of the plasma being formed in the PC (Timokhin 2010 refined this picture), and the developments of pair cascades in the magnetosphere, the idea that the charged particles, electrons and positrons, producing the γ-ray emission are accelerated by an electric field parallel to the magnetic field in charge-depleted regions, and the establishment of either curvature, synchrotron or synchro-curvature as the radiation mechanisms producing the high-energy emission.

2.3.5 Striped wind models

Apart from gap models, there is another relevant class of radiative model which addresses the production of high-energy emission from pulsars, the so-called striped wind models. One

of the main differences of these models with gap models is that they use MHD simulations to study the structure of the regions where the high-energy emission is produced, the wind outside the light cylinder, not yet the global structure of the magnetosphere. The picture drawn by striped wind models is completely different from the gap models: they do not consider radiation coming from charge-depleted regions inside the light cylinder, but instead propose that high-energy emission is produced in the MHD wind created by the pulsar outside the light cylinder. In this scenario, first proposed in Coroniti (1990) (see Figure 2.10 for a representation of the pulsar striped wind), the wind region is formed by a series of current sheets separated by strips of toroidal magnetic field of opposite direction at each side of a sheet. In this seminal work, magnetic reconnection is proposed as a way to transform magnetic energy into particle kinetic energy. Michel (1994) investigated further the model, finding that an equatorial current sheet would form outside the light cylinder, a concept very important in pulsar emission modelling which we will talk about later.

While these works, and others such as Lyubarsky and Kirk (2001); Kirk and Skjæraasen (2003) focus on the structure of the pulsar wind and the impact of magnetic reconnection, Kirk et al. (2002) computed the radiation from a striped wind, assuming that magnetic energy is dissipated into particle kinetic energy between $10-100\ R_{LC}$, with particles emitting synchrotron radiation. The model was investigated further in Pétri and Kirk (2005); Pétri (2012b), finding that phase coherence in the synchrotron radiation was due to relativistic beaming effects and defining a bulk Lorentz factor for the wind which scales with the square root of the spin-down power.

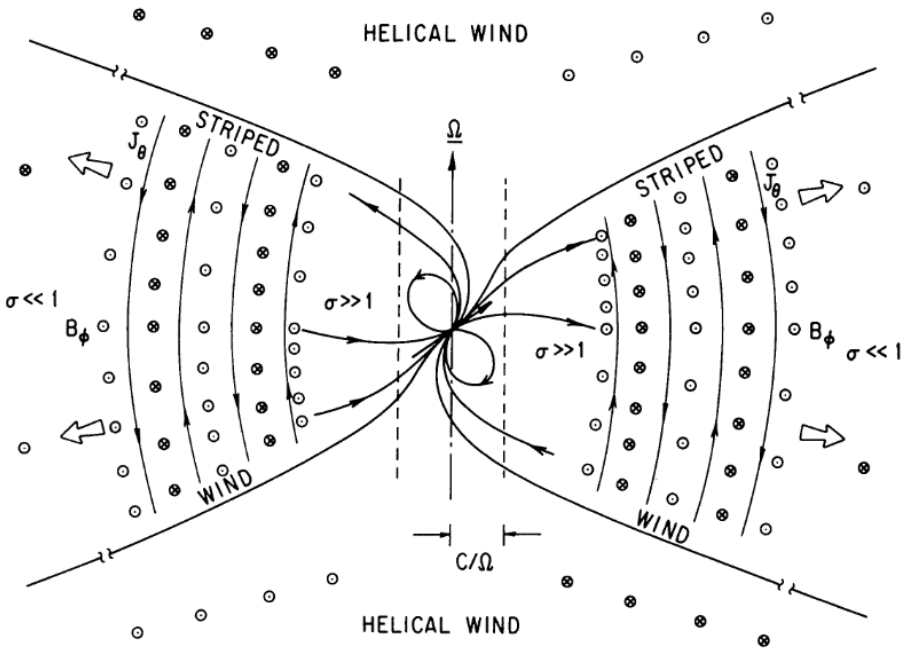


Figure 2.10: Schematic representation (not to scale) of a striped wind and its magnetic structure, showing the strips of opposite polarity of the magnetic field (figure taken from Coroniti 1990). Wide hollow arrows indicate the outwards motion of the wind.

2.4 Geometrical models

In parallel to radiative models, another class of magnetospheric models developed, focusing on the geometry of the magnetosphere to understand the spatial distribution of the high-energy emission of pulsars. Geometrical models assume one of the proposed types of gaps, PCs, SGs or OGs, and develop further their geometrical construction, generating light curves. Most of them assume a uniform high-energy photon emission from the entire gaps and do not study its energy-dependence, with few models computing the radiation emitted in the gap as a function of position and energy.

Considering an OG model, Romani and Yadigaroglu (1995) produced a sample of light curves with different geometrical angles, Ψ_Ω and θ_{obs}, and quantitatively compared them with observed pulse profiles from EGRET. See Figure 2.11 for an example of these light curves. The relative success in this comparison led the authors to appoint the OG as the most probable site of high-energy emission production, favouring the OG models over PC models. This strong claim was backed with further incarnations of the OG models and new observations of γ-ray pulsars, but challenged by new magnetospheric simulations that appeared some years after and that we will show in the next subsection. A correlation between the peak separation Δ in two-peaked γ-ray light curves and the radio lag δ (phase difference between radio and γ-ray light curves Δ) was predicted, also proposed nowadays in the 3PC.

Dyks and Rudak (2003) proposed a variation of the OG models, the two-pole caustic (TPC) model in which vacuum gaps are also located in the outer magnetosphere but present some relevant differences. The structure of the gap is similar to a thin OG, but starting in the PCs, not in the intersection of the null charge surface with the closed lines region, and extending up to the light cylinder, in the surface of the last open field lines. This geometrical model produced light curves in which the peaks are caused by caustics, and those peaks in two-peaked light curves came from opposite poles. Figure 2.11 shows some light curves produced with the TPC model.

As we have seen in the previous subsection, a new boost to the SG models was given by Muslimov and Harding (2003), but only from a geometrical approach. The main improvement was that not only open field lines with a given curvature developed a SG, but all the open ones. Also, the model was extended to further inclinations of the magnetic angle, not being restricted to nearly orthogonal rotators. Figure 2.11 shows a synthetic light curve for an almost aligned rotator. Muslimov and Harding (2004) improved further by extending particle acceleration and high-energy radiation emission at much higher altitudes, almost up to the light cylinder.

From year 2009, several works testing the geometrical sides of the different gap models were published. Relying on the vacuum retarded dipole model for the structure and considering a uniform emission all along the gap, these studies built samples of light curves for different gap geometries: PC, SG, OG or TPC. Their aim was to compare these models, and prepare for the new observational light curves that the *Fermi*-LAT instrument was expected to observe. The first of these works was Watters et al. (2009), the "ATLAS paper", generating γ-ray light curves of young pulsars with the PC, TPC and OG models. Simulating

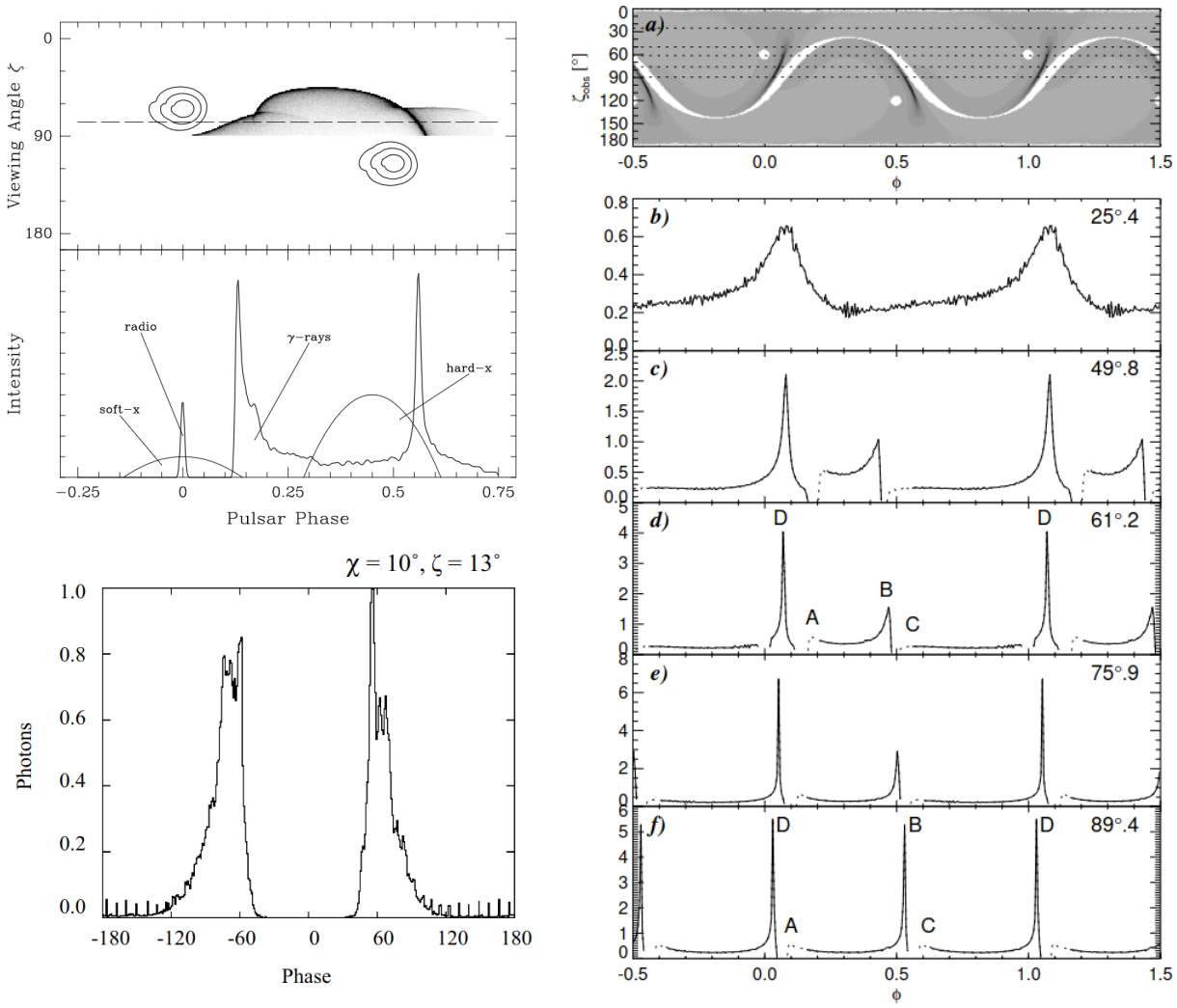


Figure 2.11: Top left: emission map in the γ-ray band (upper subpanel) assuming Vela pulsar parameters from the OG model of Romani and Yadigaroglu (1995). For a better visualisation, only the emission with a viewing angle θ_{obs} above 90° is shown, and the contours correspond to the radio PCs. The dashed line at a given θ_{obs} corresponds to the light curve and observer located at that θ_{obs} would detect. The lower subpanel shows this γ-ray light curve, together with the radio pulse and schematic pulses of the soft and hard X-ray emission. Bottom left: synthetic γ-ray light curve from the SG model of Muslimov and Harding (2003) for the Crab pulsar parameters with inclination angle $\Psi_\Omega = 10°$ and viewing angle $\theta_{obs} = 13°$. The small spikes are numerical artifacts. Right panel: synthetic emission map in the γ-ray energy range (upper subpanel) from the TPC model of Dyks and Rudak (2003) with inclination angle $\Psi_\Omega = 60°$. The white dots correspond to the location of the PCs. The rest of the subpanels show the γ-ray light curves for different viewing angles, indicated in the upper right corner of each subpanel and corresponding to each of the dashed lines of the upper subpanel.

a pulsar population as in Weltevrede and Johnston (2008) and with a uniform distribution of inclination angles Ψ_Ω, the authors generated a set of emission maps. Figure 2.12 shows together the emission maps from OG, TPC and PC models for a given Ψ_Ω. Emission maps display the spatial distribution of the radiation as a function of rotational phase of the pulsar and the viewing angle θ_{obs}, the angle between the plane perpendicular to the rotational axis of the pulsar and the line of sight of an observer detecting that pulsar. Cutting emission maps at a given θ_{obs}, a light curve is obtained. The authors found that light curves strongly depend on the two geometrical parameters, θ_{obs} and Ψ_Ω, and explored further the impact of these geometrical parameters on the morphology of the light curves. They also assessed how different was this impact in the three models studied. The morphology of the synthetic light curves was defined by three main parameters, the number of peaks, the separation between peaks and the beaming factor f_Ω. The beaming factor is defined as the ratio of the total pulsed emission of the pulsar averaged over the sky to the phase-averaged emission detected by an observer (Abdo et al., 2013):

$$f_\Omega(\Psi_\Omega, \theta_{\rm obs}) = \frac{\int\int F_\gamma(\Psi_\Omega; \theta'_{\rm obs}, \phi) \sin\theta'_{\rm obs}\, d\theta'_{\rm obs}\, d\phi}{2\int F_\gamma(\Psi_\Omega; \theta_{\rm obs}, \phi)\, d\phi} \tag{2.30}$$

where F_γ is the detected flux in the *Fermi* γ-ray energy range and ϕ is the rotational phase of the pulsar. See Chapter 6 for more details on f_Ω. It is found to be ~ 1 for a majority of light curves, an order of magnitude larger than the assumed value before this work, of $1/(4\pi)$, i.e. assuming a beaming of 1 sr. One of the main conclusions obtained in this work was the problems that the PC model had to generate realistic light curves, while the TPC and OG light curves showed features also observed in observational light curves, like abundance of two-peaked profiles or complex light curves with many peaks. This result was also found by Romani and Yadigaroglu (1995) many years before, but now the PC model was more clearly disfavoured by the larger population of observed γ-ray pulsars. Romani and Watters (2010) continued the work and considered the TPC and OG models but with three different magnetic field structures: a magnetic dipole, the retarded vacuum dipole model and a more realistic magnetic field configuration. This increased atlas was fitted to the observational light curves of the 5 pulsars better known at that time, finding a better agreement in light curves generated with an OG model and a realistic magnetic field.

Venter et al. (2009) performed a study complementary to the two previous ones, but for MSPs, with very similar conclusions. TPC and OG models were found to better reproduce observational data than the PC model. The beaming factor f_Ω was also found to be ~ 1 on average, which contributed to the use of a fiducial value of $f_\Omega = 1$, which is still used nowadays in some studies. The advent of the *Fermi* telescope allowed to perform fits of a larger sample of observational γ-ray light curves, and thus to obtain more reliable conclusions for the whole population. One of the goals was to obtain constraints on the Ψ_Ω and θ_{obs}. Johnson et al. (2014) considered TPC, SG and OG models and fitted the γ-ray light curves of the MSPs on the 2PC, jointly with radio light curves generated with a hollow-cone beam with or without core depending on the pulsar. The authors found that a great number of MSP light curves were similar to those of young pulsars.

A very similar approach, but with the young pulsars in the 2PC, was taken by Pierbattista et al. (2015), using the framework built in the population synthesis study of Pierbattista et al.

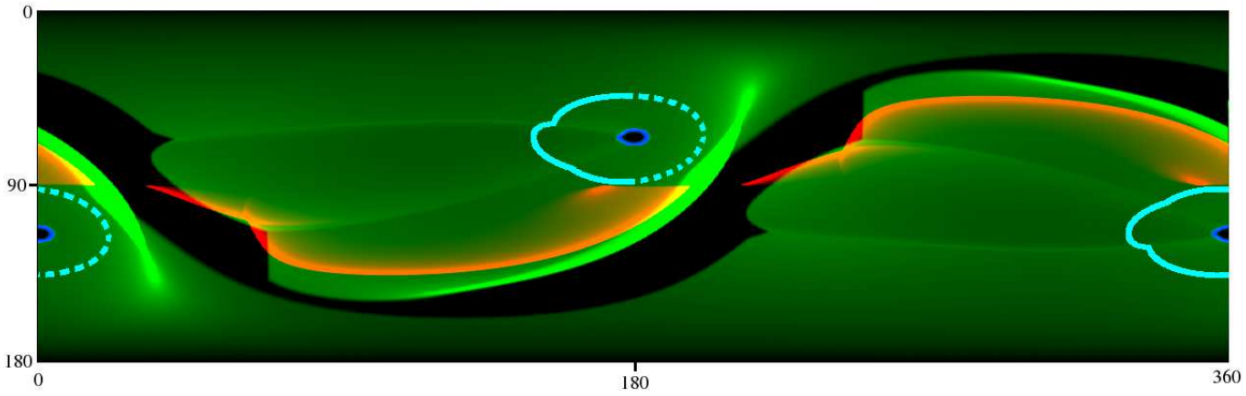


Figure 2.12: Emission maps in the γ-ray band showing the radiation intensity as a function of rotational phase (x-axis) and viewing angle (y-axis) for an inclination angle $\Psi_\Omega = 65°$ from an OG model (green), a TPC model (orange) and a PC model (blue). Cyan line shows the location of the radio emission computed together with the γ-ray emission in the three models.

(2012) with the PC, SG and OG models. The PC model again struggled to reproduce the observational pulse profiles, while the SG and OG performed well in general, but had some differences in the best-fitting parameters of the entire population. However, none of them was able to explain the light curves of the whole population of γ-ray pulsars. The authors argued that this implied that the real geometry could indeed be a mixture of both models. They also investigated the differences between radio-quiet and radio-loud pulsars, finding that a joint fitting of light curves in γ-ray and radio (when available) gives significantly different best-fitting values of Ψ_Ω and θ_{obs} than a fit only with the γ-ray light curve. Finally, it is relevant to mention the modelling done in Pierbattista et al. (2016), where using a sample of γ-ray and radio light curves as that in Pierbattista et al. (2015), a morphological classification of γ-ray and radio light curves was proposed. This classification was based on several morphological features of the light curves: the number of peaks, the number of minima (defined as valleys in the pulse profile with a non-zero intensity), full width at half maximum of a peak, width of the base of a peak in one-peaked light curves and the number of emission windows (i.e. the number of sets of contiguous phase bins with non-zero intensity). Depending on the values of each feature, several classes were proposed, and each light curve was placed in one of the classes. Using this classification, synthetic and observational γ-ray light curves were compared. The conclusion extracted from this comparison was very similar to the one obtained in Pierbattista et al. (2015).

2.5 Motivation of the model presented in this thesis

As we have seen in this section, magnetospheric models for pulsars can be divided into three big groups: radiative models, geometrical models and global magnetosphere models. The three types are based on different approaches, and vary in their complexity, applicability and results. Despite their differences, these models share the goal of understanding the high energy emission of pulsars. This is the central problem addressed in this thesis.

Radiative and geometrical models are mainly focused on obtaining observables, spectra

and light curves, respectively, that can be compared with observational data. Their main goal is to reproduce observations of pulsars. Therefore, the global form of the magnetosphere is not addressed in depth and the electromagnetic fields are not self-consistently computed, and instead are taken those obtained with the global magnetosphere models or are just parametrized with a simple expression. In addition, these models implement some real physical processes, while parametrizing others. This approach allows one to generate spectra and light curves easily, without a huge computational demand. All this makes them very suitable to be compared with observational data with good results, and permits one to perform systematic fits of spectra and light curves of the whole population of high-energy pulsars. Although these models can reproduce spectra and light curves reasonably well, the two observables are usually treated separately; few models generate both spectra and light curves within the same framework, almost none doing so for the whole population of γ-ray pulsars. These models were the first ones that addressed the question of high-energy emission from pulsars and had a great impact on its understanding, paving the way and laying the foundations of this field.

Global magnetosphere models use complex numerical simulations to understand the structure of the magnetosphere. With different levels of complexity, from simple vacuum magnetospheres to full kinetic simulations, these models give a description of the electromagnetic fields. This in itself is a powerful result, because it helps one understand the pulsar surroundings, as well as its geometry, and at the same time lays the framework to study the emission from the pulsar. High-energy emission depends particularly on the electromagnetic fields, since it is produced by charged particles moving in these fields and emitting radiation as a result of this motion. Therefore, a proper description of the configuration of the magnetosphere is a useful tool to better understand the high-energy emission of pulsars. In the last two decades, global magnetosphere models have enlarged our knowledge of the pulsar surroundings and its emission. A relevant drawback of these models is their large computational cost, particularly accentuated in the most complex ones. Running one of these models requires many hours of computation, which makes them difficult to scale and to apply to the entire population of pulsars: these simulations are usually run for a particular pulsar configuration (Ψ, P, $\dot{P}$, B). In addition, the huge cost diminishes the capacity to explore large parameter spaces with enough resolution.

The model presented in this thesis occupies an intermediate regime between these approaches. The main goal of this model is to reproduce high-energy spectra and light curves of pulsars that can be compared with observational data in order to improve our understanding of the high-energy emission of pulsars. It solves the dynamics of charged magnetospheric particles, as well as their emission along their trajectory. At the same time, some relevant quantities, such as the magnetic field strength and the curvature radius along the particles' trajectories, are parametrized with simple expressions. This, together with a few more simplifications and assumptions, allows us to generate pulsar observables, spectra and light curves, for the whole population of high-energy pulsars. At the same time, we can explore the space of parameters of our model with sufficient resolution and in realistic ranges. This has allowed us to systematically compare our model with observational spectra and light curves of the whole population of high-energy pulsars, as we will see further in this thesis. The

model occupies a barely-explored intermediate regime between purely radiative and geometrical prescriptions and global kinetic simulations. It retains an explicit treatment of particle dynamics and synchro-curvature radiation along trajectories, while parametrizing quantities that remain computationally prohibitive to compute self-consistently for population-scale studies. Thus, it is able to reproduce well spectra and light curves of high-energy pulsars, allowing us to extract information about these objects as a result of the comparison. In Chapter 3 we present the radiative version of the model, followed by the spectro-geometrical version in Chapter 4. We show the comparison of the model with observational data in Chapter 5, where correlations between model parameters are explored. Chapter 6 shows a study on the dispersion of the observational γ-ray efficiency of pulsars. Finally, Chapter 7 presents the main conclusions of this thesis.

3

Radiative model

In this chapter we present a radiative model that aims at explaining the high-energy emission of pulsars. This radiative model is based on an effective approach, in which several relevant quantities are parametrised and some physical ingredients are simplified. In this way, the model can be easily used to reproduce the emission of the whole population of high-energy pulsars. We consider the synchro-curvature radiation as the mechanism at work in a pulsar magnetosphere.

The radiative model is based on following the dynamics of an ensemble of charged particles travelling along a magnetic field line in an emission region of the magnetosphere, and computing the synchro-curvature radiation they emit along these trajectories. We define the emission region as the zone where the particle trajectories are located, and its exact location in the magnetosphere is flexible in our model. The calculations are done in terms of only three free parameters:

(i) the electric field parallel to the magnetic field, $E_{||}$, assumed constant throughout an accelerating region;

(ii) the local magnetic field B, which is parametrised as a function of P, $\dot{P}$, the physical distance along the field line λ, and the magnetic gradient b assumed as a free parameter:

$$B = B_{\rm s}(R_\star/\lambda)^b \ , \tag{3.1}$$

(iii) and the (normalised) spatial extent of the observationally-relevant emitting region of the particles, x_0/R_{LC}, which enters by means of a weighting function that encapsulates the underlying complexity of the electromagnetic field and particle distributions.

The ultimate goal of the radiative model is to generate spectra in the high-energy bands, in X-rays and γ-rays, i.e. from $\sim$ 1 keV to $\sim$ 300 GeV. These theoretical spectra are then compared with observed spectra of high-energy pulsars via systematic fits to the whole population. In this way we obtain the best-fitting values of the model parameters which allow us to extract some physical conclusions about the high-energy emission of pulsars.

3.1 Particles' trajectories

Our model starts from a simple description of charged particle dynamics in an inertial lab frame. These particles are accelerated by an electric field parallel to the magnetic field that develops in certain regions of the magnetosphere where the force-free condition is broken. As we have seen in Chapter 2, the ECS that extends from the Y-point is a plausible location for this to occur. Therefore, we place our emission region just outside the light cylinder, close to the Y-point, even though our model is flexible in its location. The motion of the particles is initially characterised by a non-negligible gyration component, with a Larmor radius much smaller than the magnetic lengthscale and, with relatively moderate Lorentz factors producing a peak of the emission in X-rays (Torres, 2018). While the particle parallel momentum increases due to the acceleration, the perpendicular momentum is rapidly radiated away and the pitch angle exponentially decreases, so that the particles effectively slide along the rotating magnetic field line and can reach Lorentz factors larger than 10^7, with the radiation peaking at γ-rays. Due to the drift imposed by the corotation of the magnetosphere with the neutron star, the trajectories drawn by a given charged particle deviate from the static magnetic field line (Bai and Spitkovsky, 2010). Such deviation is even more substantial beyond the light cylinder, since the plasma cannot co-rotate with the neutron star and the magnetic field lines are twisted. In this thesis λ parametrises the position along the gyration-averaged trajectory (i.e., neglecting its gyrating component), or *along the rotating field lines*, e.g. along the magnetic field line taking into account the drift given by the strong rotation velocity of the plasma in which the field lines are frozen.

Having this in mind the dynamics of charged accelerated particles in non-force-free regions of the magnetosphere results from the combination of the parallel electric field magnitude $E_{||}$, and the synchro-curvature losses coming from the combined gyration (around the lines) and parallel motion (along them). Such losses are, in turn, defined by the particle Lorentz factor $\Gamma = \sqrt{1-\beta^2}$, where $\beta = v/c$ and v is the velocity of the particle, the pitch angle α (angle between the magnetic field line direction and the particle's direction of motion), and by the local values of the magnetic field, B, Equation (3.1), and the curvature radius of the gyration-averaged trajectory, r_c (Viganò et al., 2015a). The latter is also assumed to depend on the pulsars' P and $\dot{P}$ and, in our model, is parametrised for simplicity as a function of λ as

$$r_c = R_{LC}(\lambda/R_{LC})^{\eta} \ , \tag{3.2}$$

where η is arbitrarily fixed to 0.5, since in previous works of the group, Viganò et al. (2015b,c), it was shown that the value of η has a negligible impact on the spectral prediction compared to other parameters, at least for the specific set of models explored there.

3.1.1 Equation of motion

The electrical acceleration and the radiative losses govern the dynamics of the emitting particles, and are balanced by the equation of motion of a charged particle, which follows the variation of its relativistic momentum, $\vec{p} \equiv \sqrt{\Gamma^2-1}mc\ \hat{p} \simeq \Gamma m v\ \hat{p}$, with $\hat{p}$ the direction of motion of the particle, along its trajectory (Viganò et al., 2015a; Hirotani and Shibata,

1999). For given values of P, $\dot{P}$, i.e. for a particular pulsar, and for values of the model parameters, $E_{||}$ and B, the model solves the equation of motion of the particles:

$$\frac{d\vec{p}}{dt} = ZeE_{||}\,\hat{b} - \frac{P_{\rm sc}}{v}\,\hat{p} \quad , \tag{3.3}$$

where Ze is the charge of the particle, $v \sim c$ its velocity and $P_{\rm sc}$ is the synchro-curvature power radiated by a particle. We can decompose the momentum $\vec{p}$ into its parallel ($p_{||} = p\cos\alpha$) and perpendicular components ($p_{\perp} = p\sin\alpha$) with respect to the magnetic field lines, which are directed along $\hat{b}$, obtaining

$$\frac{d(p\sin\alpha)}{dt} = -\frac{P_{\rm sc}\sin\alpha}{v} \tag{3.3a}$$

$$\frac{d(p\cos\alpha)}{dt} = ZeE_{||} - \frac{P_{\rm sc}\cos\alpha}{v} \tag{3.3b}$$

Solving these equations determines the evolution of several kinetic quantities of the emitting charged particles, among which Γ and α are particularly relevant. For an alternative approach see Kelner et al. (2015), who propose a Hamiltonian-based formulation to provide for the particle motion and their synchro-curvature radiation for a given magnetic field configuration, and a more detailed study of the radiation inside and outside the accelerating region.

3.2 Synchro-curvature spectra

3.2.1 Synchro-curvature radiation

Synchrotron and curvature radiation mechanisms can be considered as particular limits of a more general emission mechanism, synchro-curvature radiation. A charged particle emits pure synchro-curvature radiation when moving in a curved magnetic field (which is a situation that exists in a pulsar's magnetosphere) and spiralling around it, i.e. following a helicoidal movement. The synchro-curvature formalism holds provided $r_{\rm gyr}$ is non-zero and much smaller than $r_{\rm c}$, and $r_{\rm c}$ varies on lengthscales much larger than $r_{\rm gyr}$.

The radiation emitted by one charged particle at each position of the trajectory, following the complete synchro-curvature formulae (Cheng and Zhang, 1996; Viganò et al., 2015a), is:

$$\frac{dP_{\rm sc}}{dE} = \frac{\sqrt{3}(Ze)^2\Gamma y}{4\pi\hbar r_{\rm eff}}\left[(1+z)F(y) - (1-z)K_{2/3}(y)\right] \tag{3.4}$$

with the several quantities defined as:

$$F(y) = \int_y^\infty K_{5/3}(y')dy' \tag{3.5}$$

$$r_{\rm eff} = \frac{r_{\rm c}}{\cos^2\alpha}\left(1+\xi+\frac{r_{\rm gyr}}{r_{\rm c}}\right)^{-1} \tag{3.6}$$

$$r_{\rm gyr} = \frac{mc^2\Gamma\sin\alpha}{eB} \tag{3.7}$$

$$\xi = \frac{r_{\rm c}}{r_{\rm gyr}}\frac{\sin^2\alpha}{\cos^2\alpha} \tag{3.8}$$

$$z = (Q_2 r_{\rm eff})^{-2} \tag{3.9}$$

$$y = \frac{E}{E_{\rm c}} \tag{3.10}$$

$$E_{\rm c} = \frac{3}{2}\hbar c Q_2 \Gamma^3 \tag{3.11}$$

$$Q_2^2 = \frac{\cos^4\alpha}{r_{\rm c}^2}\left[1+3\xi+\xi^2+\frac{r_{\rm gyr}}{r_{\rm c}}\right] \tag{3.12}$$

where K_n are the modified Bessel functions of the second kind of index n, the solutions of the Bessel equation with complex argument. $r_{\rm gyr}$ is the Larmor radius, or gyro-radius, e and m are the charge and rest mass of a lepton, c is the speed of light, $\hbar$ is the reduced Planck constant, $r_{\rm eff}$ is an effective radius that contains the relevant lengthscales $r_{\rm c}$ and $r_{\rm gyr}$ and tends to the former when curvature radiation dominates and is proportional to the latter when synchrotron radiation dominates, and E and $E_{\rm c}$ are the photon energy and the characteristic energy of the emitted radiation, respectively. ξ is the synchro-curvature parameter, which indicates whether the emission is dominated by synchrotron or by curvature radiation, or if it is a mixture of both. Small values, $\xi \ll 1$, mean that curvature radiation dominates the emission, while large values, $\xi \gg 1$, indicate a domination of synchrotron radiation. For intermediate values, the radiation emitted is purely synchro-curvature.

Integrating the single-particle spectrum, Equation (3.4), in energy we obtain the total synchro-curvature power emitted by one particle:

$$P_{\rm sc} = \frac{2(Ze)^2\Gamma^4 c}{3r_{\rm c}^2} g_{\rm r} \ , \tag{3.13}$$

where

$$g_{\rm r} = \frac{r_{\rm c}^2}{r_{\rm eff}^2}\frac{[1+7(r_{\rm eff}Q_2)^{-2}]}{8(Q_2 r_{\rm eff})^{-1}} \ . \tag{3.14}$$

The classical synchrotron and curvature formalisms (Jackson, 1998) are recovered from the synchro-curvature formulae. In the limit $\xi \gg 1$, i.e. where the radiation emitted by the particles is synchrotron, from Equation (3.13), we recover the synchrotron radiation power:

$$P_{\rm sync} = \frac{2}{3}\frac{(Ze)^4 B^2(\Gamma^2-1)\sin^2\alpha}{m^2c^3} \ , \tag{3.15}$$

and from Equation (3.11) the synchrotron characteristic energy:

$$E_{\rm c}^{\rm sync} = \frac{3}{2}\frac{\hbar e B\sin\alpha}{mc}\Gamma^2 \ . \tag{3.16}$$

In the opposite limit $\xi \ll 1$, in which the emission of the particles is purely curvature, from Equation (3.13), we recover the curvature radiation power:

$$P_{\rm curv} = \frac{2}{3}\frac{(Ze)^2 c\Gamma^4}{r_{\rm c}^2} \quad , \tag{3.17}$$

and from Equation (3.11) the curvature characteristic energy:

$$E_{\rm c}^{\rm curv} = \frac{3}{2}\frac{\hbar c}{r_{\rm c}}\Gamma^3 \quad . \tag{3.18}$$

These expressions give one a way to qualitatively estimate whether the emission from a particle is dominated by synchrotron or curvature radiation. Different combinations of Γ, α, B and $r_{\rm c}$, lead to different $P_{\rm sync}$ and $P_{\rm curv}$. If the combination of these quantities for a given particle results in e.g. $P_{\rm sync} \gg P_{\rm curv}$, that particle emits basically synchrotron radiation, and vice versa. In the same way, comparable $P_{\rm sync}$ and $P_{\rm curv}$ are indicative of a genuine synchro-curvature regime. Ultimately, this is encoded in the parameter ξ, which gives a more formal way to estimate the nature of the radiation emitted by a particle, but doing this qualitative exercise helps in understanding better the radiative model and interpreting properly the results obtained. For instance, large (small) magnetic field strengths B imply a large (small) synchrotron emitted power, which can overcome the curvature emission, which does not depend on B. The same occurs with the pitch angle α, the decrease of which entails a drop of $P_{\rm sync}$. On the other hand, different curvature radii $r_{\rm c}$ only impact (inversely) the curvature emission, and not the synchrotron one. Unlike in the previous cases, both $P_{\rm sync}$ and $P_{\rm curv}$ depend on Γ, but the latter more steeply than the former. Therefore, an increase in Γ produces a greater increase in curvature emission than in synchrotron power.

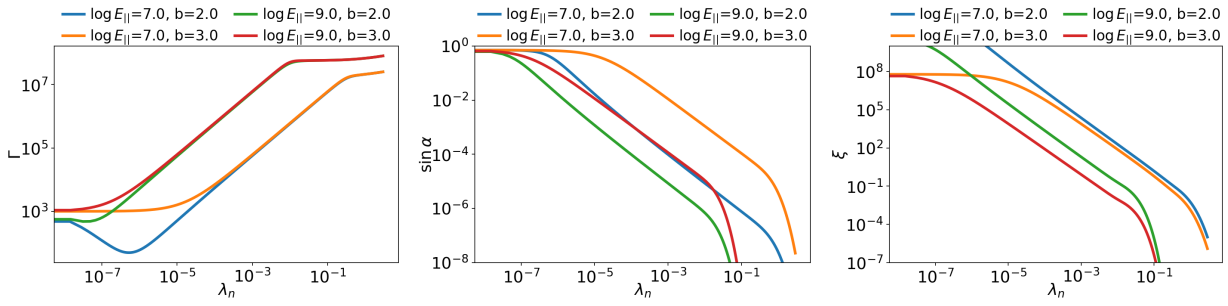


Figure 3.1: Evolution along the trajectory of several quantities: Γ (left panel), $\sin\alpha$ (middle panel) and ξ (right panel), for J0205+6449 and different values of the spectral parameters $E_{||}$ and b (in different colours indicated in the legend of each panel). The x-axis represents the position along the trajectory normalised to R_{LC}.

Figure 3.1 shows examples of the evolution along a particle's trajectory of these quantities in our model, for different spectral parameters. In the left panel, Γ increases as a result of the electric acceleration, implying that curvature radiation becomes more relevant as the particle moves forward. From an initial value[1] of 10^3, Γ reaches a saturation value $\Gamma_{\rm st}$ when the radiation-reaction force compensates the acceleration. The particular value

[1]The lines on the left panel of Figure 3.1 do not start at 10^3, but this is a resolution issue. A zoom at $\lambda_{\rm n} < 10^{-7}$ would show a smooth transition between the initial Γ value and the rest of the line.

of $\Gamma_{\rm st}$ depends on the strength of the accelerating electric field: larger $E_{||}$ results in larger saturation Γ, and vice versa. Typically, $\Gamma_{\rm st} \sim 10^{7-8}$, which for electrons/positrons represents an energy of $\sim 5 - 50$ TeV. This implies that photons emitted by these particles have an energy in the GeV range. It is clearly seen that b only affects the evolution of Γ at the initial parts of the trajectory, and as the particle moves through the region, $E_{||}$ dominates the Γ evolution and the impact of b is negligible. Small b means a smooth decay of B with distance, and thus more synchrotron losses. The electric acceleration has to compensate these larger synchrotron losses, and thus particles should travel a larger distance to increase their energy, as can be seen in the left panel of Figure 3.1 comparing the blue and orange lines, and the green and red lines. The blue line, which is produced by small $E_{||}$ and b, shows a decrease of Γ at the beginning of the trajectory. The reason is that the small $E_{||}$ is initially not able to compensate the strong synchrotron losses close after injection and thus the particle's energy decreases. However, soon the particle starts to gain energy, because the synchrotron losses have diminished due to the loss of most of its perpendicular momentum. This is clearly seen in the middle panel of Figure 3.1, which shows the evolution of α. As the particle moves through the region, perpendicular momentum is radiated away by synchrotron emission and α decreases. This, together with the fact that B, Equation (3.1), decreases along the trajectory of the particle, implies that synchrotron radiation is more dominant at the beginning of the trajectory, and its relevance declines as the particle advances. Notice that with the same $E_{||}$, smaller b produce a faster decay of α. The reason is the smoother B decay produced by the smaller b, which implies higher B at the beginning of the trajectory and thus more synchrotron emission and loss of perpendicular momentum. Finally, the curvature radius, Equation (3.2), increases as the particle travels along the trajectory, implying a greater importance of curvature radiation far from injection.

In our model, the nature of the radiation emitted results from a non-trivial combination of all these effects, and as we have seen depends on the values of the spectral parameters. Still, a clear conclusion is extracted: the emission of a particle at the beginning of its trajectory is dominated by synchrotron radiation, which transitions into a pure synchro-curvature radiation as the particles advances, and ends up being dominated by curvature radiation far from injection. This conclusion can be expressed in a more quantitative way by looking at the right panel of Figure 3.1, which shows the evolution of ξ, and Figure 3.2, which shows the evolution of the synchro-curvature, synchrotron and curvature emitted powers, Equations (3.13), (3.15) and (3.17), respectively. At the beginning of the trajectory, ξ is large and $P_{\rm sync} \gg P_{\rm curv}$: synchrotron radiation dominates. As the particle advances ξ decreases and reaches intermediate values, $\mathcal{O}(1)$, and at the same time $P_{\rm sync} \approx P_{\rm curv}$, i.e. both contribute to the total emitted power. This indicates a pure synchro-curvature radiation. Far from injection, ξ has already dropped to very small values and $P_{\rm sync} \ll P_{\rm curv}$: emission is dominated by curvature radiation. These figures give us additional intuition on how the nature of the radiation along the whole emission region depends on the spectral parameters. On the one hand, we have the red line/scale with large $E_{||}$ and b, i.e. more acceleration and a steeper decrease of B compared to the other lines. ξ decreases fast and the transition to curvature-dominated emission occurs early in the trajectory, so curvature radiation is especially important in the total emission. On the other hand, there is the blue

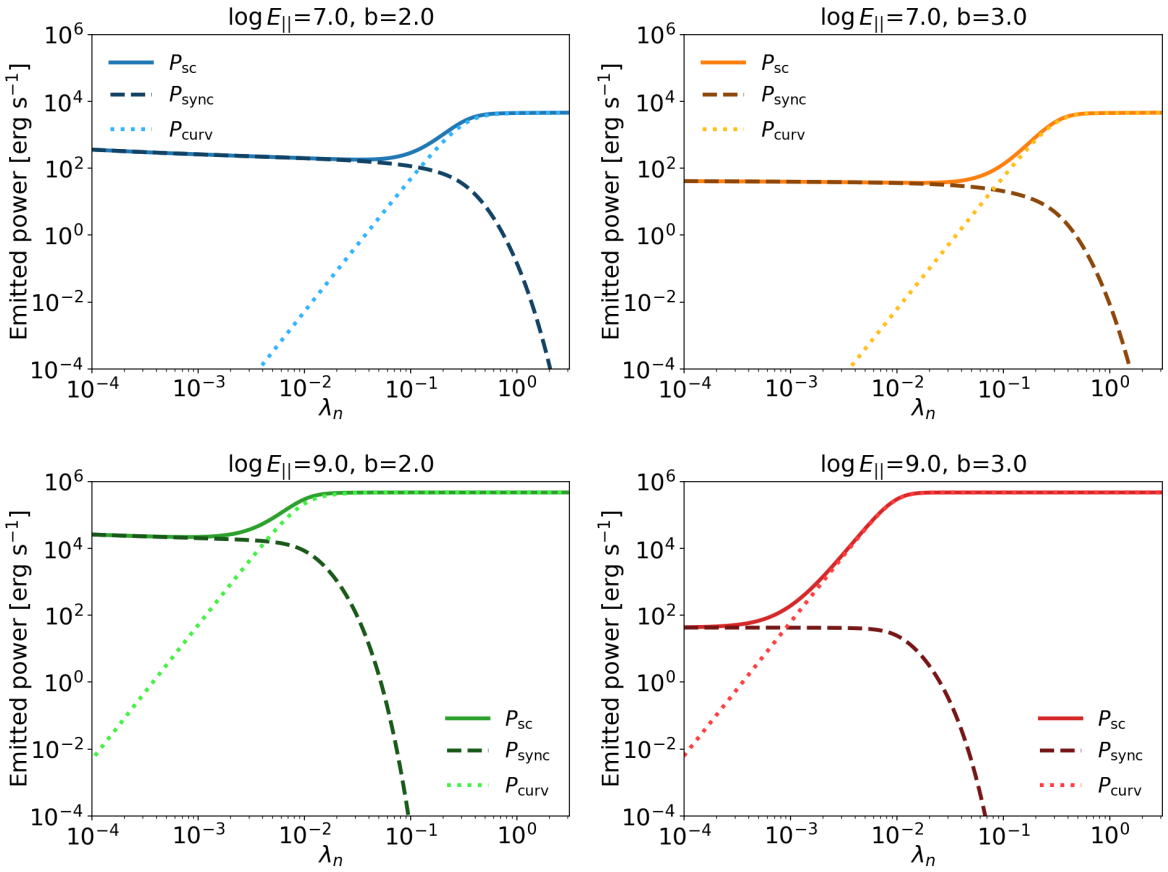


Figure 3.2: Evolution along the trajectory of the synchro-curvature (solid line), synchrotron (dashed line) and curvature (dotted line) emitted powers for J0205+6449. Each panel has different values of the spectral parameters $E_{||}$ and b, as indicated on top of each panel.

line/scale with small $E_{||}$ and b, i.e. less acceleration and a slower decrease of B. ξ decreases more slowly and the emission is dominated by synchrotron radiation in more parts of the trajectory. This is a scenario in which synchrotron radiation is more relevant to the total emission.

3.2.2 Single-particle spectrum

Equation (3.4) gives an expression for the emission by a charged particle all along its trajectory. With this expression and the set of quantities of Equations (3.7)-(3.12), it is clear that at any position along the trajectory of an emitting particle, the emission of radiation $dP_{sc}/dE(B, E_{||}, r_c, \Gamma, \alpha)$ is completely specified by:

(i) the local kinetic properties of the particle (Lorentz factor Γ, pitch angle α, position),

(ii) the local properties of the magnetic field (intensity B and curvature radius r_c).

Figure 3.3 shows single-particle spectra for different combinations of these quantities. For all different combinations, the shape of the spectra is very similar, changing only in peak energy and flux. The former is close to the value of the characteristic energy of the radiation emitted, while the latter is specified by the emitted power. The cases shown in Figure 3.3 are in the synchrotron regime, since $\xi \gg 1$, meaning that the characteristic energy and the emitted power are the synchrotron ones, i.e. Equations (3.16) and (3.15), respectively. In

the left panel, with larger Γ the single-particle spectra peak at higher energies and have higher fluxes, as expected from the quadratic dependence of $E_{\rm c}^{\rm sync}$ and $P_{\rm sync}$ on Γ. $E_{\rm c}^{\rm sync}$ depends linearly on $\sin\alpha$ while $P_{\rm sync}$ depends quadratically, which is the behaviour seen in the middle panel: when α decreases, the single-particle spectra peak at lower energies and have lower fluxes. The dependence of $E_{\rm c}^{\rm sync}$ and $P_{\rm sync}$ on B is the same as that on $\sin\alpha$, and thus higher B results in single-particle spectra peaking at higher energies and having higher fluxes. Since we are in a synchrotron regime, the single-particle spectra are negligibly affected by $r_{\rm c}$.

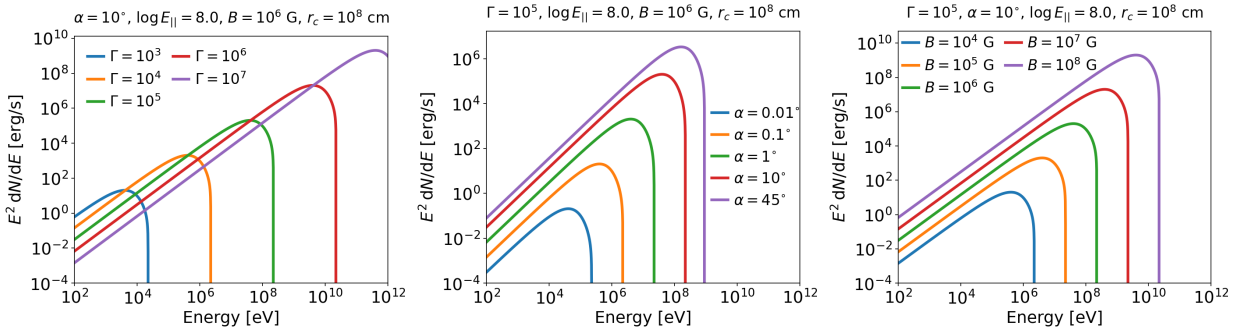


Figure 3.3: Single-particle spectra, $dP_{\rm sc}/dE$ of J0205+6449 for different combinations of values of the properties defining them. Each panel shows the effect of varying one of these properties, from left to right: Γ, α and B.

Having the evolution of these kinematic quantities (obtained from the solution of the equation of motion of subsection 3.1.1), $dP_{\rm sc}/dE(B, E_{||}, r_{\rm c}, \Gamma, \alpha)$, Equation (3.4), gives us the radiation emitted by one charged particle all along its trajectory. Figure 3.4 shows the single-particle spectra emitted at logarithmically distributed positions of the trajectory of a charged particle. Looking at all panels of this figure, it is clear that the single-particle spectra produced at different positions of the trajectory are different. The single-particle spectra emitted at the innermost region of the particle's trajectory typically peak at low energies, in the keV range. In these parts of the trajectory, as we have seen above, the emission is dominated by synchrotron radiation, since B is relatively large, α is non-negligible and Γ is still close to the relatively small value with which it is born. The spectra generated in the intermediate zone of the region usually peak at intermediate energies, $1-100$ MeV, and have moderate fluxes. As the particle advances in the trajectory it is accelerated and loses its perpendicular momentum via synchrotron radiation, i.e. Γ increases and α decreases. In addition, B decreases and r_c increases following the power laws of Equations (3.1) and (3.2), respectively. We have already seen that this implies that the emission is purely synchro-curvature radiation. Single-particle spectra produced in the outer parts of the region peak at high energies, in the GeV range. Far from injection, a particle typically reaches $\Gamma \sim 10^6 - 10^8$ and $\alpha \sim 0$, and thus curvature radiation dominates the emission.

It is interesting to remark that these are general behaviours and that some ranges can overlap. For example, some spectra from the initial parts of the trajectory shown on the bottom left panel of Figure 3.4 peak in the MeV range. This depends on the values of the spectral parameters, as we explain now.

Figure 3.4 gives us insights on how the spectral parameters shape the spectrum. First,

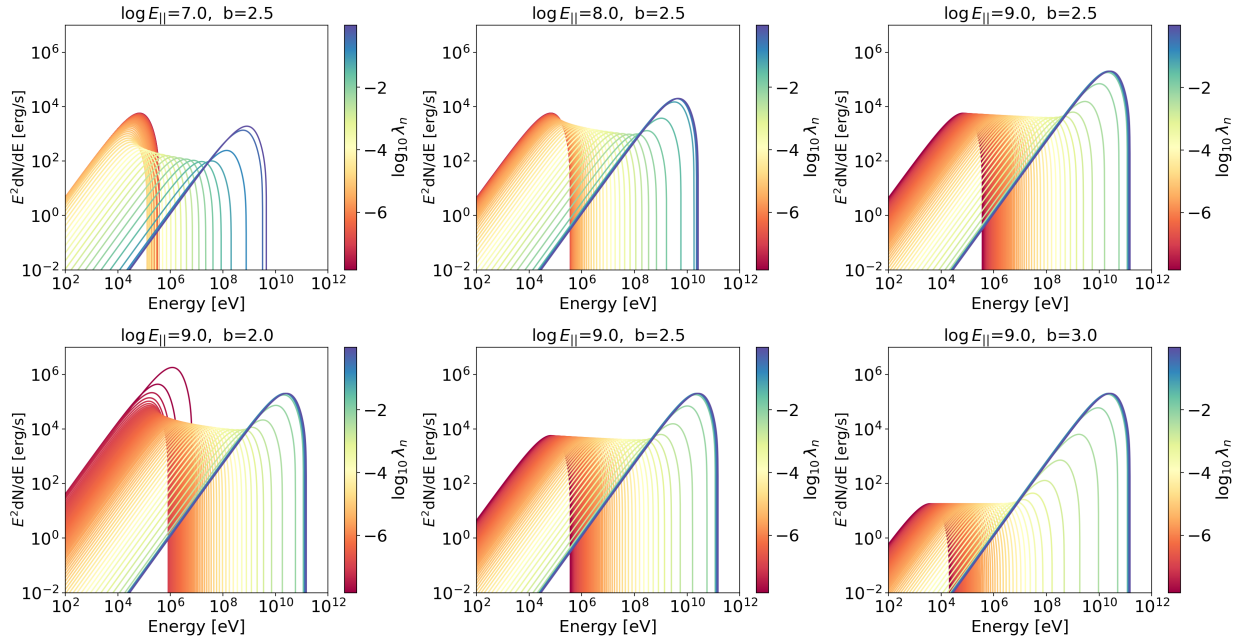


Figure 3.4: Single-particle spectra, $dP_{\rm sc}/dE$ of J0205+6449 along an entire particle trajectory, with different sets of values of the spectral parameters. Panels on the top (bottom) row have a fixed b ($E_{||}$) and differ in $E_{||}$ (b). Particular values are indicated above each panel. The colour bar indicates the position in the trajectory of each spectrum (normalised to R_{LC}).

the top row shows the single-particle spectra produced with different $E_{||}$, and we see that it shapes the spectra produced at all the positions of the trajectory, being its effect more notable in the spectra generated far from injection and in intermediate positions. In particular, larger $E_{||}$ result in spectra from intermediate and far zones of the region peaking at higher energies and having higher fluxes. This is caused by the greater acceleration given by a large $E_{||}$ that results in higher Γ, which in turn implies single-particle spectra peaking at higher energies and with higher fluxes, as shown in the left panel of Figure 3.3. Regarding b, the bottom row of Figure 3.4 shows that its effects are particularly relevant in the spectra generated in the initial and intermediate parts of the trajectory and has no impact on the spectra produced in the outer parts of the trajectory. We have already seen why this happens: at the beginning of the trajectory emission is synchrotron-dominated, and thus the value of B (which is regulated by b) affects the spectral shape, while far from injection we have a curvature regime, which is independent of B. Synchro-curvature radiation also depends on B, and thus the intermediate spectra are also affected by b. For larger values of b, which indicate smaller values of B, the spectra in the inner and medium parts of the trajectory, peak at lower energies and have smaller fluxes, as we saw in Figure 3.3.

With all this in mind, we can envision that the integrated spectrum, which is presented below in subsection 3.2.4, has its X-ray band mostly shaped in the inner parts of the trajectory, while the γ-ray band of the integrated spectrum is mostly defined in the outermost part and is minimally sensitive to the birth properties. Finally, it is interesting to emphasise the fact that the synchro-curvature formalism naturally produces a diversity of spectra for a single emitting particle, depending on given parameters, that allows one to generate a wide variety of integrated spectra.

3.2.3 Effective weight functions

We consider that the injection of particles is continuous all along the emission region, and numerically parametrise this extended injection with a finite number of injection points, $N_{\rm inj}$, located at a distance $r_{\rm in}$ from the neutron star. Appendix A presents a more detailed study on this extended injection. We do not go into the details of the creation of particles in the magnetosphere, which is generally assumed to occur via production of electron-positron pairs from photon-photon or photon-B field interaction, as we have seen in Chapter 2. Instead, we simply assume that particles appear (by pair production) at the injection points. We consider positrons as the species of charged, emitting particles. Due to the large electric field in the emission region, electrons are accelerated in the opposite direction to positrons, but for simplicity we only follow the dynamics of outward particles. This is a caveat which will be overcome in the future. The same number of particles are injected at all injection points, and the trajectories of particles from different $r_{\rm in}$ are copies of a fiducial trajectory with the only difference being the distances to the neutron star, which change the particular B and $r_{\rm c}$ of the trajectories of the particles.

We do the additional assumption that the injection of particles does not occur exclusively at each $r_{\rm in}$, but instead particles are injected at trajectory points in a region close to $r_{\rm in}$. The size of this innermost region, $\lambda_{\rm lp.in}$, for a given injection point is estimated from the trajectories of particles on a per-pulsar basis, as the extent at which a particle injected at the start of the accelerating region, and subject to the corresponding losses provided by the local magnetic field and curvature, would have traversed at least $10^{-4}R_{LC}$. We translate this assumption into the following heuristic expression,

$$\lambda_{\rm lp.in} \sim 10^{-1.0\times\log_{10}(R_{LC}[cm])+4.0} R_{LC} \ , \tag{3.19}$$

which is fixed for each pulsar and has proven successful in providing good spectral fits, as we will see in Chapter 5.

At every position of the trajectory there will be particles that have been injected at different (earlier) positions and that have travelled different distances, thus emitting differently and contributing distinctly to the integrated spectrum. In order to take this into account when computing the spectrum emitted by the whole region, we introduce an averaging of the single-particle spectra emitted by all particles in the region. With this averaging, at each position of the trajectory we weight the contributions to the integrated spectrum of each particle as a function of its travelled distance. The averaged single-particle spectrum at the position λ is to be defined as:

$$\left\langle \frac{dP_{\rm sc}}{dE}(\lambda, r_{\rm in}) \right\rangle = \frac{1}{\lambda_{\rm lp.in}} \int_0^{\min(\lambda,\lambda_{\rm lp.in})} \frac{\Delta\Omega(\lambda_{\rm nb})}{\Delta\Omega(0)} \frac{dP_{\rm sc}}{dE}(\lambda - \lambda_{\rm b}, r_{\rm in}) d\lambda_{\rm b} \tag{3.20}$$

where

$$\lambda_{\rm nb} = \min(\lambda, \lambda_{\rm lp.in}) - \lambda_{\rm b}, \tag{3.21}$$

and we set:

$$\frac{\Delta\Omega(\lambda)}{\Delta\Omega(0)} = \frac{\sin\alpha(\lambda)}{\sin\alpha(0)} \frac{\Gamma(0)}{\Gamma(\lambda)} \ , \tag{3.22}$$

which is a monotonically decreasing function, that goes like $\sim \lambda^{-2}$ for $\lambda \sim 10^{-4}$-$10^{-1} R_{LC}$. The choice of this function allows us to successfully reproduce observational spectra, as we will see in Chapter 5.

In the radiative model, the particles' trajectories and the consequent spectra are supposed to be effective averages over the diversity of magnetic field lines and trajectories within the emission region, including possibly the emission of particles going backwards and other effects not modelled in detail. Due to our lack of a complete knowledge of the conditions in the emission region, we model this in an effective way: the contributions at a given position of the trajectory are weighted by an effective particle distribution function $dN/d\lambda$, that represents particles whose radiation is directed towards the observer. As in our previous works, we adopt:

$$\frac{dN}{d\lambda} = \left[\frac{N_0}{x_0 (1 - e^{-(\lambda_{\rm out} - \lambda_{\rm in})/x_0})} \right] e^{-(\lambda - \lambda_{\rm in})/x_0} \quad , \tag{3.23}$$

where N_0 is the *normalization*, such that $\int_{\lambda_{\rm in}}^{\lambda_{\rm out}} (dN/d\lambda) d\lambda = N_0$, $\lambda_{\rm in}$ is the initial point of the trajectory, i.e. the injection point, and $\lambda_{\rm out}$ is the last point of the trajectory, the point beyond which we do not compute the particle dynamics any more. $\lambda_{\rm out} - \lambda_{\rm in} = r_{\rm max}$ is the total distance travelled by the emitting particles. The ratio $x_0/(\lambda_{\rm out} - \lambda_{\rm in})$, or its inverse, called contrast, is a measure of how uniform is the distribution of particles injected in a given $r_{\rm in}$ that are still emitting towards us at a distance λ along the magnetic field line. The larger x_0 is, the more uniform this distribution is. Note that the N_0 value does not affect the shape of the spectrum but only its absolute scaling. For each set of values of the model parameters ($E_{||}$, x_0/R_{LC} and b), N_0 is analytically computed by linear regression during the fitting procedure (we will see how in Chapter 5).

3.2.4 Integrated spectrum

The integrated spectrum emitted by the entire emission region is obtained by summing the contributions from the particles injected at the $N_{\rm inj}$ injection points. In turn, each of these contributions is defined by the convolution of the averaged-spectrum at each position, Equation (3.20), with the effective particle distribution, Equation (3.23), for the corresponding $r_{\rm in}$. Thus,

$$\frac{dP_{\rm tot}}{dE} = \int_{r_{\rm in}^0}^{r_{\rm in}^{N_{\rm inj}}} \int_{\lambda_{\rm in}}^{\lambda_{\rm out}} \left\langle \frac{dP_{\rm sc}}{dE}(\lambda, r_{\rm in}) \right\rangle \frac{dN}{dr_{\rm in} d\lambda}(\lambda, r_{\rm in}) \; d\lambda \; dr_{\rm in} \tag{3.24}$$

where $r_{\rm in}^0$ and $r_{\rm in}^{N_{\rm inj}}$ are the first and last injection points, respectively. Since we consider that each injection point introduces the same number of particles, in the (probably) realistic case of continuous injection we would have

$$\frac{dN}{dr_{\rm in}\, d\lambda}(\lambda, r_{\rm in}) = \frac{1}{(r_{\rm in}^{N_{\rm inj}} - r_{\rm in}^0)} \frac{dN}{d\lambda}(\lambda, r_{\rm in}) \tag{3.25}$$

The theoretical spectrum generated by Equation 3.24 is fully determined by the three free parameters ($E_{||}$, x_0/R_{LC}, b) plus the normalization factor N_0. Since the free parameters are thought to be a-priori agnostic, i.e. no prior assumption about their values is made, fitting this spectrum generated for a given pulsar to observed spectra of that pulsar can constrain our physical assumptions, as we will see in Chapter 5.

Figure 3.5 shows examples of integrated spectra for a particular pulsar, J0205+6449, and different sets of spectral parameters. In this way, we can see how each parameter affects the integrated spectrum. First of all, the value of $E_{||}$ defines the energy at which the spectrum peaks: larger $E_{||}$ (darker lines) implies an integrated spectrum peaking at higher energies, as can be seen in the left panel and as we already stated in subsection 3.2.2. The same reasoning explains why the highest $E_{||}$ produces such a small flux at low energies: most of the particles are rapidly accelerated and emit mainly curvature radiation, meaning that the amount of particles emitting synchrotron-dominated spectra, which peak at low energies, is smaller. The middle panel shows the impact of b: spectra with smaller b have a higher flux at low energies. Smaller b, i.e. a smoother decay of B (lighter lines) means that particles move in a relatively high B in a larger portion of the trajectory. Therefore, there is a larger amount of particles whose emission is dominated by synchrotron radiation, which produces spectra with peaks at lower energies. The panel shows that the parameter b mostly shapes the low-energy (X-rays) band of the spectrum. This connects with the discussion associated with Figure 3.1, where we have seen that b mainly affects the initial parts of the trajectory, which in turn primarily shape the X-ray energy range of the spectrum. Finally, the right panel helps to understand the effect of the $dN/d\lambda$ weight. Larger x_0 (darker line) results in a spectrum peaking at higher energies, because the portion of the trajectory relevant for the integrated spectrum is large. In this case, there is more contribution from particles with higher Γ, which we have seen that emit single-particle spectra peaking at higher energies. Conversely, with smaller x_0 (lighter line), most of the integrated spectrum is produced at the beginning of the trajectory, where the synchrotron emission is more dominant and the single-particle spectra peak at lower energies.

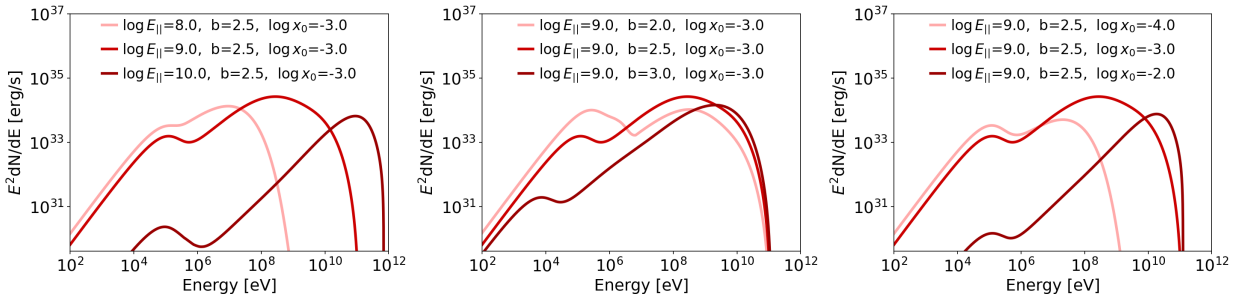


Figure 3.5: Integrated energy spectra of J0205+6449 with different sets of spectral parameters. Each panel shows the impact of each of the three free parameters on the integrated spectrum, from left to right: $E_{||}$, b and x_0.

Note that the integrated spectrum does not take into account the spatial distribution of the radiation emitted, it just gives the total radiation coming from the whole emission region. The spatial distribution of the emission is treated in Chapter 4.

3.2.5 Initial conditions of the emitting particles

The radiative model requires the initial conditions of the emitting particles to be fixed in order to generate spectra. In particular, we have to fix the distance travelled by the particles, i.e. the distance with respect to the neutron star of both the initial and last points of the

trajectory, and the initial values of some kinematic quantities. The same initial conditions are considered for all pulsars.

We place the initial point of the emission region at $1.0R_{LC}$, and discretise the extended injection in $N_{\rm inj} = 11$ injection points (Appendix A shows the convergence tests that led us to fix this number) evenly distributed in a range $\Delta R = 0.5R_{LC}$, i.e. spanning from $1.0R_{LC}$ to $1.5R_{LC}$. From each $r_{\rm in}$ particles travel a distance $r_{\rm max} = 1.0R_{LC}$, which is valid as long as $r_{\rm max} \gg x_0$, as we will see in Chapter 5. We also have to fix initial values of two kinematic quantities of the emitting particles, Γ and α. Assuming that the emitting particles are injected by pair production, their initial energy, $E_{\rm in} = \Gamma_{\rm in} m_{\rm e} c^2$, where $m_{\rm e}$ is the electron/positron mass and c is the speed of light, depends on the energy of the progenitor photon(s), E_γ. Then, $\Gamma_{\rm in} = E_\gamma/(2m_{\rm e}c^2) \sim 10^3 E_\gamma[\rm GeV]$. We assume the progenitor photon(s) to have an energy of $\sim$ GeV, which implies an initial Lorentz factor of the charged particles of $\Gamma_{\rm in} = 10^3$, which is the value we fix in our model. In the case of α, we assume for simplicity that all particles have the same initial value, 45°, when they start to be accelerated. Indeed, we do not assume that particles enter the emission region with a direction along the magnetic field line. On the contrary, since the local magnetic field far from the surface is much weaker than the critical quantum magnetic field, pairs are arguably produced mostly by photon-photon interactions, so that the initial angle would be expected to acquire random values, $\mathcal{O}(1)$. Note that, for the sake of simplicity, we omit more complex effects that could affect the α evolution, like resonant absorption of radio photons. This could provide the travelling charged particles with a non-negligible α along the trajectory (Lyubarskii and Petrova, 1998; Harding et al., 2008), beyond the initial injection.

4

Spectro-geometrical model

A key aspect of the study of the high-energy emission of pulsars is to understand the geometry of this emission, i.e. its spatial distribution, because it allows one to obtain information about the particular shape of pulsar magnetospheres. In this chapter, which is largely based on the published work Íñiguez-Pascual et al. (2024), we present a spectro-geometrical model that complements the spectral modelling seen in the last chapter with geometrical specifications. It describes the geometry of the emission region of a pulsar from which the spatial distributions of its high-energy emission is obtained. Intertwined with the geometrical description, the model contains all the machinery presented in Chapter 3: the dynamics of the particles is solved and their emission is computed. In this way, the spatial distribution of the emission also comprises spectral information. The model, which is effective in the same manner as the radiative model was, depends on the three spectral parameters ($E_{||}$, x_0/R_{LC}, b) and on several geometrical parameters that define the geometry of the emission region. From these, two are let free: the inclination angle Ψ_Ω, which is the angle between the rotational and magnetic axes of the pulsar, and the viewing angle θ_{obs}, defined as the angle between the plane perpendicular to the rotational axis of the pulsar and the line-of-sight of an observer detecting that pulsar. With this model we build emission maps, also called skymaps, in the *Fermi*-LAT γ-ray band, 100 MeV to 300 GeV, which display the spatial distribution of the high-energy emission for particular geometrical and spectral parameters. From these maps can be extracted light curves, also called pulse profiles, which show the intensity of the emission as a function of the rotational phase of the pulsar detected by different observers. We shall compare our synthetically generated light curves with observational γ-ray light curves.

4.1 Radiative and geometrical modelling

4.1.1 Trajectories

In the spectro-geometrical model, the geometry of the trajectory followed by the emitting particles is computed together with their dynamics. The dynamics are calculated in the same way presented in Chapter 3. The model uses the Frenet-Serret differential geometry formulae. This set of differential equations allow to geometrically describe the trajectory of a particle moving in a three-dimensional space, given the curvature radius r_c and torsion τ of the gyration-average trajectory followed by the particle. r_c is the distance of the particle from the centre of curvature of the trajectory, while τ is the rate of twisting of the trajectory, i.e. its deviation from the initial plane of curvature of the trajectory. At each position along the magnetic field line, λ, the gyration-average trajectory defines three directions: tangent $\hat{t}$, normal $\hat{n}$ (which points towards the centre of curvature of the line), and binormal $\hat{b} = \hat{t} \times \hat{n}$. Having r_c and τ as functions of the position λ, the evolution of these vectors is determined by the Frenet-Serret equations:

$$\frac{d\hat{t}}{d\lambda} = \frac{1}{r_c}\hat{n} \ , \qquad \frac{d\hat{n}}{d\lambda} = -\frac{1}{r_c}\hat{t} + \tau\hat{b} \ , \qquad \frac{d\hat{b}}{d\lambda} = -\tau\hat{n} \ . \tag{4.1}$$

We solve these equations with a fourth-order Runge-Kutta method sampling thousands of trajectory points, with a spatial gridding which increases as the particles get faster, in order to capture better the initial, slower, synchrotron-dominated part.

In the first incarnation of the spectro-geometrical model, Viganò and Torres (2019), a zero torsion was assumed, which is valid as long as the twist of the magnetic field lines is small compared to its curvature. In Íñiguez-Pascual et al. (2024), we got rid of such an assumption and allowed a non-zero torsion, being of the same order as the curvature, i.e. $\tau(\lambda) = 1/r_c(\lambda)$, which is compatible with what is expected in the non-corotating regions, close or beyond the light cylinder. In this way, trajectories are twisted as well as curved, and thus require all three spatial dimensions to describe them.

4.1.2 Emission directions of the travelling particles

Due to the high Lorentz factor $\Gamma \gtrsim 10^6$ reached by the particles, the emission beam ($\propto \Gamma^{-1}$) is very narrow, so in our numerical scheme we consider the radiation emitted exactly in the direction of motion. The latter is determined as follows. At each λ, we consider a local particle coordinate system. In this coordinate system, the instantaneous emission direction of a particle is $(\theta_e(\lambda), \phi_e(\lambda)) = (\alpha(\lambda), \chi)$, where χ is the gyration angle, $\chi \in [0, 2\pi]$.

We write the particle emission directions at each position in a pulsar coordinate system, in which the azimuthal coordinate ϕ_Ω tracks the rotational phase of the star, and the meridional coordinate θ_{obs} corresponds to a given observer. The transformation of the emission directions among the different coordinate systems, $\hat{r}_e = (\theta_e(\lambda), \phi_e(\lambda)) \rightarrow \hat{r}_{map} = (\theta_{obs}, \phi_\Omega)$, is calculated by a series of rotations considering several relevant angles and the time delay. Note that ϕ_Ω and θ_{obs} depend on $\alpha(\lambda)$ and χ, as well as on the angles entering into the rotations,

dependencies that are left implicit hereafter to ease the reading. The expression that encodes these rotations is:

$$\hat{r}_{\rm map} = \mathbf{R}^{\rm z}(-\xi_{\rm f})\,\mathbf{R}^{\rm y}(-\Psi_\Omega)\,\mathbf{R}^{\rm z}(-\xi_\mu)\,\mathbf{R}^{\rm y}(-\Psi_\mu)\,\mathbf{R}^{\rm x}(-\xi_{\rm t})\,\mathbf{R}^{\rm y}(-\Psi_{\rm t})\,\hat{r}_{\rm e}\ . \tag{4.2}$$

where $\Psi_{\rm t}$ and $\xi_{\rm t}$ are the projections of the direction of motion of a particle onto the sky of a coordinate system in which the gyration-averaged trajectory is still; Ψ_μ and ξ_μ are the magnetic colatitude and longitude, respectively, which are the angles of the initial position of a given trajectory with respect to the magnetic moment; and $\xi_{\rm f}$ is the phase flight delay, originated by the differences in the path length from emission to observer of the different positions of the trajectory. In Viganò and Torres (2019) can be found the detailed explanation of this series of rotations. We map the emission directions through these rotations which only change the coordinates. It is relevant to mention that we do not consider different relativistic frames, we only change the coordinates we use to map directions in the sky, following the same concept explained in subsection 2.4 of Pétri (2020).

We construct the emission map by collecting the particles' emission in a unit sphere centred at the star, in the pulsar coordinate system, and considering time delay. For each particle, we can then consider the corresponding distribution of emission directions at each λ, per unit solid angle of the pulsar coordinate system $d\Omega_{\rm p} = \sin\theta_{\rm p} d\theta_{\rm p} d\phi_{\rm p}$, as:

$$\frac{dD(\lambda)}{d\Omega_{\rm p}} = \frac{1}{2\pi\sin\theta_{\rm p}} \int_0^{2\pi} \delta[\theta_{\rm p} - \theta_{\rm obs}(\chi)]\delta[\phi_{\rm p} - \phi_\Omega(\chi)]d\chi \tag{4.3}$$

The distribution of emission directions is averaged over a gyration period of χ, because this period is much smaller than any other timescale present in this problem, which means that we can safely assume that a large number of particles are emitting from all the gyration positions at the same time. The Dirac delta functions $\delta[\cdot]$ project onto the pulsar coordinate system sky the emission directions swept by the particles during a gyration at each position along their trajectories. Such distributions are simply circles with radius α in the local particle coordinate system which are distorted in the pulsar coordinate system due to the rotations, and approach a single point in the sky as the particle accelerates - because α decreases as a result of the loss of perpendicular momentum due to synchrotron losses.

We have now to specify how the coordinate λ translates into the three-dimensional space, for a given location and shape of the accelerating region.

4.1.3 Location in the magnetosphere and shape of the emission region

To guide our description of the emission region, we have taken into account the results of the latest magnetospheric FFE and PIC simulations, which we have presented in Chapter 2, all based on a magnetic dipole at the pulsar surface (thus giving the topology a plane of symmetry). We have seen that these simulations agree in locating the place of high-energy emission production just outside the light cylinder, in an ECS that extends from the Y-point and completely surrounds the pulsar in the azimuthal direction. The Y-point is located at a magnetic colatitude $\Psi_\mu = \pi/2$ (being Ψ_μ the meridional angle from the

magnetic axis). Considering the outward extent, the regions have a shape similar to that of a "ballerina skirt" (as dubbed by Cerutti and Beloborodov 2017), i.e. having a magnetic colatitude which oscillates with the azimuthal angle and increases with the radial distance. Such oscillations are maximum for an orthogonal rotator ($\Psi_\Omega = \pi/2$) and vanish for an aligned rotator ($\Psi_\Omega = 0$). An exact, realistic prescription of the shape of the emission region is not available to our knowledge, as we have seen in Chapter 2. The shape we propose here is close to the Y-point, and it actually resembles qualitatively the innermost part of the wavy behaviour of the current sheet location in the meridional plane shown by Figure 4 of Bogovalov (1999).

In order to take into account such qualitative characteristics, we define the emission region with a central value of the magnetic colatitude Ψ^c_μ given by the following function:

$$\Psi^c_\mu(\xi_\mu, R, \Psi_\Omega) = \frac{\pi}{2} + A(R, \Psi_\Omega) \sin(\xi_\mu - \pi/2) \ , \tag{4.4}$$

where A represents the amplitude of the oscillations, which is effectively modelled as linear with Ψ_Ω and quadratic with the distance:

$$A(R, \Psi_\Omega) = K \ \Psi_\Omega \ (R/R_{LC} - r^0_{\rm in}/R_{LC})^2. \tag{4.5}$$

R is the distance from the beginning of the trajectory and $r^0_{\rm in}$ is the first injection point, and thus is the innermost point of the trajectory, also indicating the distance between the neutron star's surface and the beginning of the emission region, and is fixed to $r^0_{\rm in} = 1.0 R_{LC}$. The particular form of this formula, as well as the chosen and fixed value of $K = 5$, qualitatively represents the shape of the likely emitting regions (outer current sheets), as seen in the plots from PIC simulations in the cited literature. It is relevant to remark that the regions built with this prescription do not present any physical inconsistency, such as very tiny or very large regions or overlapping layers. The region is located around $\Psi^c_\mu(\xi_\mu, R, \Psi_\Omega)$, and has a meridional extent of $\Delta\Psi_\mu$, reaching magnetic colatitude values between $\Psi^c_\mu + \Delta\Psi_\mu/2$ and $\Psi^c_\mu - \Delta\Psi_\mu/2$.

We numerically sample the directions Ψ_μ (over the meridional extent $\Delta\Psi_\mu$) and ξ_μ (over 2π) with a step of $\delta = 0.88°$, meaning that we consider a set of $(2\pi \ \Delta\Psi_\mu)/\delta^2$ discrete particle trajectories. With this resolution we are able to have well resolved emission maps, without relevant numerical features or noise in the light curves. The numerical convergence tests we have performed showed that the results remain basically unchanged when choosing a better resolution.

We show the resulting shape of the emitting region in Figure 4.1, for an arbitrary geometry. The parameters Ψ_Ω and $\Delta\Psi_\mu$ are relevant geometrical parameters of our model. We remark the difference between these two parameters: while the former is the widely used inclination angle, the latter is an effective parameter of our model to quantify the meridional extent of the region. Another physical parameter is required to fully describe the location of the region: the injection range ΔR in which the N_{inj} injection points are (evenly) distributed. Our model is flexible in this regard and we can consider different radial extents of the region and different number of injection points. Even though in Appendix A we show that the spectra of high-energy pulsars remained quasi unchanged when considering several $r_{\rm in}$'s instead of a single one, the extension of ΔR affects the skymaps, as we will see later on.

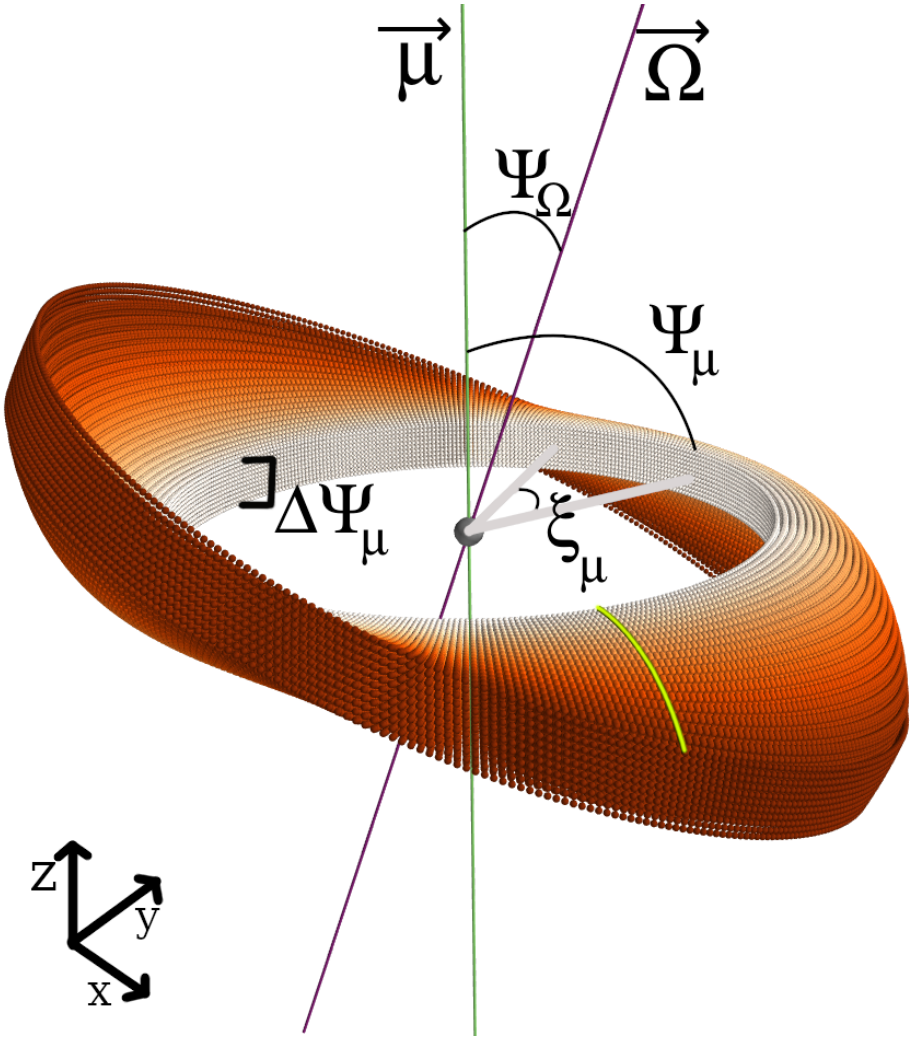


Figure 4.1: Geometrical representation of the magnetospheric emission region assumed in this work, for a pulsar with a geometry $\Psi_\Omega = 18°$, $\Delta\Psi_\mu = 10°$ and $\Delta R = 0.5 R_{LC}$. This region is drawn here as the set of the gyration-average trajectories of the emitting particles attached to different rotating magnetic field lines. The yellow line is one of such trajectories. The gyration radius would be invisible in this scale. The color scale indicates the position λ on the trajectory from the beginning of the region. The purple line is the rotational axis $\vec{\Omega}$ and the green line is the magnetic axis $\vec{\mu}$. The central gray sphere represents the position of the pulsar (its dimension is roughly at scale only if the period is a few milliseconds). The light gray lines (which represent a distance from the star of $r_{\rm in}^0 = 1.0 R_{LC}$) that connect the star and the base of the region are contained in the plane perpendicular to the magnetic axis.

Once we have the three-dimensional description, we can associate each injection place and following values of λ to a specific point in space, so that for each point of a trajectory starting at a given $r_{\rm in}$, we can calculate the corresponding emission directions, via the distribution $dD(\lambda)/d\Omega_{\rm p}$, Equation (4.3).

4.1.4 Radiation emitted from the emission region

In the spectro-geometrical model we also compute the radiation emitted by the charged particles. We do it in the same way as in the radiative model of Chapter 3. With the dynamics of the particles solved along their trajectories, we compute the synchro-curvature radiation emitted by the particles at each location with Equation 2. The single-particle spectra are then averaged to account for the contributions of particles that travel different distances, as in Equation (3.20), as well as convolved with the effective particle distribution $dN/d\lambda$, and the contributions of the different injection points are summed, as in Equation (3.24), to obtain the total spectrum. In the spectro-geometrical model, this radiation is not the one emitted by the whole region, but instead from a single magnetic field line, along which particles are injected and travel. To keep our effective approach simple for the time being, we consider that the radiation produced by the particles at each rotating magnetic field line and the effective particle distribution in it are the same in all the lines of the region. We only consider particles moving outward from the neutron star, and neglect those moving backward. The total radiation emitted from the whole emission region is then the summed contribution of the emission from all lines in the region.

4.1.5 Emission skymap

The skymap for a given set of spectral parameters is obtained by considering all the lines, the injection points and integrating over the solid angle the distribution of directions. The final expression for the energy-dependent emission skymap is then:

$$M_{\rm E}(\theta_{obs},\phi_\Omega,E)=\int_{r_{\rm in}^0}^{r_{\rm in}^0+\Delta R}\int_{\lambda_{\rm in}}^{\lambda_{\rm out}}\int_0^{2\pi}\int_{\Delta\Psi_\mu}\frac{dD(\lambda)}{d\Omega_{\rm p}}\left\langle\frac{dP_{\rm sc}(\lambda)}{dE}\right\rangle\frac{dN(\lambda)}{d\lambda}d\Psi_\mu\,d\xi_\mu\,d\lambda\,dr_{\rm in}\ , \quad (4.6)$$

which represents the photon flux per unit energy, per unit solid angle, emitted by particles injected all along the region. $\lambda_{\rm in}$ and $\lambda_{\rm out}$ are the first and last positions of the gyration-averaged trajectory, respectively. We shall consider that the final map is normalized to the total emission, i.e. to the summed emission of the whole map, therefore being insensitive to the normalization N_0 used in the spectral fit. Note that the rotational phases 0° and 180° of the maps correspond to the magnetic poles, i.e. to the plane containing the rotational and magnetic axes of the pulsar.

Such a skymap represents the projection over a sphere at infinity of the radiation emitted by the whole population of accelerated particles. For a given observer with viewing angle θ_{obs}, the light curve is given by an azimuthal cut on the skymap, integrating $M_{\rm E}$ over a given energy range. In this study we focus on the Fermi-LAT γ-ray band, 100 MeV – 300 GeV. Note that in order to generate these maps, values of the spectral parameters ($E_{||}$, x_0/R_{LC}, b) are required, they enter in the solution of the dynamics and in the computation of the

spectra. The values of these parameters that we consider, for a particular pulsar, are the ones better fitting its corresponding spectrum.

4.2 Synthetic skymaps and light curves of selected pulsars

Consider now a given pulsar, with certain timing properties P, $\dot{P}$, and a given set of the three parameters ($E_{||}$, x_0/R_{LC}, b). We focus on studying the variety of observed light curves, for different geometrical parameters. The inclination angle Ψ_Ω can vary from case to case, since it is still not clear how it evolves (Philippov et al., 2014). We also consider different values of our parameters $\Delta\Psi_\mu$ and ΔR. For each combination of values of Ψ_Ω, $\Delta\Psi_\mu$ and ΔR we build a skymap, from which different light curves are obtained when varying θ_{obs}.

4.2.1 Effects of the geometry on the skymaps and light curves

Let us start by studying the effect of the geometrical parameters for a given pulsar, focusing on J0205+6449. The second rows of Figures 4.2 and 4.3 show a selection of skymaps for different geometries, visualized in the first rows (recall that these skymaps, as well as their corresponding light curves, are obtained by integrating $M_{\rm E}$ in energies, in the γ-ray band, 100 MeV – 300 GeV). In each figure we can separately see the impact on the emission map of the geometrical parameters Ψ_Ω and $\Delta\Psi_\mu$. The second row of Figure 4.2 shows how the skymap is clearly modified when the inclination angle varies. For low inclinations, the emission is concentrated around the equatorial plane, whereas more structures appear for larger inclination angles. On the other hand, the second row of Figure 4.3 shows the broadening of the intensity region when $\Delta\Psi_\mu$ increases. Looking at Figure 4.1 we can see how the region bends as a function of the radial distance to the star, although in the innermost part of the region this bending is not very strong. In this way, there is a certain radial extent R of the region in which the particles point mostly in the same direction, or in a small angular range. Therefore, their emission is concentrated in a band, with a width around $\Delta\Psi_\mu$, which is what we see in the skymaps. At the same time, in the outer parts of the region, the bending is stronger, meaning that the particles there point to a broader angular range, thus spreading their emission more widely, as is also seen in the skymaps.

The third rows of Figures 4.2 and 4.3 show examples of several light curves of the same pulsar, for the same particular set of geometrical parameters of the corresponding skymap on the second row, and different viewing angles. We observe how the synthetic light curves we generate have general shapes compatible with the observational ones found in the 2PC and 3PC. This can be seen by qualitatively comparing the coloured lines (synthetic) against the black line (observational from the 3PC). Note that we are only showing some particular geometries, not necessarily the best-fitting ones. Our set shows a wide diversity of light curve features, having one up to several peaks, with different peak separations, and peak widths. The goal of this Chapter is indeed to show that our spectro-geometrical model generates realistic light curves, rather than performing quantitative fits, which we face in Chapter 5.

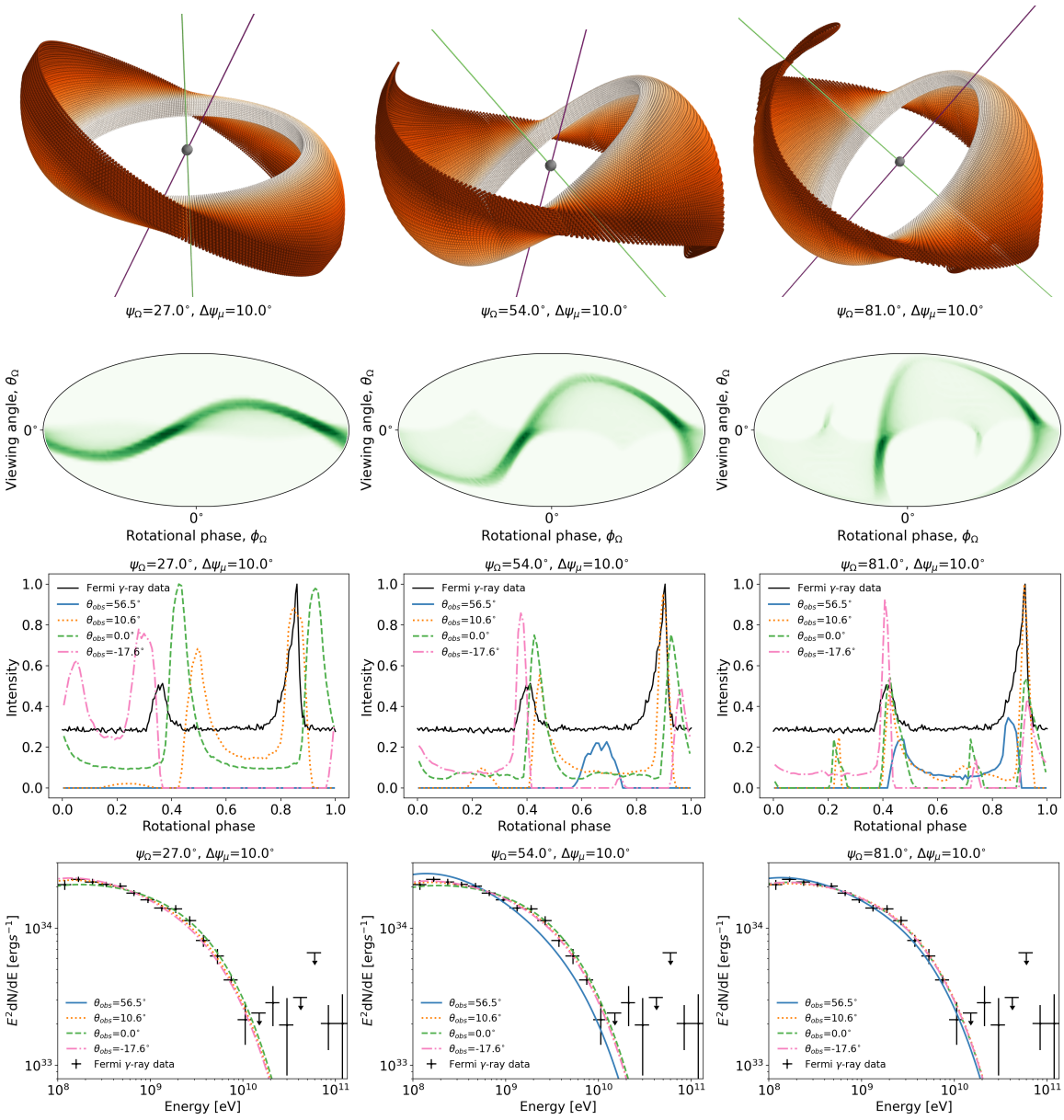


Figure 4.2: First row: representative examples of the geometry of the magnetospheric emission region of the pulsar J0205+6449 for different values of the inclination angle $\Psi_\Omega = \{27°, 54°, 81°\}$ (increasing from left to right). The meridional extent of the region is $\Delta\Psi_\mu = 10°$ and the injection range $\Delta R = 0.5\ R_{LC}$. Second row: corresponding synthetic emission maps. These skymaps (as well as their corresponding light curves) are obtained by integrating $M_{\rm E}$ in energies, in the γ-ray band, 100 MeV – 300 GeV. Third row: corresponding synthetic light curves (in colours) for a few, arbitrarily chosen, observers θ_{obs}. Notice that light curves are not normalized at the maximum intensity, which is only done for peak classification, but at the maximum intensity of the emission map, just for visualization and comparison purposes. Black lines correspond to the observational light curve of J0205+6449 seen by the *Fermi* telescope and released in the 3PC, normalized to its maximum intensity. For simplicity it is arbitrarily aligned with the light curve seen by the observer at $\theta_{obs} = 10.6°$ (we could also rotate the synthetic light curves in phase in order to compare them with the observational one). Recall that producing a light curve fitting is not our goal here, we show this just for qualitative comparison of the real case with results coming from an assumption of fixed values of the parameters. Fourth row: corresponding γ-ray spectra seen by the same observers, showing differences in shape, together with observational γ-ray data from *Fermi*.

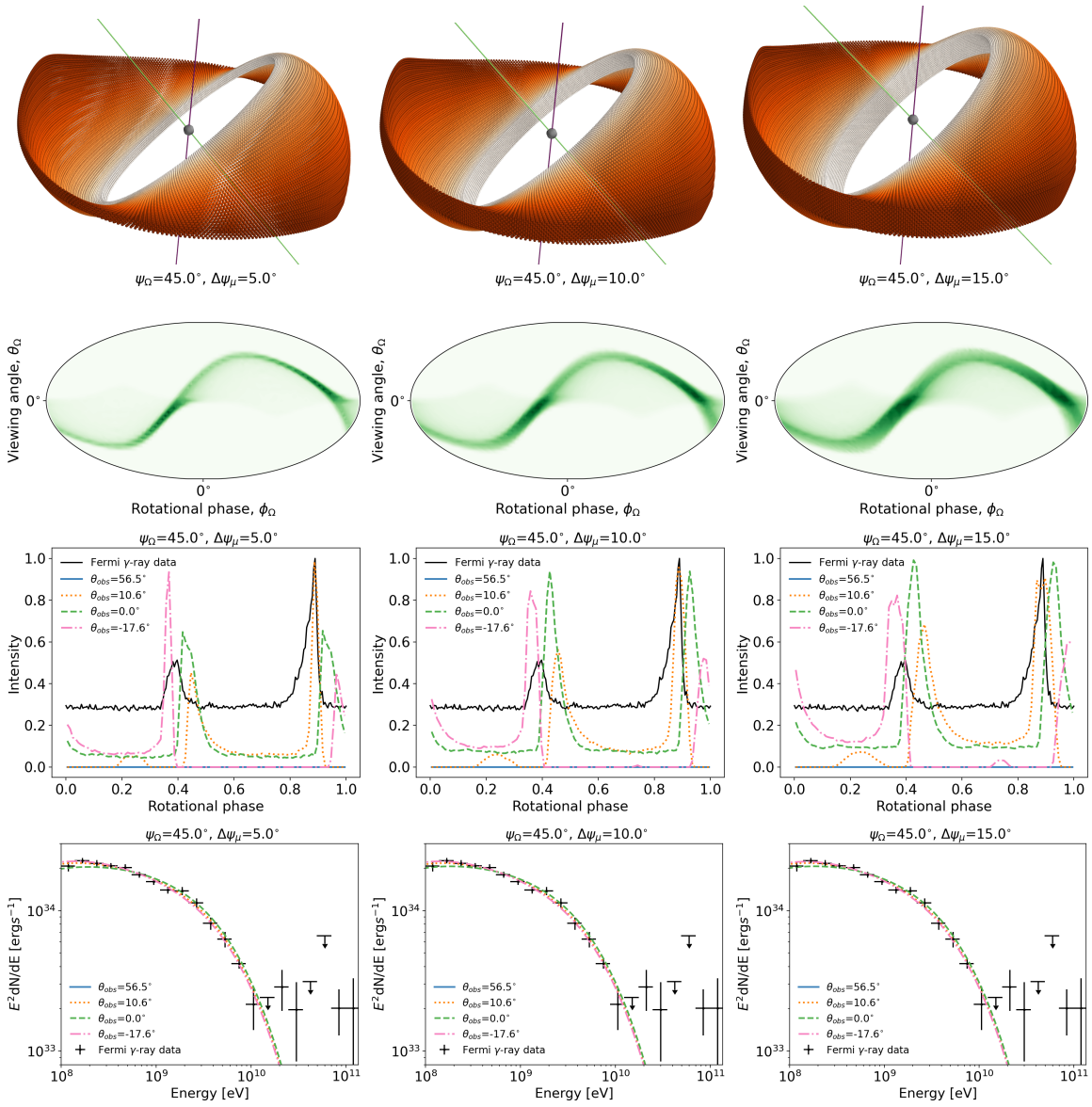


Figure 4.3: Same as Figure 4.2, but varying the meridional extent of the region $\Delta\Psi_\mu = \{5°, 10°, 15°\}$ (from left to right), for an inclination angle $\Psi_\Omega = 45°$ and an injection range $\Delta R = 0.5\ R_{LC}$.

Light curves obtained from geometries with large inclination angles present a richer morphology than those coming from lower inclinations. All the non-zero light curves in the left panel of the third row of Figure 4.2 have two peaks, while those in the middle and right panels also show three and four peaks.

We also note that for higher inclination angles the skymap gets more filled, because the whole region is more inclined and the particles in it can span a broader range of emission directions. This can be clearly seen with the observer $\theta_{obs} = 56.5°$, the one closer to the pole. For $\Psi_\Omega = 27°$, this observer would not detect anything, while for $\Psi_\Omega = 54°, 81°$, she would. Increasing the meridional extent does not have such a critical impact on the light curves. It modifies the width of the peaks, making them wider, as can be seen in the third row of Figure 4.3. It also has the effect of filling the skymaps, to a lower degree than with the increase of the inclination angle, and at the same time increases the intensity of the regions where radiation is collected. This latter effect occurs because increasing the meridional extent implies the presence of more lines along the magnetic colatitude. Since the angular increase is rather small (in our case, 2.5° at each hemisphere when increasing from $\Delta\Psi_\mu = 5°(10°)$ to $\Delta\Psi_\mu = 10°(15°)$, or 5° at each hemisphere when increasing from $\Delta\Psi_\mu = 5°$ to $\Delta\Psi_\mu = 15°$), those new lines have a very similar direction to those already present with a smaller $\Delta\Psi_\mu$. In this way the amount of emitting particles (which point in similar directions) increases, and thus more radiation is collected in the sections of the skymap already populated in the smaller $\Delta\Psi_\mu$ case, increasing the intensity of these sections.

We note that some observers, e.g. the one located at $\theta_{obs} = 56.5°$ in Figure 4.3, would see no emission at all, at any phase. This likely happens in nature too, i.e., there could be high-energy pulsars as powerful as the one taken here as example, J0205+6449, which we do not detect simply because we are not in the line of sight of their emission. Below we will assess the percentage of observers which actually do detect emission in our skymaps.

Finally, Figure 4.4 shows the skymaps resulting from different values of $\Delta R = \{0, 0.25, 0.50, 0.75\}\ R_{LC}$ (keeping the same radial injection resolution, i.e. having 1, 11, 21 and 31 injection points, respectively), considering one particular geometry, $\Psi_\Omega = 36°$ and $\Delta\Psi_\mu = 10°$. We observe how the increase of the injection range has the effect of filling more sections of the skymap, due to the modulation of the outer parts of the trajectory (see Figure 4.1). A larger injection range produces a more elongated region, and thus the radiation emitted spans a broader set of directions, as seen in the skymaps, which are more filled for a larger ΔR.

4.2.2 Effects of the spectral parameters on the skymaps and light curves

So far we have seen the effects of the geometry, i.e. of the geometrical parameters, for a given pulsar. Let us now compare different pulsars, i.e. different spectral properties of the emission, for the same geometry. In Figure 4.5 we show the light curves generated for three of our selected pulsars, for a particular geometry, $\Psi_\Omega = 54°$ and $\Delta\Psi_\mu = 10°$, the one corresponding to the central panels of Figure 4.2. They are basically similar, with only small variations in the intensity. Therefore, changing the spectral (and the timing) properties

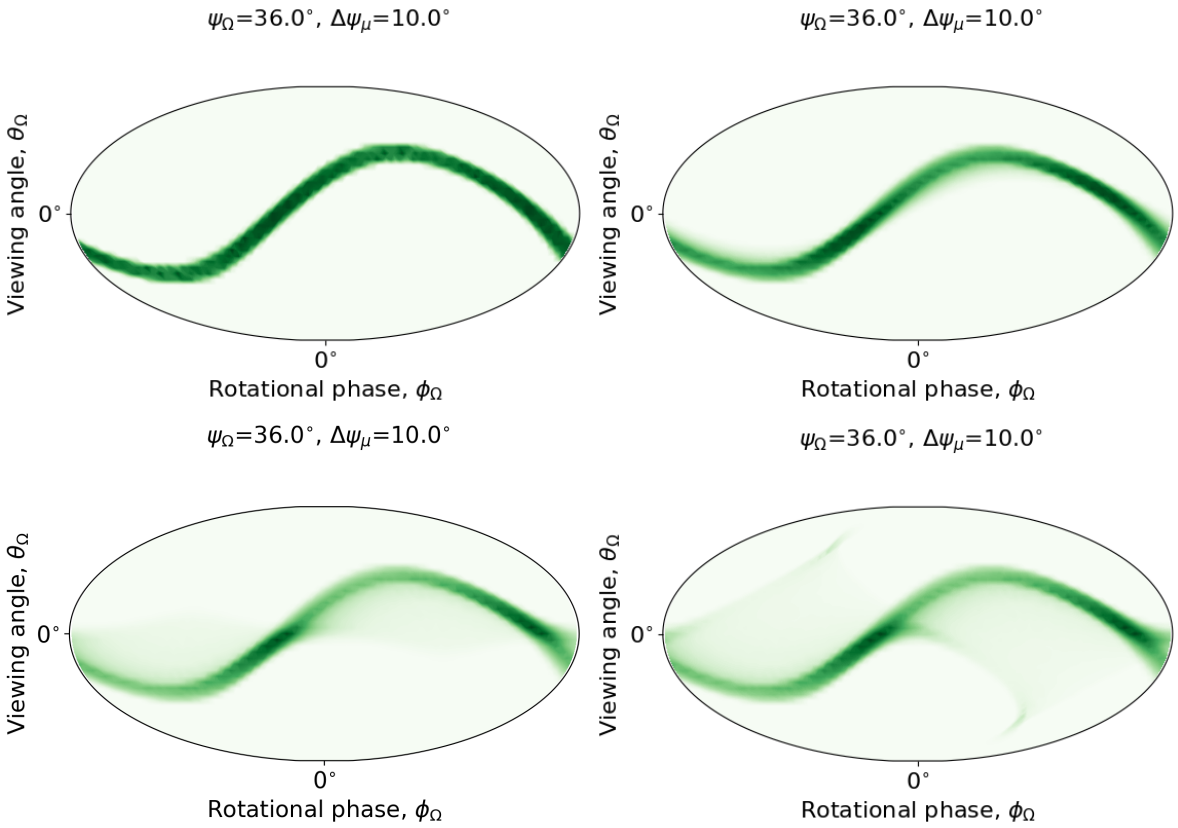


Figure 4.4: Skymaps of J0205+6449 for a particular geometry, $\Psi_\Omega = 36°$ and $\Delta\Psi_\mu = 10°$, and different values of ΔR. These skymaps are obtained by integrating $M_{\rm E}$ in the energy range 100 MeV – 300 GeV. Top row (from left to right): $\Delta R = 0.0, 0.25$. Bottom row (from left to right): $\Delta R = 0.50, 0.75$.

alone produces changes in the skymap which are barely visible, in any case much smaller than the effects produced when the geometry is changed. This implies that the geometrical parameters are much more important than the spectral ones in determining the light curves.

4.2.3 Spectra seen by different observers

If we integrate azimuthally $M_{\rm E}(\theta_{obs}, \phi_\Omega, E)$ for a given observer, we obtain the phase-averaged spectrum seen by they. Therefore, once we build a map, we can get the spectra that all observers would detect.

Bottom rows of Figures 4.2 and 4.3 show the synthetic spectra seen by selected observers. Even though differences are not extreme, they have different shapes and resemble the data differently. The reason for these differences is the non-trivial geometry of the emission region. Its modulated shape and the fact of having injection points all along the region, have the effect of observers receiving radiation from particles located at different radial distances from the star as well as at different positions from their injection points into the region. This implies different values of the kinetic quantities, e.g. Lorentz factor Γ and pitch angle α, of these particles, which therefore emit different spectra.

In the light of these results, it is possible to appoint an observer, or at least a group of observers, as preferred, i.e. to give a preferred value or a range of values, for instance, of the possible viewing angle(s), for the particular pulsar studied, by how well the spectra of the

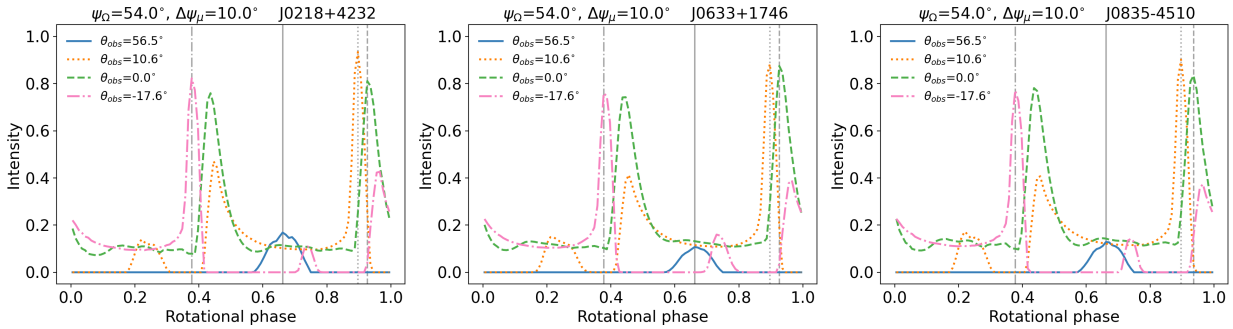


Figure 4.5: Selection of γ-ray light curves of the particular geometry $\Psi_\Omega = 54°$ and $\Delta\Psi_\mu = 10°$, for three pulsars, from top to bottom: J0218+4232, J0633+1746 and J0835-4510. Light curves are obtained by integrating $M_{\rm E}$ in the energy range 100 MeV – 300 GeV, and cutting an horizontal slice. Vertical grey lines indicate the phase of the highest-intensity peak of each light curve, which basically do not change between the light curves of different pulsars having the same geometry.

observers match the observational data of this pulsar.

We can quantify the degree of resemblance of each spectrum by computing a reduced χ^2, $\overline{\chi^2}$. Doing so for each observer, we obtain values (evenly distributed) between $\sim 0.8 - 1.7$ (with 18 data points), meaning that the difference among spectra is statistically significant. In the same way as we did in Íñiguez-Pascual et al. (2022), following the prescriptions of Avni (1976), we can define a 1 σ confidence interval around the smallest $\overline{\chi^2}$ found. Taking into account that $\overline{\chi^2}$ values below 1 can be regarded as statistically equal, for the corresponding degrees of freedom we get a $\overline{\chi^2}_{limit}$ of 1.19. Thus, most of the observers have $\overline{\chi^2}$ values outside the 1 σ confidence interval of the observer with the lowest $\overline{\chi^2}$. Still, for different observers, the difference in their spectra is much smaller than the difference in their light curves, as shown by the comparison of the third and fourth rows of Figures 4.2 and 4.3.

Also, we foresee even larger differences in spectra of different observers when extending the spectra to lower energies, due to an increased dominance of synchrotron radiation. We will explore this in the future.

4.2.4 Set of geometries and sample of pulsars

To span the possible outcome of our model we consider 10 values of the inclination angle, $\Psi_\Omega \simeq [9°, 18°, 27°, 36°, 45°, 54°, 63°, 72°, 81°, 90°]$; and 3 for the meridional extent of the base of the emission region, $\Delta\Psi_\mu \simeq [5,°, 10°, 15°]$. In order to adhere to the radiative model, in the spectro-geometrical model we assume $\Delta R = 0.5 R_{LC}$, but with $N_{inj} = 21$, since convergence is achieved at this value (see Appendix A). The injection points are still equally distributed from 1.0 R_{LC} to 1.5 R_{LC}. In addition, fixing $\Delta R = 0.5 R_{LC}$ produces region shapes more similar to those obtained with PIC simulations than other values. With our particular choice of the grid of the parameters, we have a total of 30 different geometries. For each corresponding skymap we consider 51 different types of observers, covering from the North to the South poles. Due to discretization, such observers are indeed a bin in the skymap latitude, with a thickness of $\pi/50 \simeq 3.5°$ centered on a value of θ_{obs}. Thus, each light curve represents the radiation collected inside that bin. The values of θ_{obs} we will give later correspond to the central value of each bin.

In this way, we end up with a set of 1530 different light curves for a given pulsar [10 (inclination) × 3 (meridional extent of emission region) × 51 (observers)]. Notice that this number is given solely by our choice of the number of geometries and observers, which is a compromise between computational cost and sufficient size of the synthetic sample. For a given pulsar, the computational time required is typically a few hours.

We aim at studying the variety of obtained light curves (in general and as a function of parameters) by looking at how many observers detect light and which features the curves have. To this purpose, we apply a peak recognition algorithm to each of the light curves. The details of the algorithm are shown in subsection 4.3.1. Using it, we can thus extract basic information from each light curve, such as the number of peaks, as well as the width, intensity and location (rotational phase) of each peak.

Here we consider as a first example ten pulsars having good *Fermi*-LAT data both for their spectra and light curves. The ten pulsars are: J0007+7303 (a young pulsar), J0205+6449 (a bright young pulsar), J0218+4232 (a millisecond pulsar), J0633+1746 (Geminga), J0835-4510 (Vela, the brightest γ-ray source in the sky), J1513-5908 (one of the few pulsars detected at MeV energies), J1809-2332, J2021+3651, J2021+4026, J2229+6114 (four young pulsars as well). Table 4.1 shows their timing and spectral parameters. They are representative of the variety of the γ-ray pulsar population in terms of their timing properties, the number of peaks of their light curves in the 2PC and 3PC, and the values of their best-fit spectral parameters, for instance.

Table 4.1: Timing and best-fitting spectral parameters of the ten selected pulsars. The spectral model here considers 21 injection points evenly distributed from 1.0 to 1.5 R_{LC}. Last two columns show the number of peaks of the observational light curve released in the 2PC and 3PC for each pulsar.

Pulsar	P [ms]	$\dot{P}$ [s/s]	$\log E_{\|\|}$ [V/m]	$\log(x_0/R_{LC})$	b	$\log N_0$	$B_{LC}^{b=3}(G)$	Peaks 2PC	Peaks 3PC
J0007+7303	315.9	3.57×10^{-13}	$8.29^{+0.01}_{-0.01}$	$-2.67^{+0.01}_{-0.01}$	$2.49^{+0.02}_{-0.02}$	33.95	6.28×10^3	2	3
J0205+6449	65.7	1.92×10^{-13}	$8.98^{+0.01}_{-0.01}$	$-3.08^{+0.01}_{-0.01}$	$2.62^{+0.02}_{-0.02}$	34.02	2.32×10^5	2	2
J0218+4232	2.3	7.74×10^{-20}	$9.27^{+0.02}_{-0.01}$	$-2.43^{+0.01}_{-0.01}$	$2.68^{+0.05}_{-0.05}$	33.90	6.32×10^5	2	1
J0633+1746	237.1	1.10×10^{-14}	$7.66^{+0.01}_{-0.01}$	$-1.92^{+0.01}_{-0.01}$	$2.25^{+0.02}_{-0.01}$	32.35	2.26×10^3	2	3
J0835−4510	89.4	1.25×10^{-13}	$8.24^{+0.01}_{-0.01}$	$-2.38^{+0.01}_{-0.01}$	$2.87^{+0.02}_{-0.02}$	33.77	8.73×10^4	3	4
J1513−5908	151.6	1.53×10^{-12}	$7.31^{+0.01}_{-0.01}$	$-2.42^{+0.01}_{-0.01}$	$3.23^{+0.01}_{-0.01}$	37.51	8.19×10^4	1	1
J1809−2332	146.8	3.44×10^{-14}	$8.25^{+0.01}_{-0.01}$	$-2.56^{+0.01}_{-0.01}$	$2.58^{+0.03}_{-0.02}$	33.77	1.32×10^4	2	3
J2021+3651	103.7	9.56×10^{-14}	$8.51^{+0.01}_{-0.01}$	$-2.78^{+0.01}_{-0.01}$	$2.95^{+0.01}_{-0.01}$	34.82	5.26×10^4	2	3
J2021+4026	265.3	5.42×10^{-14}	$7.97^{+0.01}_{-0.01}$	$-2.51^{+0.01}_{-0.01}$	$2.78^{+0.05}_{-0.04}$	35.03	3.78×10^3	2	3
J2229+6114	51.7	7.79×10^{-14}	$8.56^{+0.01}_{-0.01}$	$-2.55^{+0.01}_{-0.01}$	$2.70^{+0.01}_{-0.01}$	34.28	2.72×10^5	2	2

4.3 Light curves features and comparison with observations

Out of the total number of synthetic light curves generated for a given pulsar as a result of the application of our model, the percentage of detected light curves, i.e. of observers that do

see a non-zero intensity, is typically 60%. The remaining are non-detections, i.e. observers whose viewing angles do not cut through the bulk of the emitted radiation, corresponding to pulsars we do not detect due to geometrical reasons. This result may have an impact in population synthesis studies, since it gives an estimate of how many pulsars can indeed be detected given sufficient sensitivity out of the total real population.

We now consider the distribution of morphological features of the detected light curves:

- Number (or percentage) of light curves with n peaks
- Flux ratio between two peaks (P1/P2, where P1 is taken as the highest)
- Phase separation between two peaks
- Width of the peaks

For the first one, we compute the percentages over detected light curves (i.e. discounting from the total number of light curves generated (1530) the non-detections). For each percentage we associate an uncertainty of 3%. Such a value is the typical maximum variation that includes the uncertainty due to both the resolution of the region size, and the algorithm that defines the peaks (in particular, changing the threshold cut between 5% to 1%, see subsection 4.3.1 for details). The second and third features (flux ratio and phase separation) apply to the subset of light curves with just two peaks, and the fourth one (width) is calculated for each one of the peaks in each light curve.

We construct histograms for each of these three features. Figure 4.6 shows the percentages of light curves with n peaks for the selected pulsars. Figure 4.7 shows examples of the histograms for the other three features. In Figure 4.6 we can see that most of the detected light curves possess two peaks, while few have more than 3 peaks. The agreement with the global result of the 2PC/3PC is impressive. We comment more on this below. Figure 4.7 shows clear trends in the distributions of the flux ratio and width of the peaks. The former peaks at ~ 1.3 and decreases towards to ~ 3, indicating the rather small difference in the intensity of each peak in two-peaked light curves. The widths distribution also peaks at low values, with the majority of the peaks having a width of $0.05 - 0.30$ in phase and almost no peaks with a width larger than 0.5. In the distributions of the phase separation between peaks such behaviour is less pronounced. Still, we do see a preference for larger separations than not.

4.3.1 Details of the peak recognition algorithm

In order to obtain these light curve features, we need to detect their peaks, i.e. know at which rotational phase they are and the rotational phase range they cover. With the number of light curves we deal with, 1530 per pulsar, it is not affordable to perform the peak recognition manually. To automate this task we use our own peak recognition algorithm, which detects the peaks of a given light curve and outputs its features. This algorithm has some particularities worth mentioning.

First of all, in order to discard numerical noise (coming from lack of resolution in the trajectories or in the light curve code), we have applied a threshold cut to the intensity

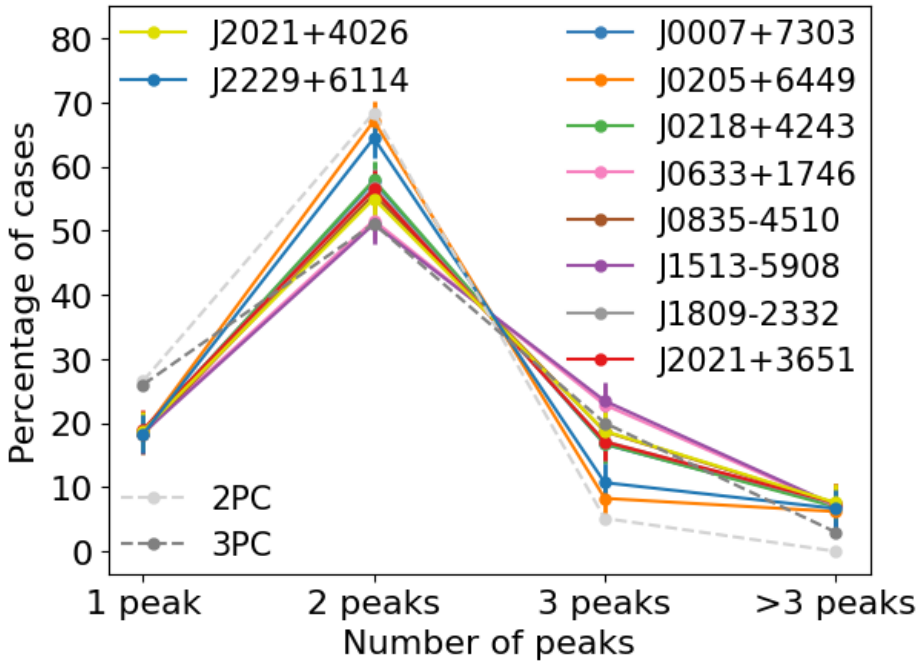


Figure 4.6: Percentages of synthetic light curves with n peaks for different pulsars. Grey lines show the observed distribution (from all pulsars) in the 2PC (117) and the 3PC (236). Error bars of 3% indicate the estimated uncertainties as explained in the text.

of the emission map below which we consider that there is no emission. Note that this choice also practically mimics the limited signal-to-noise ratio in γ-ray observations, which makes weak signals undetectable (depending of course on the source, its brightness, distance, etc.). We have set this threshold to 5% of the maximum of the emission map. In this same direction, we apply a uniform moving average filter, also called top-hat filter, up to the third neighbour in order to reduce the noise and smooth the shape of the light curves, which helps in detecting peaks.

In order to calculate the number of peaks seen by each observer and geometry, we normalize each light curve to its maximum intensity. Then, any excess of intensity larger than 0.1 (i.e. 10% of the maximum), is classified as a peak. In addition we require a minimum phase distance of 0.1 between peaks. The algorithm then stores the phase position and intensity of each peak of the particular pulsar. The width of the peaks is computed by fitting the light curve to a (multi-)gaussian distribution and computing the FWHM of each gaussian (the FWHM of a gaussian is $\approx 2.355\sigma$, where σ is the standard deviation of the gaussian).

The choice of the two thresholds and the minimum peak separation allows us to have a reliable description of the main features of the synthetic light curves, and we have checked that other reasonable values would not give very different results in the statistics. Note that our algorithm is not directly comparable to the ones used for observational data, since the latter have non-zero background which hides part of the light curves. Indeed, as shown in the main text, the peak statistics changed non-negligibly from the 2PC to the 3PC, due to both an enlarged sample and better background treatment.

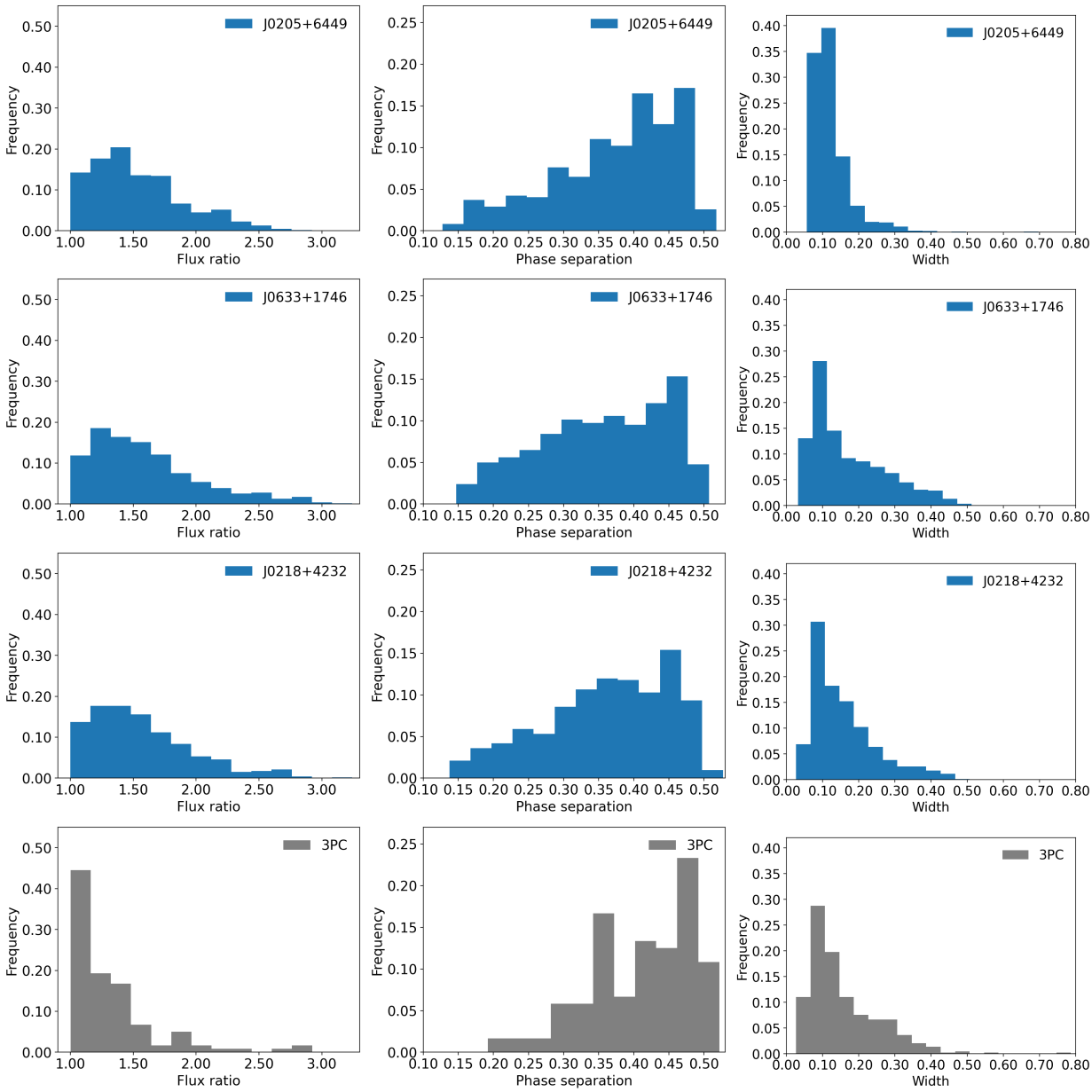


Figure 4.7: Normalized frequency histograms of flux ratio (left column), phase separation (middle column) and width of the main peak (right column), coming from the synthetic light curves over geometry variations for three pulsars (first three rows, respectively J0205+6449, J0633+1746 and J0218+4232), and from the observed pulsar 3PC sample (last row). For the latter, we have used the same peak recognition algorithm, except for the width which has been computed manually.

4.4 Comparing the distribution of features of different pulsars

Figures 4.6 and 4.7 show that the statistics of the different features of the light curves, while being different for different pulsars, follow the same trend. This fact agrees with what we have seen in subsection 4.2.2, where the skymaps and light curves are very similar among different pulsars. This reinforces the idea that the geometry plays a major role in shaping the light curves, being much more relevant than the spectral parameters.

Figure 4.6 shows a line corresponding to the percentages of light curves with n peaks in the 2PC and 3PC. We observe how it follows a very similar behaviour to the lines of particular pulsars. The similarity becomes even larger with the 3PC, which has brought better and more γ-ray light curves than those in the 2PC. The better signal-to-noise ratio of the new catalogue has brought the appearance of new peaks which in the previous one were overtaken by noise, resulting in the presence of more light curves with 3 peaks or more. It has also led to the detection of peaks in light curves that were previously too noisy.

This implies that a set of synthetic light curves produced for a fixed set of best-fit spectral parameters but varying the geometry (inclination, observer line of sight) is also representative of the global set of all observed pulsars, for which the values of such angles are also randomly distributed.

4.5 Impact of the geometrical parameters on the distribution of features

Having a large sample of synthetic curves, we can look for correlations between the geometrical parameters and the distribution of the values representing the light curve features. Here we show how the percentages of light curves with n peaks differ for different values of Ψ_Ω and $\Delta\Psi_\mu$. Figure 4.8 shows interesting trends, such as the decrease (increase) of the number of light curves with one (three or more than three) peak(s) when increasing the inclination angle. This relates to what we have seen in Figures 4.2 and 4.3, where a higher inclination angle implied the appearance of more structure in the skymaps and thus of light curves with more features and peaks. Very similar trends, with different absolute values are observed for the other pulsars.

Taking into account the trends shown, together with the fact that all pulsars show the same behaviour and the statement in the previous subsection that the set of light curves created for a particular pulsar can be considered as equivalent to the population of observed light curves, this opens the possibility of constraining the distribution of the inclination angle in the global pulsar population.

It is also interesting to check how the number of detected and non-detected light curves vary as a function of the parameters. Figure 4.8 also shows how the number of detected light curves, i.e. observers which would detect a non-zero intensity, increases with the inclination angle. The percentage of detected light curves goes from less than 20% to more than 90% as

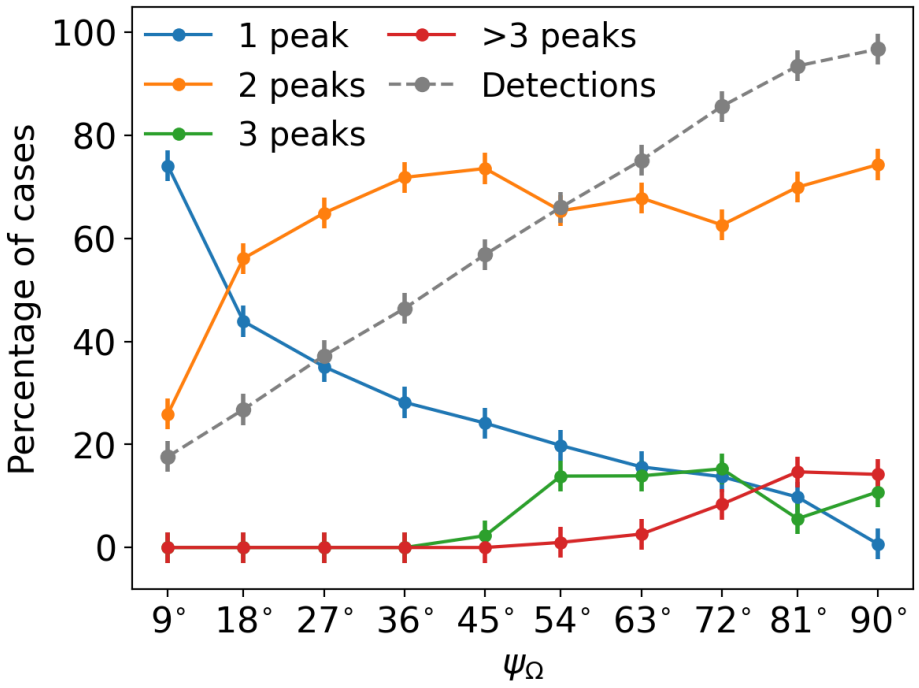


Figure 4.8: Percentages of synthetic light curves (calculated over the observers seeing some signal) with n peaks as a function of the inclination angle Ψ_Ω for J0205+6449. Gray dashed lines represent the percentage of observers detecting signal, calculated over the total set of light curves generated. Error bars represent the estimated statistical 3% absolute error on the percentages, as explained in the text.

the inclination increases. This shows the possibility that an observational bias could exist towards seeing orthogonal rotators, which can be relevant for population synthesis models or studies of the time evolution of the inclination angle (Philippov et al., 2014). Again, this is expected from the skymaps in Figures 4.2 and 4.3, since more sections of the skymap are filled with radiation when increasing the inclination angle.

In the case of the meridional extent, almost no variation is observed. The reason is that the increase of $\Delta\Psi_\mu$ does not significantly populate new sections of the skymap as the increase of Ψ_μ does, but instead increases the intensity of the regions already populated, as seen in subsection 4.2.1.

4.6 Concluding remarks

In this Chapter we have presented a spectro-geometrical model for the pulsar magnetospheric emission regions. This model allows us to build emission regions with arbitrary shapes and placed in arbitrary locations in a pulsar's magnetosphere, ultimately depending on two geometrical parameters, the inclination angle Ψ_Ω and the meridional extent of the region $\Delta\Psi_\mu$, and on the injection range ΔR. This flexibility allows us to produce very different emission regions and test their ability to produce realistic light curves.

For a given set of geometrical parameters, we build emission maps, or skymaps, in which the azimuthal direction represents the rotational phase of the pulsar and the meridional direction θ_{obs} represents the viewing angle of a given observer. From the skymaps we can

extract the light curve (and spectrum) a given observer would detect.

This formalism allows us to geometrically represent the trajectory of the emitting particles in the magnetosphere and contains a realistic shape of the emission region (defined as the zone where the trajectories of the particles are located). This shape is achieved by having the magnetic colatitude Ψ_μ as a function of the magnetic longitude ξ_μ, as well as making this colatitude dependent on the radial distance R and the inclination angle Ψ_Ω. In this way, the shape of the emission region is in qualitative agreement with the magnetospheric topology found by PIC and force-free simulations. Our formalism also includes the implementation of the full synchro-curvature radiation mechanism on top of this geometrical machinery, describing the radiation generated by the particles that travel through the emission region together with its spatial distribution. Synchro-curvature emission is thus intertwined in the geometrical model itself, and we are able to extract light curves from synchro-curvature emission maps, not just from geometrical maps, which are overall consistent with the spectral, phase-averaged prediction.

With this formalism, we have been able to build realistic skymaps, from which we have obtained γ-ray light curves, for a selected sample of high-energy pulsars. The light curves generated resemble reasonably well the observational ones measured by *Fermi*-LAT. All the features that are seen in observational light curves, such as different number of peaks, diverse morphology, a variety of peak widths, phase separations and flux ratios, are also present in our synthetic sample.

The skymaps and light curves generated for a set of different pulsars possessing good observational data are very similar, with no large observable differences. At the same time, these are greatly modified when the geometrical parameters, both the inclination angle Ψ_Ω and the meridional extent of the region $\Delta\Psi_\mu$, change.

In addition, we have computed global features of our light curves sample, which helps us in qualitatively study the synthetic light curves generated. We have found that, in agreement with the global results of the 2PC/3PC a majority of light curves have two peaks, being a minority those that possess more than three peaks. The percentage of detected light curves is a 60% of the total sample, giving an estimate of the pulsars that would not be detected in the gamma-ray regime simply due to geometrical reasons. At the same time, the distributions of flux ratios and widths of the peaks show the dominant presence of small values of these two features in the sample of synthetic light curves, peaking at small values and decreasing steeply for larger ones. On the other hand, the distributions of phase separations show a preference for large separations. Different pulsars show similar trends on these features when all the possible light curves are considered, pointing to the consistency of the spectro-geometrical model as well as to the likely similarity among their magnetospheres. This is impressive when considering that our sample contains very different pulsars, both in energetics and slow down rate, and include standard and millisecond systems.

The fact that considering different pulsars, i.e. to consider different timing and spectral parameters, has such a small impact in the skymaps, implies that the geometry widely dominates over the spectra in shaping the light curves. Therefore, considering a sample of light curves generated for the same pulsar, but for different geometries and observers, is substantially equivalent to exploring the population of all observational light curves, since

each pulsar has its own (unknown) geometry.

Another interesting outcome is that a direct comparison of our synthetic sample with the sample of observational gamma-ray light curves could constraint the geometry. The trends seen on the percentage of the number of peaks of the light curves as a function of the inclination angle, together with the overall agreement between the synthetic light curves sample for particular pulsars and the global features observed from the pulsar population as a whole, opens the door to the possibility of inferring the global population distribution of the inclination angle of high-energy pulsars in our Galaxy. We have also observed the drastic increase in the percentage of detected light curves as the inclination angle increases, going from less than 20% in an almost aligned rotator to more than 90% in an orthogonal rotator. This uncovers a bias bound to be important for population synthesis studies.

In addition, we have shown that different observers see different γ-ray spectra due to the non-trivial shape of the emission region. This allows us to distinguish observers by the resemblance with observational data of the spectra they see, and at the same time opens the door to the possibility of giving possible value(s) of the viewing angle of the pulsar being studied. The observed difference in spectra are enlarged when the full spectra is considered. In particular, if the non-thermal X-ray emission is considered together with the γ-ray radiation, as was done in previous spectral-only studies by the group (Torres, 2018; Torres et al., 2019; Íñiguez-Pascual et al., 2022).

5

Concurrent fitting of spectra and light curves

The models presented in this thesis, the radiative of Chapter 3 and the spectro-geometrical of Chapter 4, aim at generating observables of high-energy pulsars, spectra and light curves, respectively. In this chapter we present the comparison of these theoretical spectra and light curves with observational ones of the whole population of high-energy pulsars. This chapter is largely based on the published work Íñiguez-Pascual et al. (2025a). In these systematic fittings, we allow to vary the free parameters of each model – $E_{||}$, x_0/R_{LC} and b for the radiative and Ψ_Ω and θ_{obs} for the spectro-geometrical – and find their best-fitting values, i.e. the values of these parameters for which the theoretical spectra and light curves better reproduce the observational spectra and light curves. First of all, we perform the spectral fitting, which will give us information about the physical process responsible for the high-energy emission. With the best-fitting values of the spectral parameters as inputs, we perform the light curve fitting, which in turn provides information about the geometry of the pulsar and the shape of its magnetosphere. Table 5.1 shows the most relevant parameters of the two models: those that are fixed and those that are let free. Recall that both models are intertwined, not only because the spectro-geometrical uses the results of the radiative as inputs, but because the dynamics and emission of the latter are also implemented in the former.

Table 5.1: Relevant parameters entering into our calculation, together with a brief description of their function in the model and the values used.

Parameter	Function	Value/range selected
Pulsar		
P	Period	Depending on the pulsar
$\dot{P}$	Period derivative	Depending on the pulsar
$B_{\rm s}$	Magnetic field at the surface of the star	From the timing properties, assuming a dipolar field
$R_\star$	Radius of the neutron star	10 km
d	Distance of the pulsar from the Earth	Depending on the pulsar
Trajectories		
$E_{\|\|}$	Parallel electric field	Fitted
B	Local magnetic field strength	$B_{\rm s}(R_{\rm s}/\lambda)^b$
b	Magnetic gradient	Fitted
$r_{\rm max}$	Distance travelled by the emitting particles	$1.0R_{LC}$
$\alpha_{\rm in}$	Initial value of the pitch angle α	45°
$\Gamma_{\rm in}$	Initial value of the Lorentz factor Γ	10^3
r_c	Local radius of curvature	$r_{\rm c} = R_{LC}(\lambda/R_{LC})^\eta$
η	Dependence of r_c on the position	0.5
τ	Torsion parameter	$1/r_c$
$N_{\rm inj}$	Number of injection points, r_{in}	11(radiative) / 21 (spectro-geometrical)
ΔR	Injection range along the lines (in R_{lc})	0.5
$r_{\rm in}^0$	First injection point, i.e. height at which the emission region begins	$1.0R_{LC}$
$r_{\rm in}^{N_{\rm inj}}$	Last injection point	$1.5R_{LC}$
Spectra		
x_0/R_{LC}	Lengthscale	Fitted
N_0	Normalization	Analytically computed by linear regression, Equation (5.2)
Map		
Ψ_Ω	Inclination angle	Fitted
$\Delta\Psi_\mu$	Meridional extent of the emission region	10°
$\Delta\xi_\mu$	Azimuthal extent of the emission region	360°
N_χ	Number of angles over which the cone of emission is divided	20

5.1 Spectral fitting

This section presents the procedure and results of the spectral fitting. The goal is to compare the high-energy band (γ-rays, and X-rays when available) of observational spectra with theoretical spectra produced with the radiative model of Chapter 3. For each pulsar we let our free spectral parameters to vary and search for the best set of parameters by minimizing the reduced χ^2, $\overline{\chi^2}$. This, thanks to the effective nature of the radiative model, will allow us to draw several conclusions about the high-energy emission of pulsars. For pulsars with available X-ray data the three parameters ($E_{||}$, x_0/R_{LC}, b) are let free, while for those pulsars having only γ-ray data, the magnetic gradient b is fixed to 2.5, since this parameter has a low impact in the γ-ray band and mainly affects the X-ray regime of the spectra, as we have seen in Chapter 3. The value is chosen based on average best-fit values obtained from previous studies (Torres, 2018; Íñiguez-Pascual et al., 2025a).

5.1.1 Minimization algorithm

To perform the spectral fitting, we use a classical minimization method, called Nelder-Mead method, or downhill simplex method (Nelder and Mead, 1965). We first introduced it in Íñiguez-Pascual et al. (2022), as an alternative to the fitting approach taken previously by the group, e.g. in Viganò et al. (2015d), in which a gridding over the free parameters was performed.

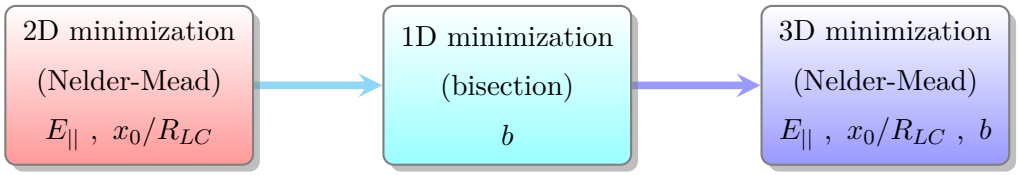
The Nelder-Mead method (Press et al., 1992) only involves the evaluation of the function, not its derivatives, and is based on the geometrical figure of a simplex. A simplex is the generalization to N dimensions of a triangle and thus has $N+1$ vertices, where N is the dimension of the problem. Each vertex is a point in an N-dimensional parameter space, with the coordinates being the parameters of the function to minimize. This function is evaluated at each vertex, promoting a motion of the simplex through the parameter space with the aim of minimizing the function's return values. See Appendix B for more details on the Nelder-Mead method. In our problem, the parameters are ($E_{||}$, x_0/R_{LC}, b), and the function to minimize is the reduced χ^2, $\overline{\chi^2}$, computed on the observed luminosity:

$$\overline{\chi^2} = \frac{1}{N_{\rm bin} - 3} \sum_{\rm bin} \frac{(L^{\rm bin}_{\rm obs} - L^{\rm bin}_{\rm theo})^2}{(\delta L^{\rm bin}_{\rm obs})^2} \tag{5.1}$$

where $N_{\rm bin}$ is the number of data points, $L^{\rm bin}_{\rm theo}$ is the theoretical luminosity produced by our model, $L^{\rm bin}_{\rm obs}$ is the observational luminosity and $\delta L^{\rm bin}_{\rm obs}$ is the experimental error of the data. The value of 3 stands for the number of free parameters.

The fastest way to a solution begins with implementing a two-dimensional (2D) Nelder-Mead minimization having $\log_{10}(E_{||})$ and $\log_{10}(x_0/R_{LC})$ as free parameters. Afterwards, we do a one-dimensional (1D) minimization with a bisection method, to search for b, having $E_{||}$ and x_0/R_{LC} fixed to the values found in the 2D minimization done before. In this way, we end up with an initial set of values of the three model parameters which is likely close to the solution, and with that we do a three-dimensional (3D) Nelder-Mead minimization with all free parameters at once to nail it down.

We have called this `2+1+3` procedure, standing for the number of parameters that are let free in each step, schematically summarized in the following diagram:



The reason why this approach is better than doing directly a 3D minimization from the start is that $E_{||}$ and x_0/R_{LC} drive the spectral shape in the γ-ray band, while b mainly affects the X-ray band. Thus, we can iteratively approach the whole solution, and only when sufficiently close to it, go into the more costly part of the minimization with all parameters included. In this way, also the risk of falling into local minima is minimized.

Recall that for pulsars with only γ-ray data available, the `2+1+3` procedure is not done completely, but only the first step, the 2D Nelder-Mead minimization.

Before the algorithm starts, an initial simplex has to be defined. All its vertices are built from an initial point $\vec{p_0}$, as follows: $\vec{p_i} = \vec{p_0} + \lambda \cdot \hat{e}_i$, where λ is the characteristic length of the problem (we choose it to be 0.1) and $\hat{e}_i$ are unit vectors with $i = 1, \ldots, n$. The closer the simplex is initialized with respect to the real minimum, the fewer steps will be needed for the algorithm to find the minimum, i.e. the smaller the computational time will be. Therefore, we have to find convenient coordinates for the initialization $\vec{p_0}$ (that is, values of $E_{||}$, x_0/R_{LC} and b). The existence of some hints about the model parameters could help in this task. For that we used the fact, as shown by Viganò et al. (2015d) with γ-ray data and by Torres (2018) with both X-rays and γ-day data, that $E_{||}$ is anti-correlated with x_0, with a best-fit given by $\log x_0 \sim -1.28 \log E_{||} + 16.9$ (with non-negligible dispersion). Similarly, a reasonable correlation exists between $E_{||}$ and the magnetic field strength at the light cylinder, defined as $B_{LC} = 5.9 \times 10^8 P^{-2.5} \dot{P}^{0.5}$. The best-fit relation was found to be $\log E_{||} \sim 0.78 \log_{10} B_{LC} + 4.95$. The initial value of the parameter b is fixed here to a fiducial value of 3, qualitatively expected for a dipolar magnetic field and close to the typical best-fit values found in previous studies.

Finally, the normalization N_0 allows one to scale the theoretical spectrum without affecting its shape in accordance with the observational one. Its best-fit value is analytically computed by linear regression during the fitting procedure, for any given set of the other free parameters:

$$N_0 = \frac{\sum_{\text{bin}} \frac{L^{\text{bin}}_{\text{obs}} \cdot L^{\text{bin}}_{\text{theo}}}{(\delta L^{\text{bin}}_{\text{obs}})^2}}{\sum_{\text{bin}} \frac{(L^{\text{bin}}_{\text{theo}})^2}{(\delta L^{\text{bin}}_{\text{obs}})^2}} \tag{5.2}$$

which secures minimizing $\overline{\chi^2}$ for that particular model incarnation.

The algorithm stops when the fractional distance in $\overline{\chi^2}$ between the vertices of the simplex with higher and lower function evaluations is smaller than 10^{-4}. This represents a proper balance between precision and computational time. The errors of the model parameters are estimated following the prescriptions of Avni (1976), which defines $\overline{\chi^2}_{\text{limit}}$, a 1 σ confidence interval for the corresponding degrees of freedom. This interval is computed from the non-reduced χ^2 as $\chi^2_{\text{limit}} = \chi^2_{\text{min}} + q$, where q is a factor that depends on the number of degrees

of freedom of the problem and the required confidence level and indicates the increment of χ^2. For a 1σ confidence interval and three (two) degrees of freedom $q = 3.5$ ($q = 2.3$), see Table 1 of Avni (1976) for more options.

With the new approach, the computational time required for the spectral fitting of a high-energy pulsar is, on average, less than half an hour. In addition, this approach brings a very good accuracy of the best-fit parameters, of at least 0.01. This means a significant reduction in computational cost with respect to previous fittings, in which the required time per pulsar was $\sim 5-10$ hours, and an improvement on the accuracy of the best-fitting values, which was at most 0.02. The systematic fitting of the whole population of high-energy pulsars required $\sim 3 \times 10^3$ CPU hours and was performed in the LADON High-Performance Computing Cluster at the Institute of Space Sciences, ICE-CSIC. The numerical codes used are written in Interactive Data Language (IDL).

5.1.2 Sample selection

Out of the 297 γ-ray pulsars presented in the 3PC, there is a fraction that is currently not eligible for fitting. This happens either because their spectra are described with too few data points, or because the pulsars lack a measured $\dot{P}$. With regards to the former, we only consider fitable pulsars those having five consecutive bins with a measured flux (not upper limits) in their spectra. In this way, the fitting sample consists of 129 pulsars, 39 of them having also detected X-ray pulsations, the same sample studied in Coti Zelati et al. (2020). We shall draw our conclusions based on the results found fitting this sample.

Even though spectra of many previously unknown γ-ray pulsars have been released in the 3PC, a dedicated spectral analysis of each pulsar in the catalogue has not been performed yet. The spectra given in the catalogue relate to those published in the Incremental Fermi-LAT Fourth Source Catalog (Abdollahi et al., 2022). For this reason, in some pulsars the spectral data in the 3PC may be less detailed than that publicly available before its release, coming either from the 2PC (Abdo et al., 2013), where a dedicated spectral analysis for each pulsar was done, or in dedicated studies of particular pulsars.

Therefore, we do not take the whole sample of spectra directly from the 3PC, but instead make a mix between those and the spectral data we used in Íñiguez-Pascual et al. (2022). Last column of Table D.1 explicitly states the origin of the data in a case-by-case basis. See Appendix C for a comparison of the data from 2022 and from the 3PC. For the new pulsars we obviously take the 3PC data. For those with already-available data, we decide between the spectra from the 3PC or the older ones (meaning 2PC or dedicated studies) based on their quality and following the criterion of having at least five consecutive bins with a measured flux (i.e. not upper limits). In pulsars for which it is not immediately obvious which set to pick, we choose the data providing the largest number of consecutive data points, always checking that the overall shape between the sets is similar and/or that their difference lies within the errors. For these pulsars we consider systematic errors on the best-fit parameters (being the difference between the best-fit parameters obtained with the 3PC observational spectra and the alternative spectra) in addition to the statistical ones. In a few cases, the spectra of the two sets of data differ widely. We do not consider these

pulsars in our systematic fitting, but show them in Appendix C, for completeness. They are interesting candidates for further study and the light curves are mostly unaffected (see below) by spectral changes.

5.1.3 Results

Figure 5.1 shows examples of our spectral fits for some pulsars. The model is able to reproduce the spectra of the whole population of γ-ray pulsars. Thanks to its flexibility, it can resemble the wide variety of γ-ray spectra, from those with very narrow peaks to those with broader peaks, looking almost flat at energies of ~ 1 GeV. Regarding pulsars with X-ray data, the γ-ray range is reproduced in all the cases, and the X-ray band is well matched in the majority of them. This means a successful match across eight orders of magnitude in energy. Young pulsars and MSPs are equally well fitted, i.e. the radiative model is able to fit spectra of a pulsar regardless of its timing properties. We show the whole set of fits in Appendix E. There we also show the fits performed on the pulsars which do not fulfil the restriction on the quality of their spectral data imposed in subsection 5.1.2, i.e. those with less than five consecutive spectral bins with measured flux. The fit of these is not as reliable as for those selected in the fitting sample, because fitting three or four points with two free parameters is rather straightforward, and is not very informative. We show them for completeness, but do not consider them to extract conclusions. This enlarged sample contains 253 pulsars.

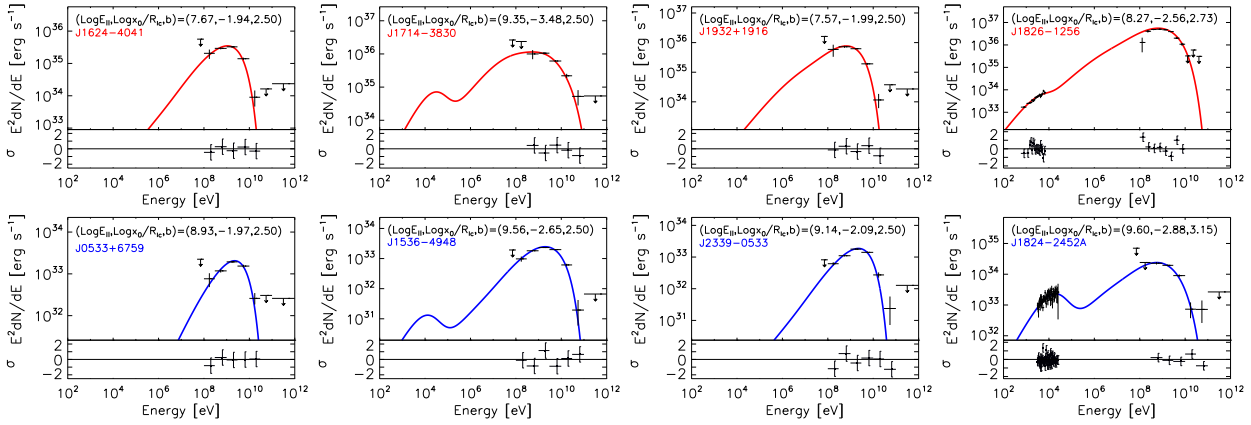


Figure 5.1: Examples of best-fitting spectra of some high-energy pulsars, with and without detected X-ray emission. Red (blue) lines are used for young (millisecond) pulsars.

The best-fitting values of the spectral parameters are shown in Table D.1. Best-fitting values of $E_{||}$ are always above $\sim 10^7$ V/m, which represents a potential drop in the emission region that agrees with typical values found in radiative models. We see a clear preference for small values of the lengthscale x_0/R_{LC} for all pulsars. This parameter regulates the non-uniformity of the effective particle distribution $dN/d\lambda$, which weights the contribution to the total spectrum of the different positions of the particles' trajectories. Small x_0/R_{LC} means that more importance is given to the radiation emitted in the initial parts of the trajectories. Recalling that we have seen that synchrotron radiation dominates close after particle injection, this result reinforces the idea that a relevant synchrotron contribution

is required to explain the zoo of observed γ-ray spectra. Best-fitting parameters of young pulsars and MSPs are rather similar except for a preference of the latter for larger values of the parallel electric field $E_{||}$ and lower values of the lengthscale x_0/R_{LC}. When b is let free, the values found are in the range $\sim 1-4$, clustering around 2.5. This indicates a wide diversity of magnetic field decay with distance across the high-energy pulsar population. However, in most of the cases we found a decay smoother than an ideal dipole, which is $\propto x^3$.

The results presented in this thesis are consistent with what has been found in the series of systematic fittings performed by the group in the last decade: Viganò et al. (2015d); Íñiguez-Pascual et al. (2022, 2025a). It is worth mentioning that the radiative model, which has been gradually improved in its physical description, has been able to properly resemble the population of high-energy pulsars as it has grown through the years, from the 81 sources fitted in Viganò et al. (2015d) (from the 117 sources of the 2PC), up to the 129 – enlargeable to 253 with those pulsars with few data – fitted here (from the 297 sources of the 3PC).

Fitting the spatial scale $\lambda_{\rm lp.in}$

Some pulsars of the subsample of objects with X-ray data available are not perfectly fitted by the radiative model. In order to try to achieve a good fit for those pulsars, we have done the test of letting free the parameter $\lambda_{\rm lp.in}/R_{lc}$, the (normalized) extent of the innermost region of the trajectory where particles are injected, i.e. having it as a fourth free parameter of the radiative model. In addition, this will serve to test the validity of the assumption of a fixed $\lambda_{\rm lp.in}/R_{lc}$ introduced in Chapter 3 Introducing another free parameter implies a higher computational cost per fit. In order to keep this cost affordable we have performed this test with a simplified incarnation of our model having a single injection point instead of eleven. The arguments given in Appendix A, where we show that minimal changes are introduced in the spectra when considering one or several injection points, assure us that the results obtained here can be extrapolated to the more realistic case of $N_{\rm inj} = 11$.

To perform this four-dimensional (4D) fitting, in addition to the minimization for the three parameters described in subsection 5.1.1, we implemented an overarching bisection method for $\lambda_{\rm lp.in}/R_{lc}$. That is, for each evaluation within the bisection, an $(\lambda_{\rm lp.in}/R_{lc})$-value is considered and we perform the `2+1+3` procedure explained in subsection 5.1.1, which in this case acts as the function to minimize. The searching range for $\lambda_{\rm lp.in}/R_{lc}$ was set at two orders of magnitude above and below Equation (3.19). We shall refer to the case when we choose to fix $\lambda_{\rm lp.in}/R_{lc}$ at the value given by Equation (3.19) as minimal model (i.e. three parameters with $\lambda_{\rm lp.in}/R_{lc}$ fixed as explained above), and use that as a reference for a comparison with results arising with a varying $\lambda_{\rm lp.in}/R_{lc}$ (i.e., having four parameters in total). In both the minimal model and the one in which $\lambda_{\rm lp.in}/R_{lc}$ is a free parameter, particles are injected at trajectory positions in a region close to $r_{\rm in}$ and travel in the same direction through the acceleration funnel.

For those pulsars in which the minimal model provides a good fit, considering $\lambda_{\rm lp.in}/R_{lc}$ as a free parameter would in general lead to recovering values close to the one assumed in the minimal scenario, confirming all such previous fits. We are thus particularly interested

in those cases where the fits with the minimal model were not particularly good, those with $\overline{\chi^2} > 2$. Table 5.2 shows the results of the model with $\lambda_{\rm lp.in}/R_{lc}$ free and compares them with those for the minimal case for the latter. The pulsars listed are those with $\overline{\chi^2} > 2$, and are divided between those with $2 < \overline{\chi^2} < 3$ and those with $\overline{\chi^2} > 3$.

Table 5.2 also shows the results of an F-test that compares the two models (the minimal model and the model with $\lambda_{\rm lp.in}/R_{lc}$ free) under the null hypothesis of no improvement when increasing the number of free parameters. The F-value is defined as

$$F = \frac{\dfrac{RSS_1 - RSS_2}{n_1 - n_2}}{\dfrac{RSS_2}{n_2}} \ , \tag{5.3}$$

where RSS is the residual sum of squares of the model and n is the number of degrees of freedom of each model, defined as $N_{bin} - p$, with p the number of free parameters. In our case, RSS is χ^2. The F-value is then compared to a critical value of the F-distribution, which depends on the numbers of degrees of freedom of the models that are being compared and a desired confidence interval. The critical value of an F-distribution is the value of the distribution for which, if the F-value of the comparison of models is larger than it, the null hypothesis is rejected (in our case: the model with free $\lambda_{\rm lp.in}/R_{lc}$ is preferred).

Figures 5.2 and 5.3 show the fit results for the cases in which the minimal model did not show a totally good fit. The current approach is nevertheless seen to be quite good in describing the spectra in all cases shown in Figure 5.2. Only for J2229+6114, the F-value is smaller than the critical one, meaning that in this case letting $\lambda_{\rm lp.in}/R_{lc}$ free does not provide a significantly better fit than fixing it (i.e. using the minimal model). This is reinforced by looking at the panel of Figure 5.2 corresponding to this pulsar, in which none of these spectra resembles the data points significantly better than the other. For the other pulsars, adding a fourth parameter provides a significantly better fit.

Despite obvious improvements in some cases, the observational spectra in Figure 5.3 are not satisfactorily reproduced by the theoretical best-fit spectra with a variable $\lambda_{\rm lp.in}/R_{lc}$. $\overline{\chi^2}$ values (shown in the lower section of Table 5.2) are relatively high and some systematic deviations are observed in the residual panels. While in several cases (e.g. J1709-4429, J1124-5916) the new fits are better than those obtained with the minimal model; in some others (e.g. J1057-5226, J1231-1411) both fits are similar.

We note that the values of $\lambda_{\rm lp.in}/R_{lc}$ chosen by the fitting for pulsars which were already well reproduced with three parameters are very similar to those given by Equation (3.19). We also note that by adding this fourth parameter, the number of pulsars with X-ray emission detected that are successfully modelled by the radiative model is enlarged.

Higher values of $\lambda_{\rm lp.in}/R_{lc}$, $\sim 10^{-3}$, are preferred in the few MSPs we studied in comparison with a more distributed set of values for normal pulsars, ranging from $\sim 10^{-3}$ to $\sim 10^{-7}$, weighted towards lower values. The minimum $\lambda_{\rm lp.in}$ is about 70 cm for Vela and J1838, and about 1 m for MSPs, being larger for the rest. Physically, such small spatial scales imply that there is a small region after a particle starts its acceleration where the large pitch angle particles dominate the average spectrum, being contributed significantly by more evolved particles beyond.

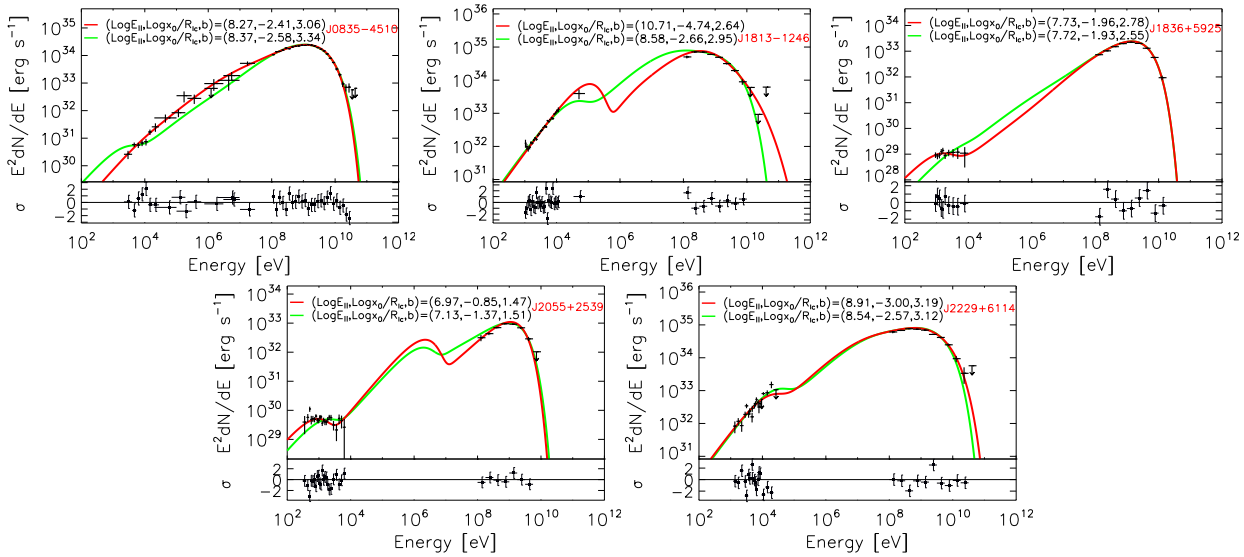


Figure 5.2: Comparison of the theoretical spectra produced with the minimal model (green lines) and with the model having $\lambda_{\rm lp.in}/R_{lc}$ as a free parameter (red lines). The residuals are those of the spectrum where $\lambda_{\rm lp.in}/R_{lc}$ is free. Pulsars shown here are those whose fit with the minimal model has $2 < \overline{\chi^2} < 3$.

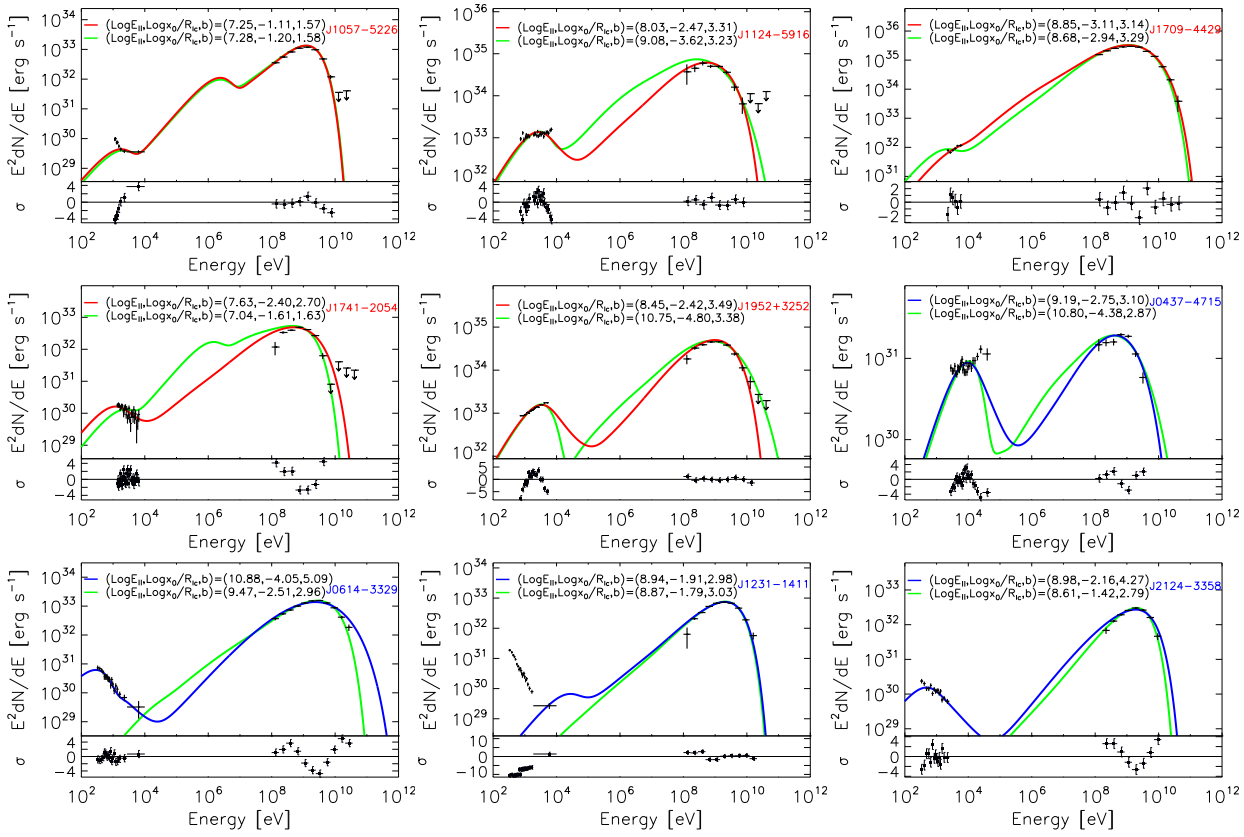


Figure 5.3: As in Figure 5.2 for pulsars for which the minimal model has $\overline{\chi^2} > 3$. Red lines for young pulsars PSRs and blue lines for millisecond pulsars MSPs.

Table 5.2: F-test for the pulsars whose fit by the minimal model gives $\overline{\chi^2} > 2$. This model (in which the value of $\lambda_{\rm lp.in}/R_{lc}$ is given by Equation (3.19)) is compared with the model with $\lambda_{\rm lp.in}/R_{lc}$ free. D.O.F is the number of degrees of freedom of the model, defined as the difference between N_{bin} and the number of model parameters. Critical values are defined by the pair of numbers of degrees of freedom of the two models that are compared. To define such values a 1 % confidence level is chosen. Pulsars on the upper section are those with $2 < \overline{\chi^2} < 3$ and shown on Figure 5.2, while those on the lower section are those with $\overline{\chi^2} > 3$ and shown on Figure 5.3.

Pulsar	Model	$\log E_{\parallel}$ [V/m]	$\log(x_0/R_{lc})$	b	$\log N_0$	$\log \lambda_{\rm lp.in}/R_{lc}$	$\overline{\chi^2}$	D.O.F.	F-value	Critical value
J0835−4510	Minimal	$8.37^{+0.01}_{-0.01}$	$-2.58^{+0.01}_{-0.01}$	$3.34^{+0.03}_{-0.02}$	33.73	-4.63	2.13	37	37.71	2.20
	$\lambda_{\rm lp.in}$ free	$8.27^{+0.01}_{-0.01}$	$-2.41^{+0.01}_{-0.01}$	$3.06^{+0.03}_{-0.03}$	31.65	$-6.78^{+0.97}_{-\ldots}$	1.07	36		
J1813−1246	Minimal	$8.58^{+0.01}_{-0.01}$	$-2.66^{+0.01}_{-0.01}$	$2.95^{+0.03}_{-0.03}$	34.00	-4.36	2.13	31	23.12	2.38
	$\lambda_{\rm lp.in}$ free	$10.71^{+0.02}_{-0.02}$	$-4.74^{+0.02}_{-0.02}$	$2.64^{+0.01}_{-0.01}$	31.74	$-6.02^{+0.06}_{-0.02}$	1.25	30		
J1836+5925	Minimal	$7.72^{+0.01}_{-0.01}$	$-1.93^{+0.01}_{-0.01}$	$2.55^{+0.04}_{-0.03}$	31.79	-4.92	2.47	16	26.44	3.49
	$\lambda_{\rm lp.in}$ free	$7.73^{+0.01}_{-0.01}$	$-1.96^{+0.01}_{-0.01}$	$2.78^{+0.02}_{-0.02}$	33.04	$-3.73^{+0.08}_{-0.11}$	0.95	15		
J2055+2539	Minimal	$7.13^{+0.03}_{-0.03}$	$-1.37^{+0.03}_{-0.02}$	$1.51^{+0.03}_{-0.03}$	31.03	-5.18	2.43	27	30.52	2.54
	$\lambda_{\rm lp.in}$ free	$6.97^{+0.04}_{-0.05}$	$-0.85^{+0.03}_{-0.04}$	$1.47^{+0.03}_{-0.02}$	31.69	$-4.12^{+0.08}_{-0.05}$	1.16	26		
J2229+6114	Minimal	$8.63^{+0.01}_{-0.01}$	$-2.50^{+0.01}_{-0.01}$	$2.65^{+0.03}_{-0.03}$	33.27	-4.39	2.28	25	1.06	2.64
	$\lambda_{\rm lp.in}$ free	$8.91^{+0.01}_{-0.01}$	$-3.00^{+0.01}_{-0.01}$	$3.19^{+0.02}_{-0.02}$	33.96	$-4.92^{+0.05}_{-0.06}$	2.27	24		
J0437−4715	Minimal	10.80	-4.39	2.87	31.50	-4.44	5.64	32	10.69	2.34
	$\lambda_{\rm lp.in}$ free	$9.19^{+0.01}_{-0.01}$	$-2.75^{+0.01}_{-0.01}$	$3.10^{+0.02}_{-0.02}$	32.92	$-2.49^{+0.02}_{-0.02}$	4.33	31		
J0614−3329	Minimal	9.47	-2.50	2.95	30.01	-5.18	15.27	28	145.15	2.49
	$\lambda_{\rm lp.in}$ free	$10.88^{+0.01}_{-0.01}$	$-4.05^{+0.01}_{-0.01}$	$5.09^{+0.02}_{-0.02}$	35.34	$-3.34^{+0.01}_{-0.01}$	4.43	27		
J1057−5226	Minimal	7.28	-1.21	1.58	30.86	-4.97	7.23	13	1.77	4.10
	$\lambda_{\rm lp.in}$ free	$7.25^{+0.02}_{-0.02}$	$-1.11^{+0.03}_{-0.03}$	$1.57^{+0.02}_{-0.02}$	31.01	$-4.76^{+0.08}_{-0.05}$	6.83	12		
J1124−5916	Minimal	9.08	-3.62	3.23	35.43	-4.81	3.89	30	11.36	2.41
	$\lambda_{\rm lp.in}$ free	$8.03^{+0.01}_{-0.02}$	$-2.47^{+0.01}_{-0.01}$	$3.31^{+0.01}_{-0.01}$	36.40	$-2.90^{+0.04}_{-0.04}$	2.89	29		
J1231−1411	Minimal	8.87	-1.79	3.03	29.13	-5.24	53.40	28	0.81	2.49
	$\lambda_{\rm lp.in}$ free	$8.94^{+0.02}_{-0.02}$	$-1.91^{+0.03}_{-0.02}$	$2.98^{+0.19}_{-0.15}$	31.04	$-3.26^{+0.22}_{-0.10}$	53.77	27		
J1709−4429	Minimal	8.68	-2.94	3.30	35.18	-4.69	4.27	14	28.34	3.86
	$\lambda_{\rm lp.in}$ free	$8.85^{+0.01}_{-0.01}$	$-3.11^{+0.01}_{-0.01}$	$3.14^{+0.02}_{-0.02}$	34.14	$-5.81^{+0.09}_{-0.11}$	1.45	13		
J1741−2054	Minimal	7.04	-1.61	1.63	31.14	-5.30	6.24	38	46.74	2.17
	$\lambda_{\rm lp.in}$ free	$7.63^{+0.01}_{-0.01}$	$-2.40^{+0.01}_{-0.01}$	$2.70^{+0.01}_{-0.01}$	34.25	$-3.32^{+0.04}_{-0.04}$	2.83	37		
J1952+3252	Minimal	10.75	-4.80	3.39	34.16	-5.28	10.09	25	8.95	2.64
	$\lambda_{\rm lp.in}$ free	$8.45^{+0.01}_{-0.01}$	$-2.42^{+0.01}_{-0.01}$	$3.49^{+0.01}_{-0.01}$	36.35	$-2.36^{+0.02}_{-0.02}$	7.66	24		
J2124−3358	Minimal	8.61	-1.42	2.79	29.16	-4.37	34.23	20	194.80	3.00
	$\lambda_{\rm lp.in}$ free	$8.98^{+0.02}_{-0.02}$	$-2.16^{+0.01}_{-0.01}$	$4.27^{+0.02}_{-0.02}$	35.52	$-1.40^{+0.01}_{-0.01}$	3.20	19		

5.2 Light curves fitting

In this section we show the procedure and results of the light curve fitting. The idea is to compare the synthetic light curves generated with the spectro-geometrical model of Chapter 4 with observational γ-ray light curves from the *Fermi*-LAT collaboration, in particular those published in the 3PC. In order to generate the emission maps of a particular pulsar from which to get the light curves, we need as inputs the spectral parameters ($E_{\|}$, x_0/R_{LC}, b). We take the best-fitting values of each pulsar, obtained in the previous spectral fitting. The light curve fitting will provide us best-fitting values of the geometrical parameters, Ψ_Ω and θ_{obs}, with which we aim at extracting information about the geometry of high-energy pulsars.

5.2.1 Important considerations prior to fitting

Fitting synthetic light curves to observational ones is not a straightforward task and several considerations have to be taken into account before addressing it.

Fermi γ-ray light curves in the 3PC differ in the number of phase bins with which they are described. For each particular pulsar we then adapt the construction of the theoretical emission maps depending on its number of phase bins. For pulsars with 25, 50 or 100 observational phase bins, we fix the number of synthetic azimuthal bins to 25, 50 or 100, respectively. For pulsars with 200, 400 or 800 observational bins, we set the number of synthetic bins to 100, in order to keep the computational time affordable, since having more bins in the map requires adding more trajectories to the simulation to have an acceptable map resolution. We thus rebin the observational light curves with 200, 400 and 800 bins to have 100 bins in total. Notice that by doing this we are losing some information, but what we lose are small-scale features of the observational light curve that our model at its current stage is still not able to reproduce.

In addition, observational light curves have a certain level of background resulting from detected photons that do not come from the pulsar itself. In the 3PC, a background level is estimated for each pulsar, being computed from the photon weights and indicated in the pulse profile plots by a black dashed line. Our synthetic light curves do not have such background, because the theoretical emission maps represent all the emission coming from the pulsar, and only from the pulsar. Therefore we subtract from each observational light curve its corresponding background level obtained from the 3PC before comparing with synthetic predictions.

We shall impose a data quality criterion before fitting light curves, and do not consider light curves with only 25 observational bins. These have very large errors and their shape is generally not well defined yet. We also require that a spectral fit can be performed for the pulsars for which we fit the light curves, but here without imposing any restriction on the quality of their spectral data, since in Chapter 4 we have seen the small impact of the spectral parameters on the shape of the light curves. The population available for our fitting contains 226 γ-ray light curves after these quality cuts.

For each one of these 226 pulsars (with particular values of P, $\dot{P}$ and spectral parameters) we generate 30 emission maps, evenly sampling Ψ_Ω values from 3° to 90° (we avoid the case

of an aligned rotator, $\Psi_\Omega = 0°$, because no pulsed emission would be seen), and consider 51 observers, θ_{obs}, evenly distributed between $-90°$ and $90°$. We fix $\Delta\Psi_\mu = 10°$, because it represents a meridional extent of the emission region comparable to the one found in FFE and PIC simulations, and $\Delta R = 0.5 R_{LC}$, in order to consider the same injection range as in the radiative model.

5.2.2 Fitting procedures

We compare the whole synthetic sample of light curves we have generated for each particular pulsar with the corresponding observational light curve from the 3PC. For such a comparison, we have decided to use different metrics, which we present, discuss and compare below.

Fitting procedure in the time domain

The reduced χ^2 method can be used similarly to what is done in the spectral fitting, here to assess the goodness of the fit of $I_{\rm i}^{\rm obs}$ by $I_{\rm i}^{\rm syn}$, i.e. the intensities (in weighted counts/bin units) of the observational and synthetic light curves, respectively. In our synthetic light curves, phase $\phi_\Omega = 0$ corresponds to the plane containing the rotational and magnetic axes, but this is arbitrary. For this reason, synthetic and observational light curves are not necessarily aligned. In order to find the best alignment, we rotate each synthetic light curve and compute the $\overline{\chi^2}$ value for all rotations (as many as the number of observational bins), keeping the smallest one as the $\overline{\chi^2}$ of that synthetic light curves set. We reverse each synthetic light curve to obtain an additional one available for fitting. Two pulsars with the same geometrical parameters but spinning in opposite directions would a priori create different light curves. However, since an inversion in the direction of rotation of the star is equivalent to a pulsar turned upside down and our region possesses an equatorial symmetry, in our model one light curve would be the reversed version of the other. In addition, we normalize the synthetic light curves to the observational ones by using the standard, analytical linear regression formula: a normalization factor N_{LC} is found by solving $\partial\chi^2/\partial N_{LC} = 0$, similarly to the spectra normalization, Equation (5.2), and multiplied to our synthetic light curves.

However, fitting light curves with $\overline{\chi^2}$ has some intrinsic caveats (see García and Torres (2025) for a deeper discussion). For example, a small phase variation of one peak in multi-peaked light curves results in a large $\overline{\chi^2}$ value, even though the two light curves compared are visually very similar. Figure 5.4 shows two examples of cases in which $\overline{\chi^2}$ selects a best fit for which the peak structure is not well reproduced, and therefore it is not convincing from a human eye's perspective.

In addition, in light curves with narrow peaks, $\overline{\chi^2}$ can be biased towards synthetic light curves reproducing the observational bins with emission close to the background but failing to reproduce the peaks: since all bins contribute with equal weights to $\overline{\chi^2}$, a good adjust to many low-flux bins could give an overall small value for $\overline{\chi^2}$ even when the peaks are not matched at all. In order to reduce this effect, an approach similar to the one proposed in Churazov et al. (1996) can be taken, and consider a weighted reduced $\overline{\chi^2}$ (we shall keep calling it $\overline{\chi^2}$ for simplicity), in which each bin's squared difference is weighted by the normalized flux of the observational light curve at that bin, $\bar{I}_{\rm i}^{\rm obs}$, in order to give more weight to the

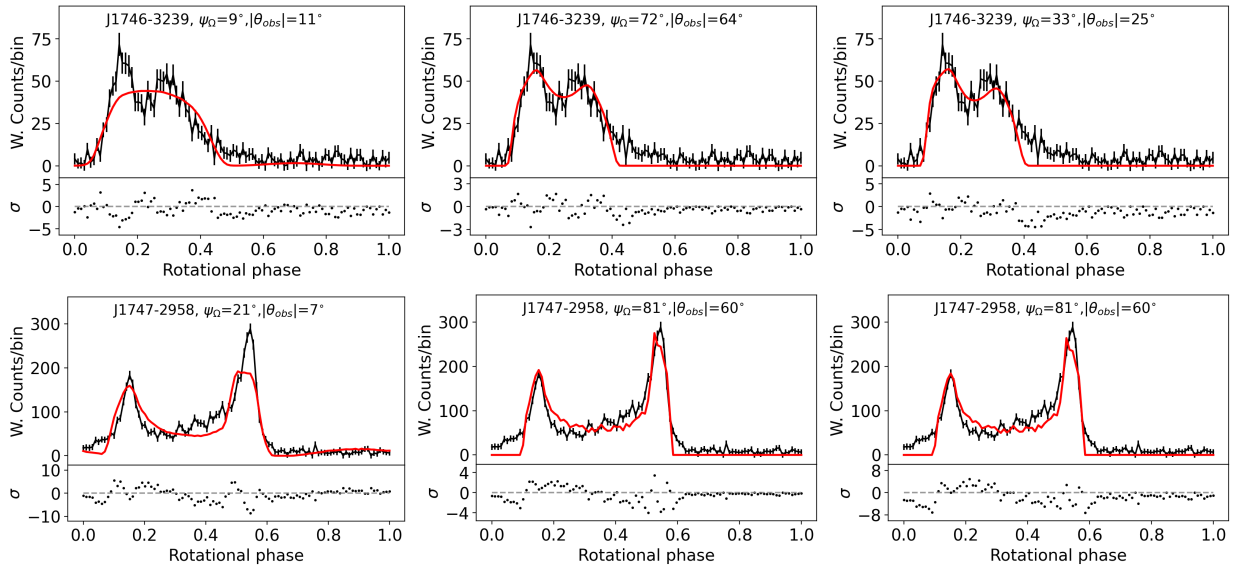


Figure 5.4: Examples of the caveats intrinsically associated with a fitting with $\overline{\chi^2}$ and possible solutions, for the pulsars J1746 (top row) and J1747-2958 (bottom row). From left to right: best-fitting light curve with a regular $\overline{\chi^2}$, best-fitting light curve with a weighted $\overline{\chi^2}$ and best-fitting light curve recovered with the inverse transform from fitting in the frequency domain.

bins with higher flux, as

$$\overline{\chi^2_{\rm w}} = \frac{1}{n-2}\sum_{\rm i}\frac{(I_{\rm i}^{\rm obs}-I_{\rm i}^{\rm syn})^2\bar{I}_{\rm i}^{\rm obs}}{(\delta I_{\rm i}^{\rm obs})^2} \quad , \tag{5.4}$$

where n is the number of bins of a light curve in time domain, the 2 value represents the number of free parameters in the fitting, $I_{\rm i}^{\rm obs}$ and $I_{\rm i}^{\rm syn}$ are the intensities of the observational and synthetic light curves, respectively, and $\delta I_{\rm i}^{\rm obs}$ is the observational error. In this way, more weight is given to the peaks, and we are promoting the proper reproduction of the peaks rather than the low-flux level parts of the light curves. Middle panels of Figure 5.4 present the best-fitting light curves found with the weighted $\overline{\chi^2}$, showing that the caveats associated with the regular $\overline{\chi^2}$ no longer appear. Notice that the weighted $\overline{\chi^2}$ is also not a perfect metric: the peak tails of the chosen best-fit synthetic light curves deviate more from the observational ones than in the regular $\overline{\chi^2}$ case. Hereafter, we will use Equation (5.4) for the light curve fitting, keeping in mind in any case the unavoidable freedom in choosing a given metric for the comparison, and how the choice is driven by the above mentioned visual, subjective considerations about when a fit is satisfactory or not.

Fitting procedure in the frequency domain

In parallel, we apply a Fast Fourier Transform (FFT) to all light curves existing in time domain to bring them into frequency domain, $\hat{I}_{\rm k}^{\rm obs}$ and $\hat{I}_{\rm k}^{\rm syn}$, whose amplitude is

$$||\hat{I}_{\rm k}|| = K\left|\left|\sum_{j=0}^{n-1} I_{\rm i} e^{-i2\pi\, k\, j/n}\right|\right| \quad , \tag{5.5}$$

where K is a normalization factor. We normalize the amplitude of the observational Fourier transform to its maximum. Each synthetic transform is normalized to match the peak value

of the observational one, which is usually at k = 1 or 2, with few cases being at 3 or 4. k is the harmonic, which goes from 1 to $n/2$ (we neglect $k = 0$, the average flux of the light curve). Harmonics are the sub-signals forming the complete light curve in time domain, having $k + 1$ nodes. The amplitude of the Fourier transform of a light curve with a single peak roughly symmetric in the rise and decay, will be dominated by odd harmonics, while that of a light curve with a double (roughly symmetric in rise and decay) peak, with a 0.5 phase separation, will be dominated by even harmonics. Different phase separations, the presence of sub-structures and asymmetries in the rise and decay features can redistribute the amplitude to the harmonics with the opposite parity. The width of the peak(s), and the relative peak flux between two peaks, will also determine how the amplitude is distributed over the harmonics. In order to assess the impact of the higher harmonics in the fit, we have tried to filter out the Fourier transforms by only considering the harmonics lower than a given maximum harmonic $k_{\rm max} = 5, 10$ or 15. Even with the extreme case of $k_{\rm max} = 5$, in several cases the shape of the best-fitting light curve barely differs from the complete best-fitting transform. Larger values of $k_{\rm max}$ leave untouched a growing number of best-fit solutions, and for $k_{\rm max}$ the differences are negligible. Figure 5.5 shows a couple of examples. This points out the negligible effect of the higher harmonics in the FFT fitting, which is mostly defined by the lowest harmonics. For completeness, we keep all the harmonics in the FFT fitting.

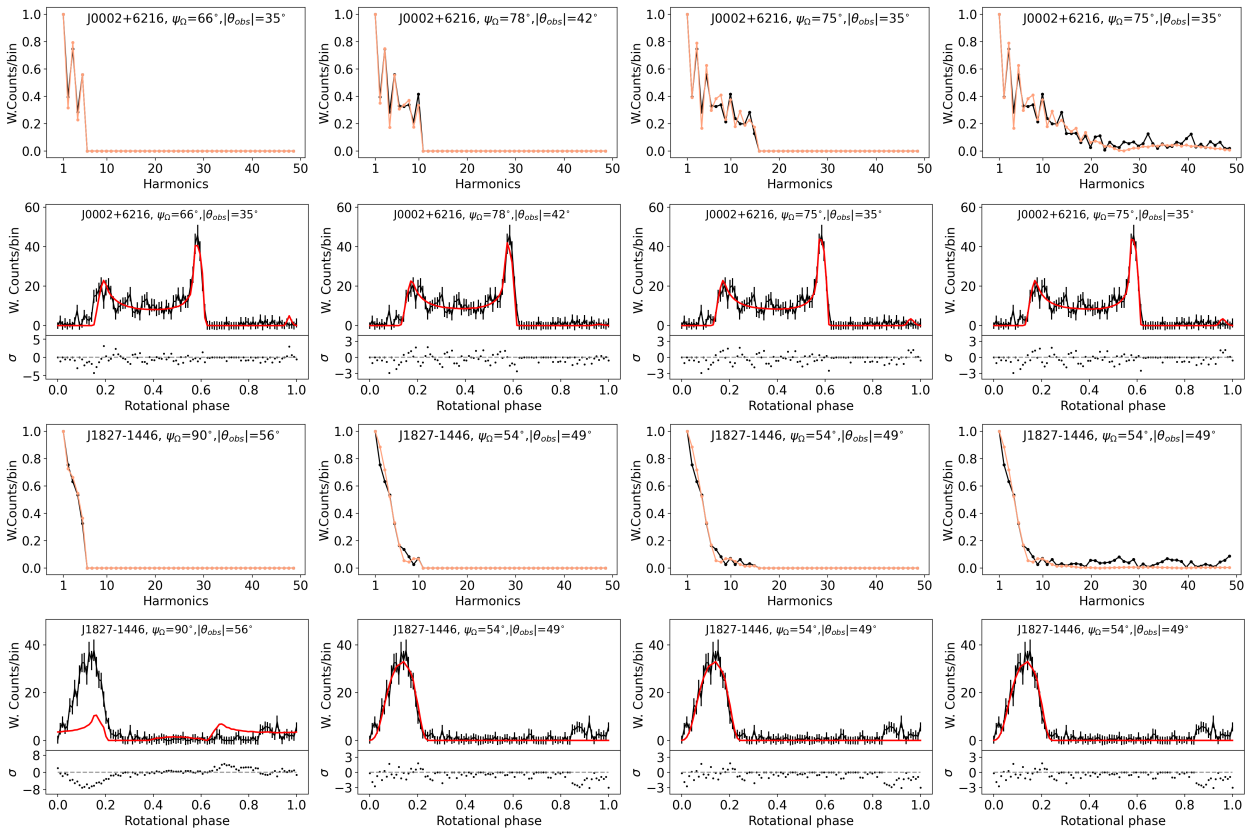


Figure 5.5: Examples of best-fitting light curves in frequency domain for different values of $k_{\rm max}$ for two pulsars, J0002 +6216 on first (Fourier transforms) and second (recovered light curve in time domain) rows and J1827-1446 on third (Fourier transforms) and fourth (recovered light curve in time domain) rows. In all rows, from left to right: $k_{\rm max} = 5$, $k_{\rm max} = 10$, $k_{\rm max} = 15$ and case without filtering.

We compare the amplitudes[1] of the observational and synthetic Fourier transforms, $||\hat{I}_{\rm k}^{\rm obs}||$ and $||\hat{I}_{\rm k}^{\rm syn}||$, respectively, with a simple euclidean distance (ED) as comparative metric,

$$ED = \sqrt{\sum_{\rm k} \left(||\hat{I}_{\rm k}^{\rm obs}|| - ||\hat{I}_{\rm k}^{\rm syn}|| \right)^2} \quad . \tag{5.6}$$

Comparing light curves in frequency domain focuses more on the symmetries and overall structures of the light curves. Moreover, it has computational benefits, since it is phase invariant. The cost of the Fourier transform is less than the cost of ranging all the possible phase alignments and inversions of the curve in the time domain, which implies a smaller computational cost of the frequency domain fitting. See subsection 5.2.2 for further computational costs considerations.

Fitting using dynamic time warping

García and Torres (2025) have recently introduced the Dynamic Time Warping (DTW) as a method to assess the similarity between light curves, which we could in principle use for our light curve fitting. DTW compares the sequence of data points between two time series without requiring alignment in phase (Berndt and Clifford, 1994). As a result, it is flexible to local stretching or compression in time, allowing it to recognize structural resemblance between light curves regardless of the values of the phases associated with each point. Therefore, a good fit can be assigned to e.g. light curves having similar overall structures of peaks and sub-peaks, but very different peak widths, or phase separations between peaks. Furthermore, its computational requirements, lasting five orders of magnitude more of time than the fitting in frequency domain and three times more than the fitting in time domain (see subsection 5.2.2), make its usage for light curve fitting still not agile enough. Therefore, DTW application for light curve fitting, although promising, with the current implementation is not practically feasible.

Computational cost of the light curve fitting procedures

The three light curve fitting techniques we have introduced in this Chapter differ substantially in their computational requirements. For the three of them we use the same machine, the LADON High-Performance Computing Cluster at the Institute of Space Sciences, ICE-CSIC. The fastest method is the euclidean distance in frequency domain, requiring ~ 0.37 minutes to fit the whole population of 226 pulsars. The weighted reduced χ^2 needs around two orders of magnitude more of time to complete the fitting, with ~ 25.42 minutes of computational time. Finally, DTW application to all pulsars (see its caveats as a fitting technique in the main text) would last $\sim 1.17 \times 10^4$ minutes, almost three orders of magnitude more than χ^2 in time domain and five more than ED in frequency domain. This huge computational requirement, amounting more than eight days, even though is affordable, limits a lot the feasibility to carry on different tests, as we have done in this work.

[1] Considering the amplitude instead of the power (which is equal to the squared amplitude) is arbitrary. We have performed tests using the power of the Fourier transforms in the fitting and very similar results are obtained.

5.2.3 Results

Figure 5.7 shows examples of best-fitting light curves resulting from both temporal and frequency techniques, for some selected pulsars, together with the contour plots of the statistics used in the fits, $\overline{\chi^2}$ and euclidean distance, respectively. All fits for those pulsars with at least 50 observational phase bins in their light curves are shown in Appendix F. Table D.1 shows the best-fit values of the geometrical parameters for all the pulsars fitted, and Figure 5.6 compares the values obtained with the two methods. In general, we note that results of the fits obtained with $\overline{\chi^2}$ in time domain and with ED in frequency domain are qualitatively similar.

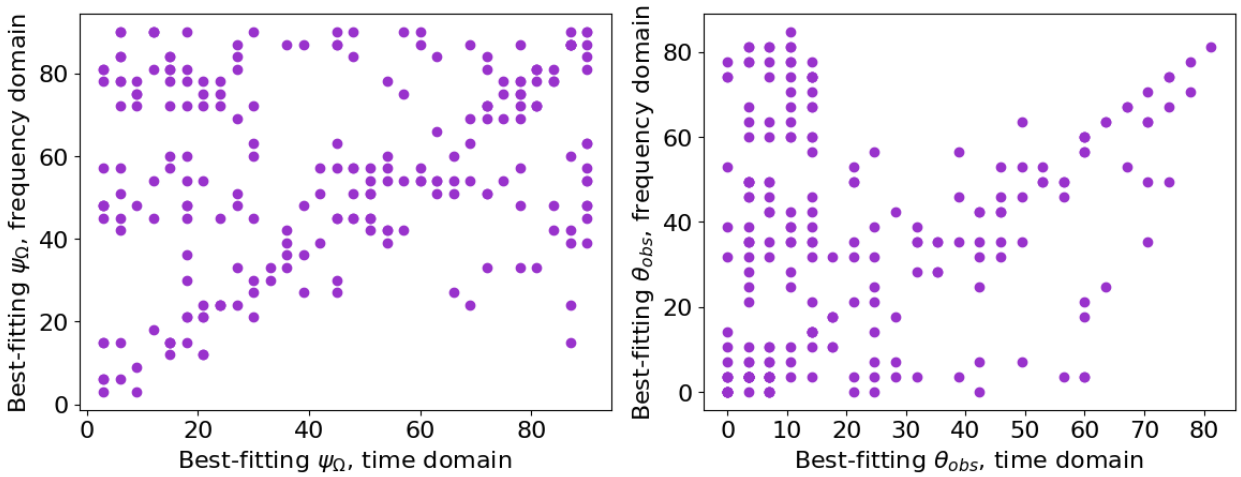


Figure 5.6: Comparison of the best-fitting values of Ψ_Ω (left) and θ_{obs} (right) obtained in the fitting in time vs frequency domains.

In many cases the best-fitting synthetic light curves visually resemble well the observational ones, with some remarkable fits, such as those of J1044-5737, J1112-6103, J1600-3053, J1641-5317, J1811-2405, J1906+0722, J1907+0602 or J2111+4606. Note the diversity of light curve shapes that we can reproduce, for both young and millisecond pulsars. In most of the cases we are able to capture the overall structure of the observational light curves, reproducing the number of peaks and their widths, the separation of peaks, and even the peak flux ratio in some cases. In several cases we also reproduce the so-called bridge emission, which, in our model, comes from the outermost parts of the trajectories, which are more curled.

However, our model is not able to capture the small scale features of the light curves of some pulsars, such as J0002+6216 or J1713+0747. Another aspect that the model struggles to reproduce is the presence of very asymmetric peaks, as in J0218+4232. In other cases, like J1124-5916 and others with high-quality data (i.e. small errors), we are not able to reproduce specific flux ratios and/or cusped peaks. With only two free geometrical parameters at play, our emission region does not have the complexity that the real magnetosphere surely possesses, meaning that we cannot generate light curves as complex as those observed for some pulsars. In a few cases, such as J1536-4948 or J1630+3734, the model is not providing a good fit.

Looking at the performance of both fitting techniques, we note that both of them find

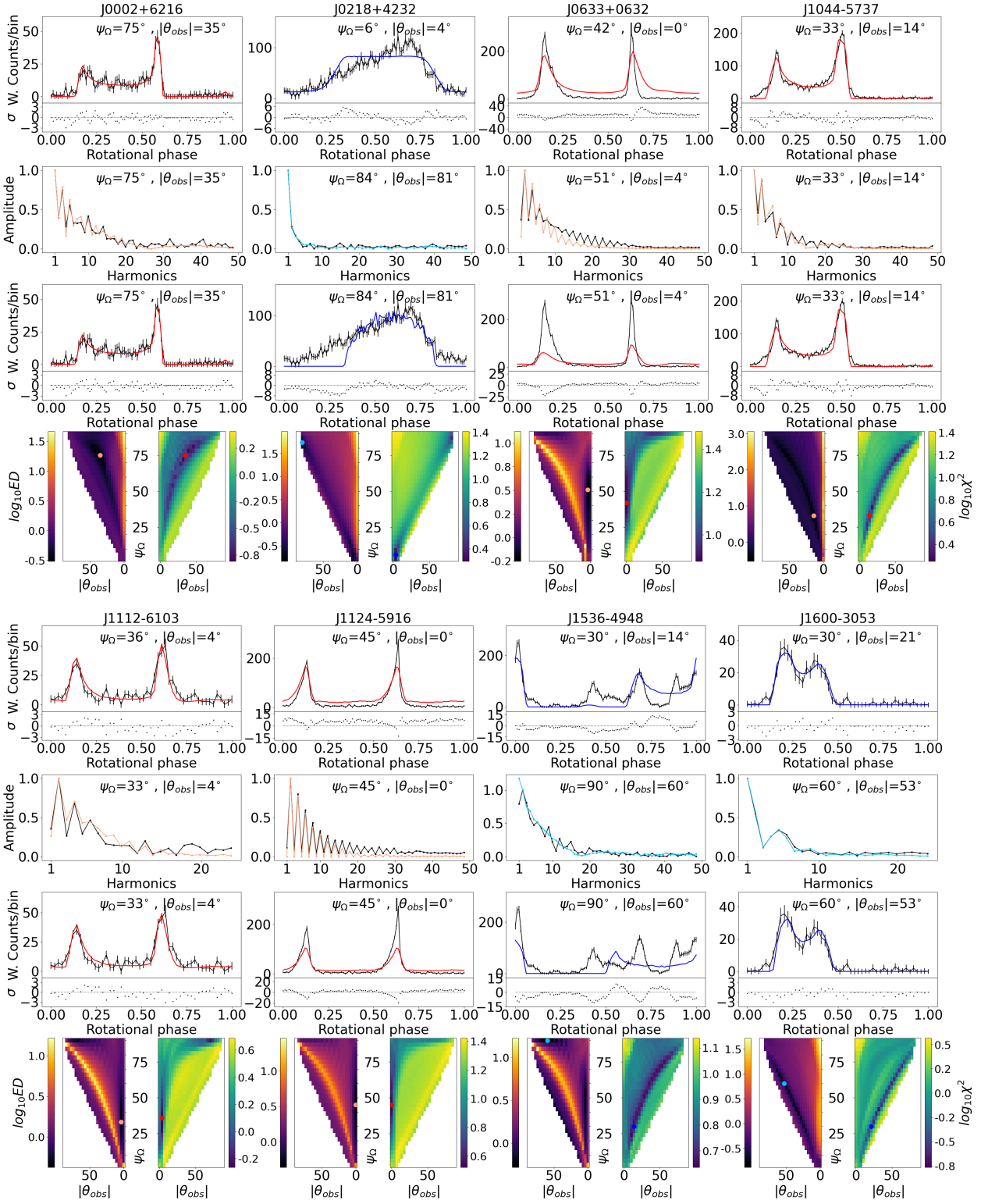


Figure 5.7: Best-fit light curves obtained in time and frequency domain for two sets (four rows each) of four pulsars (one per column). The first and fifth rows correspond to fits in the time domain. Second and sixth rows show the best-fit Fourier transform in the frequency domain fits, and third and seventh the light curve recovered with the inverse transform (with the best alignment in phase and spin direction (see Section 5.2.2). The fourth and eighth rows show the contour plots of both $\overline{\chi^2}$ in time domain and ED in frequency domain. Dots correspond to best-fit geometries from the fitting in time domain (dark colours) and from the fitting in frequency domain (light colours). Red (blue) lines correspond to synthetic light curves of young (millisecond) pulsars, and black lines to observational light curves.

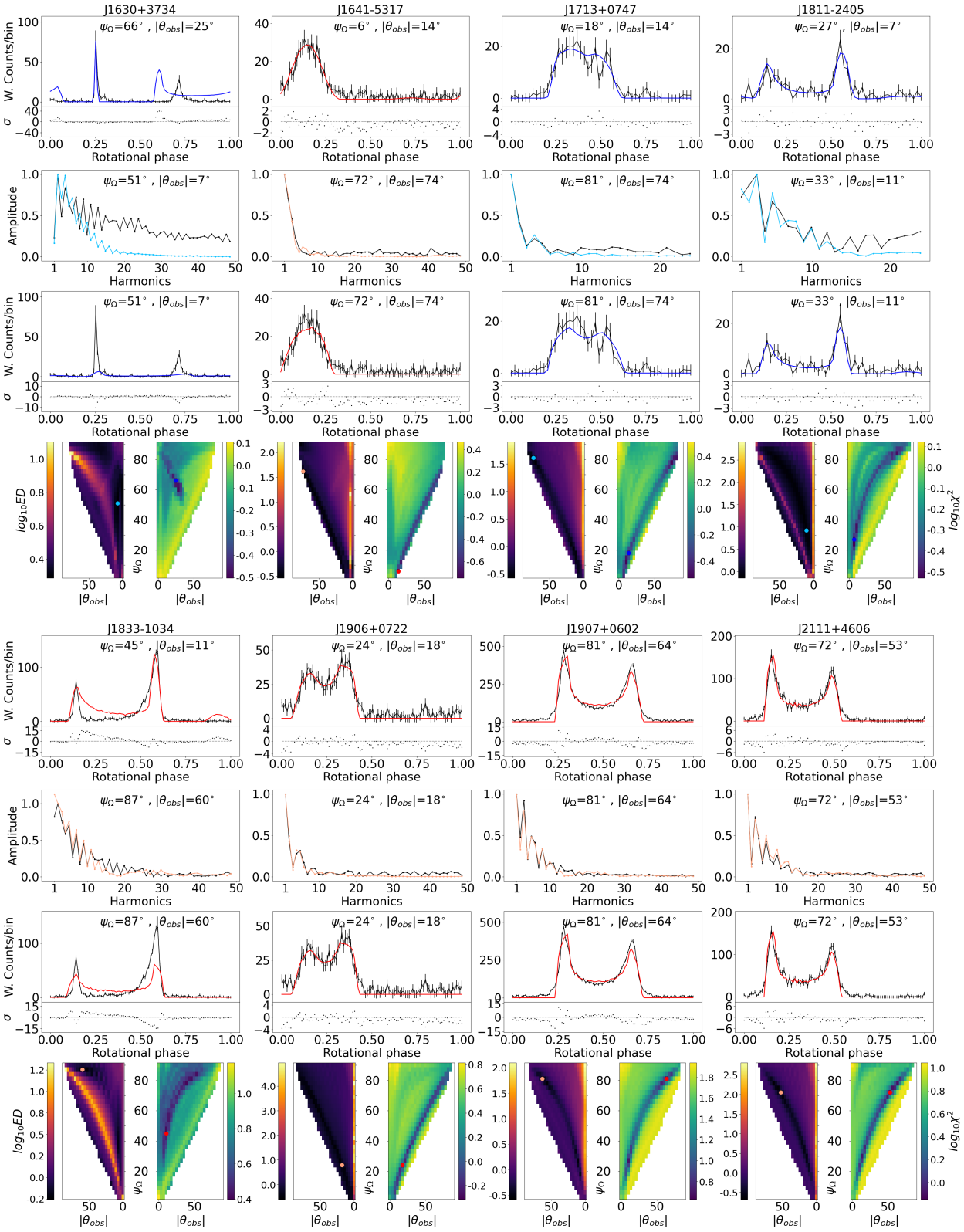


Figure 5.7: - *continued*

good fits in a number of cases and fail in others. In about a fifth of the sample, both methods give compatible best-fit parameters (within one step in the sweeping grid of values of each parameter), while in the rest of the sample these values noticeably differ. This difference highlights that the degeneracy in the parameters is large, for both methods. In other words, when one compares the general shape of the contour plots, they are generally similar, but each metric can find a specific value for the best-fit within the best-fitting 'valleys' in the parameter space (fourth and eighth rows of Figure 5.7). Therefore, the individual best-fit values should not be taken as relevant constraints.

Figure 5.7 also presents the contour plots of $\overline{\chi^2}$ and ED for each pulsar, showing the values of these statistics in the space of parameters θ_{obs}–Ψ_Ω. Due to the equatorial symmetry in the skymaps, we only show θ_{obs} from 0° to 90°. In many pulsars, the contours from both techniques are not identical but show different regions of low $\overline{\chi^2}$ and ED. This underscores the distinct performance and intrinsic focus of both methods. The most relevant features of these plots are in fact the valleys present in many cases, both in the $\overline{\chi^2}$ and the ED ones, pointing out a degeneracy in the geometrical parameters. Along the valley of parameter degeneracy, good fitting geometrical values can be found in almost the whole range of θ_{obs} or Ψ_Ω, as can be seen in the $\overline{\chi^2}$ contour plot of J1747-2958 in Figure 5.8. In this figure we also show some other light curves whose set of parameters lies in the valley, apart from the best-fitting one under the $\overline{\chi^2}$ methodology. We see that the shapes of the not-best-fitting light curves (fuchsia and green dots) are rather similar, even though their geometrical parameters are very different. For this reason, the uncertainty around the best-fitting values is large, and the latter should not be regarded as strong constraints. Models with more asymmetry in the shape of the emitting region would likely break this degeneracy.

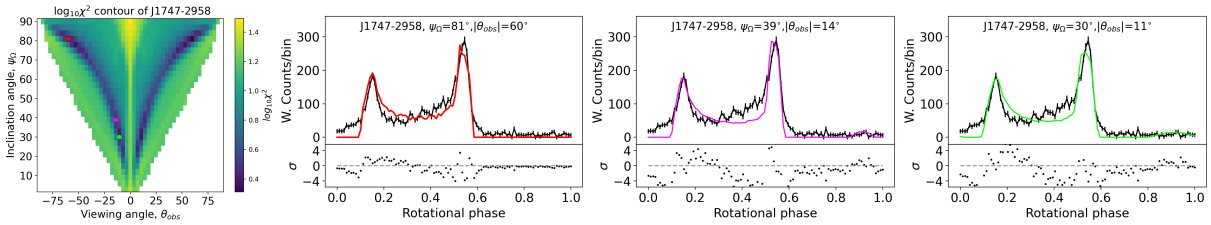


Figure 5.8: Examples of the degeneracy in the contour plots. Left panel shows the $\overline{\chi^2}$ contour plot of J1747-2958 with dots corresponding to the light curves depicted on the other three panels. From left to right: $\overline{\chi^2}$ best-fitting light curve in red, and other light curves with geometries on the $\overline{\chi^2}$ valley, in fuchsia and green.

We have investigated how the results we found are affected by the grid resolution of the geometrical parameters by performing fits of several pulsars with a thinner grid, considering 90 values of Ψ_Ω and 151 values of θ_{obs}, i.e. increasing the resolution a factor 3. The results were not significantly changed. The best fit light curves chosen were the same or with best-fit parameters close to those of the best-fit light curves with the default resolution, and the contour plots were basically the same. In particular, neither new substructures appeared in the contour, nor did it help to break the degeneracy.

Fitting all light curves with a single set of maps

In Chapter 4 we stated the idea that, in our model, the spectral and timing properties barely affect the set of light curves, which are controlled basically by the two geometrical parameters. In other words, the emission map (and the set of associated light curves) are insensitive to the spectrum that fits a specific pulsar. This implies that a set of synthetic light curves produced for a fixed set of best-fit spectral parameters but varying the geometry (inclination, observer line of sight) is also representative of the global set of all observed pulsars, for which the values of such angles are also randomly distributed. We can explore this further asking whether it is possible to fit the observational light curves of all γ-ray pulsars with just a set of synthetic emission maps in which timing and spectral parameters are fixed to those of a given, arbitrary pulsar. To answer this question, we have fitted the whole sample of light curves generated for a randomly-selected young pulsar, J1838-0537, to the whole set of observational light curves in the same way as explained before. We find that the fitting results are qualitatively very similar to those of the fitting in which each observational light curve is compared to the synthetic light curves generated for its corresponding pulsar. The same conclusions we have presented in this section in terms of quality of the fits are also found now, independently of which fitting method is used. Considering $\overline{\chi^2}$ in time domain, the distribution of the minimum $\overline{\chi^2}$ values found in the normal fitting and in the one using a single set of skymaps are almost identical, as shown in Figure 5.9. This exercise has been repeated using the maps from a millisecond pulsar, J1035-6720, and the exact same results are obtained. These results, again, support the statement that geometry is the defining aspect for the light curves shapes; and that the global structure of the magnetosphere as well as the emission processes and location of the accelerating region must be roughly the same, regardless of different timing properties, spectra. We stress that this might not be the case if also X-ray light curves were to be taken into account, since a strong link between X-γ spectral differences and X-γ light curve differences is expected, since the synchrotron radiation is spread to a broader angles. Our result is in agreement with the recent observational proof by García and Torres (2025). These authors quantified 3PC light curve similarity and showed it can be very high for very different pulsars; even some MSPs and young pulsars share detailed light curve morphology.

5.3 Searching for correlations between model parameters

5.3.1 Searching for correlations between spectral parameters

Viganò et al. (2015d) showed the existence of some trends between spectral and physical parameters of pulsars. At the present moment the number of observed γ-ray pulsars has increased with respect to that work, and thus it is a good exercise to check whether the found correlations remain or not, and if new ones appear. Taking into account that the current radiative model incarnation is a more improved version of that in Viganò et al. (2015d), it is interesting to see whether the correlations previously found were extremely

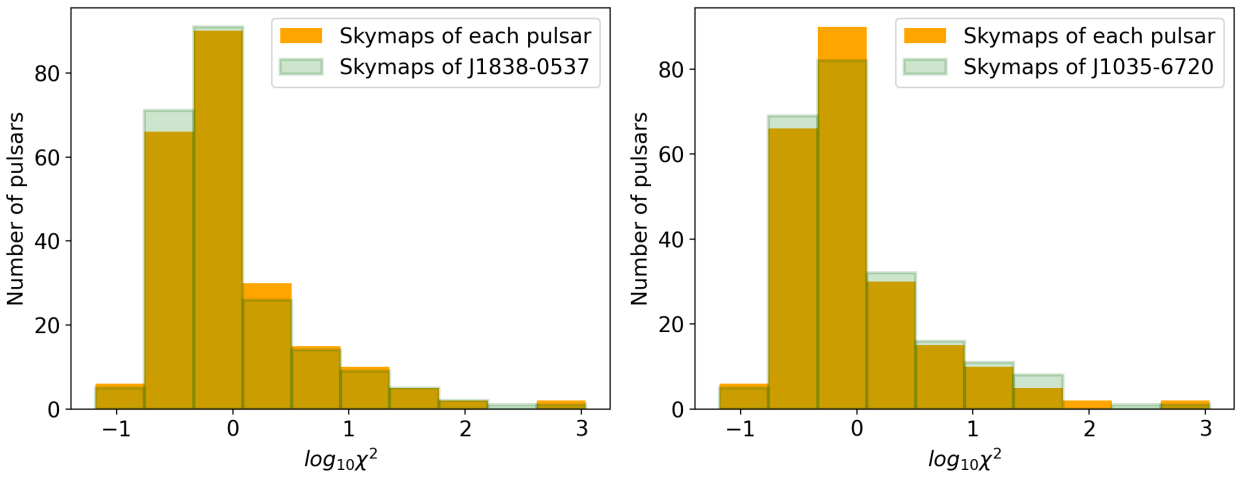


Figure 5.9: Comparison of the distributions of minimum $\overline{\chi^2}$ values from the fitting where all observational light curves are compared with each pulsars' skymaps (orange histograms) and with only one set of skymaps from a given, arbitrary pulsar (green histograms). The green histogram in the top (bottom) panel corresponds to the fitting done with the skymaps of J1838-0537 (J1035-6720).

model-dependent or instead they had some physical motivation. To identify something as a significant correlation we follow the same criterion as in Viganò et al. (2015d) and require a Pearson value $|r| > 0.85$. We only consider spectral parameters that have been correctly determined, i.e. those of pulsars whose spectral data fulfil the quality criterion stated in subsection 5.1.2. Table 5.3 shows the results of the linear fits for the most significant correlations and Figure 5.10 shows the plots of these fits. Notice that we are also showing correlations below our significance threshold. We do this for completeness, and to show the state of some correlations found in Viganò et al. (2015d), now that the population has notably increased.

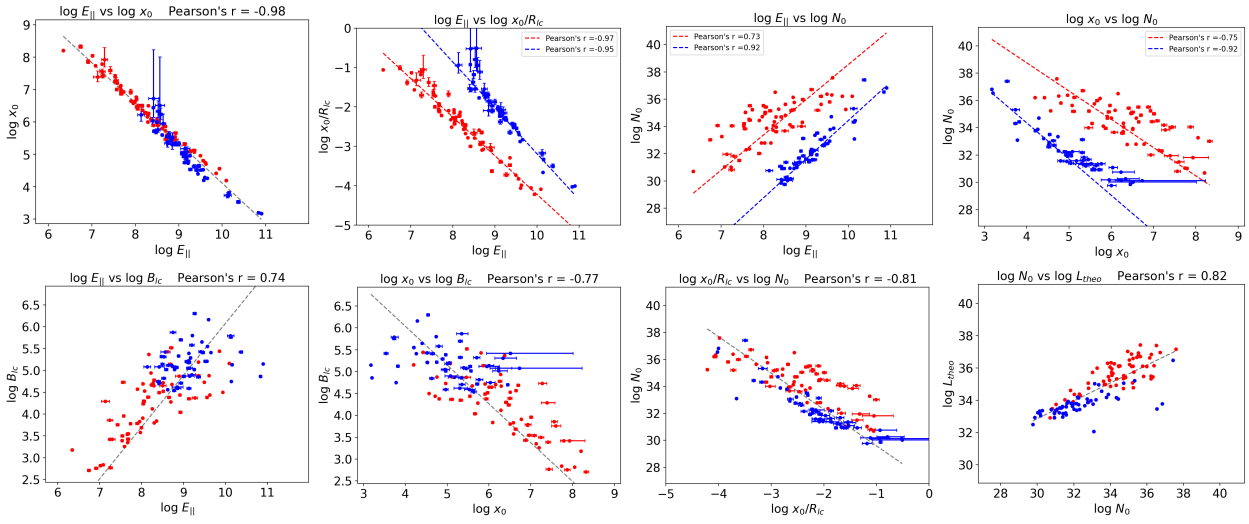


Figure 5.10: Correlation fits involving model parameter. Top row, from left to right: $\log E_{||} - \log x_0$, $\log E_{||} - \log x_0/R_{LC}$,$\log E_{||} - N_0$, $\log x_0 - N_0$. Bottom row, from left to right: $\log E_{||} - B_{LC}$, $\log x_0 - B_{LC}$, $\log x_0/R_{LC} - N_0$, $N_0 - L_{\rm theo}$. Dashed lines show the best linear fit. Red (blue) dots are used for young (millisecond) pulsars.

Table 5.3: Correlation fits involving model parameter, showing the linear best-fits $y = A + Bx$ and the corresponding Pearson r, for the whole sample of fitable pulsars, and the subsamples of young pulsars and MSPs

x	y	A	B	r
Whole sample				
$\log E_{\|\|}$	$\log x_0$	16.51	-1.24	-0.98
$\log E_{\|\|}$	B_{LC}	-5.77	1.18	0.74
$\log x_0$	B_{LC}	9.58	-0.89	-0.77
$\log x_0/R_{LC}$	$\log N_0$	26.89	-2.70	-0.81
$\log N_0$	L_{theo}	16.25	0.55	0.82
Young pulsars				
$\log E_{\|\|}$	$\log x_0/R_{LC}$	5.58	-0.98	-0.97
$\log E_{\|\|}$	$\log N_0$	12.73	2.58	0.72
$\log x_0$	$\log N_0$	47.04	-2.07	-0.75
MSPs				
$\log E_{\|\|}$	$\log x_0/R_{LC}$	8.44	-1.16	-0.95
$\log E_{\|\|}$	$\log N_0$	6.09	2.83	0.92
$\log x_0$	$\log N_0$	44.97	-2.65	-0.92

Considering the whole sample of fitable pulsars, we only find a relevant correlation between $\log E_{||}$ and $\log x_0$. Figure 5.10 shows the linear anti-correlation between these two free model parameters. This can be interpreted in the following way: on the one hand, a smaller x_0 means that the only a small portion of the region significantly contributes to the total spectrum, and therefore a high accelerating $E_{||}$ is needed for the emitting particles to reach sufficiently high energies so that the spectrum reaches the GeV range; on the other hand, with a large x_0 the part of the region that contributes to the spectrum is large, and thus $E_{||}$ has to be small, because otherwise there would be an over-representation of particles with high energies which would take over the contribution from the less energetic particles, which we have seen that are also relevant to reproduce observational high-energy spectra. Between $\log E_{||}$ and $\log x_0/R_{LC}$ there is also a significant correlation, but if the two classes of pulsars, young and MSP, are separated. This remarks the strong correlation between these two parameters, which is maintained regardless of the scale considered. The $\log E_{||} - \log x_0$ correlation was also found in the previous study, and with very similar parameters of the best linear fit, in spite of the increase of the sample and the different incarnation of the radiative model. The last correlations above the threshold are the ones between $\log E_{||}$ and N_0, $\log x_0$ and $\log N_0$, but only for the subsample of MSPs. This may be interpreted in the following way: small x_0 means that the region relevant for the total spectrum is small, which then requires a larger amount of emitting particles, i.e. a larger N_0. Other correlations found in the previous study: $\log E_{||} - B_{LC}$, $\log x_0 - B_{LC}$ and $\log N_0 - \log L_{\text{theo}}$ are now still statistically significant but do not reach our Pearson r threshold. Probable reasons for this fact are the enlargement of the population or the different radiative model incarnation used. The other correlations presented in that work involved parameters of the phenomenological

function PLEC1 (Abdo et al., 2012) from the 2PC, which has been updated to the PLEC4 (Abdollahi et al., 2022) on the 3PC. No correlations of the PLEC4 model parameters with our (radiative or spectro-geometrical) model parameters are found.

When the spatial scale $\lambda_{\rm lp.in}/R_{lc}$ is let free, the best-fitting values have no significant correlation with $E_{||}, x_0/R_{lc}$ or b, nor they show a correlation with other parameters like the strength of the magnetic field at the light cylinder B_{lc} or the spin-down power $\dot{E}$.

5.3.2 Searching for correlations between geometrical parameters

The geometrical parameters show no correlation with any other parameter of the pulsar or the model, and all pairs have a Pearson coefficient $r \leq 0.85$, i.e. there is no significant correlation of the geometry with spectral parameters, timing quantities, or PLEC4 parameters. This reinforces the idea that there is a decoupling between spectral and geometrical parameters, backing a conclusion stated in Chapter 4: spectral and timing considerations are negligible in shaping γ-ray light curves, being geometrical ones much more relevant. This conclusion may, of course, be affected by adding further complexities in our model.

5.4 Concluding remarks

In this Chapter we have presented the first concurrent fitting of spectra and light curves for the whole population of gamma-ray pulsars. Using an effective radiative model based on synchro-curvature radiation and the computation of the dynamics and emission of charged particles in a pulsar's magnetosphere, presented in Chapter 3, we generate synthetic spectra. Intertwined with the spectral calculation, we describe the geometry of the trajectory of these particles and define a particular shape for the region where they move, as presented in Chapter 4, which allows us to produce light curves. Theoretical spectra and light curves are then compared with observational spectral and light curves data to assess the ability of our models to reproduce them and to find the best-fitting values of the free model parameters, three in the radiative model and two in the geometrical model.

We have fitted the spectra of the whole population of high-energy pulsars. The source of the spectral data varied pulsar by pulsar, either from the 2PC, from dedicated spectral analysis or from the 3PC, depending on the quality. The fitting procedure we use relies on the Nelder-Mead method, a classical optimization algorithm with which we find the best-fitting spectral parameters: the set of parameters that generates the synthetic spectrum which gives the smallest χ^2. The radiative model fits well the whole population of gamma-ray spectra, with only three free parameters and a normalization factor. The model is also able to reproduce the X-ray band of the spectrum of a majority of the pulsars for which X-ray pulsations are detected together with γ-ray ones. This represents a successful fit across eight orders of magnitude in energy.

This achievement reinforces the identification of synchro-curvature radiation as the mechanism at work in pulsars' magnetospheres generating the high-energy emission of pulsars. In addition, we have confirmed that the synchro-curvature description of the pulsar's spectra requires small spatial scales. On the one hand, $\lambda_{\rm lp.in} \sim 10^{-4} - 10^{-6}\ R_{lc}$, where the spec-

trum emitted by particles injected at a given point is dominated by the large pitch angle emission via synchrotron. On the other hand, $x_0 \sim 10^{-2} - 10^{-3}\ R_{lc}$, which represent that after injection particles quickly stops being observationally-relevant for the observer. These scales should not be confused to the extent of the acceleration region, and do not imply that particle acceleration or injection occur only on them. We have also explicitly shown that, if we consider particle injection occurring all along the acceleration region (i.e., a range of r_{in} along $r_{\max}$, herein assumed to be at least R_{lc}), the fits are practically unchanged.

We have fitted individual gamma-ray light curves. We have made use of two different techniques: using the reduced χ^2 (weighted with the normalized flux of the observational light curve) to evaluate the goodness of the fits of light curves in time domain, and computing the euclidean distance to compare the light curves in frequency domain, i.e. to compare their Fourier transforms. Despite the caveats that both methods may have, the two of them give qualitatively similar results. With both fitting methods we have obtained good fits in many cases. The best-fitting values of the geometrical parameters found with the two techniques, which in both cases have a considerable degeneracy and thus cannot be regarded as strong constraints, are compatible in a fraction of the sample, but differ in the rest of the population. If one instead looks at the parameter space (fourth and eighth rows of Figure 5.7), the regions with relatively low metric values are similar. The two methods provide therefore similar results in terms of selecting the most likely loci in the geometrical parameter space, but with quantitative differences when one wants to fine tune the values well below such degeneracy-driven uncertainties (which are not easy to be assessed in a statistically sound way). Additional observational constraints, like radio or X-ray light curves, could potentially break the degeneracy and practically make the use of the two techniques more powerful.

For most pulsars we capture the general structures of the observational light curves, such as number of peaks and separation between peaks, or even flux ratio between peaks or width of the peaks, but fail to reproduce the small scale features. In a few pulsars, the observational light curves are not found in our set, either because they simply don't exist or because the fitting techniques miss them. Regarding the first possibility, the effective nature of the geometrical model provides versatility at an acceptable computational cost, but it is still lacking the complexity that a real magnetosphere may have. The model does not generate very complex synthetic light curves, for example with very asymmetric peaks or containing significant substructures (e.g. small peaks near larger ones). An improvement of the model, making it more realistic but maintaining the effective approach and the computational cost acceptable, is planned for the future.

We have found the distributions of best-fit viewing angles for both fitting methods to differ from a uniform distribution, as it should be a priori, showing an overabundance of small viewing angles. We argue that the reason is the way we model the light curves and the assumptions we make, as well as the fact that we are considering the fits from all pulsars together, without taking their goodness into account.

We have also done the exercise of fitting the whole population of gamma-ray light curves with just a single sample of emission maps, generated for a specific a set of P, $\dot{P}$ and spectral parameters. Overall results of this fitting are very similar to those obtained in the fitting in which each observational light curve is fitted with its corresponding sample of skymaps. This

seems to point towards a unique magnetospheric structure of pulsars' magnetosphere and a unique process generating the radiation, with pulsars' detected emission being solely defined by the inclination angle of the pulsar and the viewing angle of the observer. We also have to admit the possibility that the assumptions in our model, in particular the effective weight to enhance the small parts of the trajectories which give synchrotron-dominated emission, might lead to this effect, by construction. Future improvement of the underlying physics of the model, which will allow to convert effective parameters into more physical ones, will shed more light into this.

At this point is relevant to comment on the only fitting of 3PC gamma-ray light curves done so far, published in Cerutti et al. (2025), in order to contextualize the work presented here in the current panorama of modelling of pulsar high-energy emission. The results presented there and in the present work are qualitatively similar but are based on different assumptions and approaches. Both can fit well some light curves and capture the global structure of most of the cases, but fail when fitting complex light curves (with asymmetric peaks or small scale features). While we use an effective model, austere, and with low computational cost, Cerutti et al. (2025) develops magnetospheric PIC simulations in which the electromagnetic fields and charged particles are self-consistently computed and are computationally very costly. The qualitative similarity of the results obtained with such different (and complementary) models provides support for the current general understanding of the generation of the pulsar high-energy emission.

Finally, we have studied the possible correlations between pulsar parameters in the same way we did in Viganò et al. (2015d). The relevant correlation between the $\log E_{||}$ and $\log x_0$ is significantly found again, being indeed the most significant correlation. We also found a correlation of $\log E_{||}$ and $\log x_0$ with $\log N_0$, but only above our threshold in the sample of MSPs. There is no significant correlation between the PLEC4 model parameters from the 3PC and our model parameters. No correlation of the geometrical parameters with any other parameter or physical quantity is found.

6

The dispersion in pulsar γ-ray efficiency

We have seen that in plasma-filled magnetospheres, part of the rotational energy of the pulsar is transformed into acceleration of particles that ultimately emit radiation. Part of this is emitted in γ-rays that we can detect from Earth. A relevant question in pulsar physics is to know the fraction of the total energy budget of the pulsar, the spin-down power, that ends up being dissipated as high-energy emission, and if this fraction is the same for all pulsars or varies across the whole population. This can provide information about how the dissipation of the magnetic field into particle acceleration works, as well as about the radiation mechanism producing this high-energy emission. We address this topic in the present chapter, which is largely based on the published work Íñiguez-Pascual et al. (2025b).

6.1 Introduction

The observational efficiency $\eta_{\rm obs}$ is defined as the ratio of the derived isotropic-equivalent luminosity of the pulsar to the pulsar spin-down power:

$$\eta_{\rm obs} = \frac{4\pi d_{\rm obs}^2 F_{\rm obs}}{I_0 \Omega \dot{\Omega}}, \tag{6.1}$$

where $F_{\rm obs}$ is the average pulsed energy flux of a pulsar, $d_{\rm obs}$ is the estimated distance, $I_0 = 10^{45}$ g/cm^2 is the conventional value of the moment of inertia, and Ω and $\dot{\Omega}$ are the observed angular velocity and its time derivative, respectively. In this work we focus on the γ-ray range of *Fermi*-LAT (100 MeV – 300 GeV), for which the values of $\eta_{\rm obs}$ from the 3PC show a wide dispersion, with values ranging from $\sim 0.02\%$ up to $\sim 200\%$. The uncertainty on the pulsar distances and the assumed fixed value of the beaming factor $f_\Omega = 1$, are usually mentioned as the origin of this dispersion. Here we consider these two factors, plus the uncertainty on the moment of inertia (neglecting the uncertainties on the timing parameters since they are measured with notable precision), to factorize the combined efficiency as

$$\eta_{\rm obs} = \frac{4\pi d_*^2 \langle F \rangle}{I_* \Omega \dot{\Omega}} \frac{I_*}{I_0} \frac{d_{\rm obs}^2}{d_*^2} \frac{F_{\rm obs}}{\langle F \rangle} = \eta_{rad}\ \epsilon_{\rm I}\ \epsilon_{\rm d}\ f_\Omega^{-1}\ , \tag{6.2}$$

hereafter conveniently considered in its logarithmic version:

$$\log_{10} \eta_{\rm obs} = \log_{10} \eta_{rad} + \log_{10} \epsilon_{\rm I} + \log_{10} \epsilon_{\rm d} - \log_{10} f_\Omega\ . \tag{6.3}$$

We label with an asterisk two quantities (the real distance d_* and moment of inertia of the star I_*) which are unknown and might differ from the estimated values, so that $\epsilon_{\rm d} := d_{\rm obs}^2/d_*^2$ and $\epsilon_{\rm I} := I_*/I_0$ encode the uncertainties on the distance and moment of inertia, respectively. The factor $\eta_{rad} := 4\pi d_*^2 \langle F \rangle / (I_* \Omega \dot{\Omega})$ is the intrinsic efficiency of the mechanism converting the rotational energy losses into γ-ray emission (via particle acceleration), with $\langle F \rangle$ being the average γ-ray flux emitted over the sky, i.e. the entire magnetospheric emission in γ-rays. The beaming factor $f_\Omega := \langle F \rangle / F_{\rm obs}$, defined as in e.g. Watters et al. (2009), is the ratio of the total pulsed emission of the pulsar averaged over the sky $\langle F \rangle$ to the phase-averaged emission detected by a given observer $F_{\rm obs}$. This depends on the strongly anisotropic (beamed) emission of the pulsar, the magnetospheric configuration (in particular, the inclination angle Ψ_Ω between the rotational axis and the magnetic moment), and the viewing angle θ_{obs} between the pulsar equatorial plane and the line of sight of the observer. Therefore, the beaming factor can be estimated using a geometrical model of the magnetospheric emission. If the flux intercepted by the observer is exactly the averaged flux over the sky, $f_\Omega = 1$. Observers in a line of sight that crosses the bulk of the emission have small values $f_\Omega < 1$, while those observers that intercept the directions with a lower-than-average flux have $f_\Omega > 1$. Lucky observers with small beaming factors will estimate a higher observational efficiency than the average observers, which explains the possibility of measuring $\eta_{\rm obs} \gtrsim 100\%$.

In this study we quantify the a priori distribution of values of three terms (f_Ω, $\epsilon_{\rm d}$, and $\epsilon_{\rm I}$), in order to obtain an a posteriori distribution of the physical mechanism efficiency η_{rad}, by comparison with the observed distribution of $\eta_{\rm obs}$. We use the standard deviation as a measure of the dispersion of a distribution.

6.2 Ingredients contributing to the dispersion of the observational γ-ray efficiency

6.2.1 Beaming factor, f_Ω.

The beaming factor, f_Ω, is here quantitatively estimated using our spectro-geometrical model of Chapter 4.

For a given choice of the free spectral parameters and inclination angle Ψ_Ω, the synthetic sky maps consist of a discrete set of fluxes $F(\theta_{obs,i}, \phi_j; \Psi_\Omega)$, where $\phi_j \in [0, 2\pi)$ indicates the rotational phase of the pulsar, and $\theta_{obs,i} \in (0, \pi)$ the observer. For this work we use $N_i = 51$ observers and a number of phase bins, N_j, as defined in Chapter 4, typically 100, and fluxes are integrated over the *Fermi*-LAT energy range. The average flux over the sky, $\langle F \rangle$, and the phase-averaged flux detected by the observer θ_i, $F_{obs,i}$, are

$$\langle F \rangle = \frac{1}{4\pi} \sum_{j=1}^{N_j} d\phi \sum_{i=1}^{N_i} d\theta \, \sin\theta_{obs,i} \, F(\theta_{obs,i}, \phi_j; \Psi_\Omega) \ , \tag{6.4}$$

$$F_{obs,i} = \frac{1}{2\pi} \sum_{j=1}^{N_j} d\phi \, F(\theta_{obs,i}, \phi_j; \Psi_\Omega) \ , \tag{6.5}$$

and their ratio gives the synthetic beaming factor for each observer, for every sky map. To obtain the f_Ω distribution, we consider the 226 3PC pulsars whose light curves are fitted in Chapter 5. For each of them, we generate 30 emission maps, changing Ψ_Ω, uniformly distributed between 3° to 90°. For a given sky map, we discard the observers detecting no flux or a flux below a threshold of 5% of the maximum of the map, which are about 40% of the total (Íñiguez-Pascual et al., 2025a). Therefore, for every pulsar, we were left with about $\sim 10^3$ synthetic light curves, each one having a value of f_Ω. Importantly, the f_Ω distributions obtained from different pulsars are all very similar despite the different spectral and timing (Ω, $\dot{\Omega}$) configurations among the pulsars considered (which implies different free parameters of our radiative model; see Chapter 5). This is due to what we showed in Chapter 4: the geometry (Ψ_Ω and θ_{obs}) plays a dominant role in defining the emission maps in γ-rays, thus effectively decoupling the sky maps (and the f_Ω distributions) from the observed timing and spectral properties. Therefore, the impact of the geometrical configuration of the pulsar and its emission region on f_Ω overshadows that of the timing and spectral parameters: the f_Ω distribution is independent of them.

The top left panel of Figure 6.1 shows the histogram of the distribution of the logarithm of f_Ω. Not surprisingly, it peaks around $f_\Omega \sim 1$, has a standard deviation of 0.29 and is asymmetric, with a more pronounced tail at small values rather than large ones (not only due to the logarithmic representation). Although our results might depend on the assumed emission region shape, our f_Ω distribution looks qualitatively similar to results obtained in other theoretical studies considering either gap models (Pierbattista et al., 2012) or complex numerical simulations (Kalapotharakos et al., 2023; Cerutti et al., 2025).

6.2.2 Uncertainty on the moment of inertia, $\epsilon_{\rm I}$.

A conventional value of $I_0 = 10^{45}\mathrm{g/cm^2}$ is usually assumed when computing the rotational energy losses. However, each pulsar has its own I_* since it depends on the mass and radius, although these are generally unknown. In addition, the EoS for cold dense matter is still not known precisely, which is reflected in the uncertainty on the neutron star characteristic mass-radius ($M(R)$) relation.

To take into account both effects, we can estimate I_* using the expression presented by Bejger and Haensel (2002), which, considering a large sample of neutron star structures built with many different available EoSs and masses, found a best-fitting effective expression for the moment of inertia: $I = a(x)MR^2$, with $x = (M/\mathrm{M}_\odot)(\mathrm{km}/R)$ and $a(x) = x/(0.1+2x)$ for $x \leq 0.1$ and $a(x) = \frac{2}{9}(1+5x)$ for $x > 0.1$. In order to obtain an informed a priori distribution of values of I_*, we also need the distribution of M and R of neutron stars. Masses can be estimated in several cases, mainly when in binary systems (Özel and Freire, 2016), and their values are well described by a skew normal distribution, $\mathcal{SN}$ (Kiziltan et al., 2013), whose parameters are the mean μ, the standard deviation σ, and the skewness α. Using the

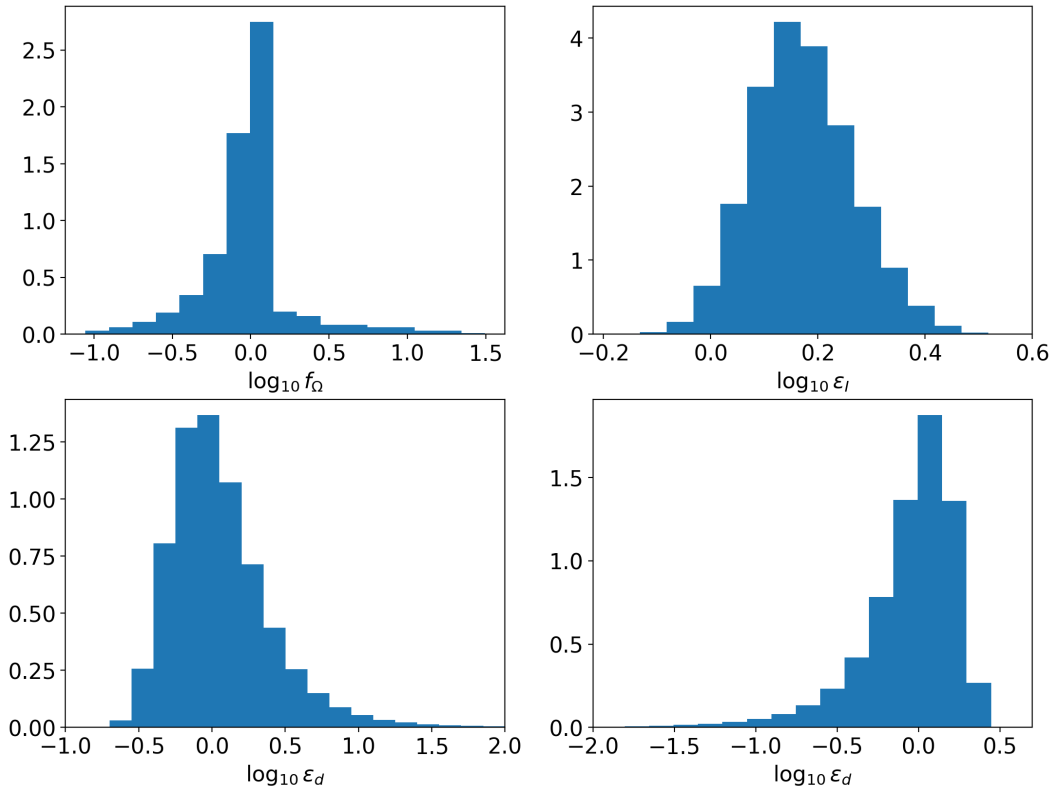


Figure 6.1: Probability density of the terms forming $\log_{10}\eta_{\rm obs}$. Top: $\log_{10} f_\Omega$ (left) and $\log_{10}\epsilon_{\rm I}$ (right). Bottom: $\log_{10}\epsilon_{\rm d}$ from different prescriptions, $P(\Delta)=\mathcal{N}$ (left) and $P(\epsilon_{\rm d})=\mathcal{N}$ (right).

best-fitting parameters to the most updated available sample,[1] we then assume an a priori distribution of the masses (in solar masses) $P(M[M_\odot]) = \mathcal{SN}(\mu=1.20, \sigma=0.31, \alpha=14.03)$. Given the substantial lack of precise constraints on the radius, we take R to be distributed as a Gaussian $P(R[\mathrm{km}]) = \mathcal{N}(\mu=12.0, \sigma=1.0)$, a representative distribution, where the dispersion assumed here is compatible with the relatively vertical shape of the $M(R)$ curve for most EoSs. Given the lesser role played by the moment of inertia (see below), we do not explore other mean values of R.

Sampling ($\sim 10^3$) values of R and M from the mentioned distributions with an acceptance-rejection method, we can obtain a distribution of physically motivated values of the moment of inertia. Dividing it by I_0 gives the uncertainty term associated with the moment of inertia $\epsilon_{\rm I}$. The right top panel of Figure 6.1 shows the histogram of the distribution of its logarithm. It is centred at $\log_{10}\epsilon_{\rm I} \sim 0.2$ and has a standard deviation of 0.09, smaller than that of the distributions $\log_{10} f_\Omega$ and $\log_{10}\epsilon_{\rm d}$ (see below).

6.2.3 Uncertainty on the distance, $\epsilon_{\rm d}$

The real distance to a pulsar from Earth, d_*, is unknown. The observationally estimated values, $d_{\rm obs}$, normally have large uncertainties and are obtained with different methods, for example the dispersion measurement method, parallax, or kinetic method. As a proxy of the distance uncertainties distribution, we take the average of the relative distance errors of the pulsar sample, as quoted in the 3PC, which is $\sigma_{\rm d,rel} = 0.341$. In the absence of a

[1] www3.mpifr-bonn.mpg.de/staff/pfreire/NS_masses.html

better estimation for the error distribution, we consider two cases. In the first case, we assume that the relative error $\Delta := (d_* - d_{\rm obs})/d_{\rm obs}$ follows a Gaussian distribution, with $\mu = 0$ and $\sigma = \sigma_{\rm d,rel}$. We then sample ($\sim 10^6$) Δ values with an inverse transform method, and obtain the corresponding set of values $\epsilon_{\rm d} = (\Delta + 1)^{-2}$. The second choice is to instead consider the distribution of $\epsilon_{\rm d}$ itself as a Gaussian (sampling $\sim 10^6$ values), with $\mu = 1$ and $\sigma_{\epsilon,{\rm d}} = (\sigma_{\rm d,rel} + 1)^{-2} = 0.556$. The resulting $P(\log_{10}\epsilon_{\rm d})$ for the two choices (bottom panels of Figure 6.1) differ in shape, but only slightly in standard deviation (0.38 and 0.31, respectively).

6.3 Distribution of the mechanism efficiency

The rotational energy losses represent the budget powering pulsar high-energy emission. However, what fraction is ultimately converted into emitted radiation is not known exactly since it depends on the details of every step of the conversion: Poynting flux $\rightarrow$ particle creation and acceleration $\rightarrow$ synchro-curvature radiation (in the γ-ray range).

We assumed a trial distribution for $\log_{10}\eta_{rad}$ and, assuming that the four distributions on the right-hand side of Equation (6.3) are independent of each other, their sum (hereafter referred to as joint distribution) is simply obtained by performing a Monte Carlo sampling of each distribution and summing the values (see e.g. Chapter 3 of Springer 1979). We then compare it with the distribution of the logarithm of the observational efficiency $\log_{10}\eta_{\rm obs}$ by applying a Kolmogorov–Smirnov (KS) test. The metric of the KS test, D_{KS}, measures the similarity between two distributions, by using their empirical distribution functions. We minimized D_{KS} by scanning the space of parameters of the trial distribution and picking up the set of parameters giving a smaller D_{KS}. The best-fitting set of parameters defining the distribution of $\log_{10}\eta_{rad}$ is the one that generates a joint distribution most closely resembling $\log_{10}\eta_{\rm obs}$. Finally, we obtain the dispersion and peak position of the best-fitting trial distribution.

Table 6.1 compares the best-fitting parameters of the trial distributions (Gaussian or skew normal) of $\log_{10}\eta_{rad}$ for the two different prescriptions of distance uncertainties. The resulting joint distributions are shown in the right column of Figure 6.2, compared with $\log_{10}\eta_{\rm obs}$. In all cases, the dispersion of $\log_{10}\eta_{rad}$ is similar, with standard deviations of $0.42 - 0.56$, which corresponds to around one order of magnitude in η_{rad}, regardless of the different shapes of distributions. The best-fitting a posteriori distributions peak at a value η_{rad}^{peak}, which changes between ~ 5 and $\sim 15\%$; the change is mainly due to the different shapes of the trial distributions.

Note that in all cases there is a slight mismatch at low $\eta_{\rm obs}$ values. This can be produced by the observational biases that affect this region: the small values may be a result of a low flux close to the *Fermi*-LAT sensitivity. Thus, the comparison at low values is not informative and we do not focus on them. Instead, note that the cases with $P(\Delta) = \mathcal{N}$ have a tail at high values ($\log_{10}\eta_{rad} > 10$), which is incompatible with the observed distribution regardless of the shape of the distribution $P(\log_{10}\eta_{rad})$, and is due to cases with very large $\log_{10}\epsilon_{\rm d} \gtrsim 1$ (i.e. an order of magnitude overestimation of d_*^2). Such a tail is indeed much less visible if we consider the distance uncertainty distributed as $P(\epsilon_{\rm d}) = \mathcal{N}(1, \sigma_{\epsilon,{\rm d}})$ because the latter has

fewer extremely high values. Moreover, for the latter case, we explored the sensitivity of the fitting on the dispersion of the a priori distribution $P(\epsilon_{\rm d})$ by taking $\sigma_{\epsilon,{\rm d}} = 0.2$ and 0.7 instead of 0.556. The result is that the peak position of the mechanism efficiency distribution barely changes, while its standard deviation changes by only $\sim 30\%$ between the two extremes of $\sigma_{\epsilon,{\rm d}}$.

Table 6.1: Best-fitting parameters of the trial distributions of $P(\log_{10}\eta_{rad})$ for different distributions of distance uncertainty.

$P(\log_{10}\eta_{rad})$	Distance uncertainty	η_{rad}^{peak}	Std dev
$\mathcal{N}$	$P(\Delta) = \mathcal{N}(0, 0.341)$	5.8%	0.42
$\mathcal{SN}$	$P(\Delta) = \mathcal{N}(0, 0.341)$	14.8%	0.47
$\mathcal{N}$	$P(\epsilon_{\rm d}) = \mathcal{N}(1, 0.556)$	7.2%	0.46
$\mathcal{N}$	$P(\epsilon_{\rm d}) = \mathcal{N}(1, 0.2)$	6.6%	0.56
$\mathcal{N}$	$P(\epsilon_{\rm d}) = \mathcal{N}(1, 0.7)$	7.1%	0.42

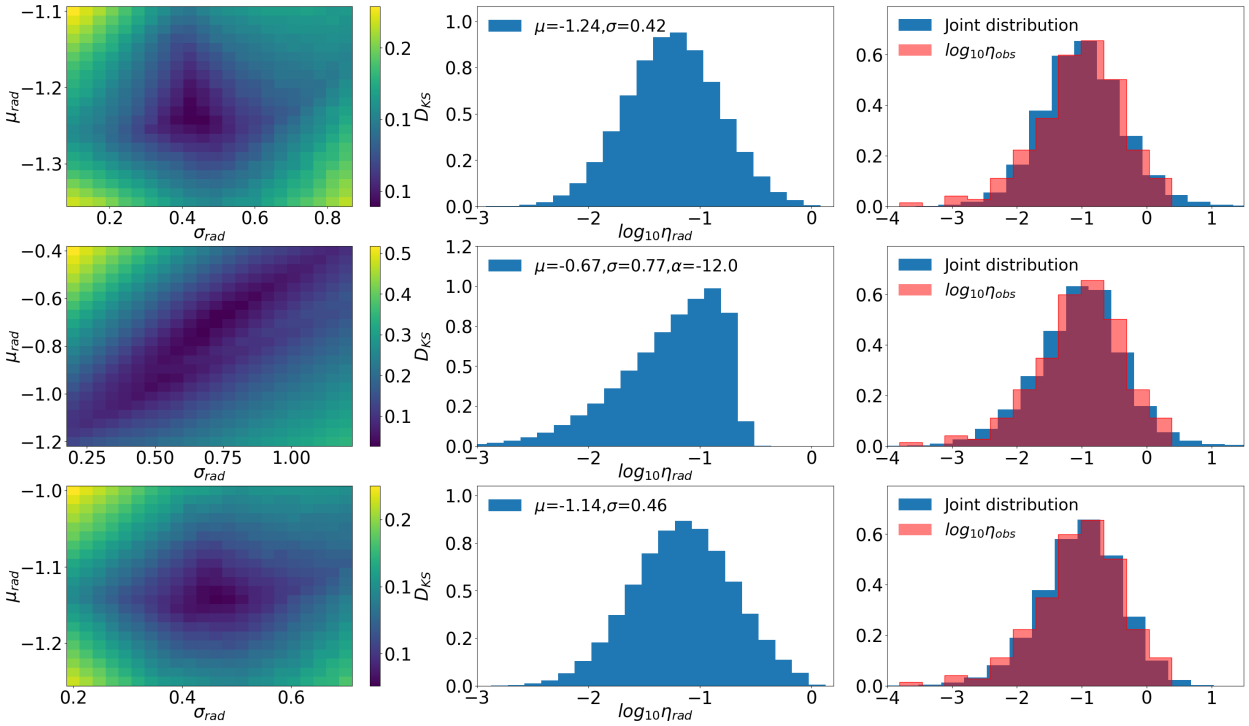


Figure 6.2: Results of the fitting to find the distribution of η_{rad}. The top (middle) row shows those obtained using the distance uncertainty distributed as $P(\Delta)$=$\mathcal{N}$, with a Gaussian (skew normal) as the trial distribution. The bottom row ones were obtained with the distance uncertainty distributed as $P(\epsilon_{\rm d})$=$\mathcal{N}$, with a Gaussian as the trial distribution. From left to right: contour plot of D_{KS} in the space of parameters μ_{rad}-σ_{rad} (in the skew normal case we collapsed all the contours for the different α considered taking the smallest D_{KS} for each pair μ_{rad}-σ_{rad}), best-fitting distribution of $\log_{10}\eta_{rad}$, overlapped distribution of $\log_{10}\eta_{\rm obs}$ (red), and joint distribution (blue).

Overall, this indicates a minor influence of the $\epsilon_{\rm d}$ prescription on the best-fitting a posteriori distribution of η_{rad}. It also implies that η_{rad} is the term dominating the dispersion of $\eta_{\rm obs}$.

6.4 Additional sources of $\eta_{\rm obs}$ dispersion

The 3PC, similarly to previous studies, proposes a correlation between the spin-down power $\dot{E} = I_0 \Omega \dot{\Omega}$ and the observational efficiency $\eta_{\rm obs}$: $\eta_{\rm obs} \propto \dot{E}^{\beta}$, with $\beta = -0.5$ (see left panel of Figure 6.3). This correlation is not strong (the Pearson r coefficient in the log-log relation is -0.48), and a much larger sample over a broader range of $\dot{E}$ would be needed for a proper assessment (see e.g. Szary et al. 2014 in the X and radio bands). However, since the weakness of the correlation can be indeed due to the other concurrent dispersion factors here studied, we have investigated the contribution of the alleged correlation to the dispersion in the observational efficiency. By removing the correlation from the observed distribution, the de-trended $\log_{10} \eta_{\rm obs}$ distribution has a slightly smaller dispersion than the original one (standard deviation of 0.60 and 0.66, respectively). If we let β free instead of fixing it to -0.5, we find a best-fitting relation of $\eta_{\rm obs} \propto \dot{E}^{-0.32}$, which leads to a de-trended distribution of $\log_{10} \eta_{\rm obs}$ with a slightly smaller standard deviation, 0.57. Figure 6.4 shows the comparison of the original distribution of $\log_{10} \eta_{\rm obs}$ with the de-trended ones with the fixed $\beta = -0.5$ and the fitted $\beta = -0.32$. In addition, middle and right panels of Figure 6.3 shows the de-trended $\eta_{\rm obs}$ as a function of $\dot{E}$.

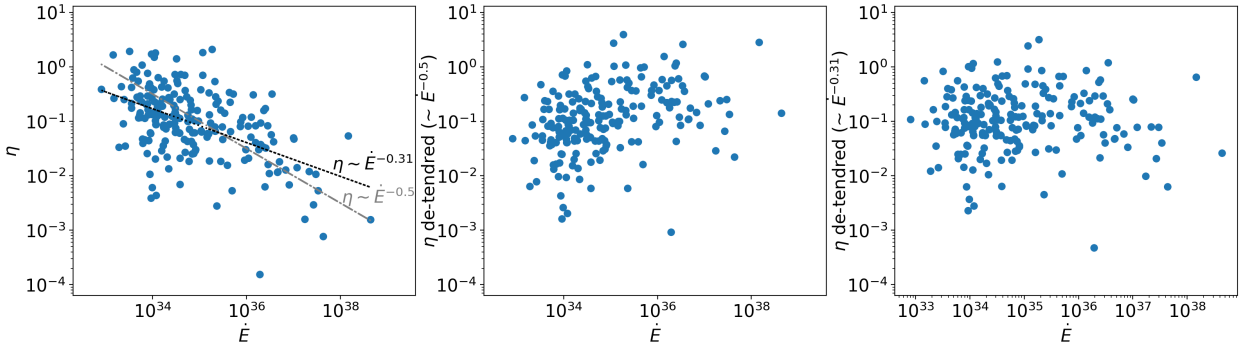


Figure 6.3: Observational efficiency $\eta_{\rm obs}$ vs spin-down power $\dot{E}$ (data taken from the 3PC Fermi Database webpage). From left to right: original $\eta_{\rm obs}$ with the best-fitting lines $\eta_{\rm obs} \propto \dot{E}^{-0.5}$ (dotted-dashed grey) and $\eta_{\rm obs} \propto \dot{E}^{-0.31}$ (dotted black), $\eta_{\rm obs}$ de-trended of the correlation $\eta_{\rm obs} \propto \dot{E}^{-0.5}$ and $\eta_{\rm obs}$ de-trended of the correlation $\eta_{\rm obs} \propto \dot{E}^{-0.31}$.

In order to see how this smaller dispersion affects the inferred η_{rad} distribution, we have repeated the procedure presented in Sect. 6.3. The corresponding best-fitting distribution of the efficiency mechanism η_{rad} are shown in Table 6.2 and Figure 6.5 show the fitting results, with a Gaussian as a trial distribution for η_{rad} and the $\epsilon_{\rm d}$ prescription in which Δ is distributed as a Gaussian. The dispersion of η_{rad} slightly decreases, as expected from the smaller dispersion of the de-trended $\eta_{\rm obs}$, while the central value is basically unaffected. These results indicate that a non-negligible, but not dominant part of the inferred η_{rad} dispersion can be attributed to the variations in $\dot{E}$. In other words, the γ-ray luminosity might scale less than linearly with $\dot{E}$, but this alone cannot explain the bulk of the inferred η_{rad} dispersion.

Other sources of dispersion could be differences in e.g. magnetic field topology at the surface or beyond the light cylinder (boundary conditions with the surrounding medium).

Table 6.2: Best-fitting parameters of $\log_{10}\eta_{rad}$ with $P(\log_{10}\eta_{rad}) = \mathcal{N}$ and $P(\Delta) = \mathcal{N}(0, 0.341)$ for the distance uncertainty, considering the original $\log_{10}\eta_{\rm obs}$ distribution or the ones de-trended with the correlation $\propto \dot{E}^{\beta}$.

$\log_{10}\eta_{\rm obs}$ distribution	$\log_{10}\eta_{\rm obs}$ std dev	η_{rad}^{peak}	$\log_{10}\eta_{rad}$ std dev
Original	0.66	5.8%	0.42
De-trended, $\beta = -0.50$	0.60	6.6%	0.34
De-trended, $\beta = -0.32$	0.57	6.5%	0.29

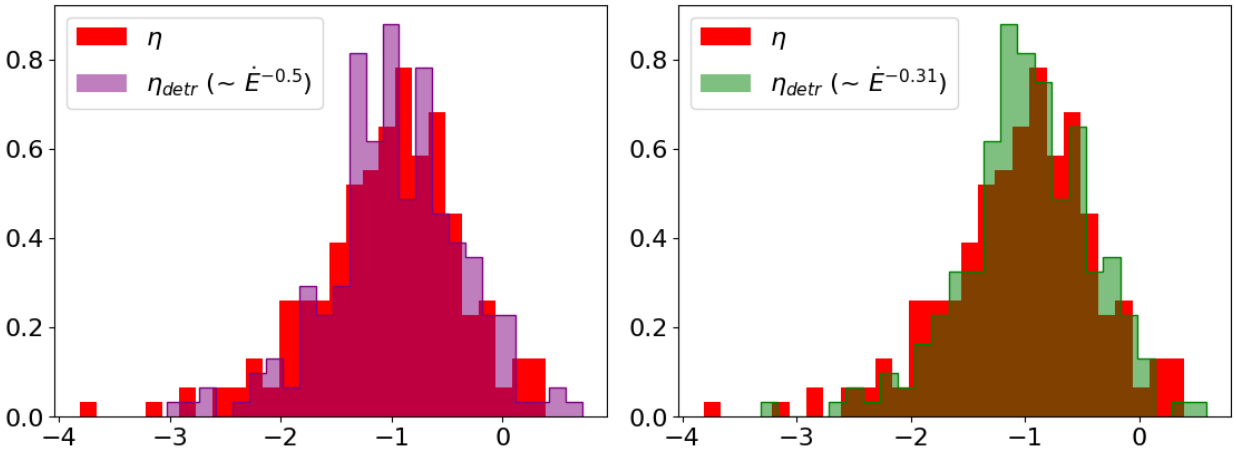


Figure 6.4: Probability density of $\log_{10}\eta_{\rm obs}$. Left: observed $\log_{10}\eta_{\rm obs}$ (red) vs $\log_{10}\eta_{\rm obs}$ de-trended of the correlation $\eta_{\rm obs} \propto \dot{E}^{-0.5}$ (purple). Right: observed $\log_{10}\eta_{\rm obs}$ (red) vs $\log_{10}\eta_{\rm obs}$ de-trended of the correlation $\eta_{\rm obs} \propto \dot{E}^{-0.31}$ (green).

General relativistic effects on the torque and pair production, which depend on the compactness (Ruiz et al., 2014; Philippov et al., 2015b; Carrasco et al., 2018), could also be a minor ingredient contributing to the dispersion.

6.5 Concluding remarks

The dispersion of the observational γ-ray efficiency $\eta_{\rm obs}$ can be explained with the four ingredients we have introduced here: f_Ω, $\epsilon_{\rm d}$, $\epsilon_{\rm I}$, and η_{rad}. We found η_{rad} to be a main contributor, at least as relevant as the distance errors and the f_Ω distribution coming from our geometrical model. The contribution of $\epsilon_{\rm I}$ is smaller compared to the other three terms, which indicates that assuming $I = 10^{45}{\rm g/cm^2}$ for all pulsars does not significantly affect the observational efficiency values. With the two trial distributions we considered for the efficiency of the physical mechanism of γ-ray emission η_{rad}, we found a peak position of around $5 - 15\%$, with a dispersion of approximately one order of magnitude. The same conclusion was obtained for a few different trial distributions of η_{rad} and/or prescriptions regarding the uncertainty on the pulsar distances.

The average values we found agree with the results found in complex magnetospheric simulations (FFE or PIC), in which $\sim 10 - 20\%$ of the Poynting flux is dissipated in the first $1 - 2$ light cylinder radius of the equatorial current sheet (Carrasco et al., 2018; Cerutti et al., 2020; Hakobyan et al., 2023). The dissipated Poynting flux in the current sheet

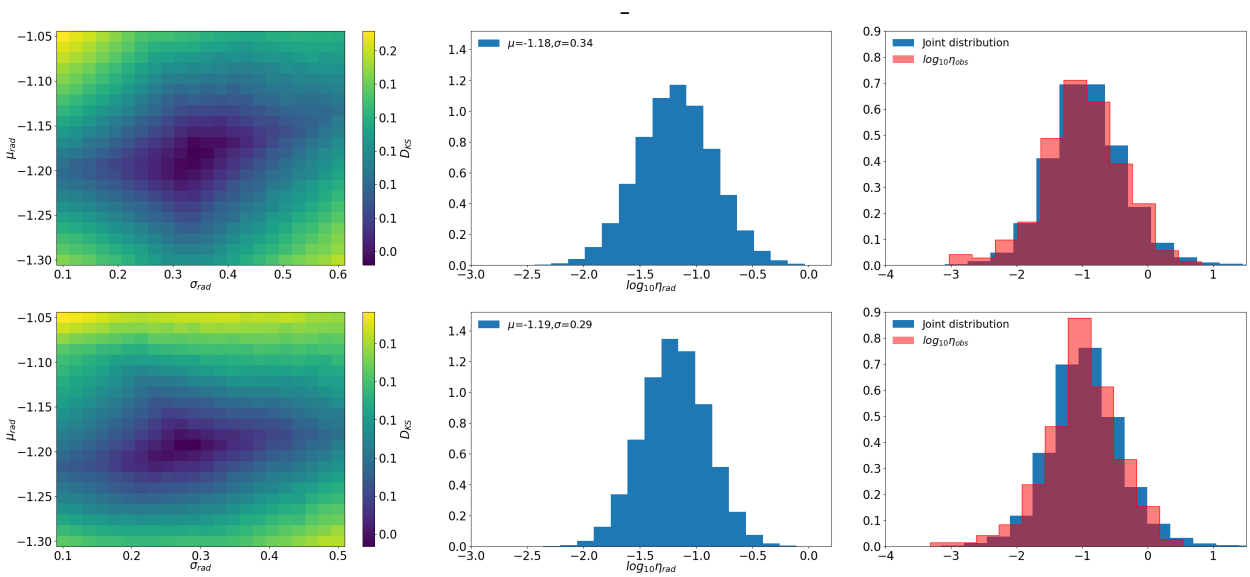


Figure 6.5: Results of the fitting to find the distribution of η_{rad}, analogous to Figure 6.2. The top (bottom) row shows those obtained with a $\log_{10}\eta_{\rm obs}$ distribution de-trended from the correlation $\propto \dot{E}^{\beta}$, with β equal to -0.5 (-0.32). Both cases were obtained using the distance uncertainty distributed as $P(\Delta)$=$\mathcal{N}$ and with a Gaussian as the trial distribution.

is converted into acceleration of particles, which then emit the high-energy radiation we detect. In our spectro-geometrical models, the γ-ray emission typically represents $\gtrsim 95\%$ of the total synchro-curvature radiation, in agreement with the tiny (always less than 1%) X-ray observational efficiencies of Fermi pulsars reported in e.g. Marelli et al. (2011). The mean values of η_{rad} also agree with the fact that pulsar wind nebulae, which are powered by the pulsar itself, require a significant amount of its energy. Regarding the relatively large dispersion of the inferred η_{rad} distribution, the alleged weak correlation $\eta_{\rm obs} \propto (I_0\Omega\dot{\Omega})^{-0.5}$ reported in the 3PC can explain a part of the dispersion but not all of it. Note that the precise shape of the distribution of η_{rad} remains unconstrained with our methodology since a good fit is obtained with the two trial distributions. In this regard, note that the tail with very high, arguably unphysical values $\gtrsim 50\%$ of efficiency is actually not needed: imposing a skew normal distribution, or, similarly, a cutoff at $\eta_{rad} \gtrsim 30\%$, essentially provides the same results in terms of inferred mean and dispersion.

Finally, it is interesting to remark that this simple methodology can be implemented to test whether different geometrical models, with their own f_Ω distributions, can change the results here presented.

7

Conclusions

In this thesis we have presented a modelling of the high energy emission of pulsars, with a theoretical and numerical approach. The main goal of this work is to develop effective radiative and spectro-geometrical models that generate high-energy spectra and light curves, respectively. These synthetic observables are then compared with observational spectra and light curves of the whole population of high-energy pulsars. With this comparison we can assess the goodness of our models in reproducing the production of high-energy emission, as well as obtain information about it.

We have presented a radiative model which aims at providing information on the processes leading to the production of high-energy emission in pulsars. The model solves the dynamics of charged particles travelling in a pulsar magnetosphere and computes their emission with the synchro-curvature radiation formulae. With its effective nature, it can produce energy spectra of the whole population of high-energy pulsars, which are described by three free model parameters: the parallel electric field $E_{||}$, the magnetic gradient b and the lengthscale x_0, together with a normalization factor N_0. We have seen that in the initial parts of the trajectory of a particle its emission is dominated by synchrotron radiation, and the spectra produced in this innermost region peak at low energies, in the keV range, i.e. the X-ray band. As the particle moves through the region, it enters in a pure synchro-curvature regime, and the spectra peak at intermediate energies, in the MeV range. Far from injection, the emission of the particle becomes curvature-dominated, and the spectra generated peak at high energies, in the GeV range. We have also seen that these ranges are not rigid: with different combinations of values of the spectral parameters the zones of the trajectory that are in either synchrotron, curvature or synchro-curvature regime vary in extent. The evolution along the trajectory of several kinematic quantities, such as the Lorentz factor Γ or the pitch angle α, also depends on the values of the spectral parameters. Therefore, we have clearly shown that the spectral parameters define the dynamics and emission of the charged particles. $E_{||}$ particularly affects the intermediate and high energy bands of the integrated spectrum, the γ-ray range. In particular, for larger values of $E_{||}$ the spectrum peaks at higher energies and has higher fluxes. b mostly shapes the low-energy parts of the

spectrum, the X-ray band, producing higher fluxes in this range for smaller values.

Complementary to the radiative mode, we have presented a spectro-geometrical model which accounts for the spatial distribution of the emission. Together with the dynamics and emission of the charged particles, we compute the three-dimensional geometry of their trajectories. In addition, we have given a prescription for a realistic shape of the emission region which mimics the results of FFE and PIC magnetospheric simulations. In this way we have created emission maps which display the spatial distribution of the radiation emitted by a pulsar and at the same time contain spectral information. Each map is integrated in the γ-ray energy band, and is described by a few geometrical parameters: the inclination angle Ψ_Ω, the meridional extent $\Delta\Psi_\mu$ and the injection range ΔR. From these maps we obtain synthetic γ-ray light curves. For different combinations of the geometrical parameters, we generate a set of emission maps from which we obtain a sample of light curves. Emission maps and light curves are greatly affected by different values of the geometrical parameters, while remaining almost unchanged when varying the timing and spectral ones. This indicates that geometrical considerations play a major role than timing and spectral ones in shaping γ-ray light curves. From this very relevant conclusion one can infer that considering a sample of light curves generated for the same pulsar, but for different geometries and observers, is substantially equivalent to exploring the population of all observational light curves, since each pulsar has its own (unknown) geometry. Looking in detail at the synthetic light curves, they are qualitatively similar to the observational ones, and show the same general features: different number of peaks, diverse morphology and a variety of peak widths, phase separations and flux ratios. In the whole sample of light curves, a majority of them have two peaks, a relatively large phase separation of $\sim 0.3 - 0.5$, small flux ratios of $\sim 1 - 2$, and thin peaks with widths of $0.05 - 0.2$. In addition, the number of detected light curves is around a 60% of the total sample, which gives an estimate of non-detectable observational γ-ray light curves due to the beaming. This percentages depends on the inclination angle, varying from less than 20% in almost aligned rotators to more than 90% in orthogonal rotators. This information can be relevant for population synthesis studies.

We have compared observational energy spectra of high-energy pulsars with synthetic ones generated with our radiative model. The fitting procedure relies on the Nelder-Mead minimization method, and uses the reduced χ^2 to assess the goodness of a fit. The model successfully reproduces the γ-ray spectra of the whole population of high-energy pulsars. It also resembles well the X-ray band of a majority of those pulsars with observed pulsations in this energy range, spanning more than eight orders of magnitude in energy. This supports the idea that synchro-curvature radiation is the mechanism producing the high-energy emission of pulsars. We find best-fitting values of the parallel electric field in the range 10^{7-10} V/m, representing electric potential drops in the emission region in agreement with values typically proposed in radiative models. Best-fitting values of the magnetic gradient b are ~ 2.5, which represents a decay of the magnetic field strength smoother than in a dipole. To obtain these good fits, our model requires the implementation of two effective weight functions which regulate the contribution of the radiation emitted at each position of the trajectory to the total spectrum. They contain all the physical complexity that we do not model. For instance, they may account for the presence of particles moving backwards in the region, a

non-constant parallel electric field, or physical differences between different magnetic field lines, among others. In this way, we have found that small scales, i.e. small values of x_0 and $\lambda_{\rm lp.in}$, are required to properly fit spectra. Taking into account that the emission produced at the initial parts of the trajectory is dominated by synchrotron radiation, we conclude that a relevant contribution from synchrotron radiation is in general necessary to produce realistic spectra. However, synchrotron alone is not enough to reproduce all the spectra (and nor is curvature radiation). Indeed, what allows us to match all γ-ray spectra is synchro-curvature radiation, which is flexible enough to resemble the wide variety of spectra available. The radiative model performs equally well with young pulsars and MSPs, which indicates a common magnetospheric structure, i.e. the physical processes occurring in the magnetosphere and producing the high-energy emission are the same regardless of the spatial scale.

For the first time in our group, we have systematically compared synthetic γ-ray light curves, generated using the spectro-geometrical model, with observational ones. For this purpose we have developed two methods: the usage of a reduced (weighted) χ^2 in time domain, i.e. with the regular light curves; and the computation of a simple euclidean distance in frequency domain, i.e. comparing the Fourier transforms of the light curves. In both cases the free parameters are the inclination and viewing angles. Despite their differences, both methods give qualitatively similar results. Best-fitting synthetic light curves visually match observational ones in many of cases, resembling their general features: number of peaks, widths and flux ratios and phase separations in light curves with more than one peak. We also reproduce the bridge emission when present, and we found no difference in performance with young pulsars or MSPs. The model struggles when faced with complex light curves, with many peaks or very asymmetric shapes. The relative simplicity of the actual incarnation cannot reproduce small scale features, but succeeds in reproducing global structures. With both techniques the best-fitting values of the geometrical parameters have a large degeneracy, and thus the particular values should be taken as estimates rather than as strong constraints. The good fits we have found seem to indicate that some of the assumptions we have adopted in our modelling, such as the region being located just outside the light cylinder and having a wavy shape, may be close to the real scenario of pulsars. At the same time, the difficulties to adjust complex and asymmetric light curves imply that the actual incarnation of the model is too simplistic in some aspects, and further modelling is required.

We have searched for correlations between pulsar parameters and found a relevant correlation between the $\log E_{||}$ and $\log x_0$ for the whole sample. We have also found correlations of $\log E_{||}$ and $\log x_0$ with $\log N_0$, but only significant in the sample of MSPs. There is no significant correlation between the *Fermi* PLEC4 model parameters from the 3PC and our model parameters. No correlation of the geometrical parameters with any other parameter or physical quantity is found.

Finally, we have studied the dispersion existing in the observational γ-ray efficiency of pulsars, $\eta_{\rm obs}$. We have parametrised $\eta_{\rm obs}$ in four terms contributing to its dispersion: the geometrical term arising from the anisotropic emission (beaming), viewing and inclination angles, the uncertainty on the pulsar distance, the uncertainty on the moment of inertia, and the intrinsic efficiency of the mechanism producing the γ-ray emission. The efficiency

of the mechanism is found to be the main contributor to the dispersion of $\eta_{\rm obs}$, and we have obtained its distribution, which peaks at $5-10\%$ and has a dispersion of around one order of magnitude. This value agrees with the fraction of Poynting flux dissipation in the equatorial current sheet found in FFE and PIC magnetospheric simulations.

Future work

The effective nature of our models makes them capable of successfully fitting energy spectra and reproducing a relevant number of light curves of high energy pulsars. In the future we want to improve the models, and get rid of some parametrisations and relax some simplifications. The goal is to make them more realistic while keeping the effective approach that allows them to reproduce observational data with the fewest free parameters possible.

First of all, we will try to substitute the two weight functions with more physical ingredients. The first, most promising option is to consider the contribution of particles moving backwards, i.e. towards the star. This is expected to produce an extra contribution from particles with large perpendicular momentum, i.e. emitting synchrotron radiation, which is what the weight functions currently provide to the model. Based on the results of magnetospheric simulations, it is very likely that the parallel electric field is not constant throughout the whole region, and thus we plan to implement an electric field decaying with distance. We will also consider that it varies azimuthally and meridionally, i.e. that the different magnetic field lines within the emission region have a different electric field. In the same direction, we want to refine the treatment of the curvature radius of the lines. The values we currently use in our model, of the order of the light cylinder radius, may be too small for the equatorial current sheet beyond the light cylinder, where magnetic field lines are less curved than inside it. In these two aspects, the variation of the parallel electric field in the region and the curvature radius of the magnetic field lines, we would greatly benefit from having the structure of the electromagnetic fields around the pulsar. For this reason, we plan to work with FFE codes like `ONION` (Carrasco and Reula, 2017). We will inspect the magnetospheric structure produced by this code, and extract some parameters, for instance how the parallel electric field varies in the region and which is the curvature radius of the magnetic field lines. We will then implement these parameters in our model to have more physically motivated ingredients. With these improvements, we should still be able to reproduce the γ-ray spectra of the whole population of high energy pulsars. It is also likely that we enlarge the number of successfully fitted pulsars with both X and γ ray data. We expect that making our models more realistic will have an impact also on the synthetic emission maps, and will provide a major complexity to the synthetic light curves, in such a way that we come closer to reproducing the small scale features of the observational light curves that at the moment we cannot capture.

In parallel to the improvement of the models, we plan to address the modelling of the very-high-energy emission of pulsars. As we have seen in Chapter 1, in the last years pulsated emission in the TeV energy range has been detected for a few pulsars, and the number is expected to grow in time thanks to the new facilities that will start observing at these wavelengths in the near future. We want to perform this modelling with the same effective

approach used to model the X-ray and γ-ray bands. In fact, the population of scattering charged particles will be the same population producing the high-energy emission presented in this thesis, and the scattered photons will be either thermal X-rays from the neutron star surface, CMB photons, or those emitted by the same charged particles, in an emission mechanism known as synchro-curvature self-Compton radiation.

A

Injection of particles

In the radiative and spectro-geometrical models presented in this thesis particles are injected at different locations along the emitting region, which we refer to as injection points $x_{\rm in}$. This represents a physical improvement with respect to previous incarnations of the models (e.g. the systematic fitting in Torres et al. 2019, in which all particles were injected at a single position). In this Appendix we show some convergence tests.

The first test was to prove that the results are not critically relevant for different values of $r_{\rm in}$. That is, if we change $r_{\rm in}$ in a broad range around reasonable values (from say 0.5 to 1.5 R_{lc}), results are not significantly affected, at least for the set of parameters here explored. As an example, Figure A.1 proves this explicitly for some exemplary pulsars, showing how the best-fitting model parameters would change by choosing a different value of $r_{\rm in}$ where all particles are assumed to be injected. Note the similar values of the fit parameters and the fit errors.

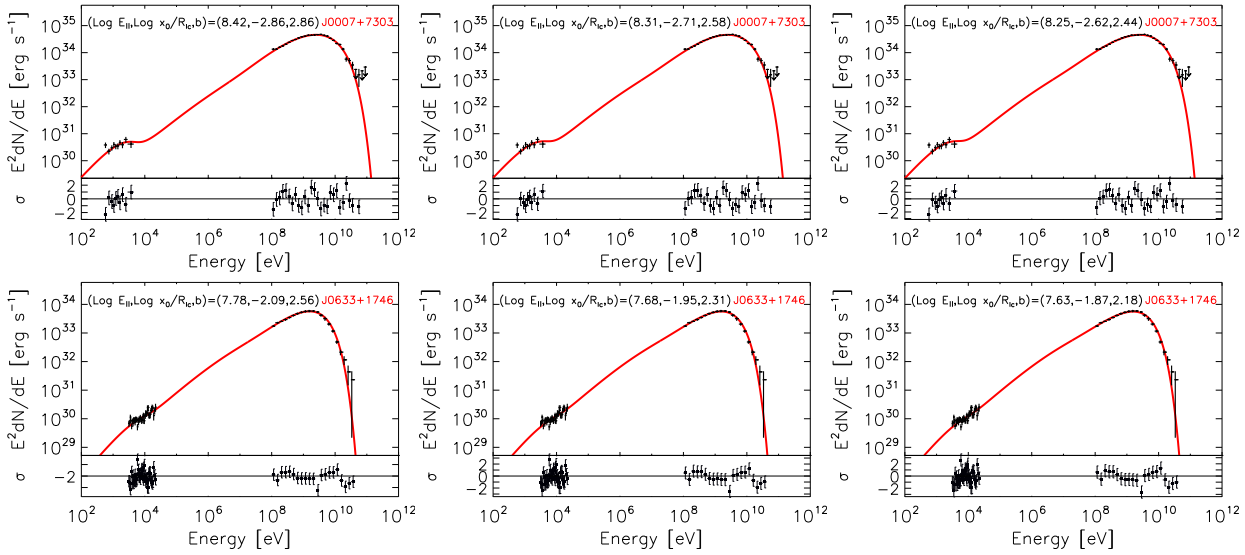


Figure A.1: Plots of the fits of J0007+7303 and J0633+1746 (Geminga) for different values of $r_{\rm in}$. From left to right: $r_{\rm in} = 0.5R_{lc}$ (as in the paper), $1.0R_{lc}$, $1.5R_{lc}$.

Figure A.2 shows how the main properties of the trajectories of particles injected along the

R_{lc} extent changes. In particular, we show the Γ, α, and ξ, for three different pulsars as an example. There is no qualitative difference in the development of these particle properties, when plotted against their relative distance to their injection points.

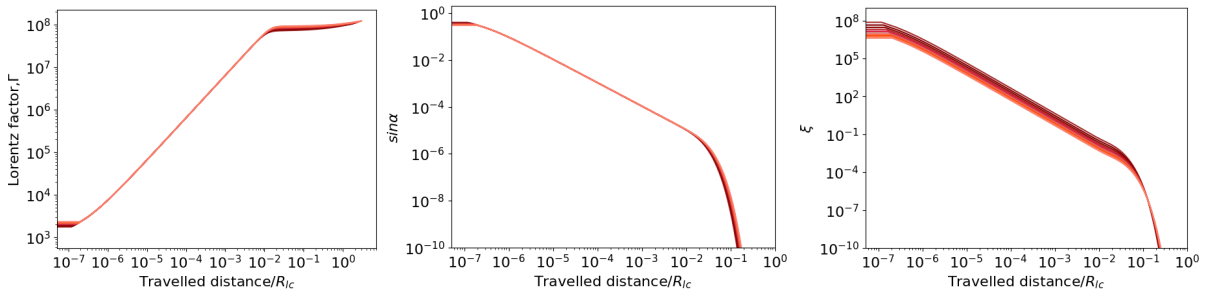


Figure A.2: Examples of the evolution of the main properties of the particle along the trajectories for the different injection points, color coded from dark (closer to the star) to light (farther away). The x-axis represents the relative distance from the corresponding injection point, of which 10 are considered to be evenly distributed from 0.5 to 1.5 R_{lc}.

Figure A.3 shows that, when considering several injection points instead of only one, the values of $E_{||}$ and x_0 are essentially unchanged, whereas the value of b is the average between the values that would be obtained in the two extremes: all particles injected only at the first point and only at the last point. This happens to compensate the distance effect reduction of the magnetic field at injection, so that the local magnetic field is similar in all cases. The magnetic gradient b is smaller, i.e., B is larger, the closer to the star are the injection points. This mimics what happens with millisecond pulsars, for which typically larger magnetic gradients are obtained to accommodate similar local magnetic fields in the accelerating region. In addition, Figure A.4 provides a visual summary, showing how the fitting parameters obtained using a distributed injection along a region of size R_{lc} compare for all the pulsars with X-ray and γ-ray data available.

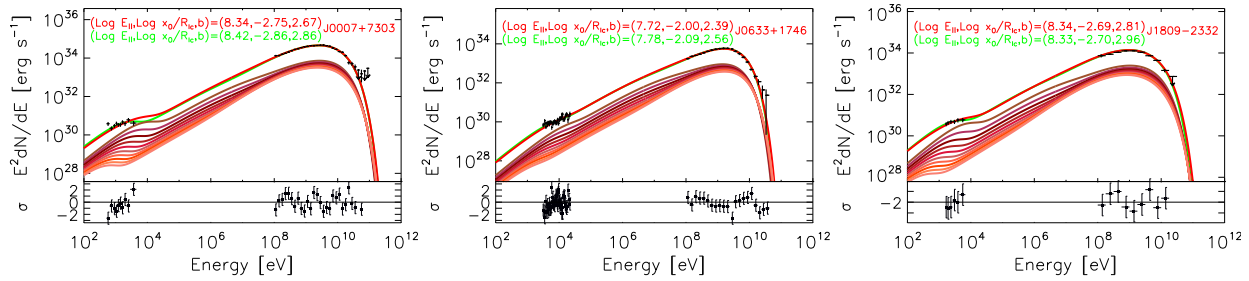


Figure A.3: Examples of the SEDs comparing the results obtained with a single injection point $r_{\rm in} = 0.5R_{lc}$ (green lines), and with 10 injection points evenly distributed from 0.5 to 1.5 R_{lc} (red lines). We also show the contributions of each of the injection points (color coded from dark (closer to the star) to light (farther away). Residuals are those of the SED obtained with 10 injection points evenly distributed from 0.5 to 1.5 R_{lc}.

Particles can thus be assumed to be injected along the whole extent of the acceleration region, of size R_{lc} or larger, and the fit results are essentially unchanged. They tell us, as before, that the values needed for x_0 are small in comparison to R_{lc}.

In order to decide the number of discrete positions at which we inject particles, N_{inj}, and having numerical convergence of the results, we perform fits with $N_{inj} = \{1, 6, 11, 16, 21, 26, 41\}$

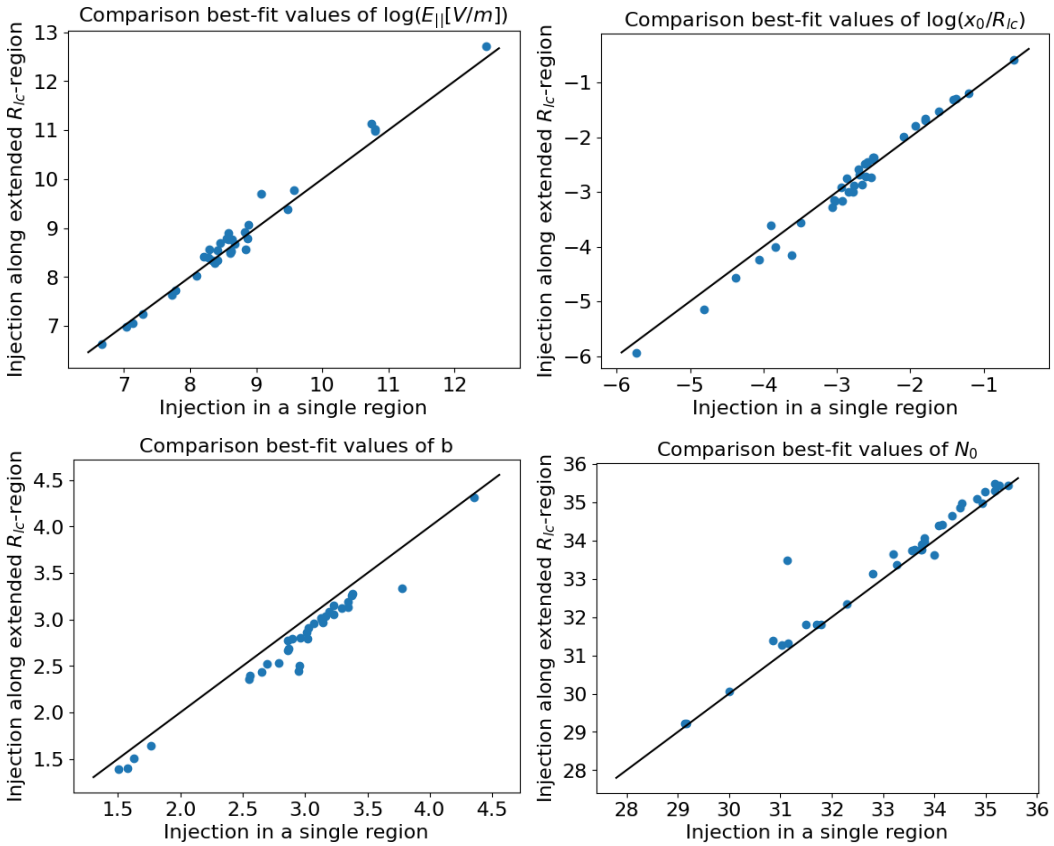


Figure A.4: Comparison between best-fitting parameters using a single injection point and those obtained using a distributed injection With $N_{\rm inj} = 10$ along a region of size R_{lc} for all pulsars with X-ray and γ-ray data available. Black lines represent equal values. The difference in the value of b is and discussed in the text.

and compare the best-fitting parameters for each one. We consider the injection points to be evenly distributed in a range $\Delta R = 0.5 R_{LC}$, i.e. from $1.0 R_{LC}$ to $1.5 R_{LC}$. Table A.1 shows the results of the convergence test realized for the pulsar J0205+6449. From $N_{inj} = 11$, the parameters vary less than a 0.5%, a situation also seen in convergence tests done for other pulsars. Therefore, we fix the number of injection points to 11.

Table A.1: Best-fitting spectral parameters of J0205+6449 for different injection points N_{inj} distributed along a region $\Delta R = 0.5 R_{LC}$.

N_{inj}	$\log E_{\|\|}(\mathrm{Vm}^{-1})$	$\log(x_0/R_{LC})$	b	$\log N_0$	χ^2
1	8.94	−3.06	2.70	33.97	1.59
6	8.98	−3.09	2.62	34.03	1.58
11	8.98	−3.08	2.62	34.02	1.58
16	8.98	−3.08	2.62	34.02	1.58
21	8.98	−3.08	2.62	34.02	1.58
26	8.97	−3.08	2.62	34.02	1.58

We have performed basic convergence tests of the peak statistics as a function of the number of injection points along the region, N_{inj}. While by eye the skymaps look similar, some observers can see different light curves if the region is under-resolved (creating artificial

noisy features). Since we have thousands of light curves, the metric used to evaluate the convergence is the variation of the peak statistics. Table A.2 shows the results, for $\Delta R = 0.5 R_{lc}$. The percentage of observers who see pulsation (detections), and, within them, the 1-peak light curves barely vary. However, for $N_{inj} < 16$, there are significant variations among the percentage of 2, 3 and more peaks. For $N_{inj} \geq 21$, such variations stabilize and become less than the estimated systematic 3% error (see text for details). Therefore, we have chosen $N_{inj} = 21$ injection points, as a compromise between convergence and computational cost.

Table A.2: Statistics for different resolution number of injection points, N_{inj} along a region with $\Delta R = 0.5\ R_{lc}$. As in the main text, we consider about 1530 light curves coming from all the $N_\theta = 51$ observers with different values of Ψ_Ω, $\Delta\Psi_\mu$, 10 and 3, respectively, for the pulsar J0205+6449. We indicated the percentage of detected, and, among them, how many have, 1, 2, 3 or more peaks. The percentages can be associated to a statistical error of $\sim 3\%$ (see main text).

N_{inj}	Detected	1 peak	2 peaks	3 peaks	>3 peaks
6	64.7	13.9	47.3	23.6	15.2
11	63.9	16.0	60.1	14.7	9.2
16	63.1	14.9	64.0	13.6	7.5
21	63.1	14.9	67.7	9.9	7.5
31	63.1	14.9	70.1	7.5	7.5
41	63.1	15.5	68.3	8.7	7.5

B

Details on the Nelder-Mead method

The Nelder-Mead method, or downhill simplex method, is a minimization algorithm proposed by J. A. Nelder and R. Mead in 1965, (Nelder and Mead, 1965). It is used for multidimensional functions and does not involve derivatives of the function, only evaluations.

This method is based on the geometrical figure of a simplex and transformations of it. A simplex is the generalization to n dimensions of a triangle. For n dimensions, it has $n+1$ vertexes, which are points in an n-dimensional space. Several transformations can be done to this object: reflection (of a point with respect to the opposite face), reflection and expansion (reflect a point and move it further away), contraction (moving a point closer to the opposite face) and multiple contraction (contraction of all the points towards one). Figure B.1 graphically shows these transformations.

The Nelder-Mead method considers the n coordinates of each vertex as the parameters of the function to minimize, and the function is evaluated to each one of these points, so that, for an n-dimensional simplex, we have a set of $n+1$ function evaluations. These evaluations allow us to classify the vertexes based on the value of its function evaluation. We define three points, the highest point (the point with the highest function evaluation), the next-to-highest point (the point with the second highest function evaluation) and the lowest point (the point with the lower function evaluation)

An initial simplex has to be defined to start the procedure. This is done by defining an initial point, which can be expressed as a vector $\vec{p_0}$ in the n-dimensional space of model parameters. The other n points are built from this initial point, by means of n unit vectors $\hat{e_i}$ and a characteristic lengthscale λ. Thus, the i-th point is $\vec{p_i} = \vec{p_0} + \lambda \cdot \hat{e_i}$, where $i = 1, \ldots, n$. The value of $\vec{p_0}$ and λ can be chosen arbitrarily, depending on the needs of the problem that is being addressed.

Once the initial simplex is defined, a number of steps are taken, and the before-mentioned transformations are applied to the simplex at each step. A loop is started, finishing when a termination criterion is fulfilled. At the beginning of each iteration, the highest, next-to-

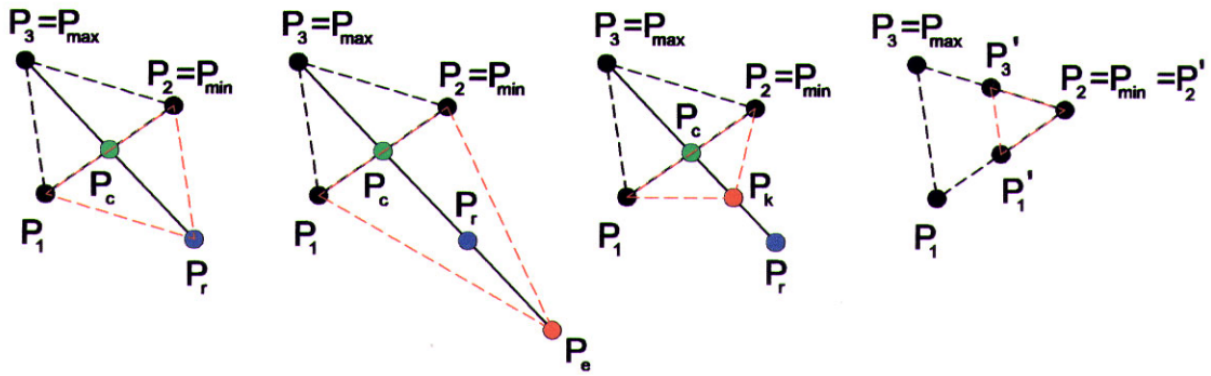


Figure B.1: Transformations that can be applied to a simplex in a space of n=2 parameters. Each figure corresponds to one different transformation. $P_{1,2,3}$ are the three vertexes of the simplex, P_{min} and P_{max} are the lowest and highest points, respectively (see below), P_r is the highest point reflected with respect to P_c, the central point of the face opposite to the highest point, P_k is the highest point reflected and contracted, P_e is the highest point reflected and expanded, and $P'_{1,2,3}$ are the vertexes of the simplex after a multiple contraction. From left to right: (upper row) reflection - reflection and expansion; (lower row) contraction - multiple contraction. Image taken from Rudolf (2006).

highest and lowest points of the simplex are identified. At this point, a series of transformations of the simplex are done, and the function evaluation of the new points arising from these transformations are compared to the evaluations of the points of the original simplex. The first transformation is a reflection of the highest point. If the new evaluation is smaller than the old ones, the new point is kept, that is, we keep the transformation applied on the simplex. This transformed simplex is the initial simplex of the next iteration. In case the new evaluation is larger than the previous ones, a contraction of the highest point is done. Again, if the function evaluation of the new point resulting from this transformation is smaller, the transformation is maintained on the simplex and a new iteration starts. On the other hand, if the evaluation is larger, a multiple contraction towards the lowest point is performed on the original simplex. After this, rather radical, transformation, the iteration finishes and a new one starts, with either the simplex untransformed or with the multiple-contracted simplex, depending on whether the transformation has provided larger or smaller function evaluations, respectively.

This can be graphically seen in Figure B.2, which shows the simplex movement through a given two-dimensional function to be minimized.

A termination criterion has to be defined in order to stop the algorithm. One way to do so is to require a minimum variation of the function in the simplex, that is, that the values of the function evaluations of the vertexes of the simplex have a minimum distance. Concretely, we use the criterion stated in Press et al. (1992), where, if the fractional distance between the value of the function evaluated at the highest and the lowest points is smaller than some given tolerance, the algorithm finishes. A small tolerance assures that the minimum found is a good one, but increases the number of steps required to achieved it and thus increases the computational time. On the other hand, a larger one is easily achieved and thus less steps and less computational time are needed, but decreases the confidence in that the minimum

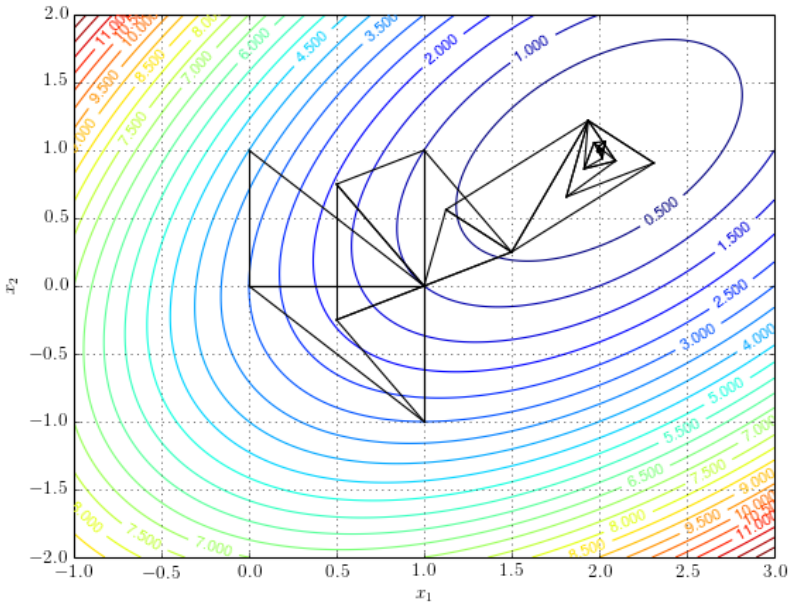


Figure B.2: Evolution of a simplex in the function to minimize as a function of the model parameters. The simplex at each step is a black triangle, and shown are the simplexes for all the steps until the minimum is reached. Subsequent simplexes share one of the edges. Image taken from http://www.jakubkonka.com/2013/10/22/nelder-mead-simplex.html.

found is a really good one.

Notice that this method does not assure that we have found a global minimum. When the algorithm is stopped (because the termination criterion has been fulfilled), we could have -in principle- found a local minimum, and the algorithm could not be able to take the simplex out of the local minimum and it gets stuck in there. There is no way to distinguish if we have found a global or a local minimum. A good way to test whether we have found a good point (a global or a local minimum close to being global) is to repeat the procedure with different initial simplexes. When the minimum is obtained, it is also good practice to perform a few iterations more with the minimum found as the initial point $\vec{p_0}$, in order to be sure that we are in a minimum, and that there has been no errors in the algorithm's performance.

C

Observed γ-ray spectra in the Second and Third Fermi Pulsar Catalogues

As mentioned in the text, the spectral data presented in the 3PC for some pulsars differs from the data previously available (either in the 2PC or in dedicated studies), in shape but also in quality. In many cases one of the two sets of spectral data is clearly preferable than the other, for example because one of the two has more data points or smaller errors. However, in some cases it is not as clear, since both data sets have a very similar shape and quality. In these cases we take the data set with more continuous data points. Fig C.1 shows the compared spectra of all pulsars for which data from both options is available. These plots helps us to decide which data set use in the spectral fitting, following the quality-based criterion explained in Chapter 5.

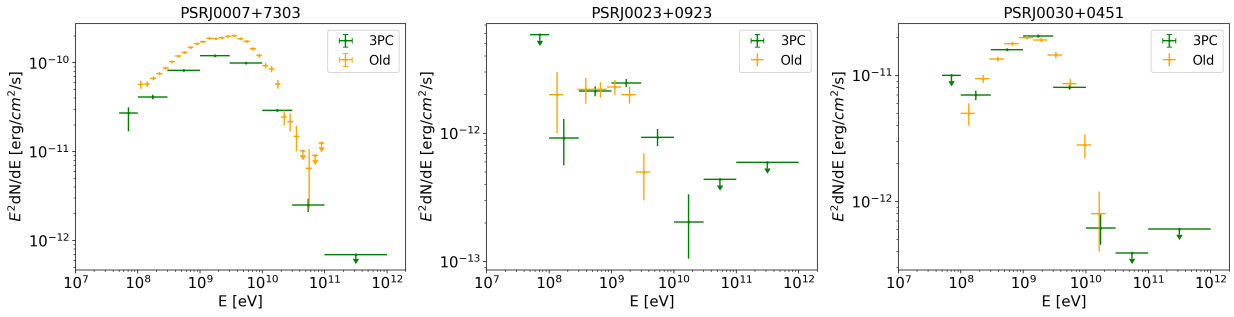


Figure C.1: Comparison of spectral data from the 2PC or dedicated studies prior to the 3PC (in orange, labelled as Old for clarity) and from the 3PC (in green).

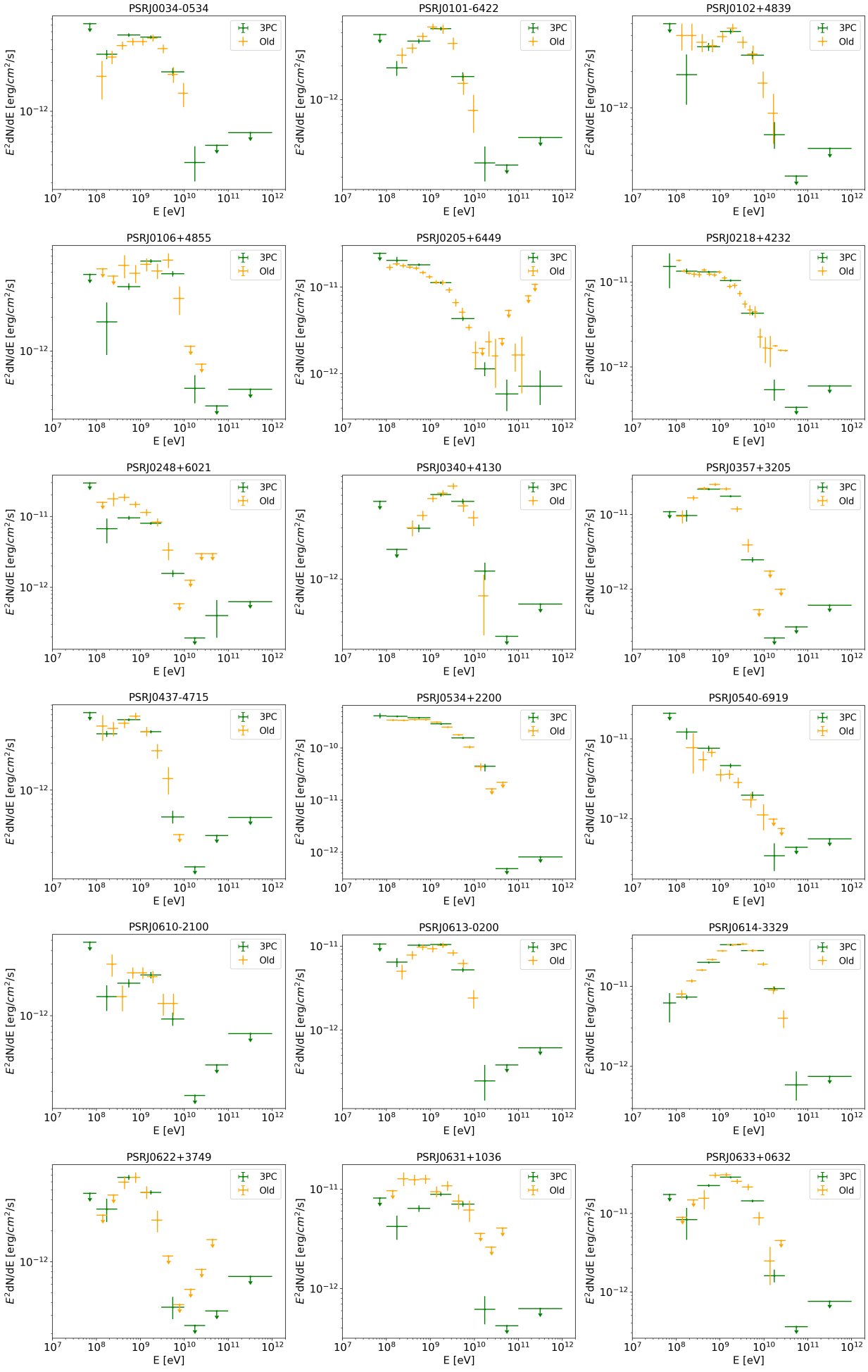


Figure C.1: - *continued*

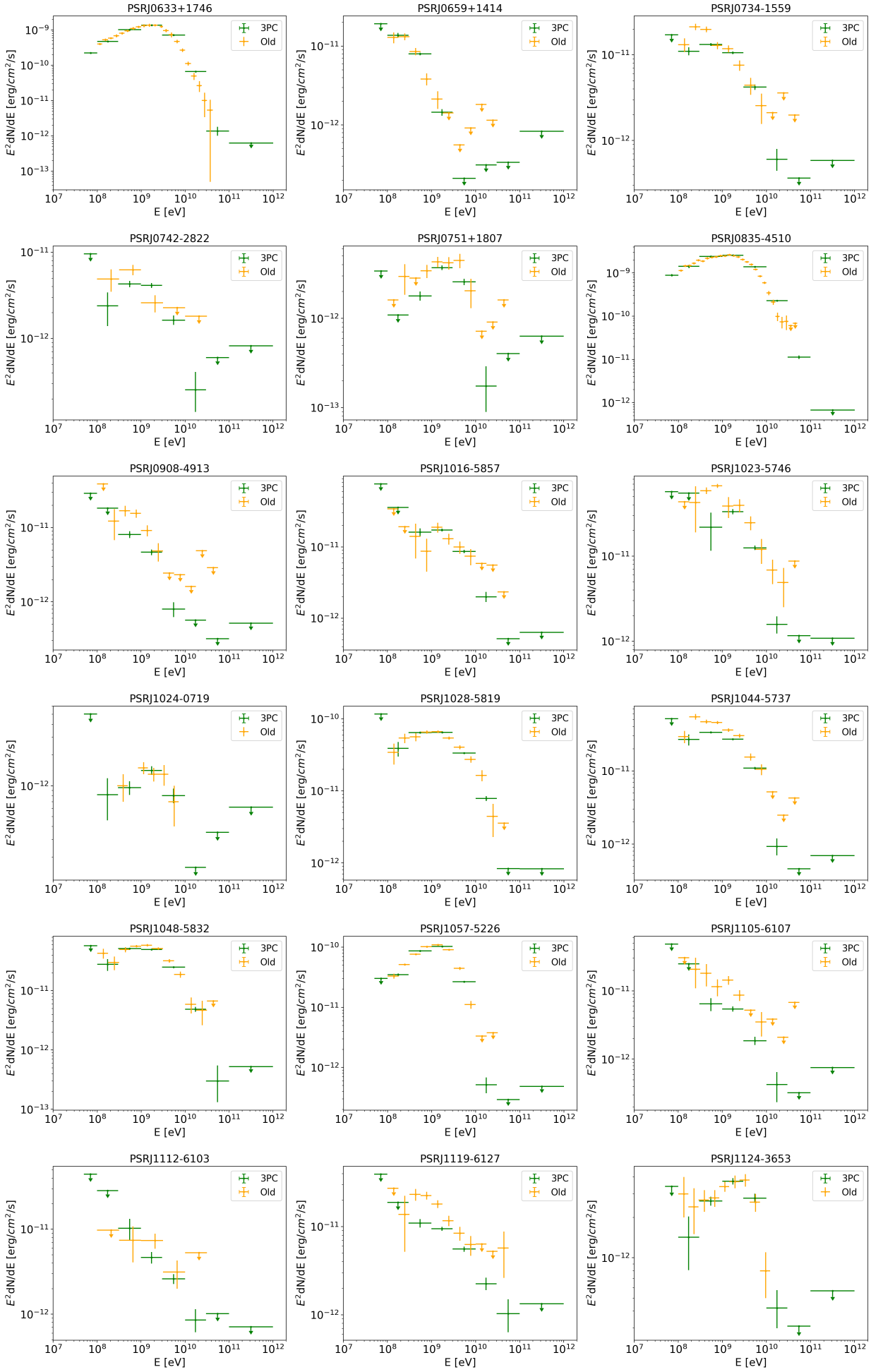


Figure C.1: - *continued*

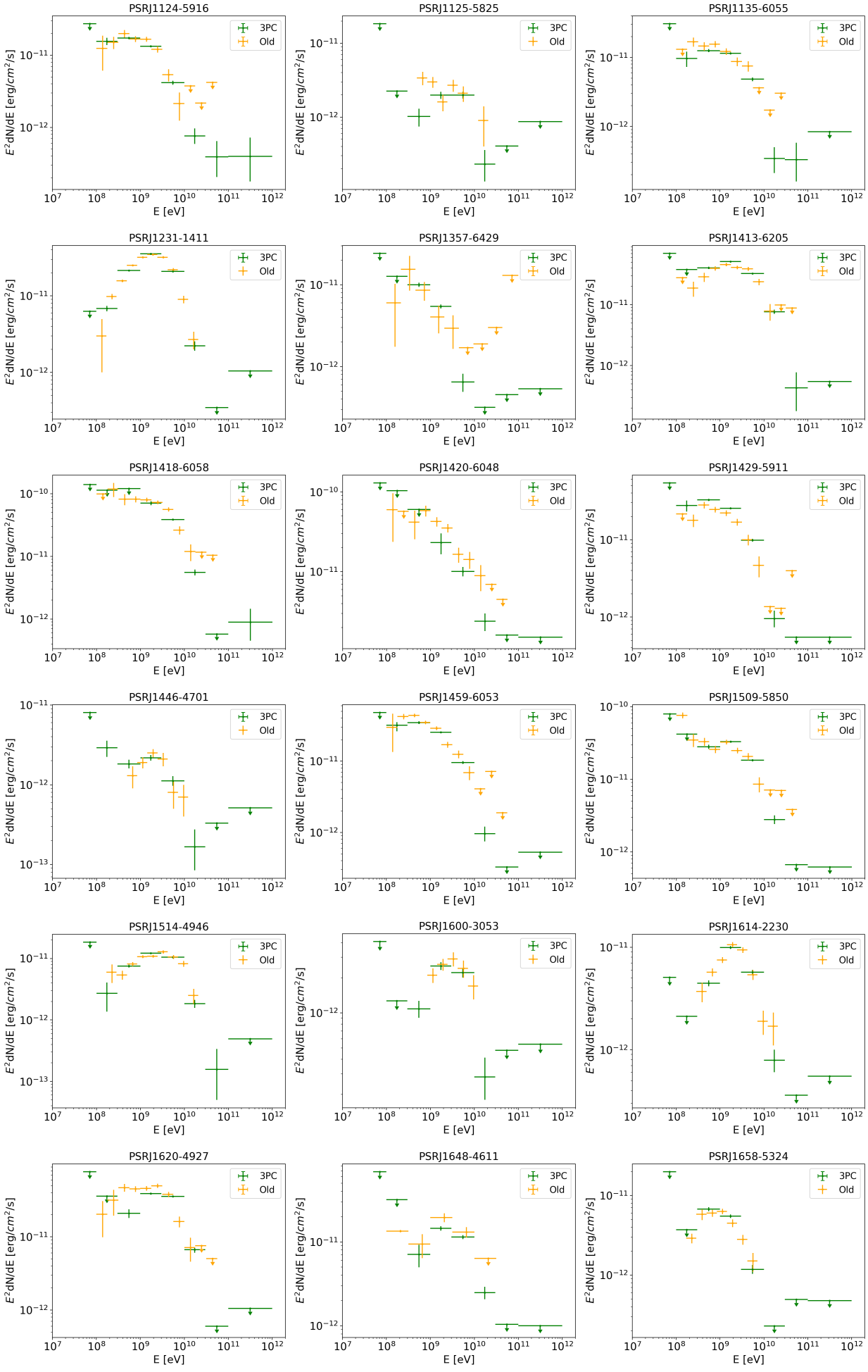


Figure C.1: - *continued*

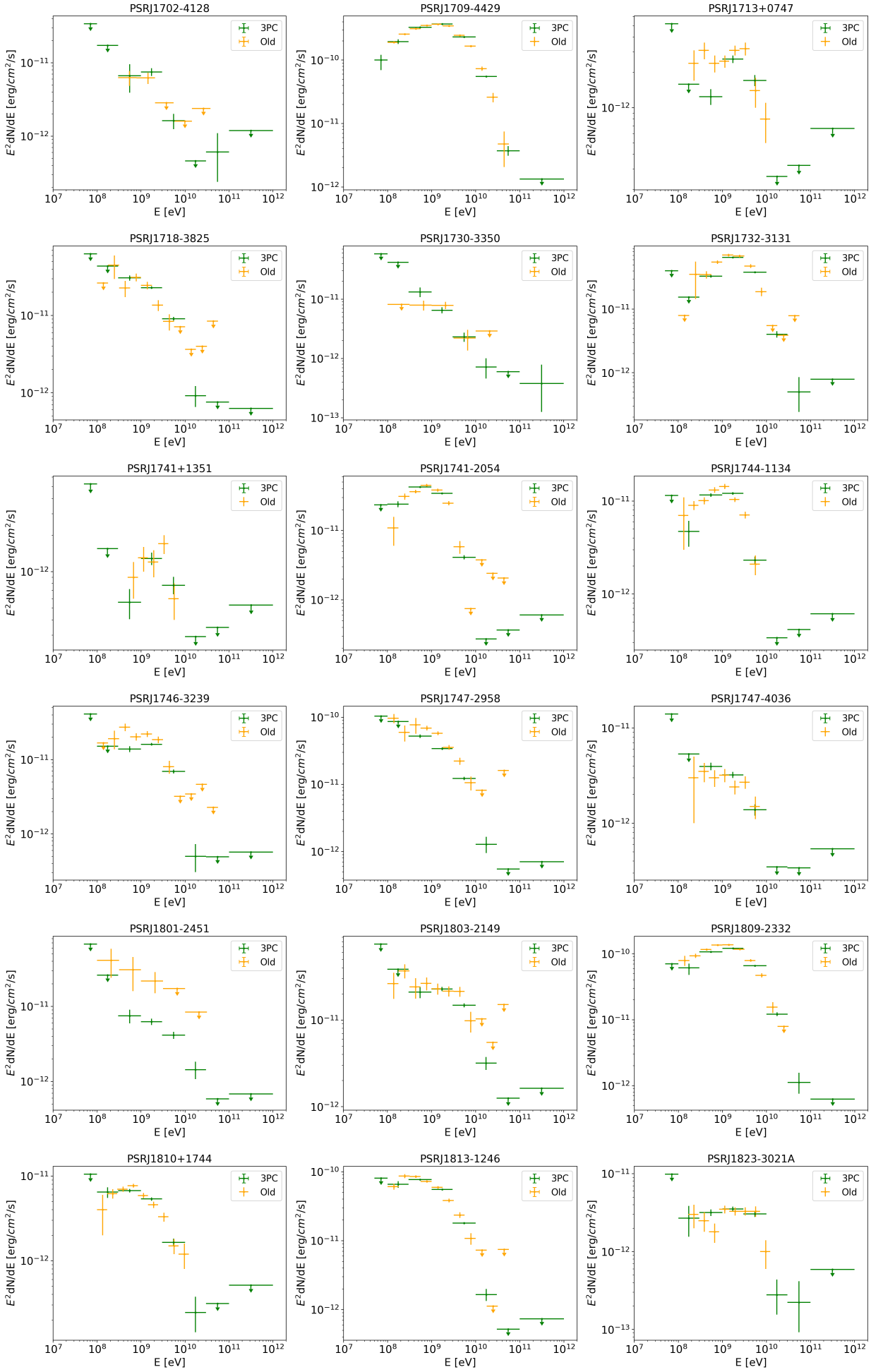


Figure C.1: - *continued*

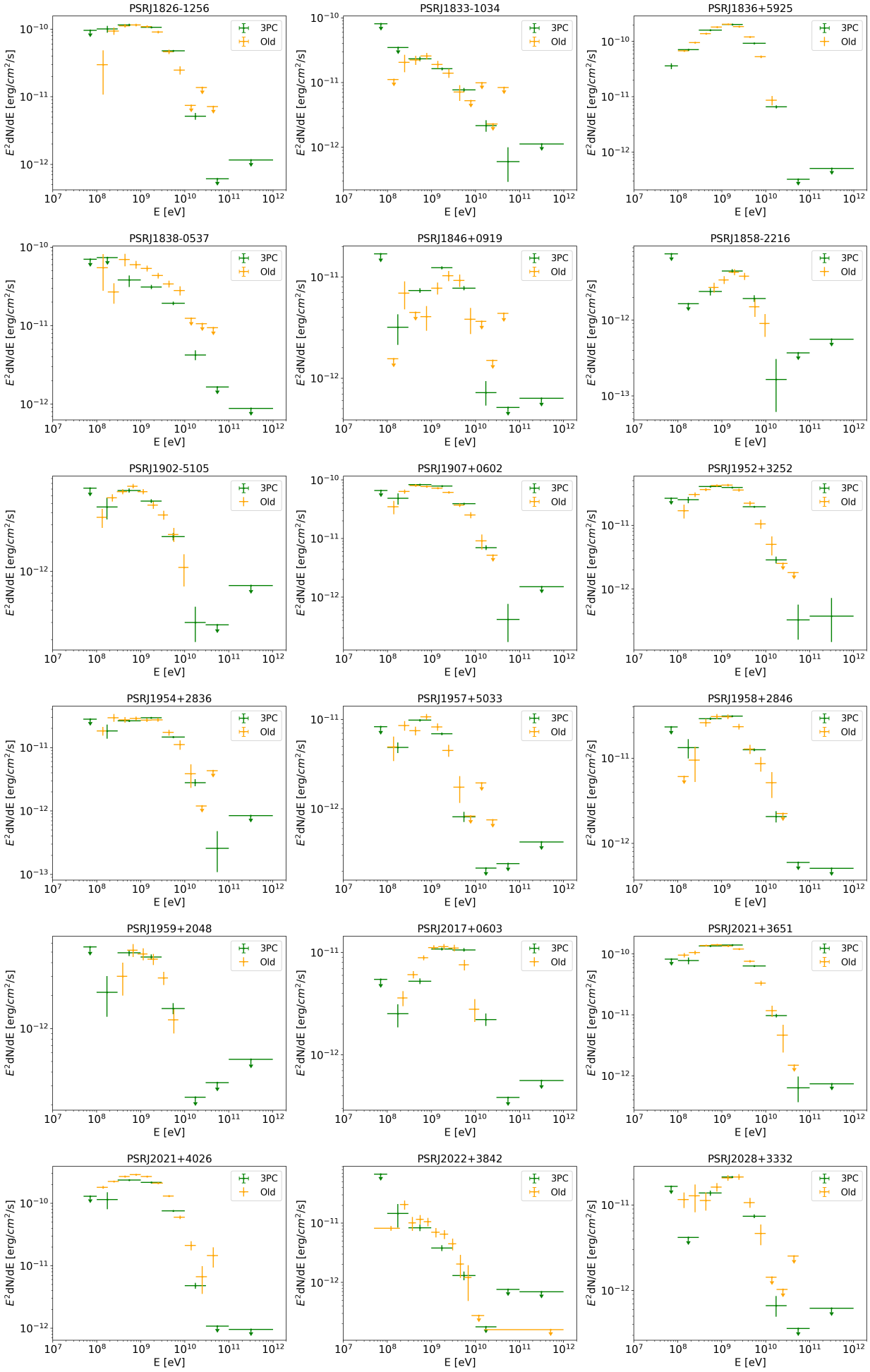


Figure C.1: - *continued*

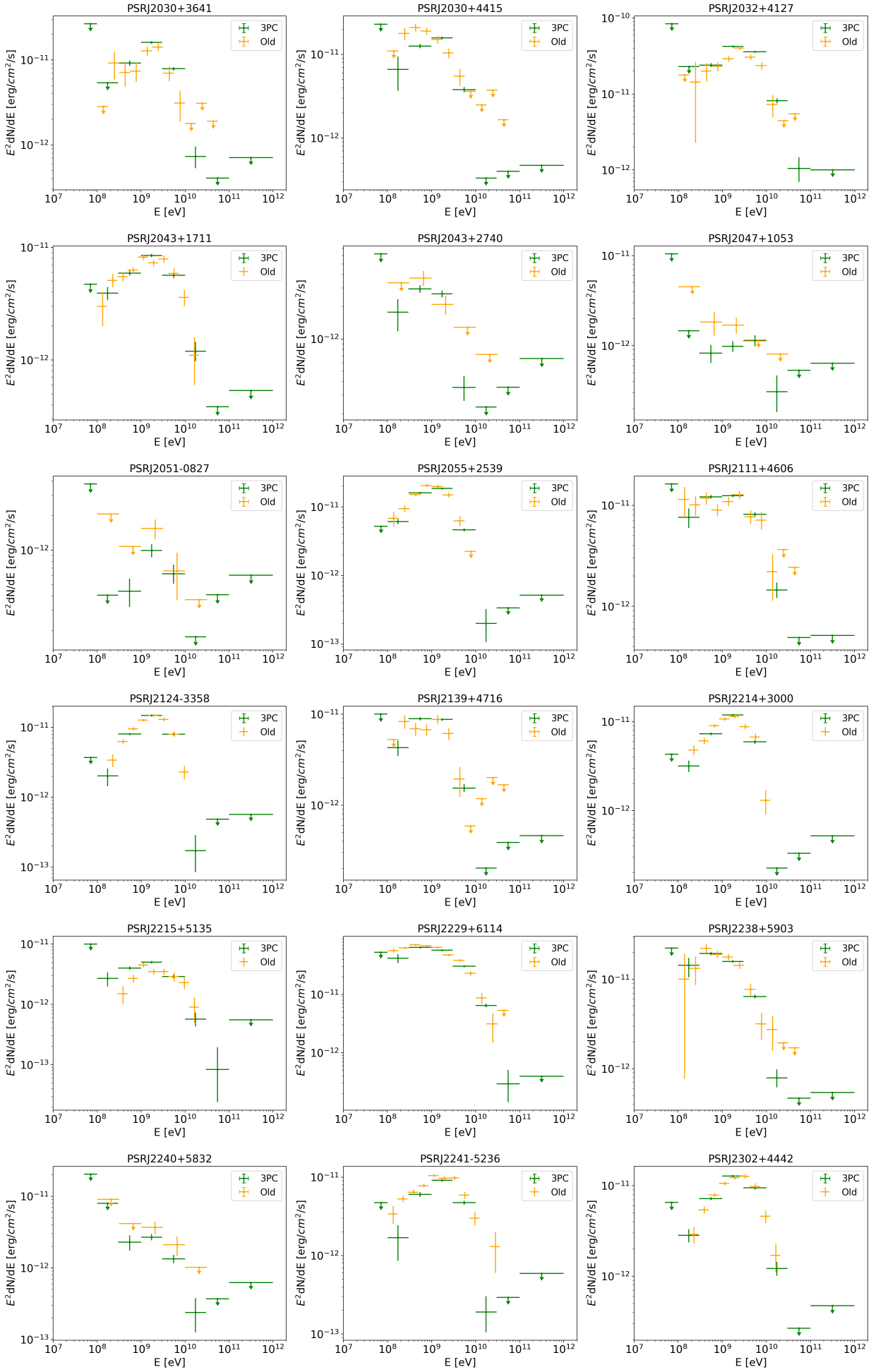


Figure C.1: - *continued*

D

Timing and best-fitting spectral and geometrical parameters of the whole sample of pulsars studied

Table D.1 shows the timing parameters of all the high-energy pulsars considered in this thesis, together with the best-fitting spectral and geometrical parameters obtained in Chapter 5.

Table D.1: Timing and best-fitting spectral and geometrical parameters (for fits in both time and frequency domain) of the pulsars on the 3PC. Last column indicates the reference from where we have obtained the spectral data of that pulsar. Pulsars with a magnetic gradient b value of 2.5 without errors are those with only γ-ray data, in which case b is fixed to 2.5. Notice that, due to the degeneracy between the geometrical parameters and the difficulty of defining an error of the parameters, pointed out in the text and shown in Figure 5.8, the values of Ψ_Ω and θ_{obs} shown here are not strong constraints. Pulsars with no values of the spectral parameters are those that do not fulfill the spectral data quality criterion (for these pulsars we left the reference slot as an ellipsis). Pulsars with no values of the geometrical parameters are those whose observational light curve has less than 50 bins. The last column indicates the sources of the spectral data used for the spectral fitting. The full light curve fitting is done with data from the 3PC.

Pulsar	P	$\log\dot{P}$	$\log E_\parallel$	$\log(x_0/R_{lc})$	b	$\log N_0$	Time domain		Frequency domain		Reference
	[ms]	[s/s]	[V/m]				$\psi_\Omega[^\circ]$	$\lvert\theta_{obs}\rvert[^\circ]$	$\psi_\Omega[^\circ]$	$\lvert\theta_{obs}\rvert[^\circ]$	spectral data
J0002+6216	115.4	−14.22	...	...	...	...	81	46	75	35	...
J0007+7303	315.9	−12.45	$8.3^{+0.01}_{-0.01}$	$-2.67^{+0.01}_{-0.01}$	$2.49^{+0.02}_{-0.02}$	33.95	21	14	21	14	Li et al. (2016)
J0023+0923	3.1	−19.96	$8.13^{+0.08}_{-0.08}$	$-0.94^{+0.32}_{-0.2}$	2.5	30.76	24	11	57	35	Xing and Wang (2016)
J0030+0451	4.9	−19.99	$8.62^{+0.02}_{-0.02}$	$-1.77^{+0.03}_{-0.03}$	2.5	30.94	81	49	81	18	Xing and Wang (2016)
J0034-0534	1.9	−20.3	$9.41^{+0.05}_{-0.05}$	$-2.43^{+0.05}_{-0.05}$	2.5	32.6	15	7	69	53	Xing and Wang (2016)
J0101-6422	2.6	−20.32	$8.75^{+0.05}_{-0.05}$	$-1.7^{+0.08}_{-0.07}$	2.5	31.2	18	4	87	49	Xing and Wang (2016)
J0102+4839	3.0	−19.93	$10.16^{+0.03}_{-0.03}$	$-3.33^{+0.03}_{-0.04}$	2.5	34.43	24	4	27	4	Xing and Wang (2016)
J0106+4855	83.2	−15.37	$7.89^{+0.04}_{-0.04}$	$-1.67^{+0.08}_{-0.07}$	2.5	32.02	33	35	57	4	3PC
J0205+6449	65.7	−12.72	$8.17^{+0.01}_{-0.01}$	$-2.13^{+0.01}_{-0.01}$	$2.08^{+0.01}_{-0.01}$	32.79	51	4	48	4	Li et al. (2018b)
J0218+4232	2.3	−19.11	$9.21^{+0.02}_{-0.02}$	$-2.3^{+0.02}_{-0.02}$	$2.2^{+0.06}_{-0.06}$	33.36	6	4	84	81	Acciari et al. (2021)
J0248+4230	2.6	−19.77	...	...	...	...	18	4	60	28	...
J0251+2606	2.5	−20.12	...	...	...	...	39	4	45	4	...
J0307+7443	3.2	−19.77	$8.5^{+0.04}_{-0.04}$	$-1.18^{+0.11}_{-0.09}$	2.5	29.76	9	7	48	46	3PC
J0312-0921	3.7	−19.71	...	...	...	...	66	49	54	32	...
J0318+0253	5.2	−19.75	...	...	...	...	45	42	45	35	...
J0340+4130	3.3	−20.23	$9.0^{+0.04}_{-0.04}$	$-1.87^{+0.07}_{-0.07}$	2.5	31.62	27	14	57	28	Xing and Wang (2016)
J0357+3205	444.1	−13.88	$6.74^{+0.04}_{-0.04}$	$-1.01^{+0.06}_{-0.05}$	$1.47^{+0.16}_{-0.15}$	33.02	81	71	75	74	2PC
J0359+5414	79.4	−13.78	...	...	...	...	9	14	75	78	...
J0418+6635	2.9	−19.86	$9.12^{+0.05}_{-0.04}$	$-2.14^{+0.07}_{-0.06}$	2.5	32.14	18	7	21	7	3PC
J0437-4715	5.8	−19.24	$10.14^{+0.01}_{-0.01}$	$-3.66^{+0.01}_{-0.01}$	$2.36^{+0.02}_{-0.02}$	33.09	15	18	15	18	Xing and Wang (2016)
J0514-4408	320.3	−14.69	...	...	...	...	18	18	87	49	...

Table D.1: - *continued*

Pulsar	P [ms]	$\log\dot{P}$ [s/s]	$\log E_{\parallel}$ [V/m]	$\log(x_0/R_{lc})$	b	$\log N_0$	Time domain $\psi_\Omega[^\circ]$	Time domain $\lvert\theta_{obs}\rvert[^\circ]$	Frequency domain $\psi_\Omega[^\circ]$	Frequency domain $\lvert\theta_{obs}\rvert[^\circ]$	Reference spectral data
J0533+6759	4.4	−19.9	$8.93^{+0.05}_{-0.05}$	$-1.97^{+0.08}_{-0.07}$	2.5	31.84	57	0	57	0	3PC
J0554+3107	465.0	−12.84	...	...	...	...	90	71	78	64	...
J0605+3757	2.7	−20.33	...	...	...	...	15	4	15	7	...
J0610-2100	3.9	−19.91	$9.36^{+0.05}_{-0.05}$	$-2.64^{+0.06}_{-0.05}$	2.5	33.05	90	81	36	4	Xing and Wang (2016)
J0613-0200	3.1	−20.02	$9.12^{+0.04}_{-0.04}$	$-2.22^{+0.05}_{-0.05}$	2.5	32.01	12	14	12	14	Xing and Wang (2016)
J0614-3329	3.2	−19.75	$10.9^{+0.01}_{-0.01}$	$-4.01^{+0.01}_{-0.01}$	$3.92^{+0.02}_{-0.02}$	36.83	33	4	33	4	Xing and Wang (2016)
J0621+2514	2.7	−19.6	...	...	...	...	87	56	84	46	...
J0622+3749	333.2	−13.6	...	...	...	...	6	4	15	7	...
J0631+0646	111.0	−14.44	...	...	...	...	81	74	84	67	...
J0633+0632	297.4	−13.1	$7.66^{+0.03}_{-0.03}$	$-2.06^{+0.05}_{-0.04}$	2.5	34.52	18	25	51	4	2PC
J0633+1746	237.1	−13.96	$7.66^{+0.01}_{-0.01}$	$-1.92^{+0.01}_{-0.01}$	$2.25^{+0.01}_{-0.01}$	32.35	90	71	54	0	Abdo et al. (2010b)
J0659+1414	384.9	−13.26	$6.34^{+0.02}_{-0.02}$	$-1.06^{+0.02}_{-0.02}$	$1.58^{+0.12}_{-0.14}$	30.7	6	14	3	4	2PC
J0729-1448	251.7	−12.95	...	...	...	...	42	46	90	35	...
J0734-1559	155.1	−13.9	$8.35^{+0.01}_{-0.01}$	$-2.78^{+0.01}_{-0.01}$	2.5	35.28	6	7	81	81	3PC
J0740+6620	2.9	−19.91	...	...	...	...	51	0	39	7	...
J0742-2822	166.8	−13.78	$7.95^{+0.01}_{-0.01}$	$-2.32^{+0.01}_{-0.01}$	2.5	32.8	30	32	87	35	2PC
J0744-2525	92.0	−15.03	...	...	...	...	90	46	63	4	...
J0751+1807	3.5	−20.11	$10.84^{+0.03}_{-0.03}$	$-4.02^{+0.02}_{-0.02}$	$3.57^{+0.04}_{-0.04}$	36.54	24	18	24	18	Xing and Wang (2016)
J0802-5613	274.0	−14.56	...	...	...	...	69	64	54	46	...
J0835-4510	89.4	−12.91	$8.22^{+0.01}_{-0.01}$	$-2.35^{+0.01}_{-0.01}$	$2.86^{+0.02}_{-0.02}$	33.73	75	32	75	32	Abdo et al. (2010c)
J0908-4913	106.8	−13.82	$7.13^{+0.1}_{-0.1}$	$-1.32^{+0.19}_{-0.14}$	2.5	31.96	60	4	54	7	2PC
J0931-1902	4.6	−20.44	...	...	...	...	6	7	51	39	...
J0940-5428	87.6	−13.48	...	...	...	...	30	25	63	56	...
J0952-0607	1.4	−20.32	...	...	...	...	21	14	54	42	...
J0955-6150	2.0	−19.84	...	...	...	...	87	56	87	56	...
J1012-4235	3.1	−20.18	...	...	...	...	57	0	63	4	...
J1016-5857	107.4	−13.09	$8.5^{+0.08}_{-0.07}$	$-2.65^{+0.09}_{-0.07}$	2.5	33.67	84	53	81	46	2PC
J1019-5749	162.5	−13.7	...	...	...	...	9	14	48	49	...

Table D.1: - *continued*

Pulsar	P [ms]	$\log\dot{P}$ [s/s]	$\log E_{\parallel}$ [V/m]	$\log(x_0/R_{lc})$	b	$\log N_0$	Time domain		Frequency domain		Reference spectral data
							$\psi_\Omega[^\circ]$	$\lvert\theta_{obs}\rvert[^\circ]$	$\psi_\Omega[^\circ]$	$\lvert\theta_{obs}\rvert[^\circ]$	
J1023+0038	1.7	−20.17	$9.90^{+0.02}_{-0.03}$	$-3.08^{+0.02}_{-0.03}$	2.50	34.48	...	...	...	...	3PC
J1024-0719	5.2	−19.73	$8.85^{+0.14}_{-0.13}$	$-2.09^{+0.19}_{-0.14}$	2.5	31.39	15	11	24	14	Xing and Wang (2016)
J1028-5819	91.4	−13.85	$8.91^{+0.03}_{-0.03}$	$-3.1^{+0.03}_{-0.03}$	2.5	34.31	39	4	42	4	2PC
J1035-6720	2.9	−19.33	...	...	...	...	15	14	48	49	...
J1036-8317	3.4	−19.51	...	...	...	...	3	4	12	0	...
J1044-5737	139.0	−13.26	$8.69^{+0.02}_{-0.02}$	$-3.09^{+0.02}_{-0.02}$	2.5	36.15	33	14	33	14	2PC
J1048+2339	4.7	−19.52	...	...	...	...	48	53	45	0	...
J1048-5832	123.7	−13.02	$8.07^{+0.02}_{-0.02}$	$-2.26^{+0.02}_{-0.02}$	2.5	33.88	72	32	42	11	2PC
J1055-6028	99.7	−11.96	...	...	...	...	9	7	84	85	...
J1057-5226	197.1	−14.23	$7.23^{+0.02}_{-0.02}$	$-1.18^{+0.02}_{-0.02}$	$1.22^{+0.01}_{-0.01}$	31.02	81	67	78	74	2PC
J1057-5851	620.4	−13.0	...	...	...	...	90	67	15	4	...
J1105-6037	194.9	−13.66	...	...	...	...	18	7	21	11	...
J1105-6107	63.2	−13.8	$8.89^{+0.09}_{-0.09}$	$-3.02^{+0.1}_{-0.09}$	2.5	34.01	51	0	48	0	2PC
J1111-6039	106.7	−12.71	...	...	...	...	87	81	87	81	...
J1112-6103	65.0	−13.5	...	...	...	...	30	4	33	4	...
J1119-6127	409.1	−11.39	$8.92^{+0.04}_{-0.04}$	$-3.63^{+0.04}_{-0.04}$	2.5	35.99	9	11	30	25	2PC
J1124-3653	2.4	−20.24	$9.07^{+0.04}_{-0.04}$	$-2.02^{+0.06}_{-0.06}$	2.5	31.41	66	35	87	53	Xing and Wang (2016)
J1124-5916	135.5	−12.12	$9.61^{+0.01}_{-0.01}$	$-4.06^{+0.01}_{-0.01}$	$2.88^{+0.01}_{-0.01}$	36.32	48	0	45	0	2PC
J1125-5825	3.1	−19.22	...	...	...	...	81	49	66	32	...
J1135-6055	114.5	−13.11	$7.9^{+0.02}_{-0.02}$	$-2.09^{+0.03}_{-0.03}$	2.5	34.44	9	7	78	74	3PC
J1139-6247	120.5	−14.39	...	...	...	...	27	21	27	21	...
J1142+0119	5.1	−19.82	$8.86^{+0.08}_{-0.07}$	$-1.85^{+0.14}_{-0.11}$	2.5	31.37	84	74	72	60	3PC
J1151-6108	101.6	−13.99	...	...	...	...	81	53	87	39	...
J1203-6242	100.6	−13.35	...	...	...	...	36	4	39	4	...
J1207-5050	4.8	−20.22	...	...	...	...	3	4	57	0	...
J1208-6238	440.7	−11.48	...	...	...	...	42	4	42	4	...
J1221-0633	1.9	−19.96	$9.2^{+0.06}_{-0.06}$	$-2.16^{+0.08}_{-0.07}$	2.5	31.58	72	71	45	42	3PC
J1227-4853	1.7	−19.88	$10.13^{+0.04}_{-0.04}$	$-3.18^{+0.04}_{-0.04}$	2.5	34.32	6	4	42	32	3PC

Table D.1: - *continued*

Pulsar	P	$\log\dot{P}$	$\log E_{\parallel}$	$\log(x_0/R_{lc})$	b	$\log N_0$	Time domain		Frequency domain		Reference
	[ms]	[s/s]	[V/m]				$\psi_\Omega[^\circ]$	$\lvert\theta_{obs}\rvert[^\circ]$	$\psi_\Omega[^\circ]$	$\lvert\theta_{obs}\rvert[^\circ]$	spectral data
J1231-1411	3.7	−19.67	$8.79^{+0.02}_{-0.02}$	$-1.67^{+0.03}_{-0.02}$	$2.03^{+0.12}_{-0.09}$	30.99	81	53	72	21	Xing and Wang (2016)
J1231-5113	206.6	−15.94	...	...	...	...	36	0	30	0	...
J1231-6511	247.5	−13.55	...	...	...	...	3	11	78	67	...
J1301+0833	1.8	−19.98	...	...	...	...	87	78	87	71	...
J1302-3258	3.8	−20.18	...	...	...	...	90	71	81	71	...
J1311-3430	2.6	−19.68	$9.66^{+0.01}_{-0.01}$	$-2.83^{+0.02}_{-0.02}$	2.5	33.88	18	7	69	42	3PC
J1312+0051	4.2	−19.77	$8.52^{+0.05}_{-0.05}$	$-1.55^{+0.09}_{-0.08}$	2.5	31.37	21	11	45	46	3PC
J1335-5656	3.2	−19.9	...	...	...	...	45	35	54	42	...
J1350-6225	138.2	−14.05	...	...	...	...	42	0	54	0	...
J1341-6220	193.4	−12.60	$10.65^{+0.07}_{-0.07}$	$-5.06^{+0.07}_{-0.07}$	2.50	36.59	...	...	...	...	3PC
J1357-6429	166.2	−12.45	$8.42^{+0.03}_{-0.04}$	$-3.0^{+0.03}_{-0.03}$	$2.76^{+0.04}_{-0.05}$	34.71	3	7	81	81	Lemoine-Goumard et al. (2011)
J1358-6025	60.5	−14.52	...	...	...	...	21	11	78	67	...
J1400-1431	3.1	−20.14	...	...	...	...	78	78	78	78	...
J1410-6132	50.1	−13.5	...	...	...	...	12	0	90	74	...
J1413-6205	109.7	−13.56	$8.15^{+0.04}_{-0.04}$	$-2.22^{+0.05}_{-0.05}$	2.5	35.15	69	46	69	42	2PC
J1418-6058	110.6	−12.77	$8.3^{+0.04}_{-0.04}$	$-2.46^{+0.05}_{-0.04}$	2.5	33.62	87	56	24	4	2PC
J1420-6048	68.2	−13.08	$8.68^{+0.04}_{-0.04}$	$-2.65^{+0.04}_{-0.04}$	$2.28^{+0.1}_{-0.08}$	33.97	24	14	72	60	2PC
J1422-6138	341.0	−13.01	...	...	...	...	24	14	21	11	...
J1429-5911	115.8	−13.62	$8.05^{+0.04}_{-0.04}$	$-2.33^{+0.04}_{-0.04}$	2.5	35.44	33	4	27	4	2PC
J1431-4715	2.0	−19.85	$9.31^{+0.04}_{-0.04}$	$-2.34^{+0.03}_{-0.04}$	$1.24^{+0.23}_{-0.16}$	31.93	...	...	...	...	3PC
J1446-4701	2.2	−20.01	$8.57^{+0.11}_{-0.11}$	$-0.51^{+1.5}_{-0.57}$	2.5	30.03	63	56	54	35	Xing and Wang (2016)
J1447-5757	158.7	−13.93	...	...	...	...	3	4	81	78	...
J1455-3330	8.0	−19.61	...	...	...	...	60	42	57	35	...
J1459-6053	103.2	−13.6	$9.63^{+0.02}_{-0.02}$	$-3.98^{+0.02}_{-0.02}$	2.5	37.59	6	7	6	7	2PC
J1509-5850	88.9	−14.04	$9.56^{+0.03}_{-0.03}$	$-3.82^{+0.03}_{-0.03}$	2.5	35.81	15	11	78	71	2PC
J1513-2550	2.1	−19.67	...	...	...	...	45	11	60	28	...
J1513-5908	151.6	−11.82	$7.73^{+0.01}_{-0.01}$	$-2.85^{+0.01}_{-0.01}$	$3.23^{+0.01}_{-0.02}$	37.88	3	0	57	53	kuiper hermsen dekker 2018
J1514-4946	3.6	−19.73	$9.26^{+0.03}_{-0.03}$	$-2.27^{+0.03}_{-0.03}$	2.5	31.92	75	53	72	49	Xing and Wang (2016)

Table D.1: - *continued*

Pulsar	P	$\log \dot{P}$	$\log E_{\parallel}$	$\log (x_0/R_{lc})$	b	$\log N_0$	Time domain		Frequency domain		Reference
	[ms]	[s/s]	[V/m]				$\psi_\Omega[^\circ]$	$\lvert\theta_{obs}\rvert[^\circ]$	$\psi_\Omega[^\circ]$	$\lvert\theta_{obs}\rvert[^\circ]$	spectral data
J1522-5735	204.3	−13.2	...	...	...	...	18	4	15	4	...
J1526-2744	2.5	−20.45	...	...	...	...	9	18	12	4	...
J1528-5838	355.7	−13.61	...	...	...	...	9	11	81	78	...
J1531-5610	84.2	−13.86	...	...	...	...	6	11	90	78	...
J1536-4948	3.1	−19.67	$9.56^{+0.02}_{-0.02}$	$-2.65^{+0.02}_{-0.02}$	2.5	32.93	18	7	90	60	3PC
J1543-5149	2.1	−19.79	...	...	...	...	78	78	42	35	...
J1552+5437	2.4	−20.55	...	...	...	...	90	81	90	78	...
J1555-2908	1.8	−19.35	...	...	...	...	48	7	84	32	...
J1600-3053	3.6	−20.02	$9.14^{+0.11}_{-0.1}$	$-2.07^{+0.18}_{-0.15}$	2.5	31.58	30	21	60	53	Xing and Wang (2016)
J1614-2230	3.2	−20.02	$8.59^{+0.04}_{-0.04}$	$-0.95^{+0.2}_{-0.15}$	2.5	30.14	90	67	63	4	Xing and Wang (2016)
J1615-5137	179.3	−13.97	...	...	...	...	27	18	69	64	...
J1620-4927	171.9	−13.98	$7.99^{+0.03}_{-0.03}$	$-2.27^{+0.04}_{-0.04}$	2.5	35.53	12	7	81	74	2PC
J1623-5005	85.1	−14.38	...	...	...	...	75	56	75	56	...
J1624-4041	167.9	−14.33	$7.67^{+0.04}_{-0.04}$	$-1.94^{+0.06}_{-0.05}$	2.5	34.46	27	4	30	4	3PC
J1625-0021	2.8	−19.67	$8.53^{+0.05}_{-0.05}$	$-0.79^{+0.32}_{-0.2}$	2.5	30.27	21	11	3	4	3PC
J1627+3219	2.2	−20.26	...	...	...	...	54	46	51	42	...
J1628-3205	3.2	−19.83	...	...	...	...	87	71	87	67	...
J1630+3734	3.3	−19.97	...	...	...	...	39	39	51	7	...
J1640+2224	3.2	−20.55	...	...	...	...	54	39	51	32	...
J1641+8049	2.0	−20.01	...	...	...	...	33	4	84	32	...
J1641-5317	175.1	−14.43	...	...	...	...	6	14	72	74	...
J1648-4611	165.0	−13.63	...	...	...	...	21	14	75	67	...
J1649-3012	3.4	−19.89	...	...	...	...	21	18	42	35	...
J1650-4601	127.1	−13.82	...	...	...	...	18	7	78	64	...
J1653-0158	2.0	−20.62	$9.13^{+0.03}_{-0.03}$	$-2.22^{+0.03}_{-0.03}$	2.5	32.31	9	4	90	81	3PC
J1658-5324	2.4	−19.96	$8.48^{+0.04}_{-0.04}$	$-1.37^{+0.08}_{-0.07}$	2.5	30.93	3	4	45	35	3PC
J1702-4128	182.2	−13.28	...	...	...	...	3	4	48	46	...
J1705-1906	299.0	−14.38	...	...	...	...	72	49	60	39	...

Table D.1: - *continued*

Pulsar	P [ms]	$\log\dot{P}$ [s/s]	$\log E_{\parallel}$ [V/m]	$\log(x_0/R_{lc})$	b	$\log N_0$	Time domain		Frequency domain		Reference spectral data
							$\psi_\Omega[^\circ]$	$\lvert\theta_{obs}\rvert[^\circ]$	$\psi_\Omega[^\circ]$	$\lvert\theta_{obs}\rvert[^\circ]$	
J1709-4429	102.5	−13.02	$9.49^{+0.01}_{-0.01}$	$-3.73^{+0.01}_{-0.01}$	$3.0^{+0.01}_{-0.01}$	36.38	24	18	24	18	2PC
J1713+0747	4.6	−20.07	$9.13^{+0.05}_{-0.05}$	$-2.38^{+0.06}_{-0.06}$	2.5	32.16	12	11	81	74	Xing and Wang (2016)
J1714-3830	84.1	−13.15	$9.35^{+0.04}_{-0.04}$	$-3.48^{+0.04}_{-0.04}$	2.5	36.23	3	0	15	11	3PC
J1718-3825	74.7	−13.88	$8.29^{+0.02}_{-0.02}$	$-2.55^{+0.02}_{-0.02}$	$2.75^{+0.03}_{-0.04}$	34.71	6	11	6	11	2PC
J1730-2304	8.1	−19.69	...	...	...	...	33	14	54	28	...
J1730-3350	139.5	−13.08	$9.27^{+0.06}_{-0.06}$	$-3.72^{+0.05}_{-0.05}$	2.5	35.2	42	11	33	7	3PC
J1732-3131	196.5	−13.55	$7.42^{+0.04}_{-0.04}$	$-1.37^{+0.12}_{-0.1}$	2.5	31.51	78	56	78	35	2PC
J1732-5049	5.3	−19.85	...	...	...	...	12	11	54	42	...
J1736-3422	347.2	−13.19	...	...	...	...	54	7	87	35	...
J1741+1351	3.8	−19.52	$8.42^{+0.12}_{-0.11}$	$-0.52^{+1.5}_{-0.58}$	2.5	30.12	54	49	57	0	Xing and Wang (2016)
J1741-2054	413.7	−13.77	$7.08^{+0.02}_{-0.02}$	$-1.56^{+0.01}_{-0.01}$	$1.31^{+0.01}_{-0.01}$	31.04	75	64	72	60	2PC
J1742-3321	143.3	−14.9	...	...	...	...	66	67	57	56	...
J1744-1134	4.1	−20.05	$8.43^{+0.03}_{-0.03}$	$-1.57^{+0.04}_{-0.04}$	2.5	30.93	54	42	48	49	Xing and Wang (2016)
J1744-7619	4.7	−20.01	...	...	...	...	87	67	75	60	...
J1745+1017	2.6	−20.6	...	...	...	...	75	60	51	35	...
J1746-3239	199.5	−14.18	$7.68^{+0.04}_{-0.04}$	$-2.11^{+0.05}_{-0.05}$	2.5	35.53	9	11	33	25	2PC
J1747-2958	98.8	−13.21	$8.72^{+0.01}_{-0.01}$	$-3.07^{+0.01}_{-0.01}$	$2.63^{+0.02}_{-0.02}$	35.76	21	7	81	60	Li et al. (2018a)
J1747-4036	1.6	−19.88	$10.12^{+0.08}_{-0.08}$	$-3.17^{+0.09}_{-0.08}$	2.5	35.32	15	0	90	74	Xing and Wang (2016)
J1757-2421	234.1	−13.90	$9.85^{+0.14}_{-0.13}$	$-4.44^{+0.14}_{-0.13}$	2.50	35.55	...	...	...	...	3PC
J1801-2451	125.0	−13.05	$9.94^{+0.02}_{-0.02}$	$-4.22^{+0.02}_{-0.02}$	$2.59^{+0.02}_{-0.02}$	35.25	54	0	54	0	3PC
J1803-2149	106.3	−13.71	$9.13^{+0.05}_{-0.04}$	$-3.39^{+0.05}_{-0.04}$	2.5	36.72	72	46	72	46	2PC
J1803-6707	2.1	−19.73	$9.62^{+0.08}_{-0.07}$	$-2.62^{+0.09}_{-0.08}$	2.50	32.34	...	...	...	...	3PC
J1805+0615	2.1	−19.64	...	...	...	...	87	74	72	60	...
J1809-2332	146.8	−13.46	$8.25^{+0.02}_{-0.02}$	$-2.56^{+0.02}_{-0.02}$	$2.58^{+0.05}_{-0.04}$	34.34	36	18	27	11	2PC
J1810+1744	1.7	−20.33	$9.57^{+0.02}_{-0.02}$	$-2.7^{+0.03}_{-0.03}$	2.5	33.78	6	7	84	81	Xing and Wang (2016)
J1811-2405	2.7	−19.87	...	...	...	...	24	7	33	11	...
J1813-1246	48.1	−13.75	$9.36^{+0.02}_{-0.02}$	$-3.29^{+0.01}_{-0.01}$	$2.22^{+0.02}_{-0.03}$	35.63	15	0	15	0	2PC
J1816+4510	3.2	−19.37	$8.88^{+0.03}_{-0.03}$	$-1.87^{+0.05}_{-0.05}$	2.5	32.2	90	56	39	7	3PC

Table D.1: - *continued*

Pulsar	P [ms]	log$\dot{P}$ [s/s]	log $E_{\parallel}$ [V/m]	log (x_0/R_{lc})	b	log N_0	Time domain $\psi_\Omega[^\circ]$	Time domain $\lvert\theta_{obs}\rvert[^\circ]$	Frequency domain $\psi_\Omega[^\circ]$	Frequency domain $\lvert\theta_{obs}\rvert[^\circ]$	Reference spectral data
J1817-1742	149.7	−13.69	...	...	...	...	30	35	90	35	...
J1823-3021A	5.4	−17.47	$8.93^{+0.04}_{-0.04}$	$-2.1^{+0.05}_{-0.05}$	2.5	33.13	51	25	51	21	3PC
J1824-0621	3.2	−20.04	...	...	...	...	69	60	48	39	...
J1824-2452A	3.1	−17.79	$9.6^{+0.02}_{-0.02}$	$-2.88^{+0.02}_{-0.02}$	$3.15^{+0.05}_{-0.06}$	34.72	9	0	90	78	3PC
J1826-1256	110.2	−12.92	$8.27^{+0.01}_{-0.01}$	$-2.56^{+0.01}_{-0.01}$	$2.73^{+0.01}_{-0.01}$	36.51	39	4	36	4	Li et al. (2018a)
J1827-0849	2.2	−19.96	$10.37^{+0.04}_{-0.05}$	$-3.5^{+0.05}_{-0.05}$	2.5	37.42	12	14	90	81	3PC
J1827-1446	499.2	−13.34	...	...	...	...	15	14	54	49	...
J1828-1101	72.1	−13.83	...	...	...	...	6	0	90	14	...
J1833-1034	61.9	−12.69	$9.86^{+0.02}_{-0.02}$	$-4.05^{+0.02}_{-0.02}$	$2.9^{+0.03}_{-0.03}$	36.22	42	46	87	60	2PC
J1836+5925	173.3	−14.82	$7.59^{+0.01}_{-0.01}$	$-1.72^{+0.01}_{-0.01}$	$2.22^{+0.03}_{-0.03}$	32.3	9	4	9	4	2PC
J1837-0604	96.3	−13.35	...	...	...	...	21	0	48	4	...
J1838-0537	145.8	−12.35	$8.03^{+0.03}_{-0.03}$	$-2.14^{+0.04}_{-0.03}$	$2.41^{+0.06}_{-0.06}$	34.94	18	11	78	71	2PC
J1843-1113	1.8	−20.02	...	...	...	...	9	4	81	64	...
J1844-0346	112.9	−12.81	$7.56^{+0.05}_{-0.05}$	$-1.46^{+0.11}_{-0.09}$	2.5	33.84	9	14	78	74	3PC
J1846+0919	225.6	−14.0	$7.53^{+0.03}_{-0.03}$	$-1.62^{+0.06}_{-0.06}$	2.5	34.03	84	74	78	74	3PC
J1846-0258	326.6	−11.15	$6.56^{+0.02}_{-0.03}$	$-1.33^{+0.02}_{-0.03}$	$2.28^{+0.03}_{-0.03}$	34.57	...	...	...	...	3PC
J1855-1436	3.6	−19.96	$9.19^{+0.09}_{-0.09}$	$-2.15^{+0.16}_{-0.13}$	2.5	32.25	12	14	90	56	3PC
J1858-2216	2.4	−20.41	$8.64^{+0.06}_{-0.06}$	$-1.11^{+0.3}_{-0.19}$	2.5	30.18	78	60	72	49	Xing and Wang (2016)
J1901-0125	2.8	−19.45	...	...	...	...	42	18	36	14	...
J1902-5105	1.7	−20.05	$9.44^{+0.02}_{-0.02}$	$-2.52^{+0.02}_{-0.02}$	2.5	33.21	24	4	21	4	Xing and Wang (2016)
J1903-7051	3.6	−19.98	...	...	...	...	6	14	51	49	...
J1906+0722	111.5	−13.44	...	...	...	...	24	18	24	18	...
J1907+0602	106.6	−13.06	$8.23^{+0.02}_{-0.02}$	$-2.42^{+0.02}_{-0.02}$	2.5	34.07	81	64	81	64	2PC
J1908+2105	2.6	−19.86	...	...	...	...	30	35	39	7	...
J1913+0904	163.3	−13.75	...	...	...	...	78	53	57	35	...
J1921+0137	2.5	−19.73	...	...	...	...	24	11	72	49	...
J1932+1916	208.2	−13.03	$7.57^{+0.03}_{-0.03}$	$-1.99^{+0.04}_{-0.04}$	2.5	35.03	6	11	78	78	3PC
J1939+2134	1.6	−18.98	$9.27^{+0.04}_{-0.04}$	$-2.33^{+0.04}_{-0.03}$	$3.07^{+0.19}_{-0.21}$	33.52	45	4	45	4	3PC

Table D.1: - *continued*

Pulsar	P [ms]	$\log\dot{P}$ [s/s]	$\log E_{\parallel}$ [V/m]	$\log(x_0/R_{lc})$	b	$\log N_0$	Time domain $\psi_\Omega[^\circ]$	Time domain $\lvert\theta_{obs}\rvert[^\circ]$	Frequency domain $\psi_\Omega[^\circ]$	Frequency domain $\lvert\theta_{obs}\rvert[^\circ]$	Reference spectral data
J1946-5403	2.7	−20.57	...	...	...	...	3	4	6	4	...
J1952+3252	39.5	−14.23	$10.09^{+0.01}_{-0.01}$	$-4.09^{+0.01}_{-0.01}$	$2.92^{+0.01}_{-0.01}$	36.22	42	4	39	4	2PC
J1954+2836	92.7	−13.67	$8.52^{+0.03}_{-0.03}$	$-2.68^{+0.03}_{-0.03}$	2.5	35.63	21	4	24	4	2PC
J1957+5033	374.8	−14.15	$6.91^{+0.04}_{-0.04}$	$-1.38^{+0.07}_{-0.06}$	2.5	34.07	84	71	72	67	2PC
J1958+2846	290.4	−12.67	$7.73^{+0.03}_{-0.03}$	$-2.22^{+0.03}_{-0.03}$	2.5	35.24	84	56	87	64	2PC
J1959+2048	1.6	−19.77	$8.75^{+0.07}_{-0.07}$	$-1.54^{+0.15}_{-0.12}$	2.5	31.3	48	0	48	0	Xing and Wang (2016)
J2006+0148	2.2	−20.48	...	...	...	...	45	32	90	28	...
J2006+3102	163.7	−13.6	...	...	...	...	15	18	48	49	...
J2017+0603	2.9	−20.08	$8.83^{+0.04}_{-0.04}$	$-1.69^{+0.07}_{-0.07}$	2.5	31.68	78	64	69	49	Xing and Wang (2016)
J2017+3625	166.7	−14.87	...	...	...	...	24	4	45	21	...
J2017-1614	2.3	−20.62	$9.14^{+0.07}_{-0.07}$	$-2.1^{+0.11}_{-0.09}$	2.5	31.55	90	71	84	49	3PC
J2021+3651	103.7	−13.02	$8.51^{+0.01}_{-0.01}$	$-2.79^{+0.01}_{-0.01}$	$2.95^{+0.01}_{-0.01}$	34.83	48	4	42	4	Li et al. (2018a)
J2021+4026	265.3	−13.26	$7.97^{+0.01}_{-0.01}$	$-2.51^{+0.01}_{-0.01}$	$2.78^{+0.06}_{-0.04}$	34.72	3	0	15	4	2PC
J2022+3842	48.6	−13.06	$8.71^{+0.04}_{-0.05}$	$-2.9^{+0.03}_{-0.04}$	$2.75^{+0.08}_{-0.12}$	35.23	33	7	87	64	2PC
J2028+3332	176.7	−14.31	$7.54^{+0.04}_{-0.04}$	$-1.69^{+0.07}_{-0.06}$	2.5	32.8	84	64	84	39	2PC
J2030+3641	200.1	−14.19	$7.29^{+0.07}_{-0.07}$	$-1.05^{+0.37}_{-0.22}$	2.5	32.8	84	67	72	60	2PC
J2032+4127	143.2	−13.94	$7.91^{+0.04}_{-0.04}$	$-1.87^{+0.07}_{-0.06}$	2.5	32.46	18	25	54	4	2PC
J2034+3632	3.6	−20.76	...	...	...	...	3	11	51	32	...
J2039-3616	3.3	−20.07	...	...	...	...	39	39	45	46	...
J2039-5617	2.6	−19.85	$9.17^{+0.03}_{-0.03}$	$-2.21^{+0.04}_{-0.03}$	2.5	32.26	12	11	72	64	3PC
J2042+0246	4.5	−19.85	...	...	...	...	3	4	48	35	...
J2043+1711	2.4	−20.24	$9.51^{+0.02}_{-0.03}$	$-2.54^{+0.03}_{-0.03}$	2.5	32.76	21	4	24	4	Xing and Wang (2016)
J2043+2740	96.1	−14.91	$7.24^{+0.07}_{-0.06}$	$-1.1^{+0.08}_{-0.06}$	$1.15^{+0.18}_{-0.06}$	30.82	81	53	75	35	3PC
J2047+1053	4.3	−19.68	...	...	...	...	69	53	60	42	...
J2051-0827	4.5	−19.9	...	...	...	...	84	64	54	39	...
J2052+1219	2.0	−20.17	...	...	...	...	63	32	54	25	...
J2055+2539	319.6	−14.39	$7.01^{+0.03}_{-0.03}$	$-1.13^{+0.02}_{-0.02}$	$1.23^{+0.02}_{-0.02}$	33.27	12	14	78	67	2PC
J2111+4606	157.8	−12.79	$8.65^{+0.04}_{-0.04}$	$-2.94^{+0.04}_{-0.04}$	2.5	35.17	78	64	72	53	2PC

Table D.1: - *continued*

Pulsar	P [ms]	$\log \dot{P}$ [s/s]	$\log E_{\parallel}$ [V/m]	$\log (x_0/R_{lc})$	b	$\log N_0$	Time domain ψ_Ω[°]	Time domain $\lvert\theta_{obs}\rvert$[°]	Frequency domain ψ_Ω[°]	Frequency domain $\lvert\theta_{obs}\rvert$[°]	Reference spectral data
J2115+5448	2.6	−19.46	...	...	...	...	75	49	63	25	...
J2124-3358	4.9	−19.69	$8.41^{+0.02}_{-0.03}$	$-0.92^{+0.03}_{-0.03}$	$0.0^{+0.02}_{-0.08}$	29.86	9	7	51	42	Xing and Wang (2016)
J2129-0429	7.6	−18.63	$8.4^{+0.05}_{-0.05}$	$-1.53^{+0.11}_{-0.09}$	2.5	31.08	90	56	60	0	3PC
J2139+4716	282.8	−14.75	$7.25^{+0.05}_{-0.05}$	$-1.7^{+0.08}_{-0.07}$	2.5	34.06	6	14	45	39	2PC
J2214+3000	3.1	−19.82	$8.72^{+0.02}_{-0.02}$	$-1.62^{+0.04}_{-0.04}$	2.5	30.93	18	4	18	4	Xing and Wang (2016)
J2215+5135	2.6	−19.63	$9.46^{+0.04}_{-0.04}$	$-2.46^{+0.05}_{-0.05}$	2.5	32.73	84	46	81	35	Xing and Wang (2016)
J2229+6114	51.7	−13.12	$8.62^{+0.01}_{-0.01}$	$-2.58^{+0.01}_{-0.01}$	$2.62^{+0.02}_{-0.02}$	34.13	9	11	30	25	2PC
J2234+0944	3.6	−19.71	...	...	...	...	54	46	57	49	...
J2238+5903	162.7	−13.01	$8.04^{+0.04}_{-0.04}$	$-2.42^{+0.04}_{-0.04}$	2.5	35.04	54	0	57	0	2PC
J2240+5832	139.9	−13.82	...	...	...	...	27	32	87	32	...
J2241-5236	2.2	−20.06	$9.12^{+0.02}_{-0.02}$	$-2.06^{+0.03}_{-0.03}$	2.5	31.94	12	4	45	11	Xing and Wang (2016)
J2256-1024	2.3	−19.94	...	...	...	...	39	0	45	4	...
J2302+4442	5.2	−19.88	$8.78^{+0.04}_{-0.04}$	$-1.75^{+0.07}_{-0.07}$	2.5	31.23	60	35	90	21	Xing and Wang (2016)
J2310-0555	2.6	−20.3	...	...	...	...	84	53	42	4	...
J2333-5526	2.1	−20.11	$9.55^{+0.06}_{-0.06}$	$-2.60^{+0.07}_{-0.07}$	2.50	31.80	...	...	...	...	3PC
J2339-0533	2.9	−19.85	$9.14^{+0.02}_{-0.02}$	$-2.09^{+0.03}_{-0.03}$	2.5	31.96	75	46	78	53	3PC

E

Spectral fits of the whole sample of pulsars studied

Figure E.1 shows the plots of the best-fitting spectra of the whole population of high-energy pulsars.

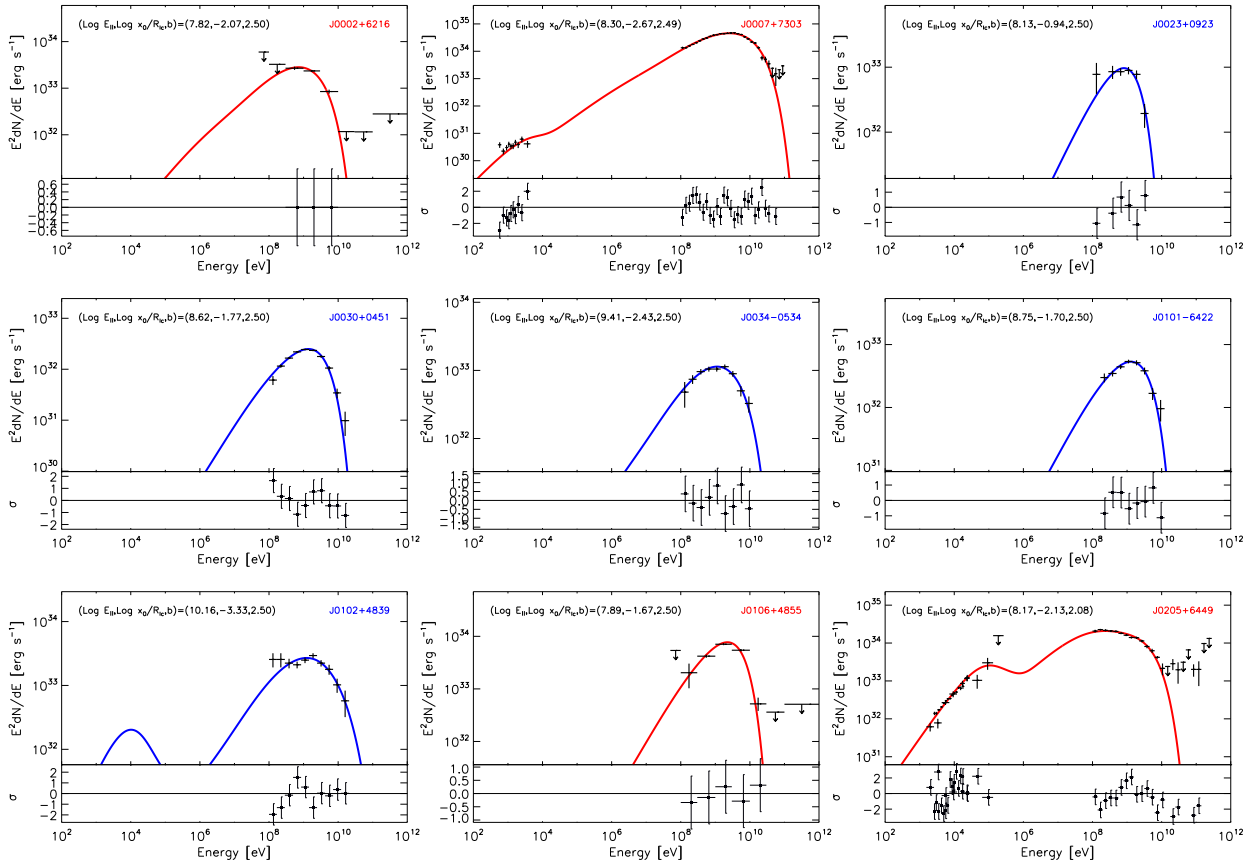


Figure E.1: Best-fitting spectra for the sample of high energy pulsars. Red lines for young pulsars and blue lines for MSPs. γ-ray data is taken from the references indicated in the last column of Table D.1, while X-ray data is taken from Coti Zelati et al. (2020).

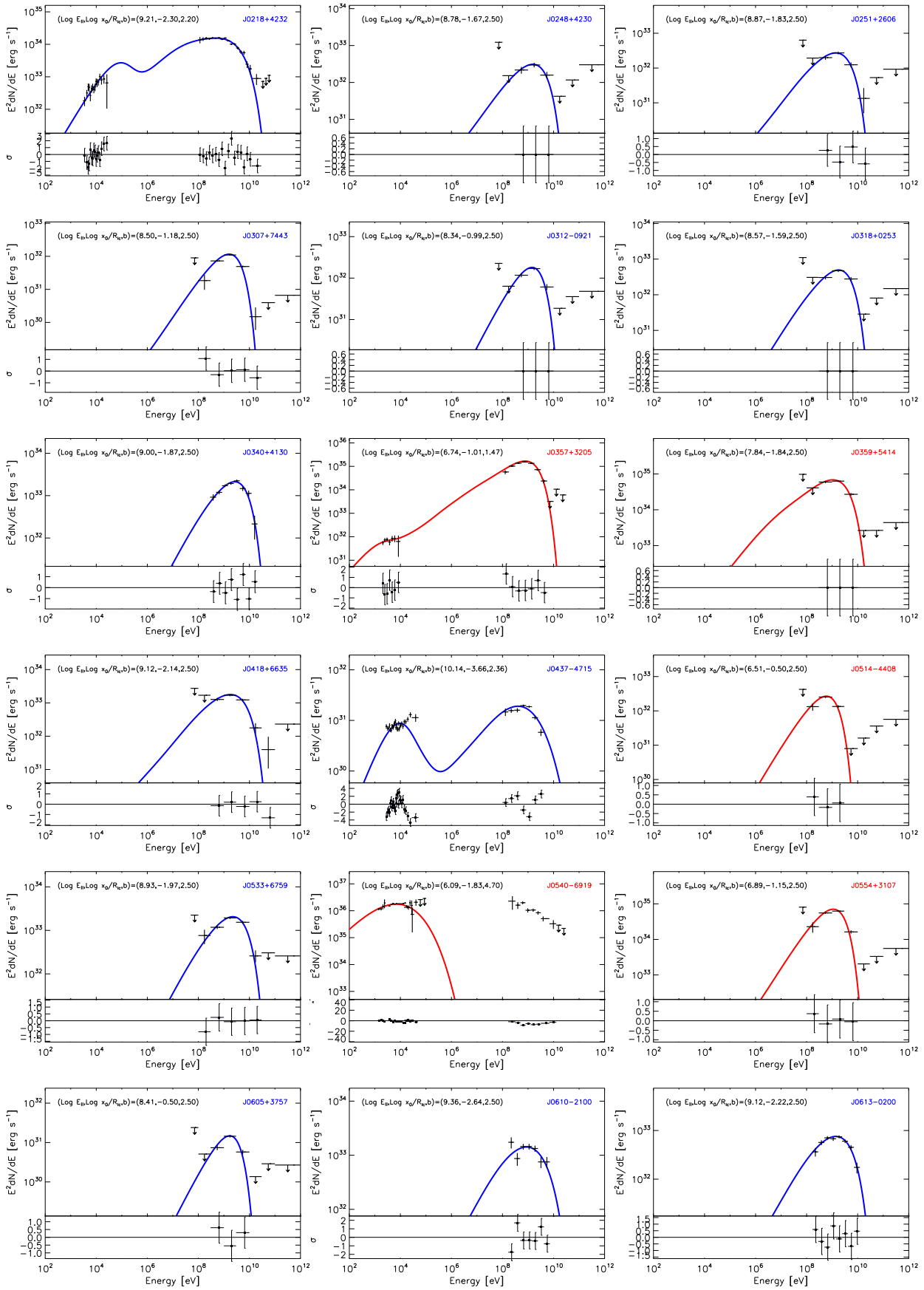


Figure E.1: - *continued*

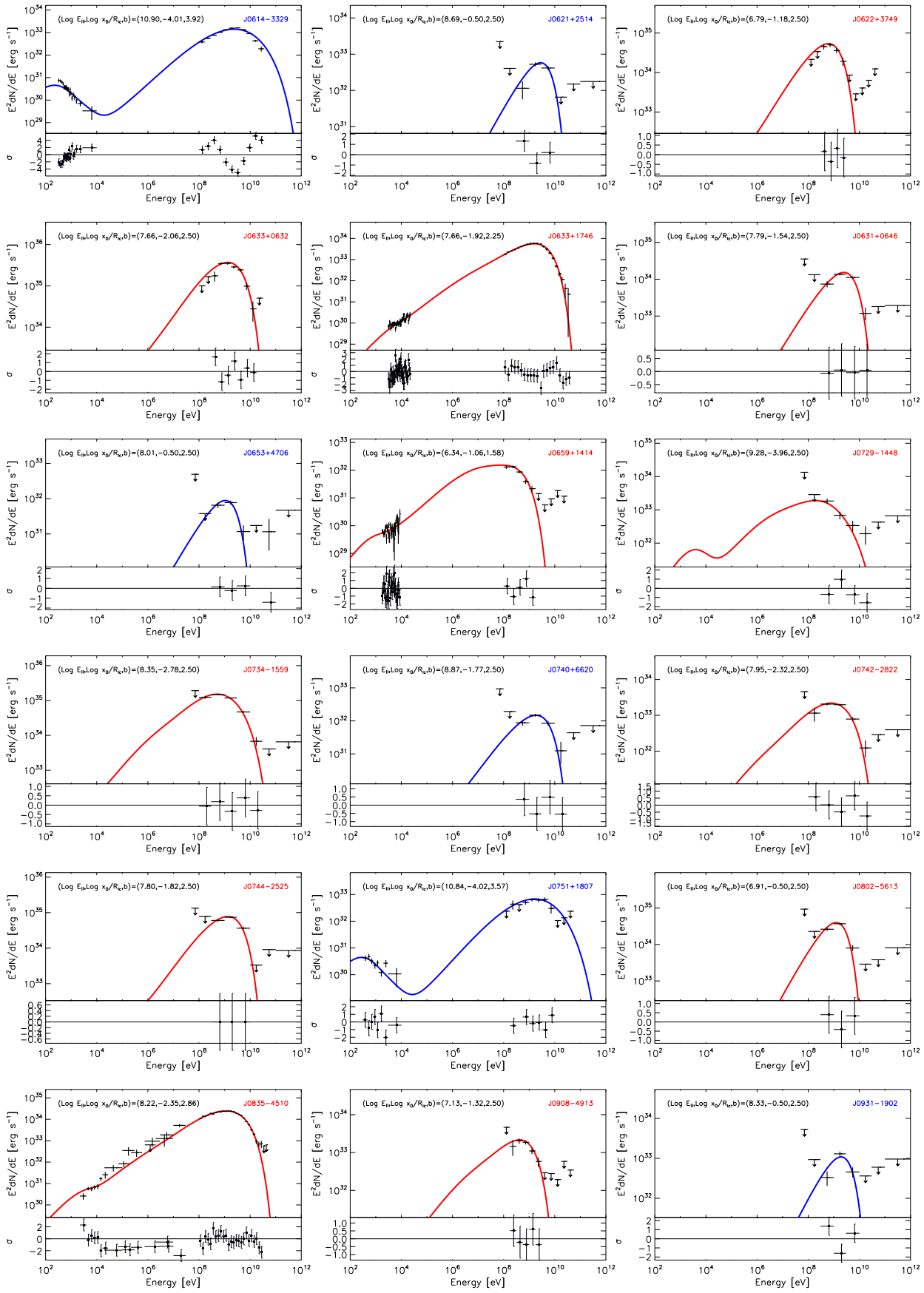


Figure E.1: - *continued*

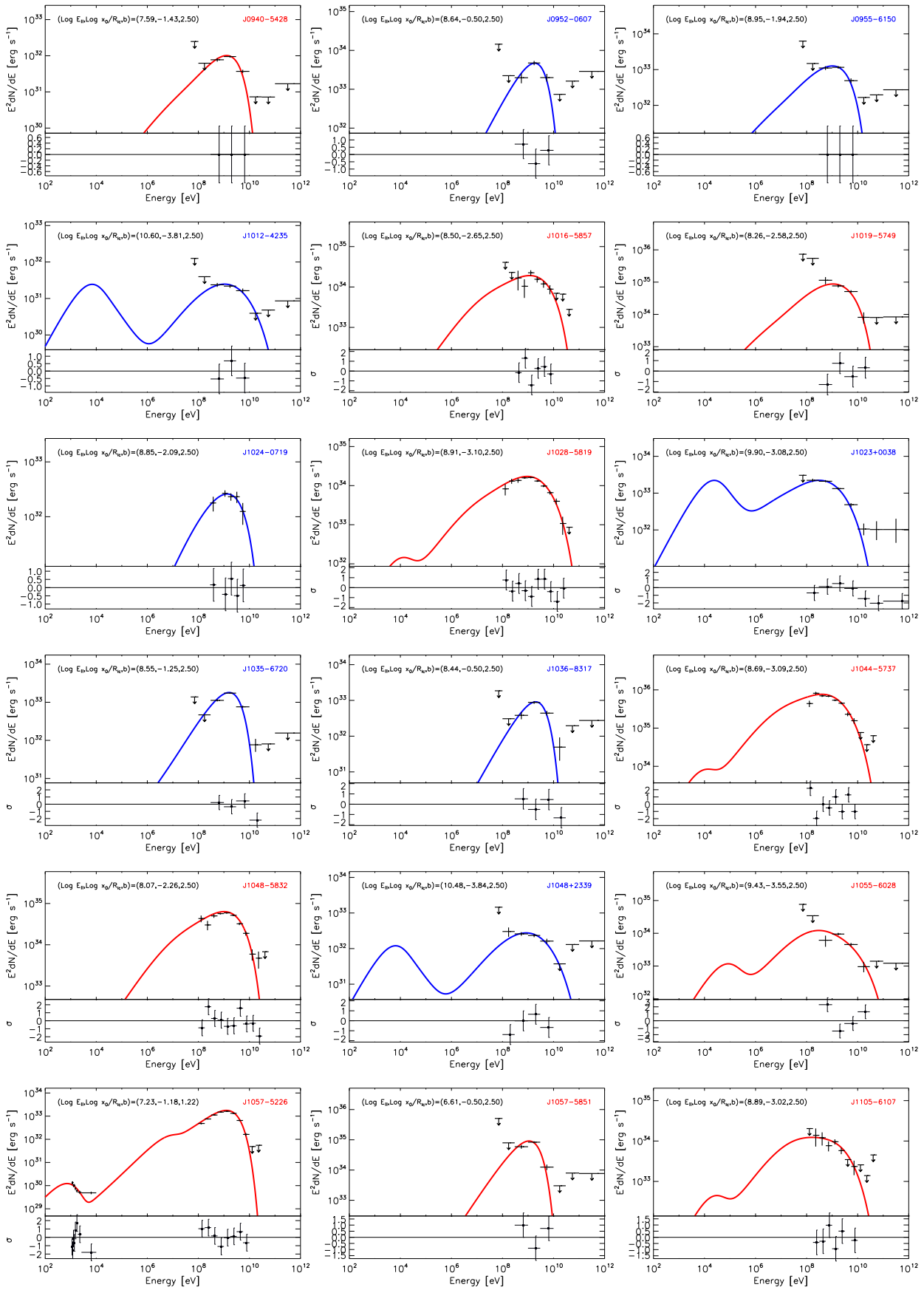


Figure E.1: - *continued*

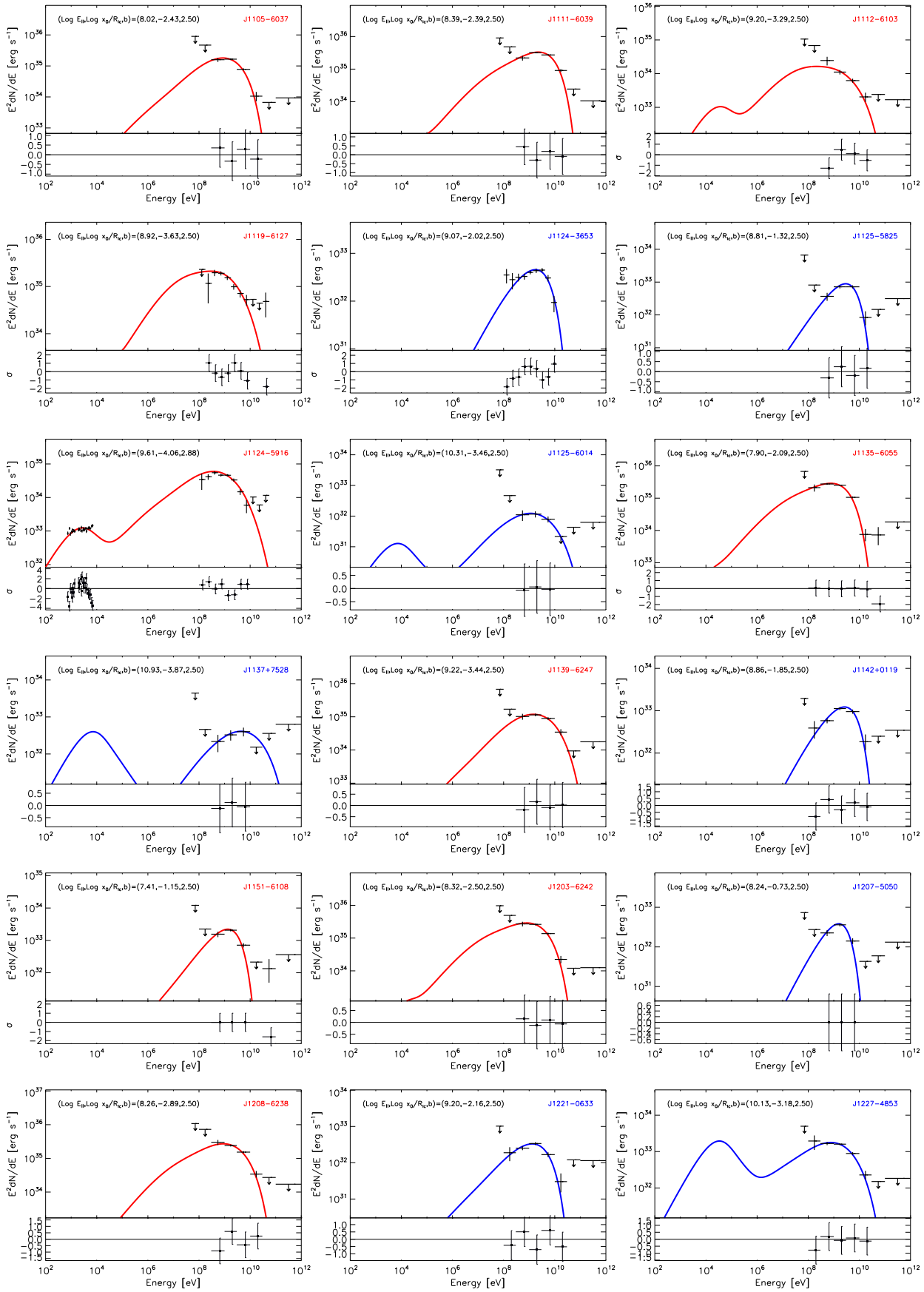


Figure E.1: - *continued*

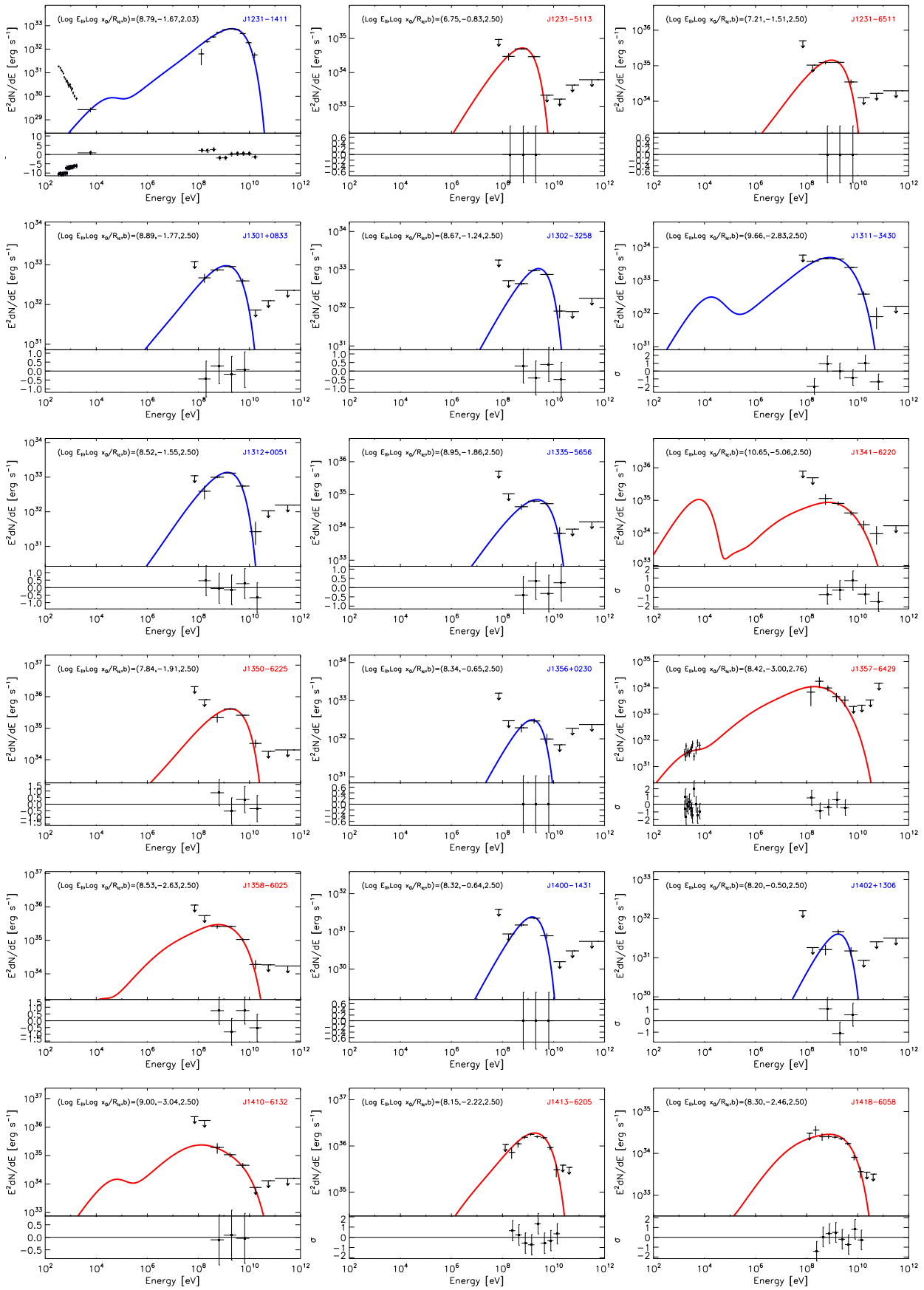


Figure E.1: - *continued*

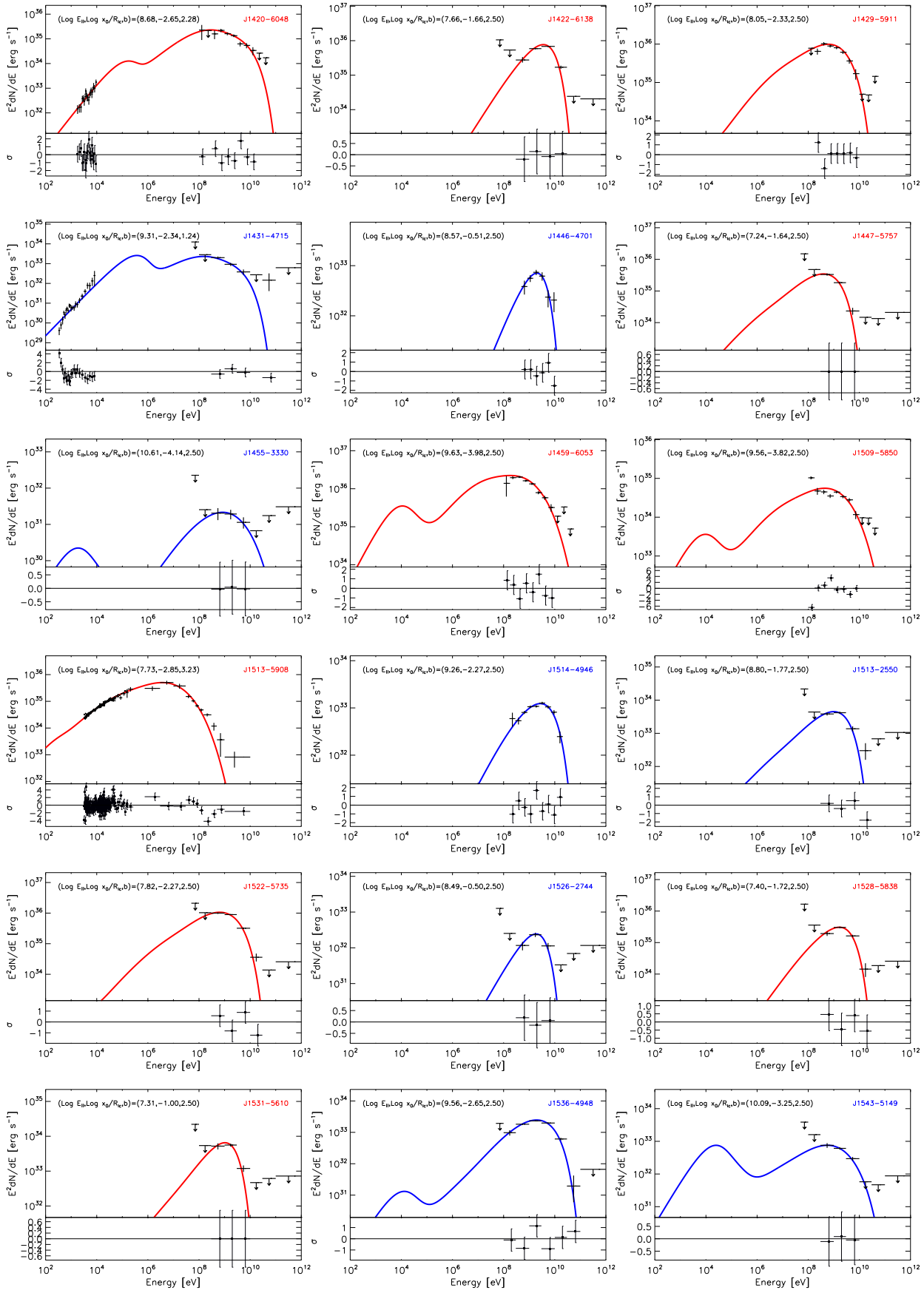


Figure E.1: - *continued*

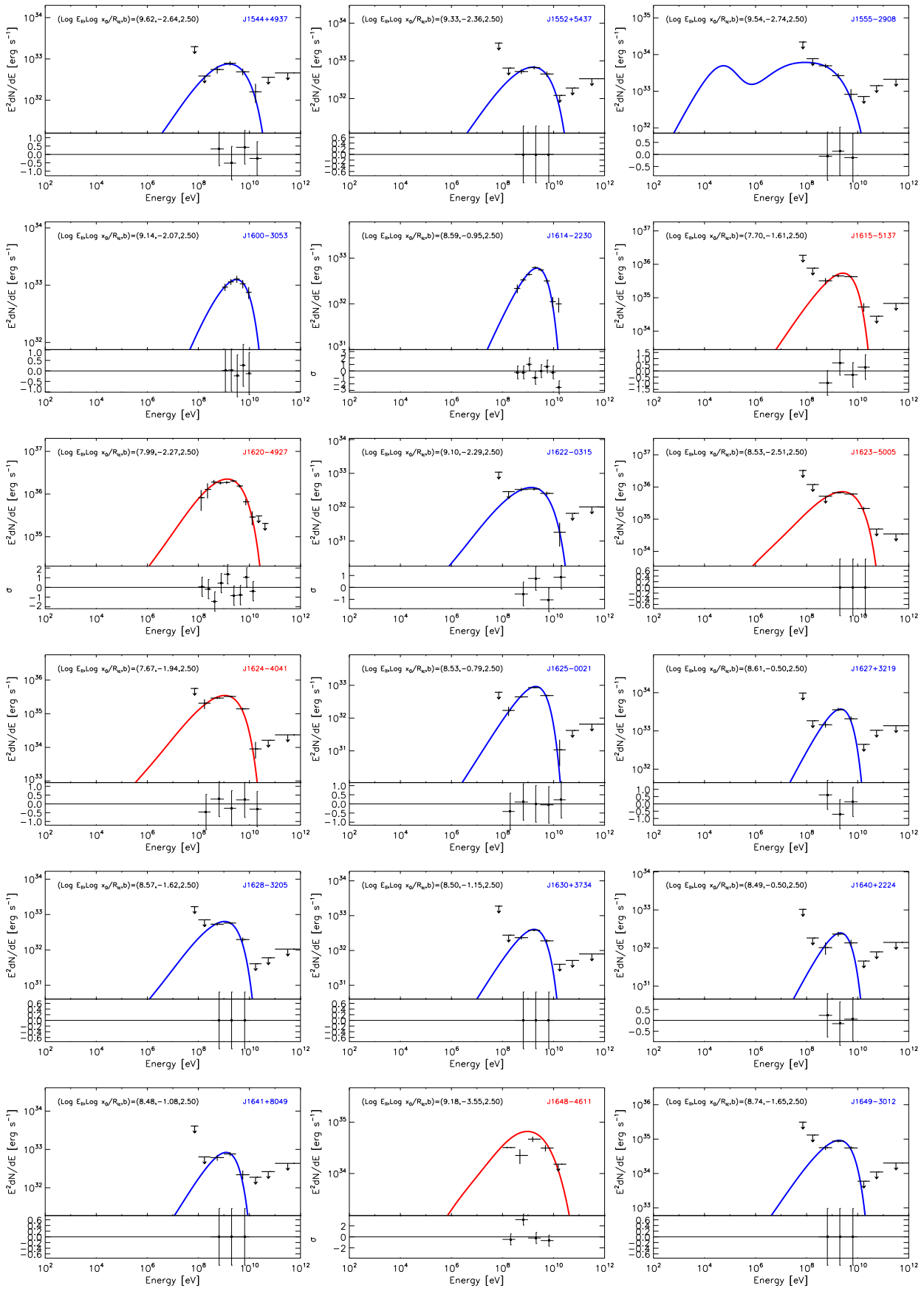


Figure E.1: - *continued*

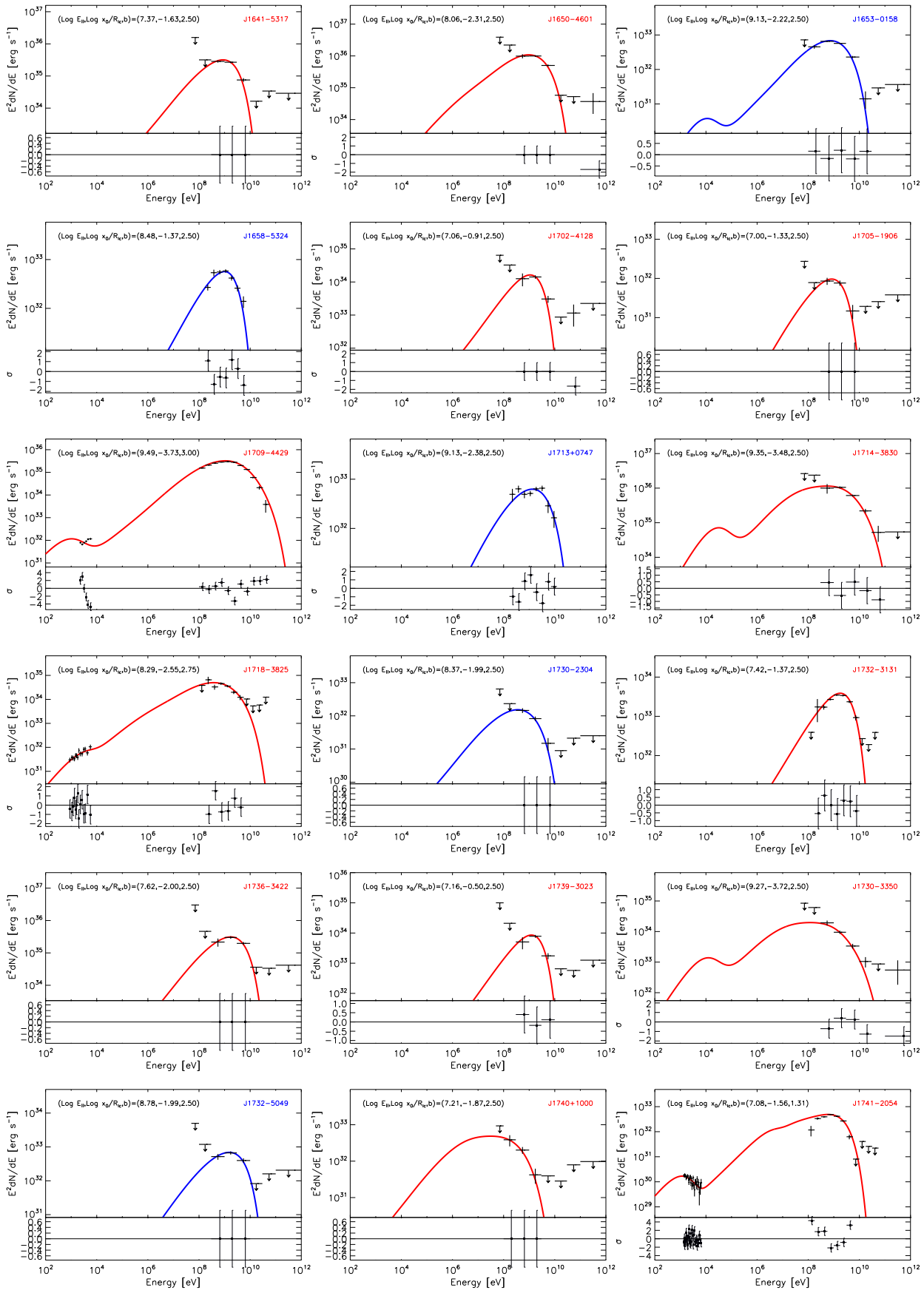


Figure E.1: - *continued*

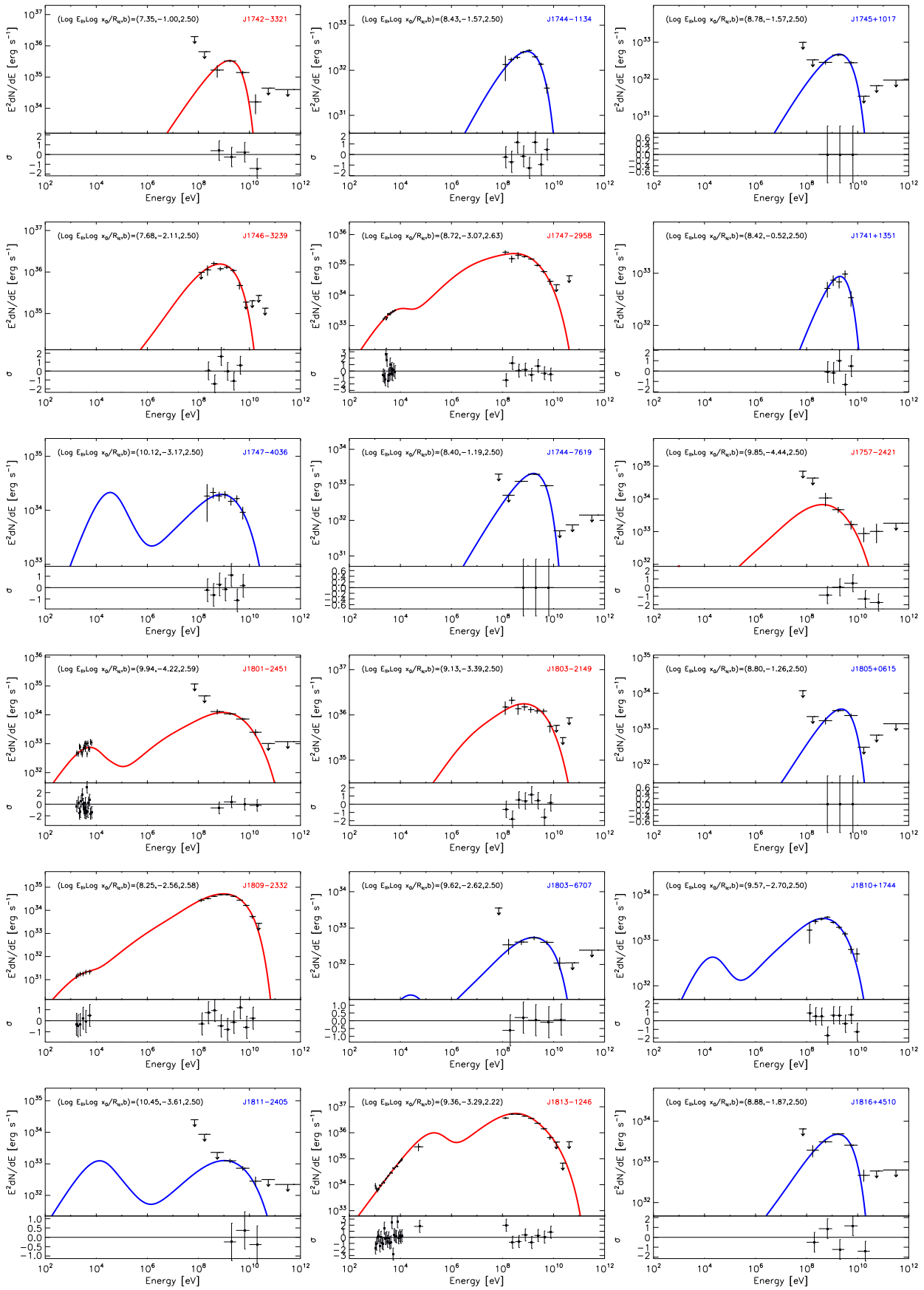


Figure E.1: - *continued*

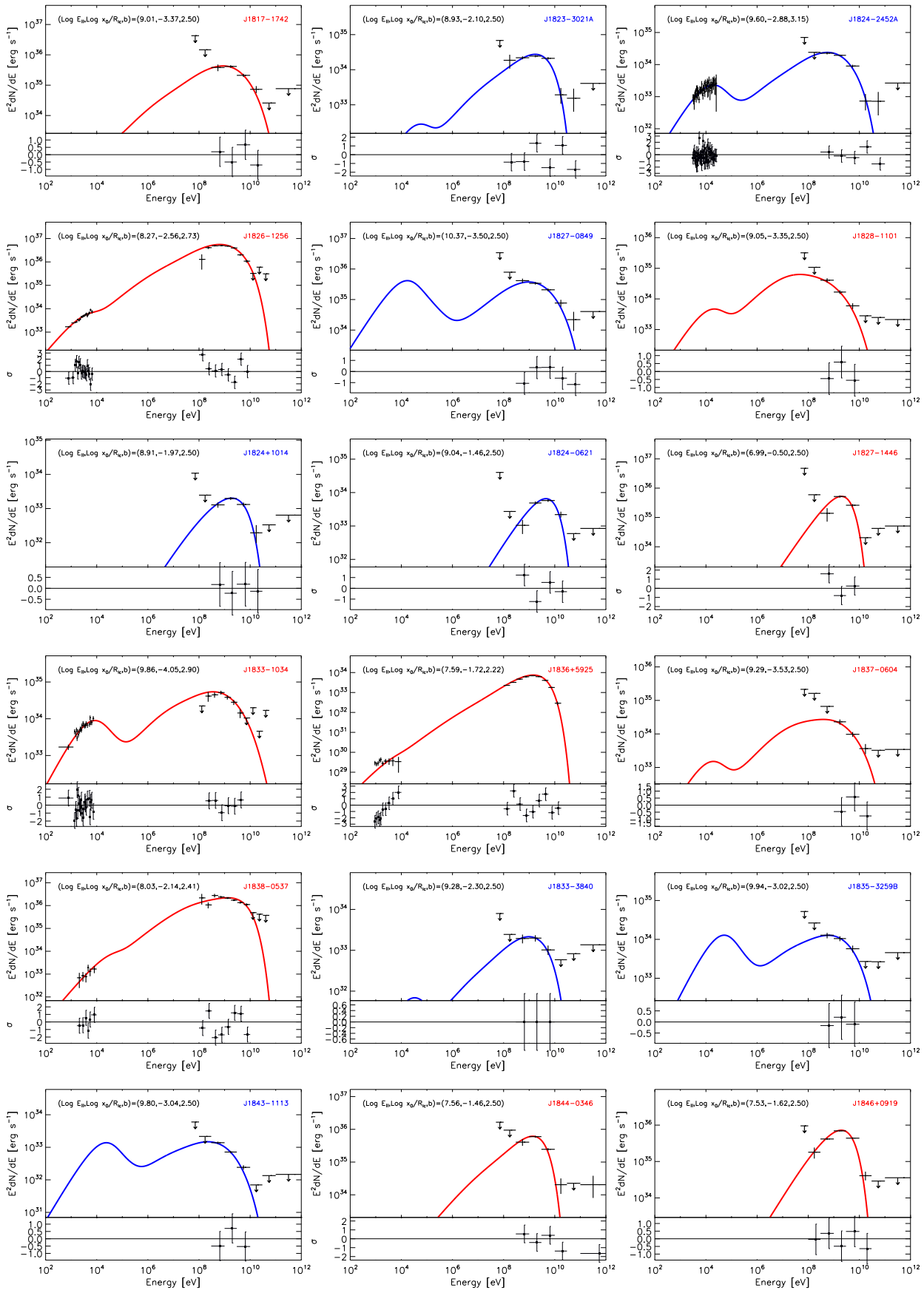


Figure E.1: - *continued*

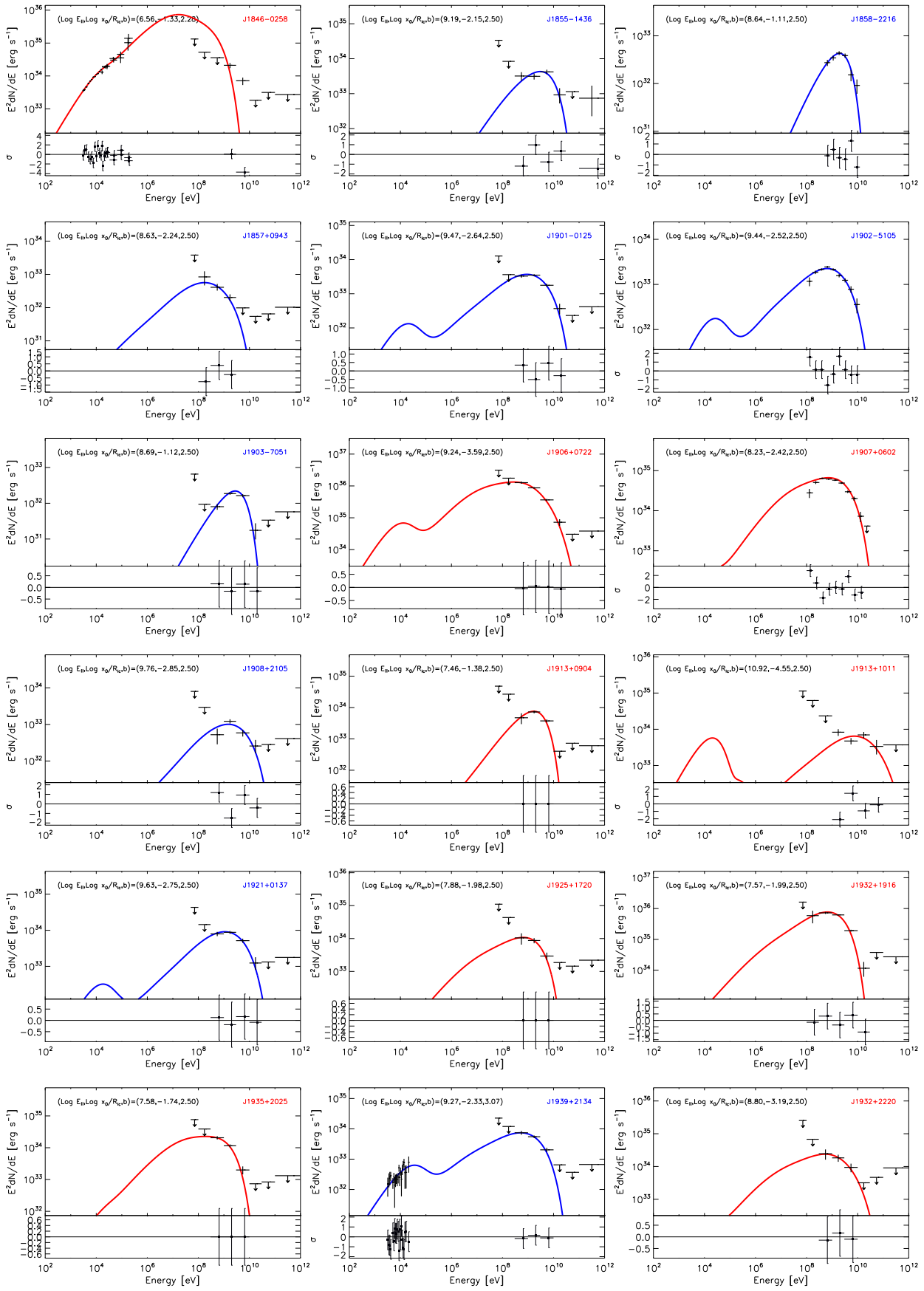


Figure E.1: - *continued*

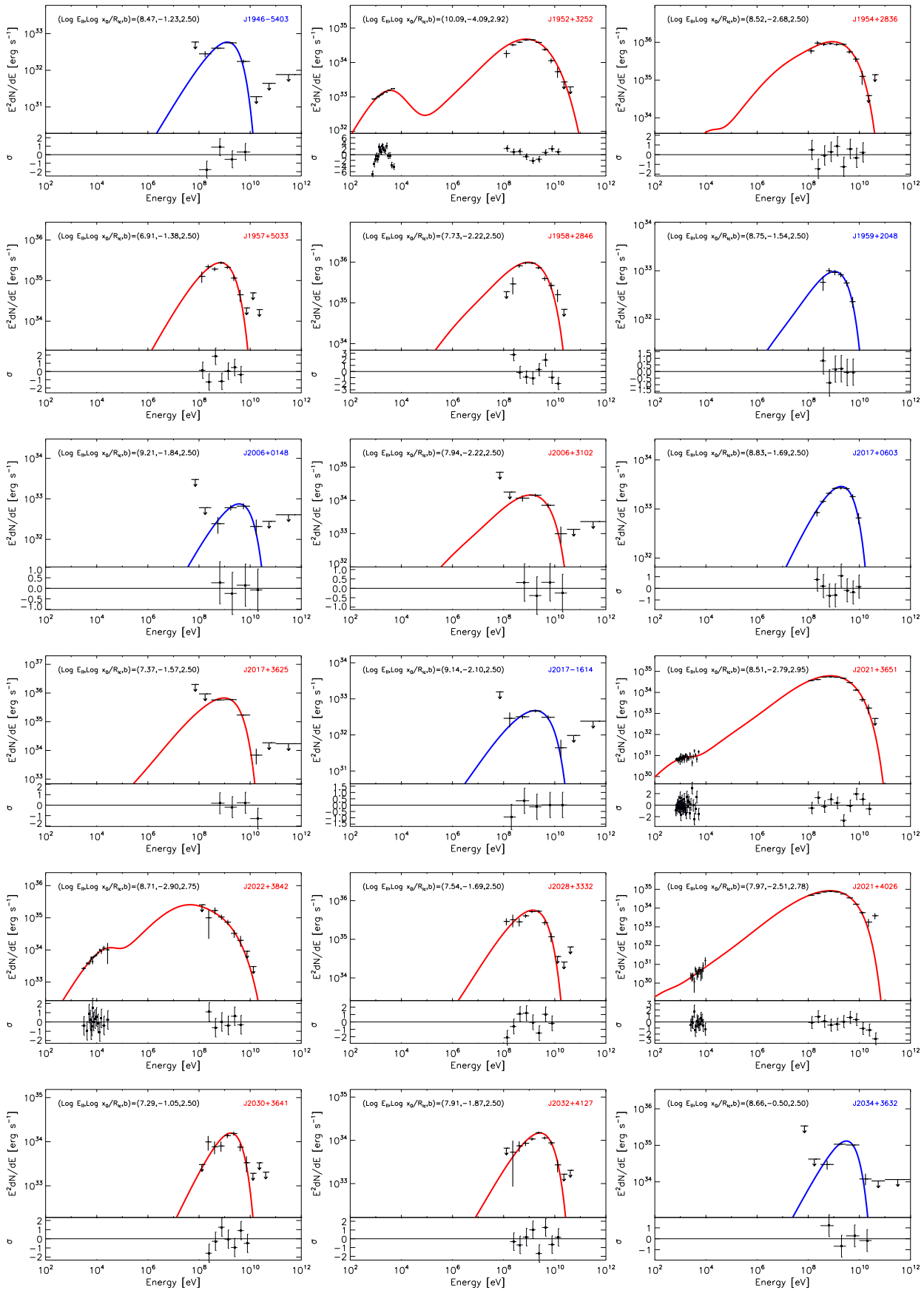


Figure E.1: - *continued*

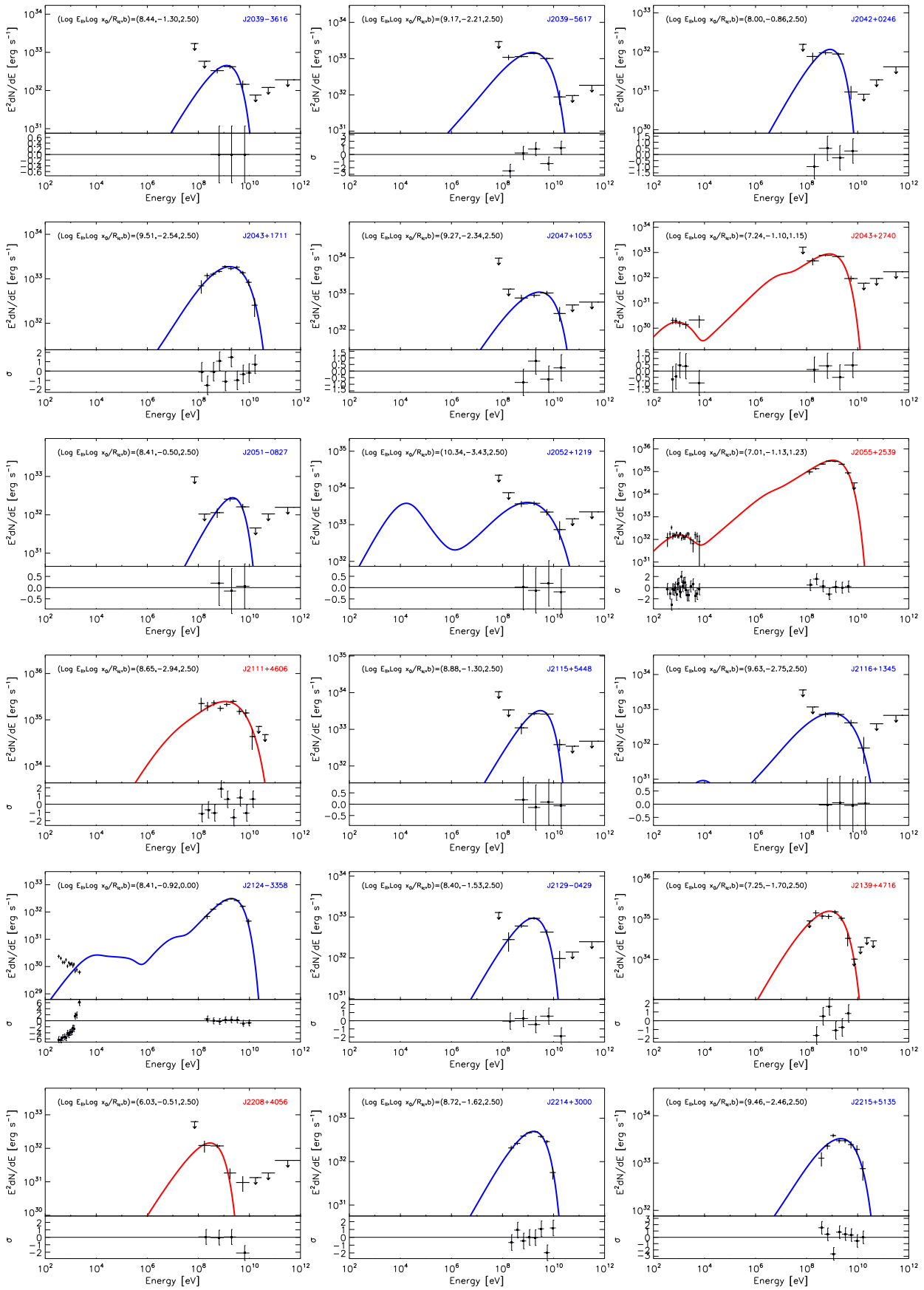


Figure E.1: - *continued*

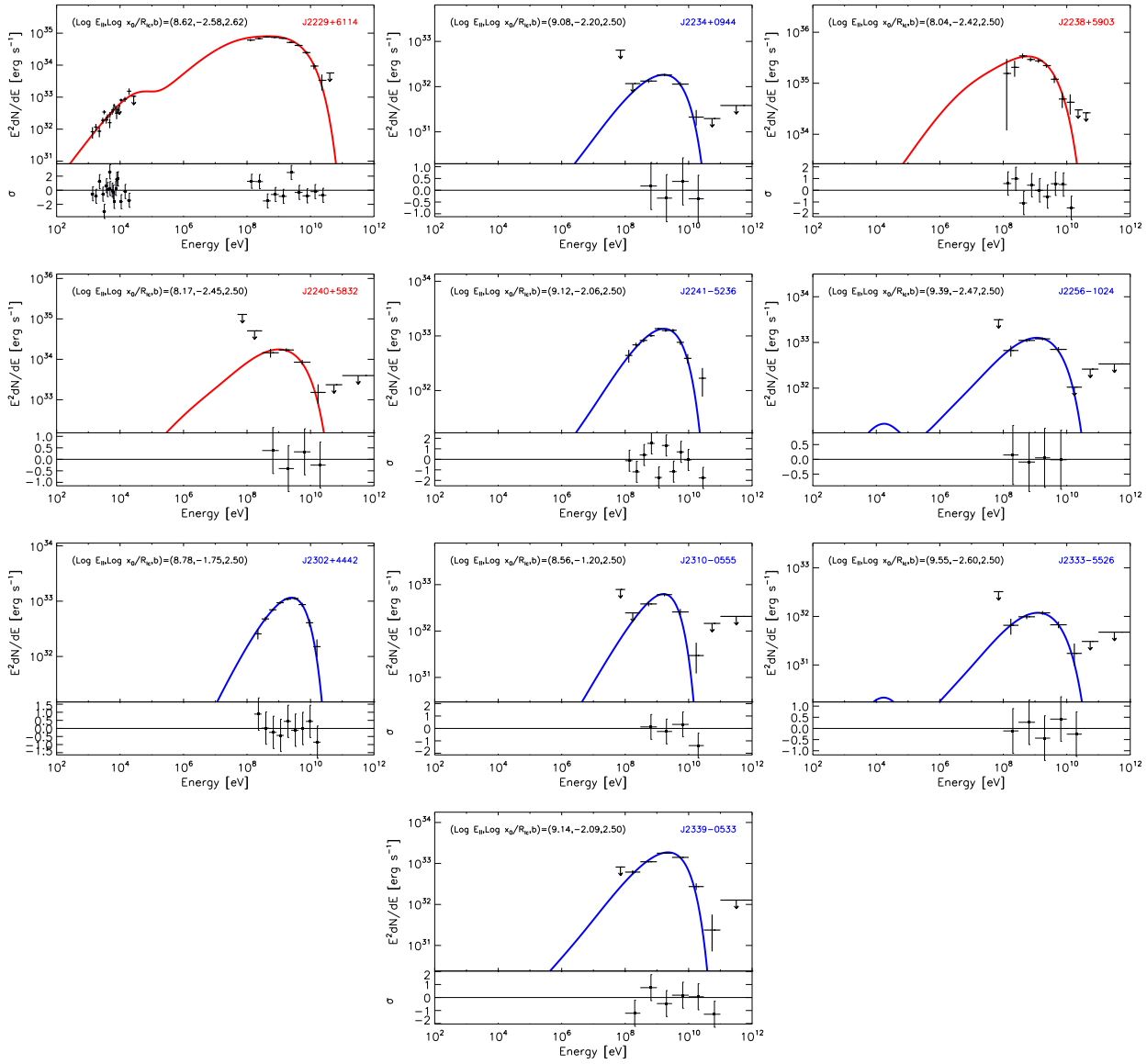


Figure E.1: - *continued*

F

Light curve fits of the whole sample of pulsars studied

Figure F.1 shows the plots of the best-fitting light curves in time and frequency domain, together with the contour plots of the statistics used in the fits, χ^2 and euclidean distance, respectively.

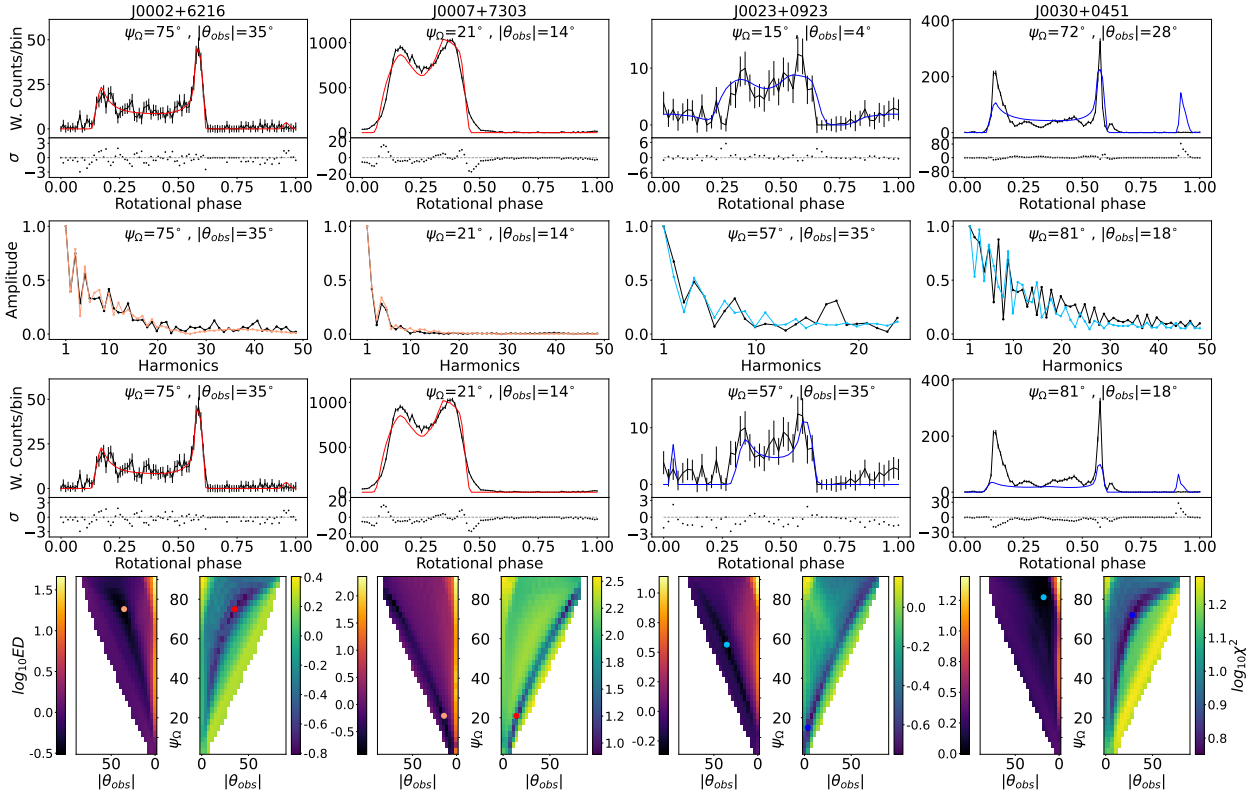


Figure F.1: Best-fit light curves obtained in time and frequency domain. Panels and colours as in Figure 5.7.

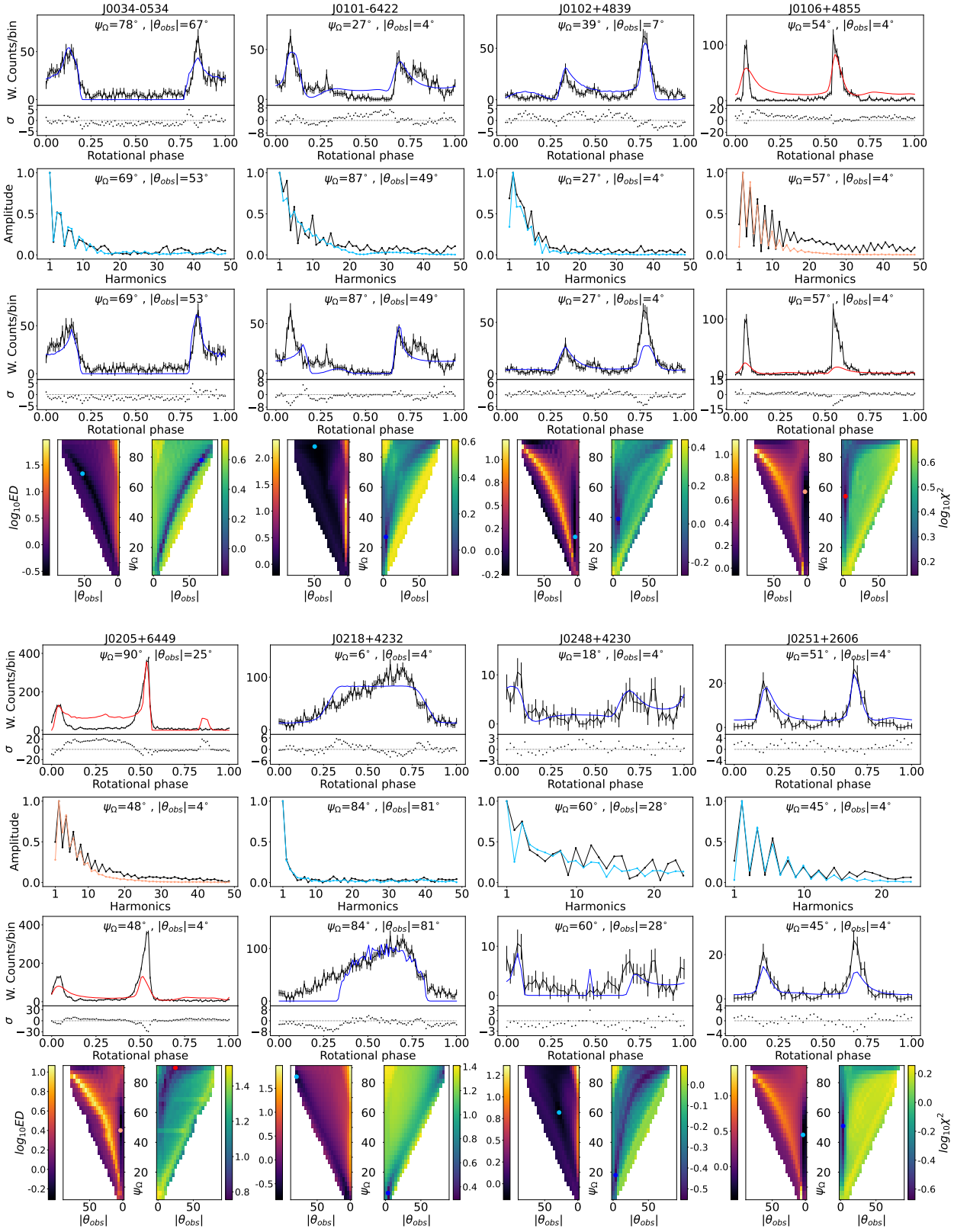


Figure F.1: - *continued*

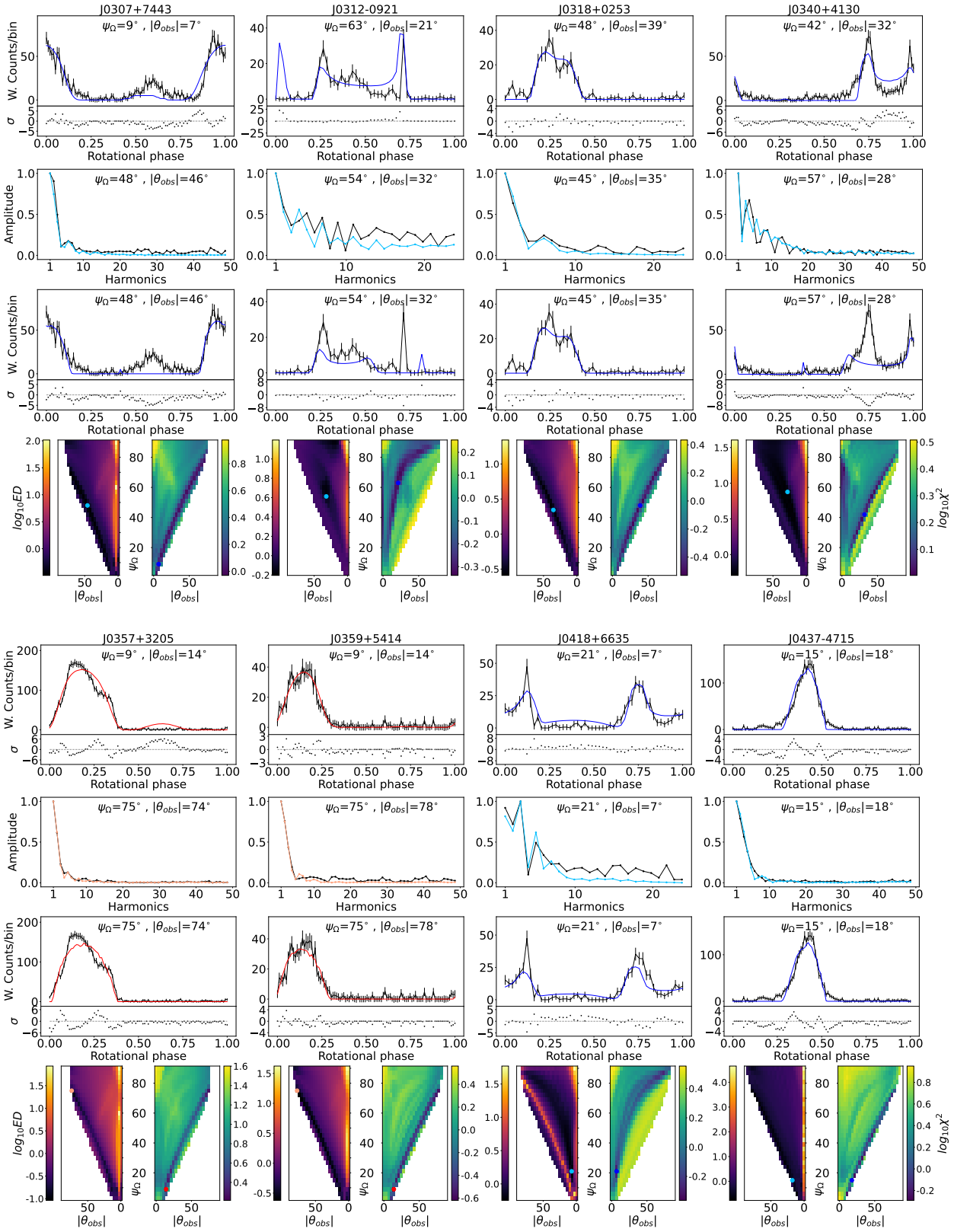


Figure F.1: - *continued*

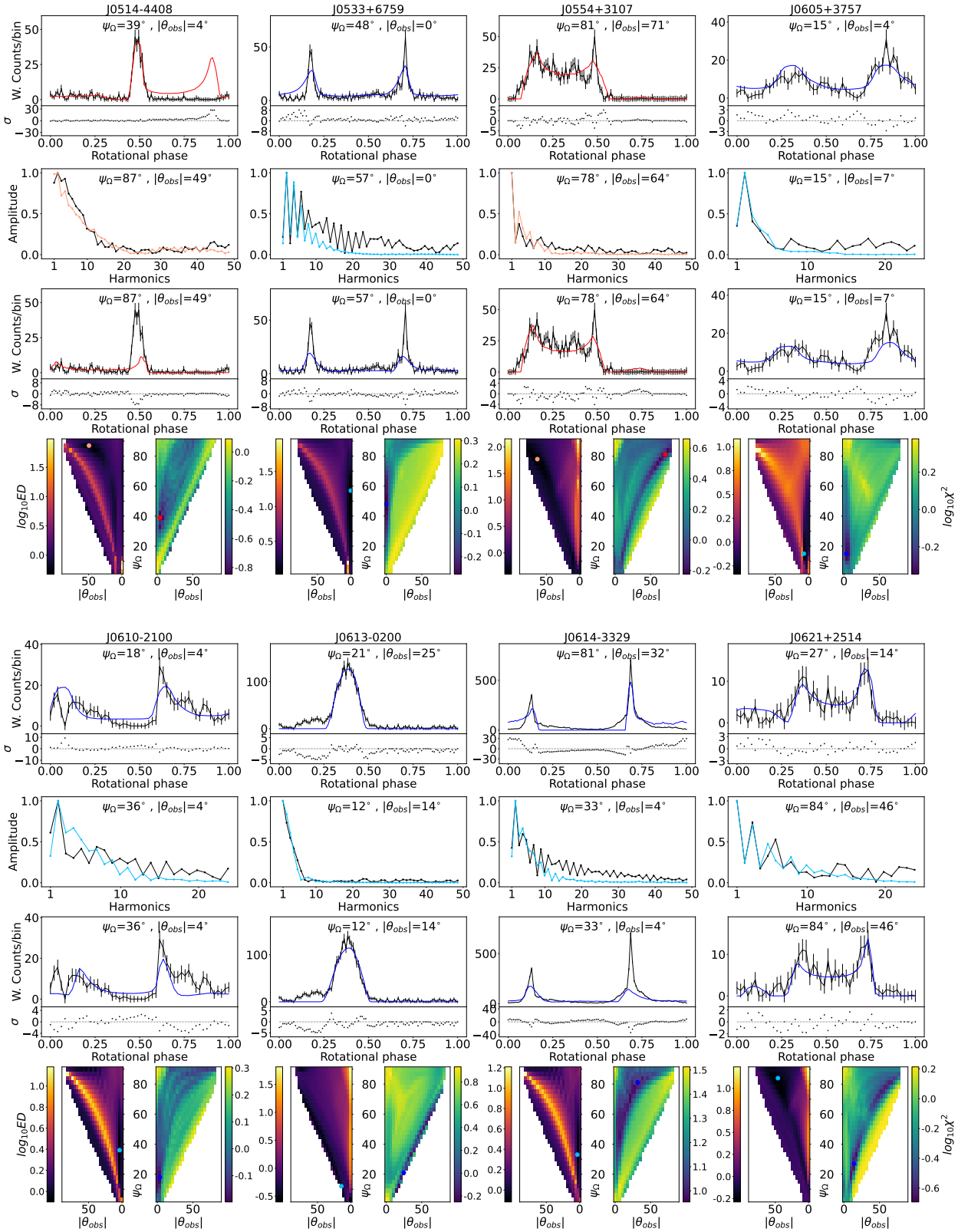


Figure F.1: - *continued*

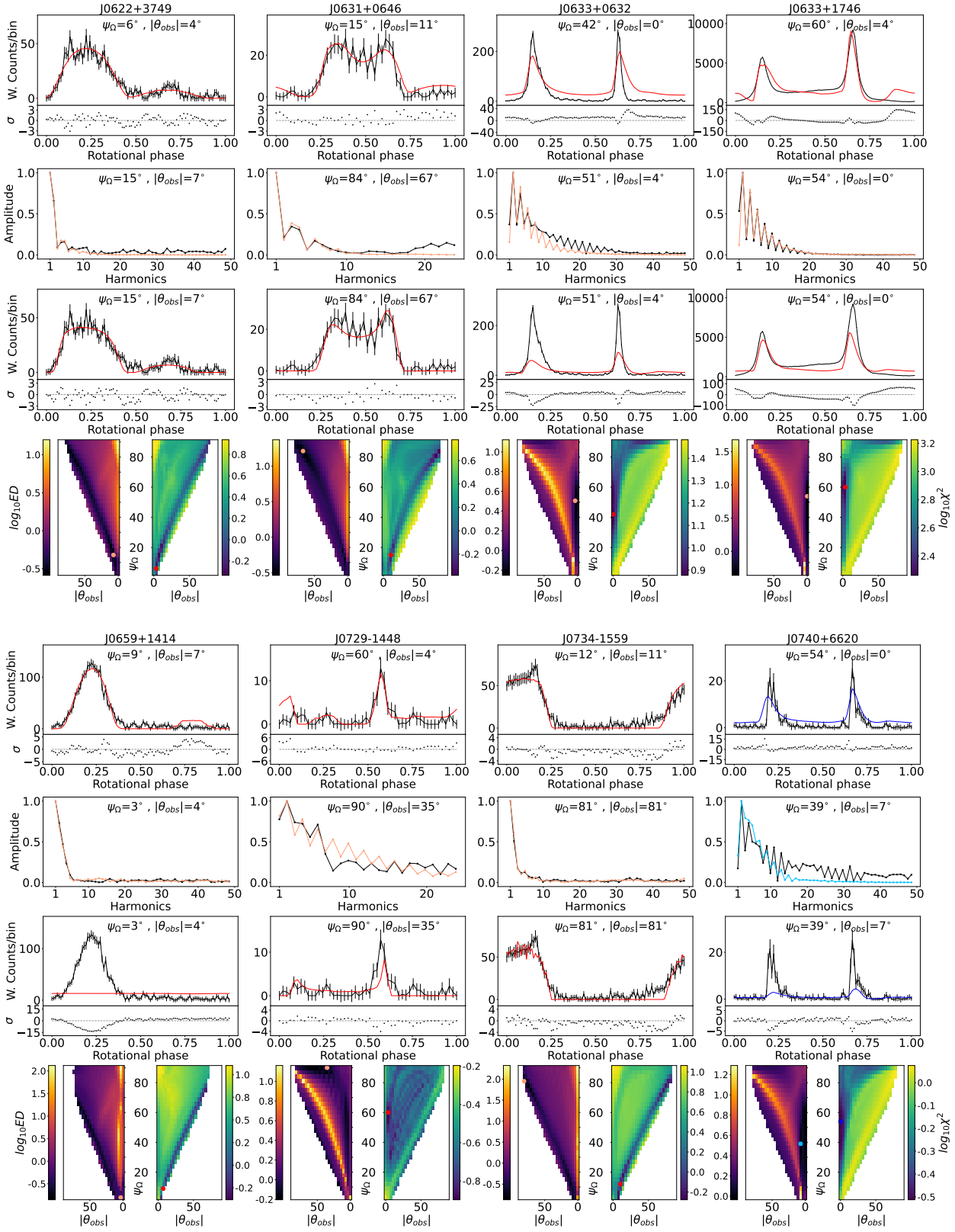


Figure F.1: - *continued*

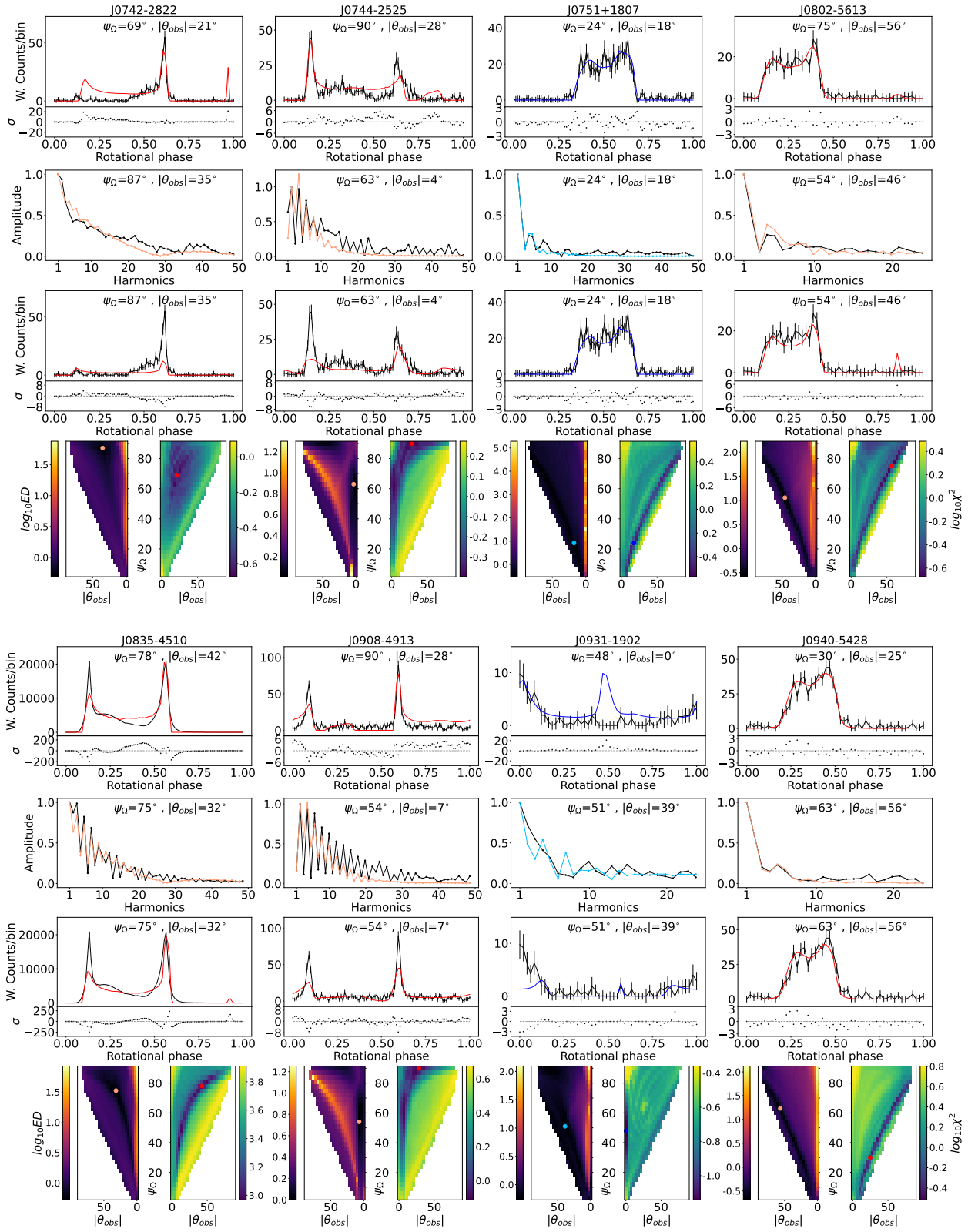


Figure F.1: - *continued*

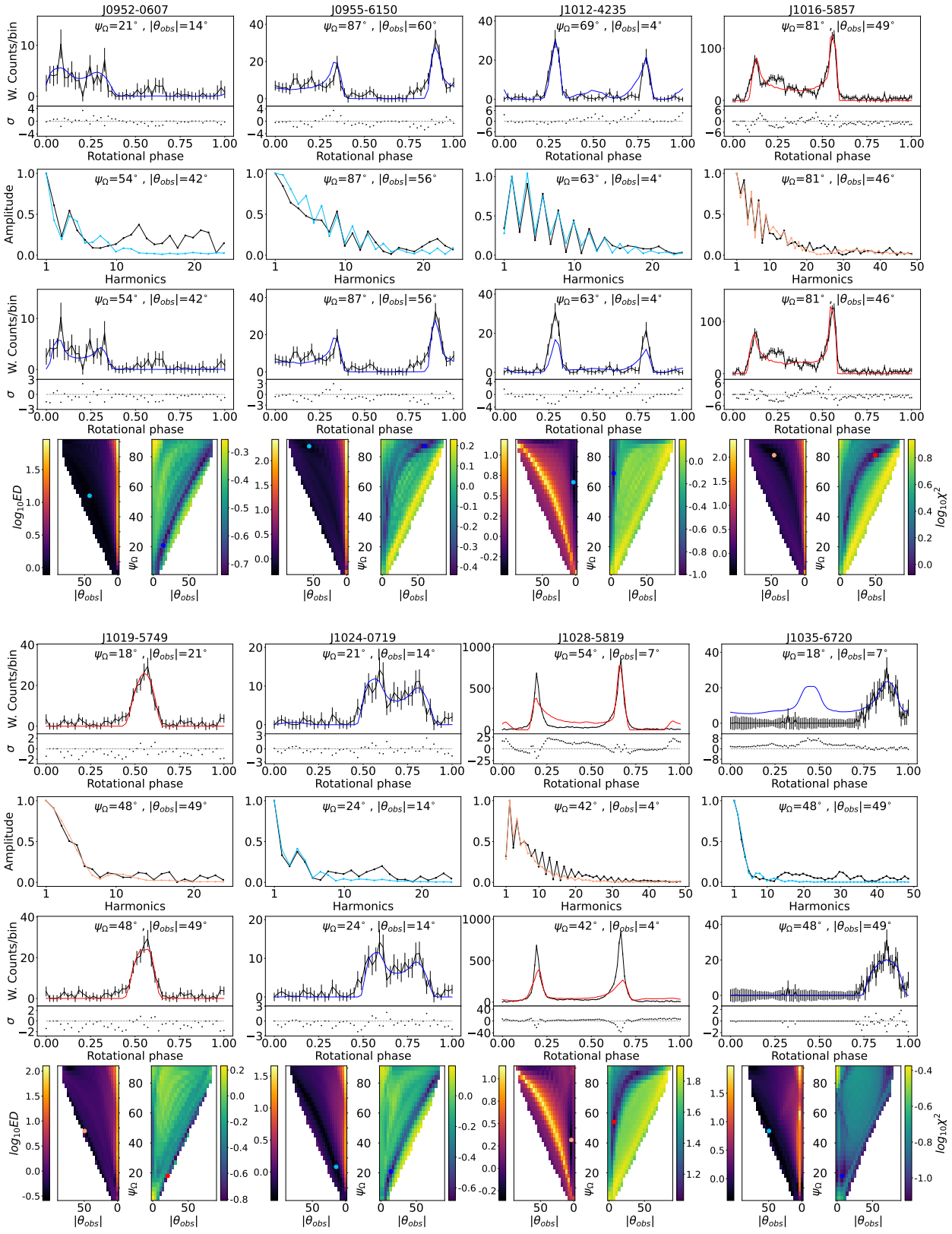


Figure F.1: - *continued*

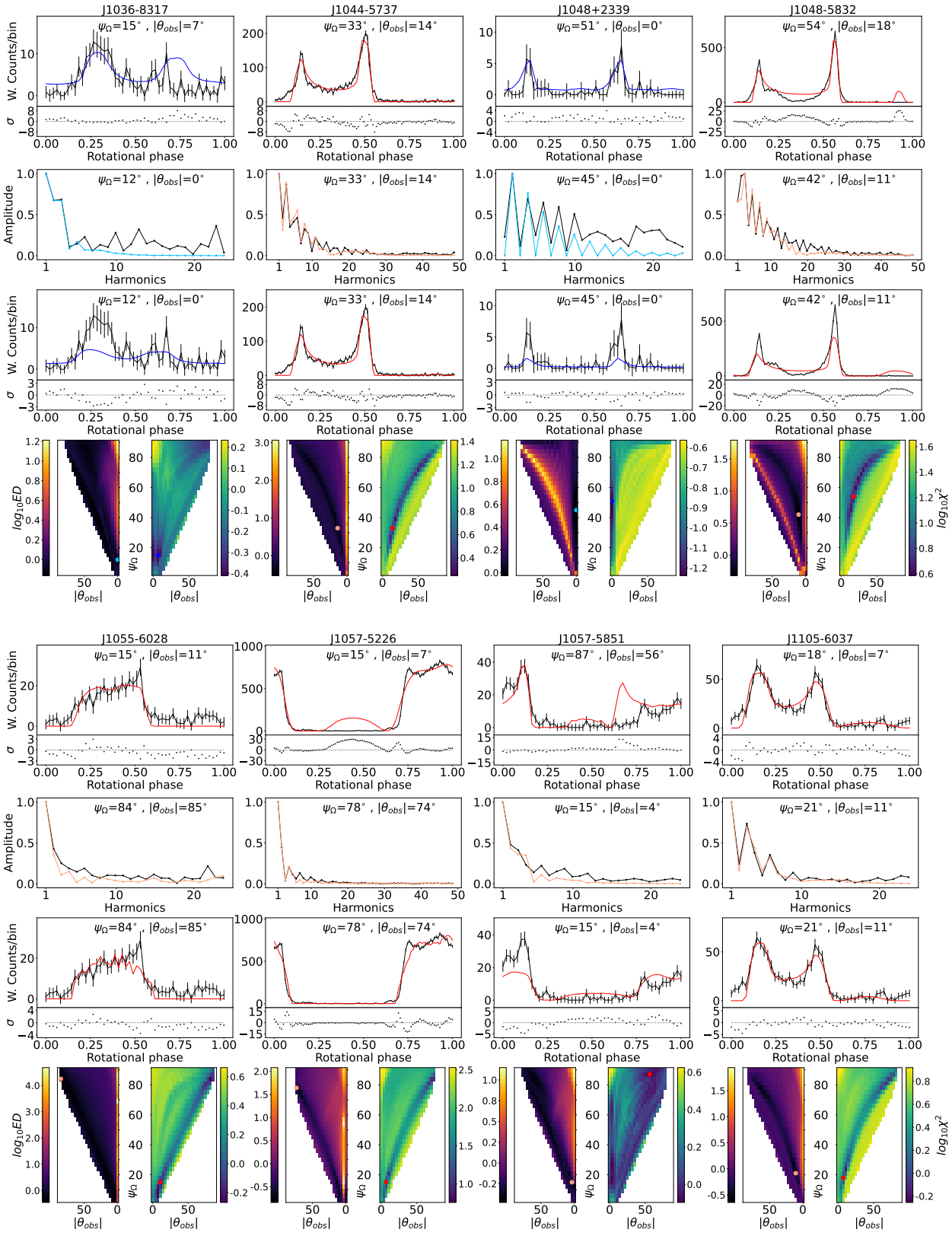


Figure F.1: - *continued*

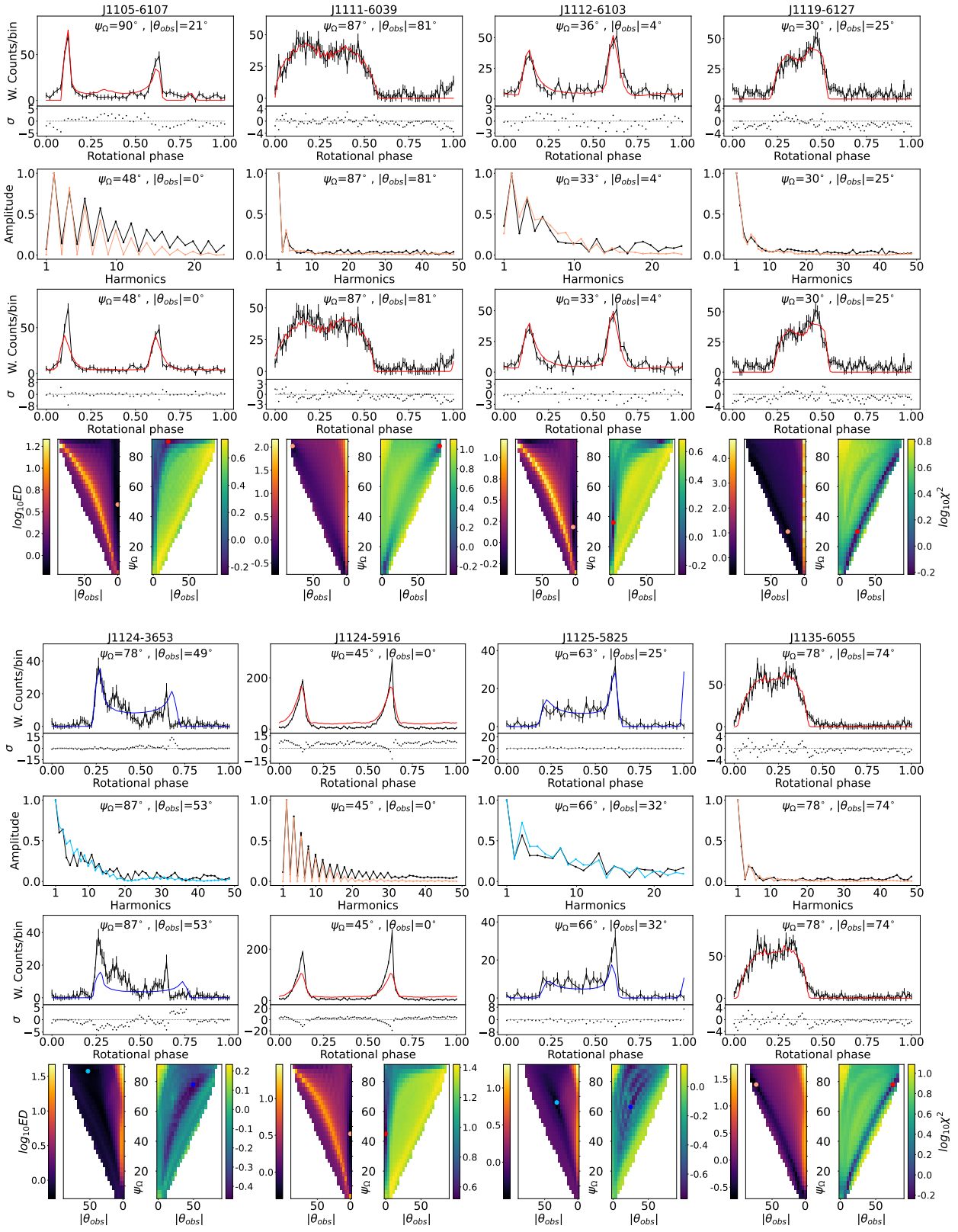


Figure F.1: - *continued*

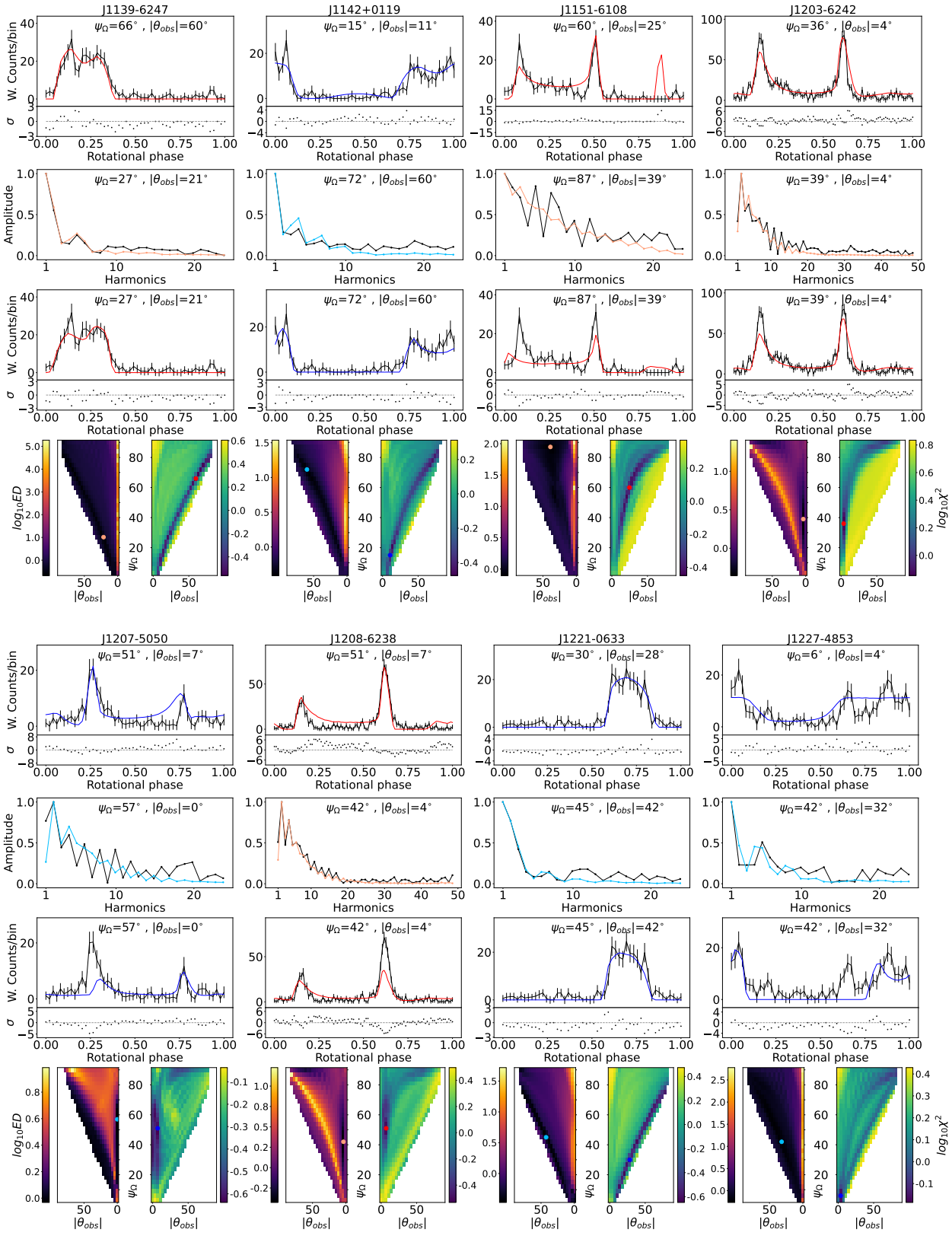


Figure F.1: - *continued*

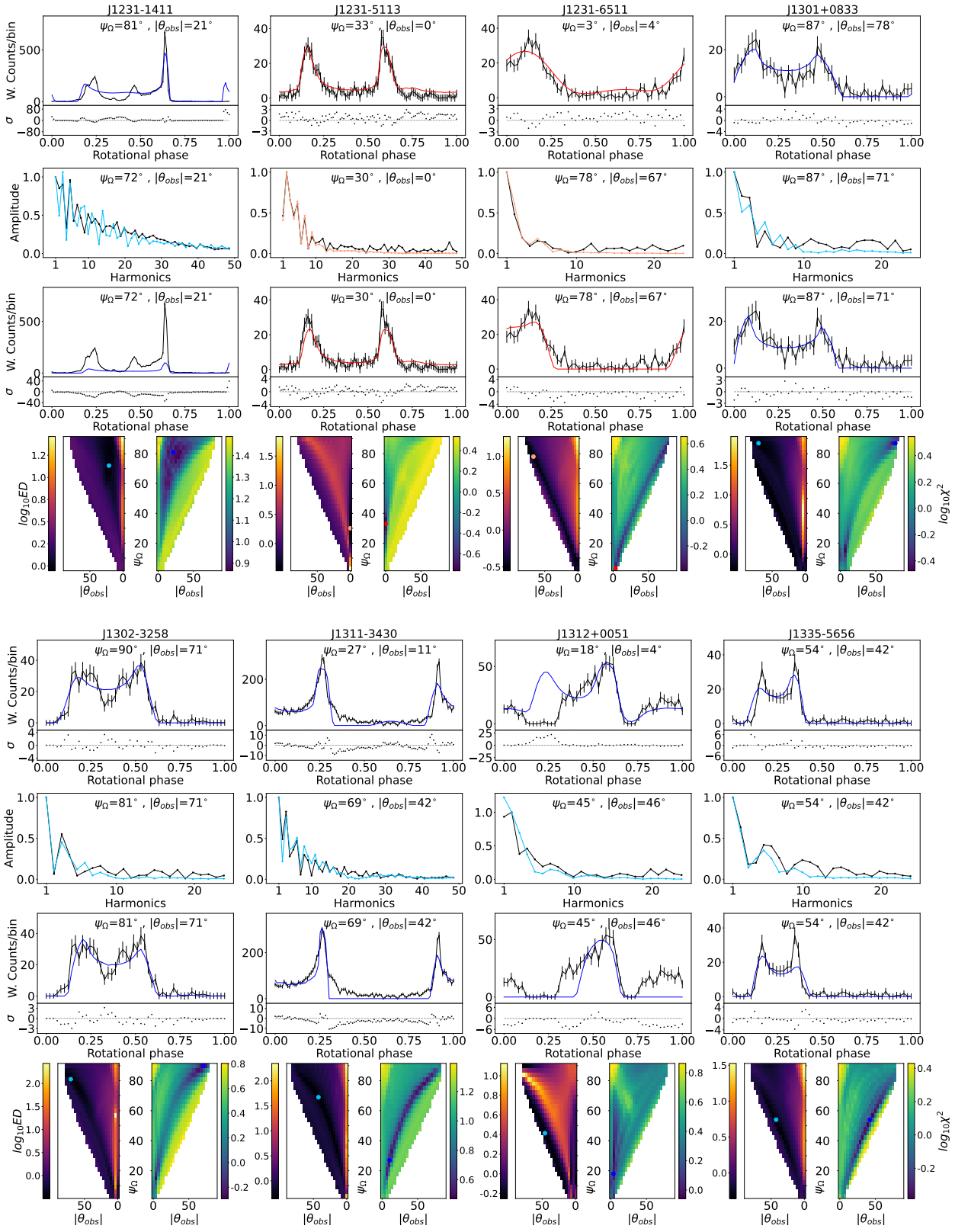


Figure F.1: - *continued*

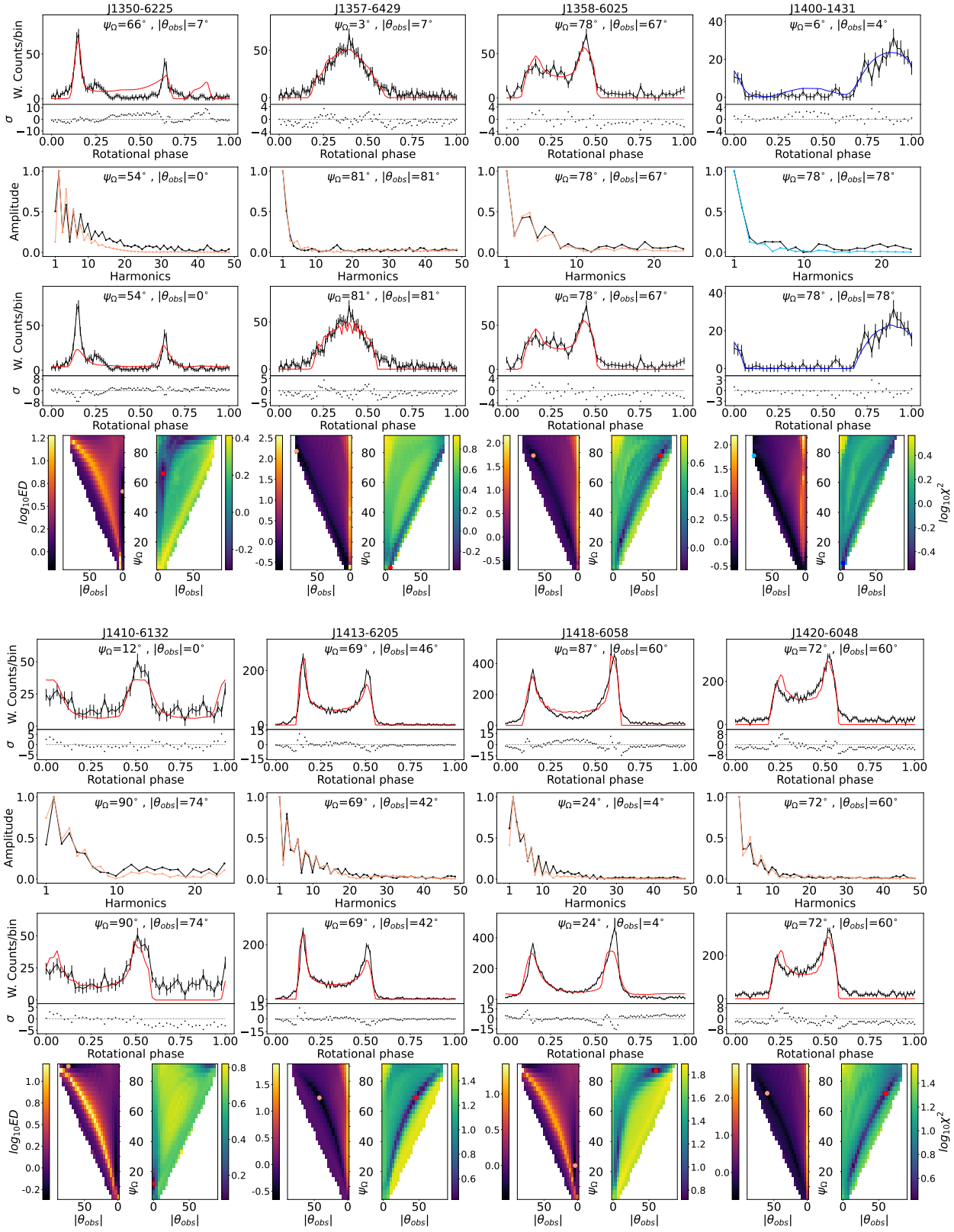


Figure F.1: - *continued*

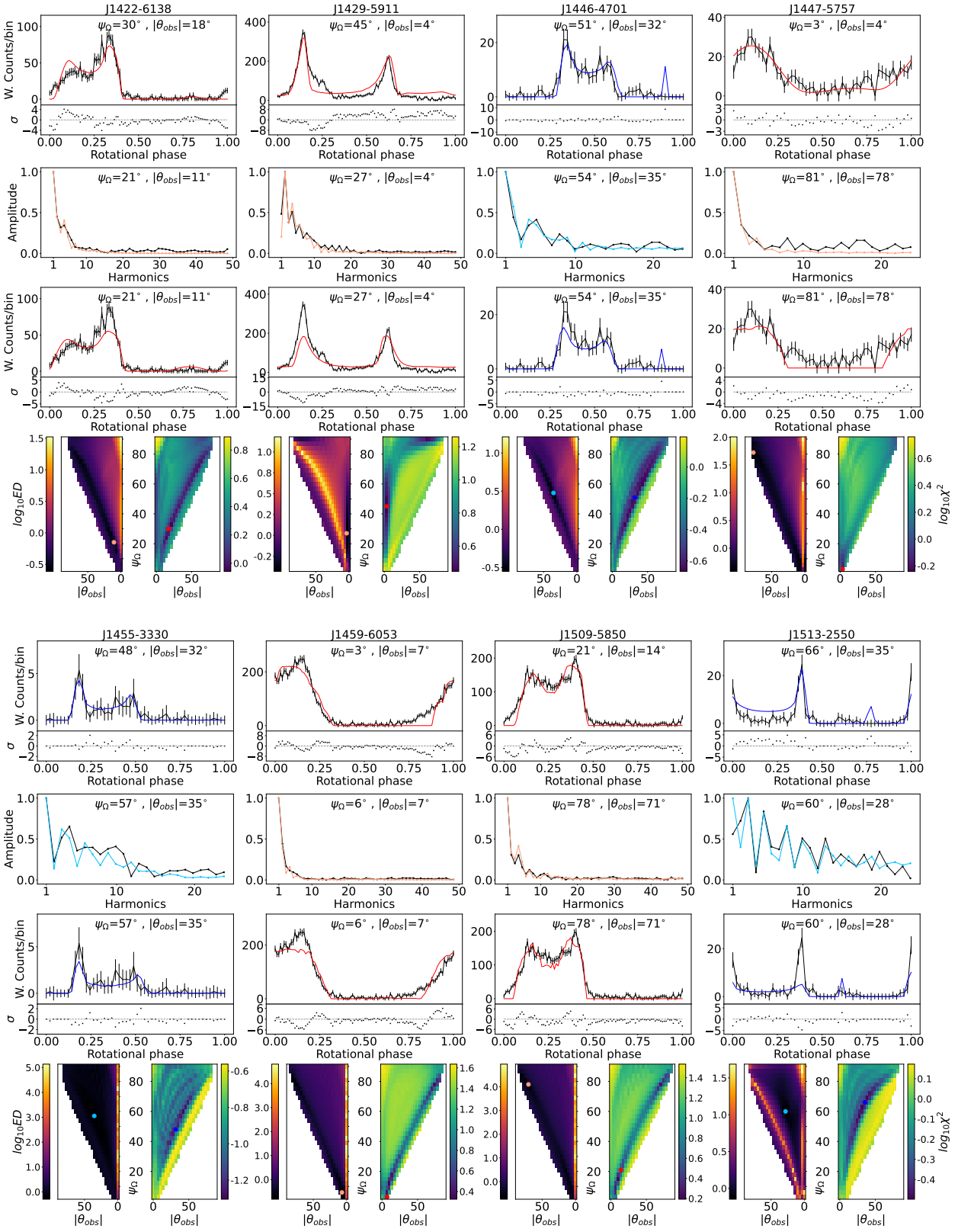


Figure F.1: - *continued*

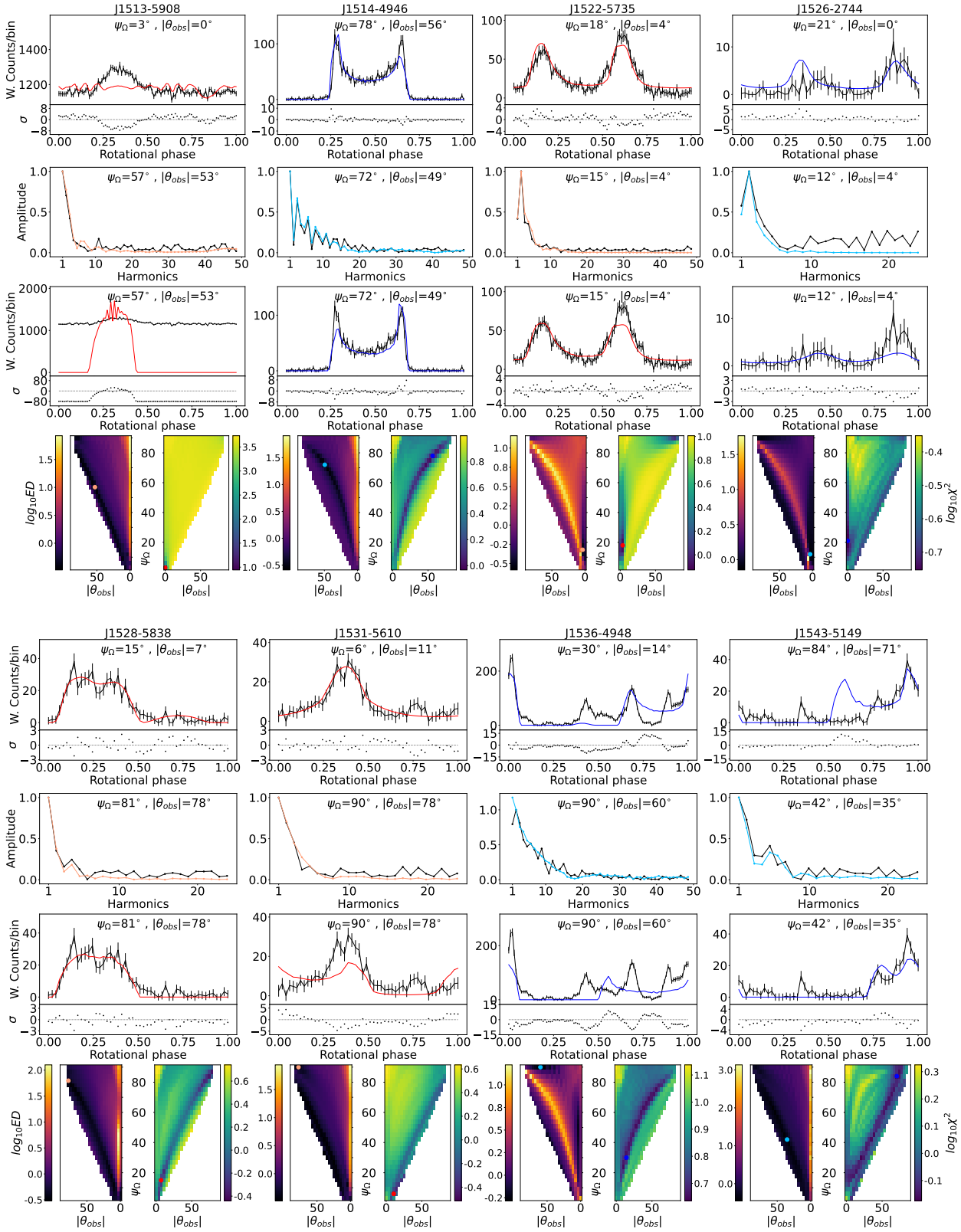


Figure F.1: - *continued*

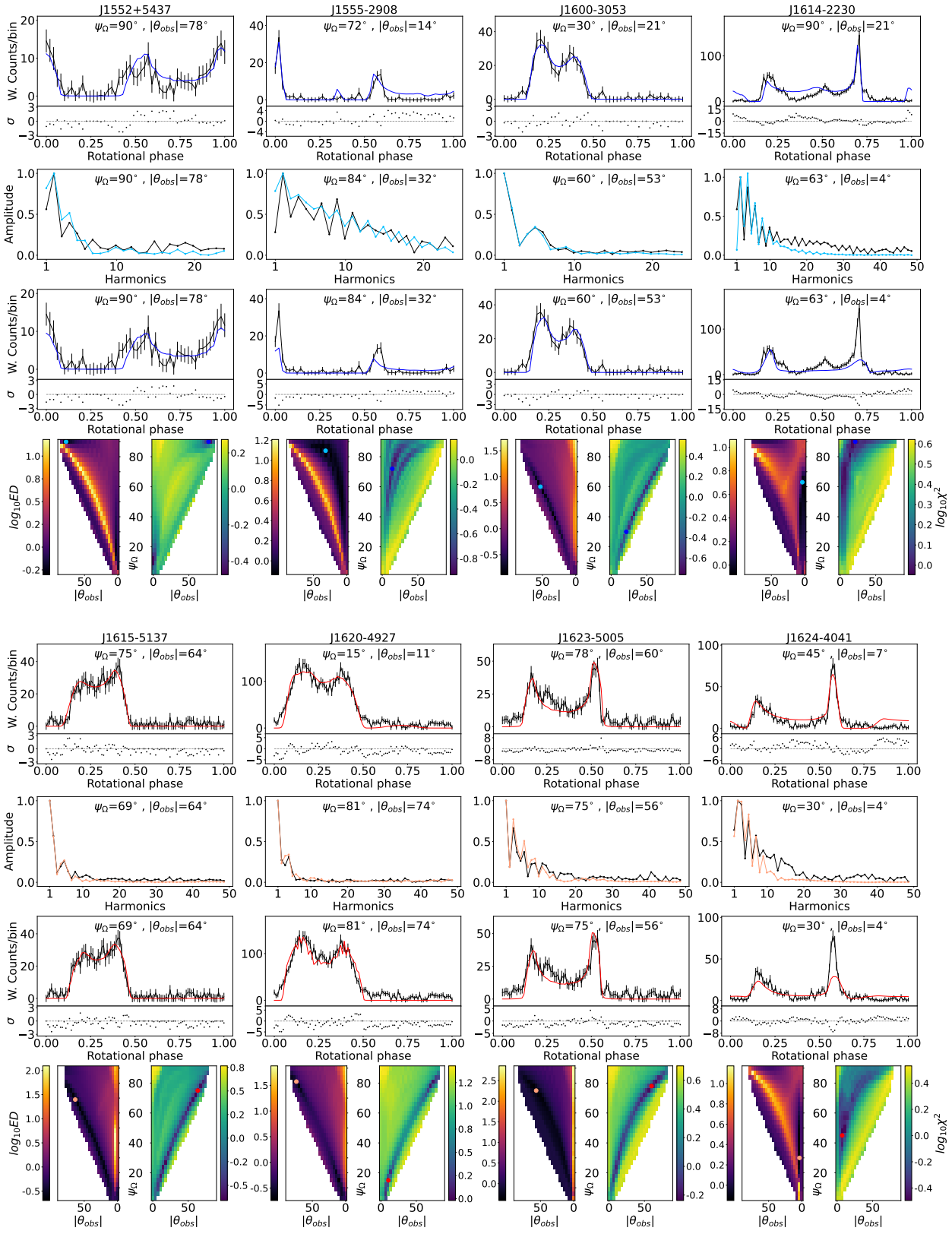


Figure F.1: - *continued*

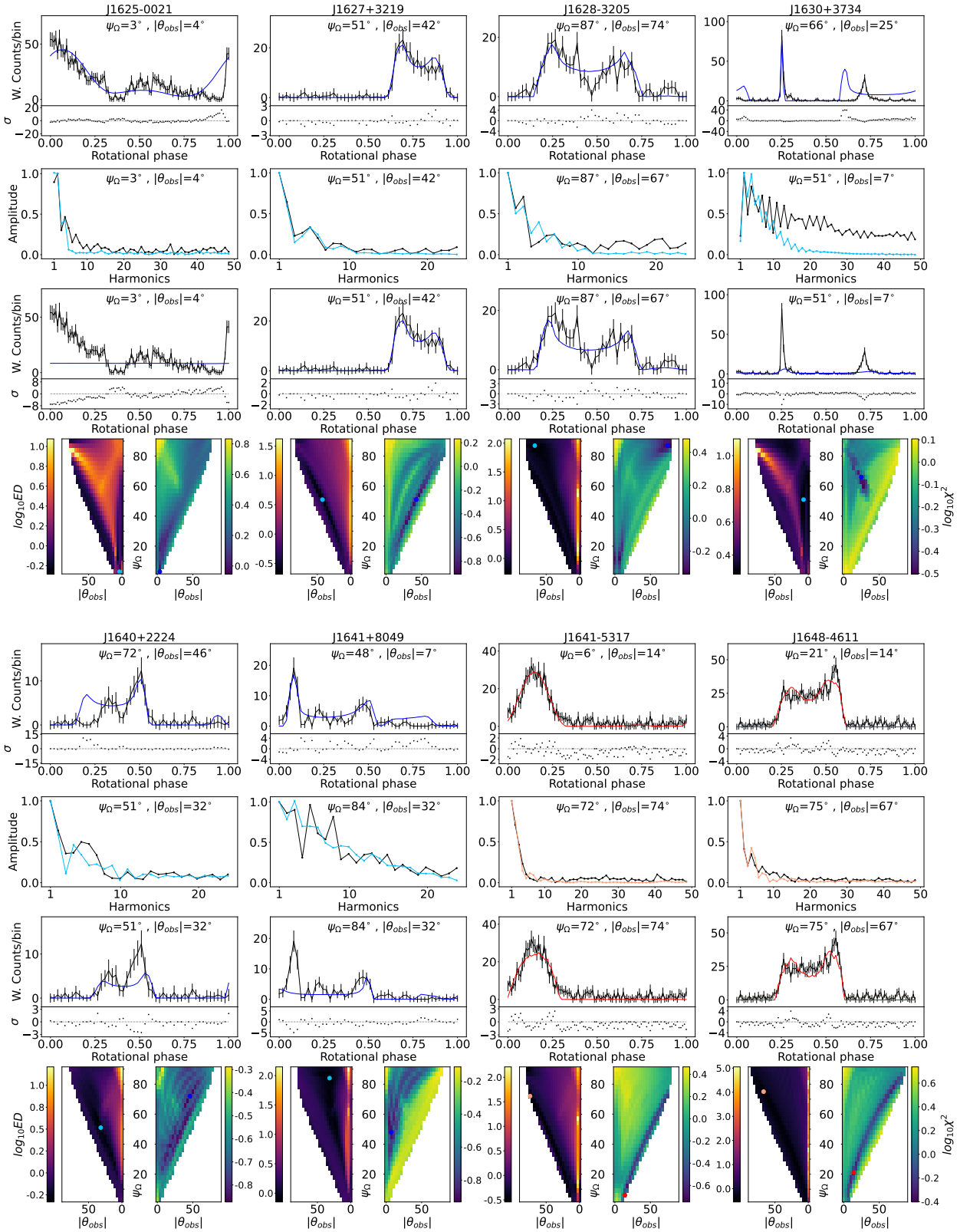


Figure F.1: - *continued*

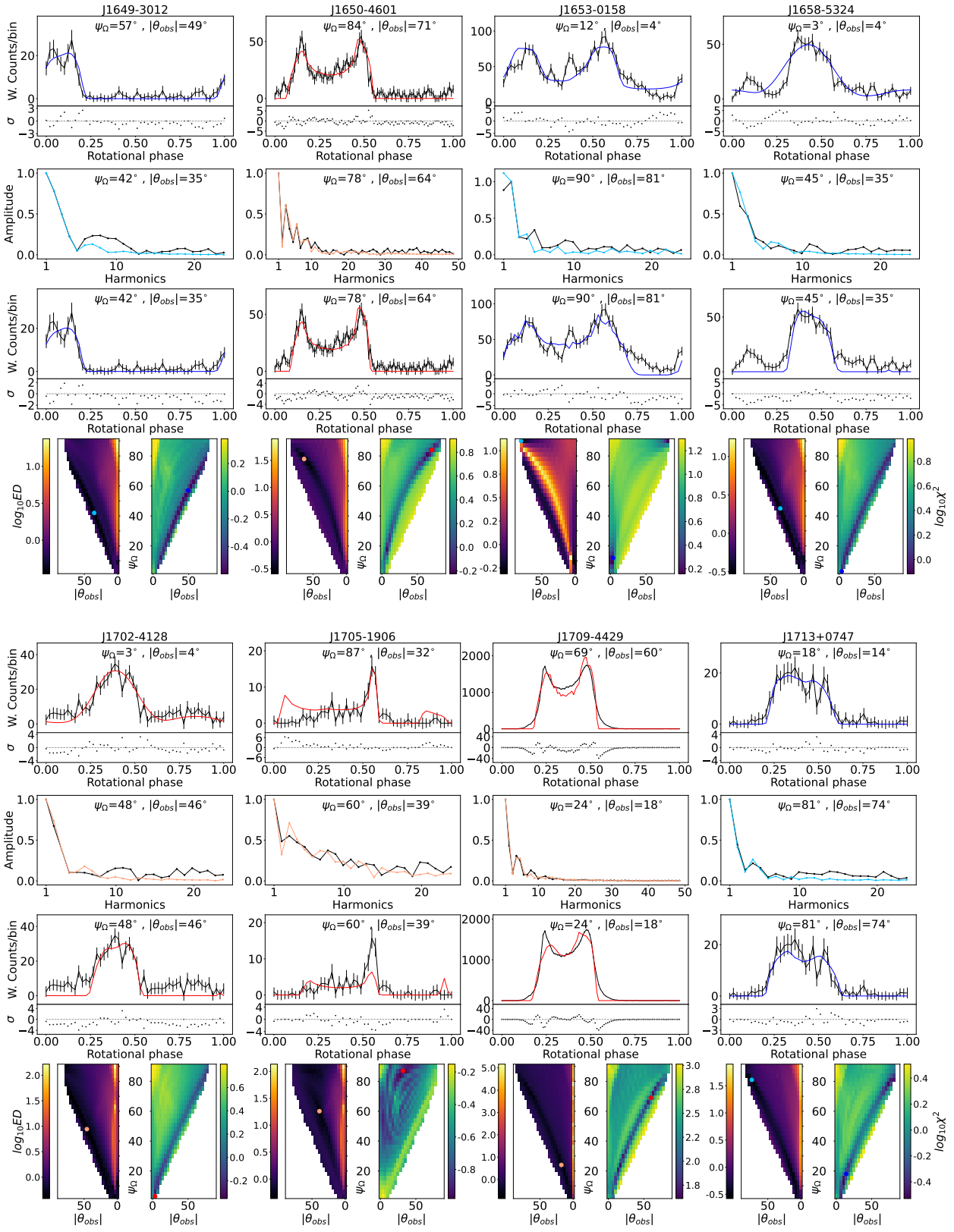


Figure F.1: - *continued*

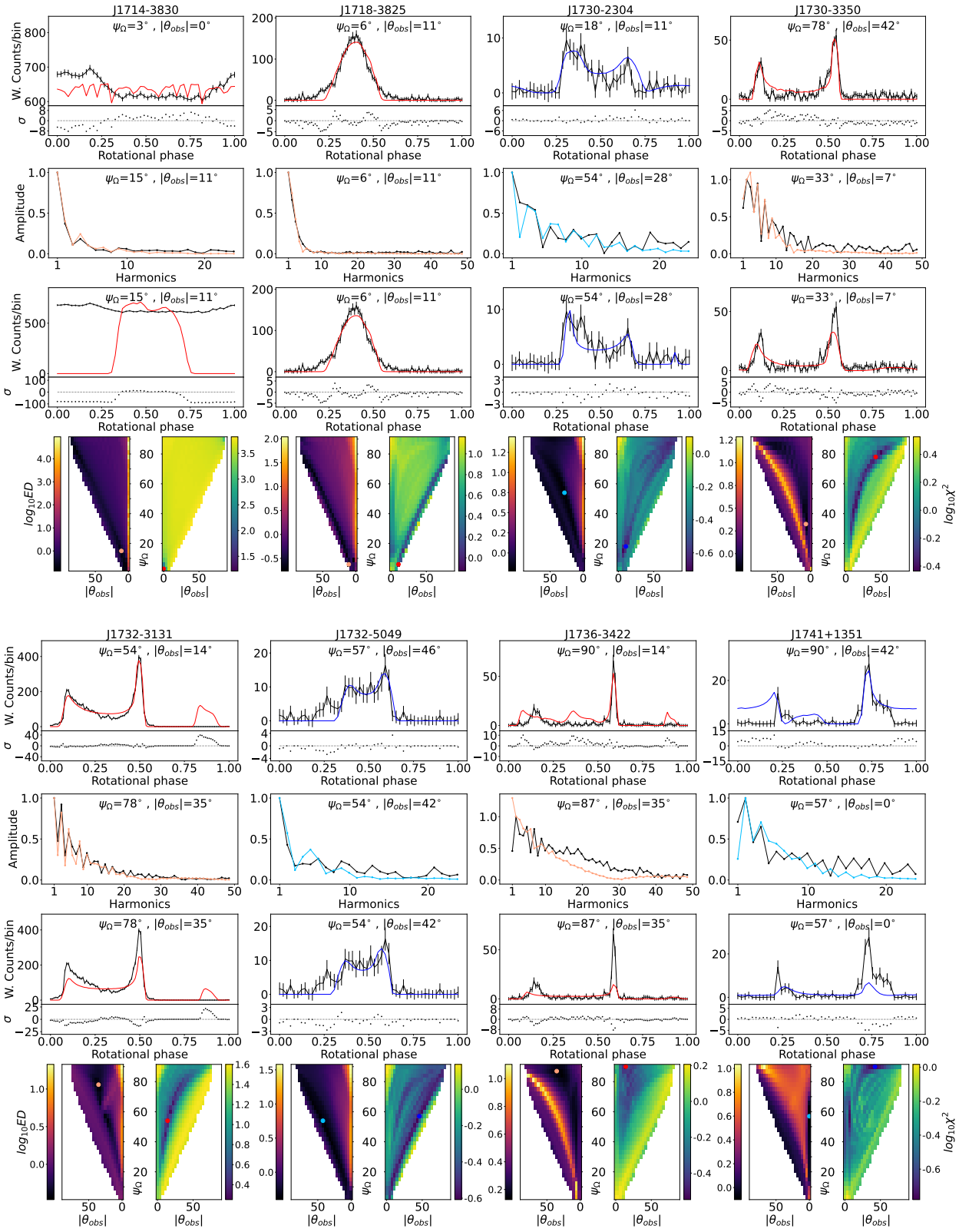


Figure F.1: - *continued*

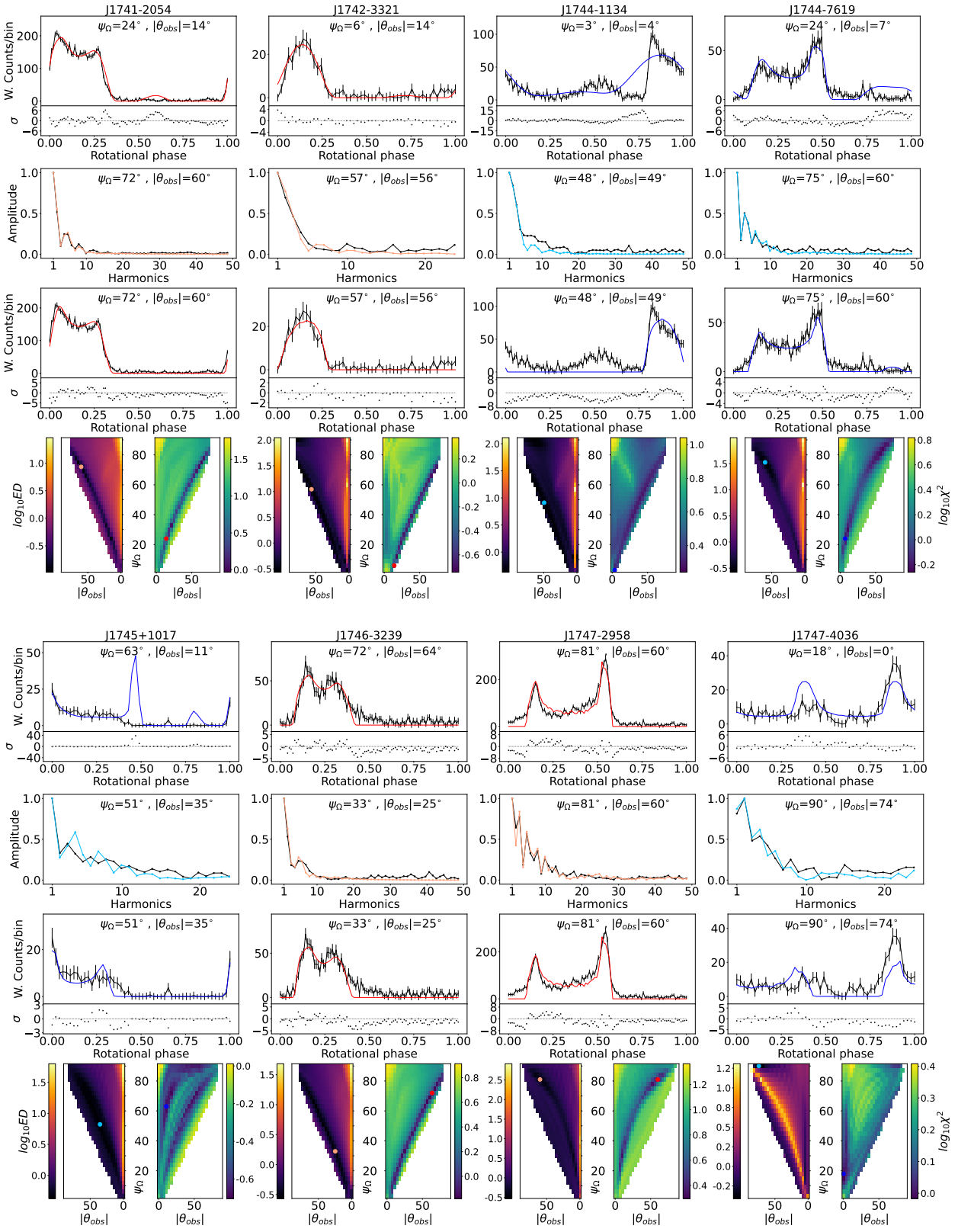


Figure F.1: - *continued*

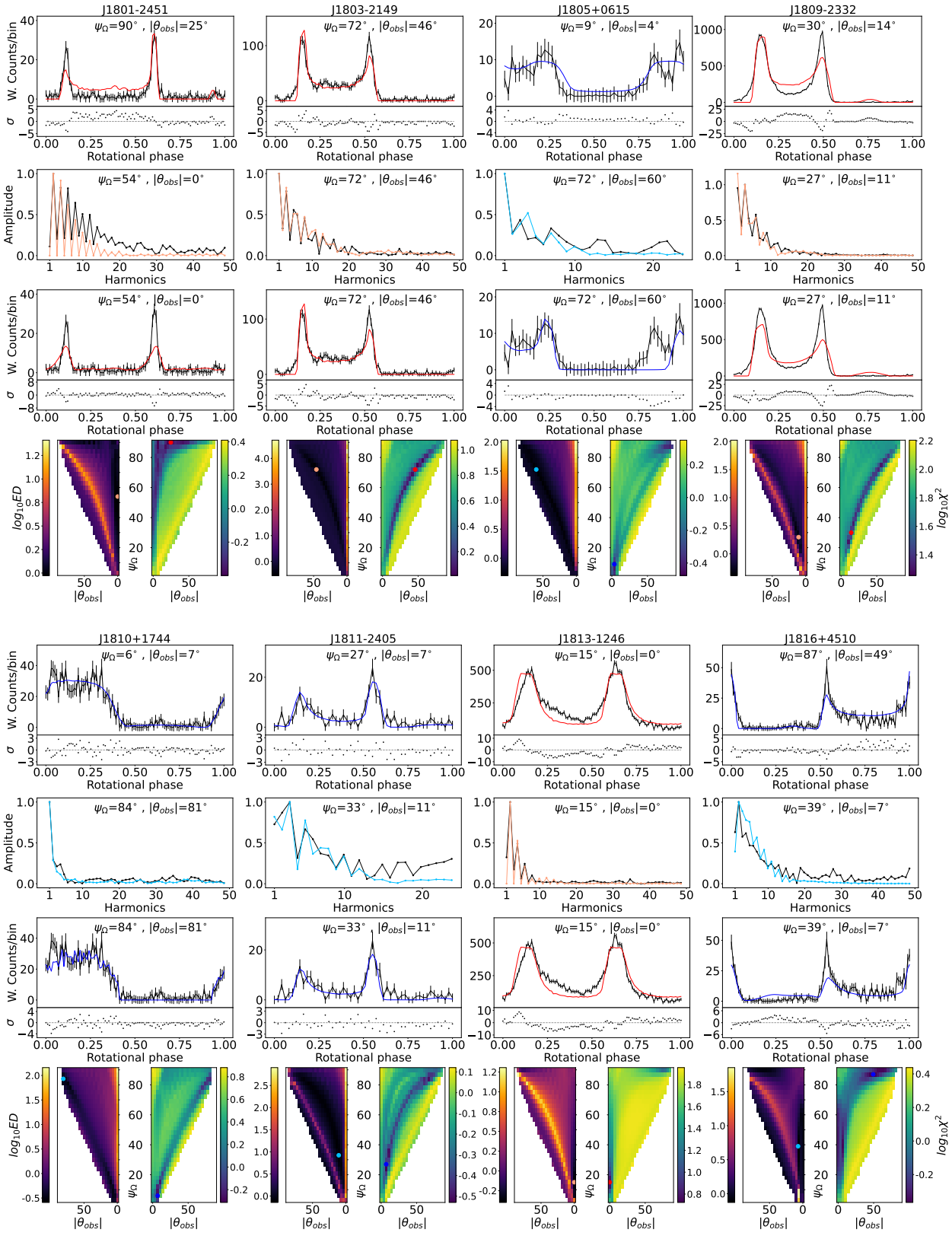


Figure F.1: - *continued*

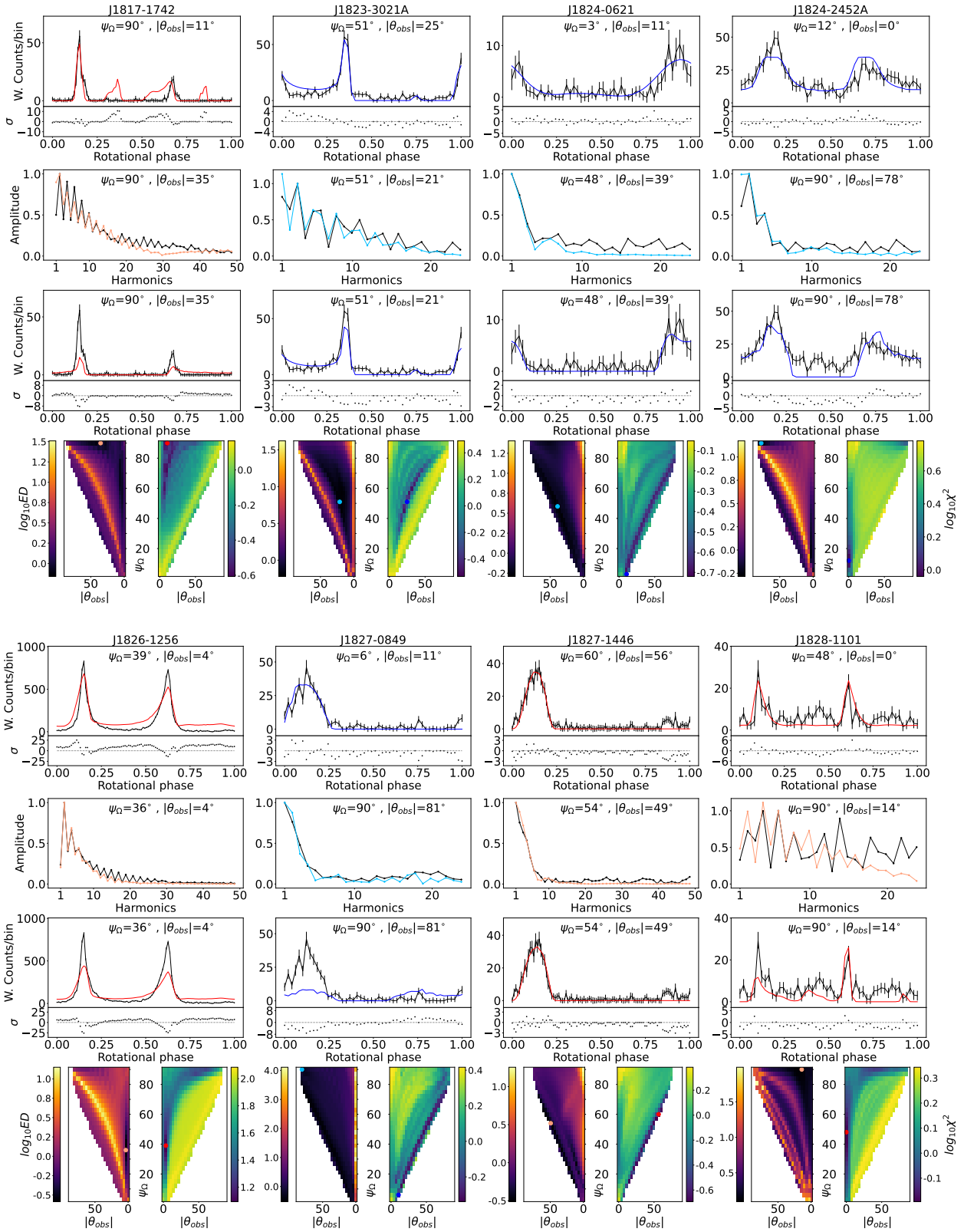


Figure F.1: - *continued*

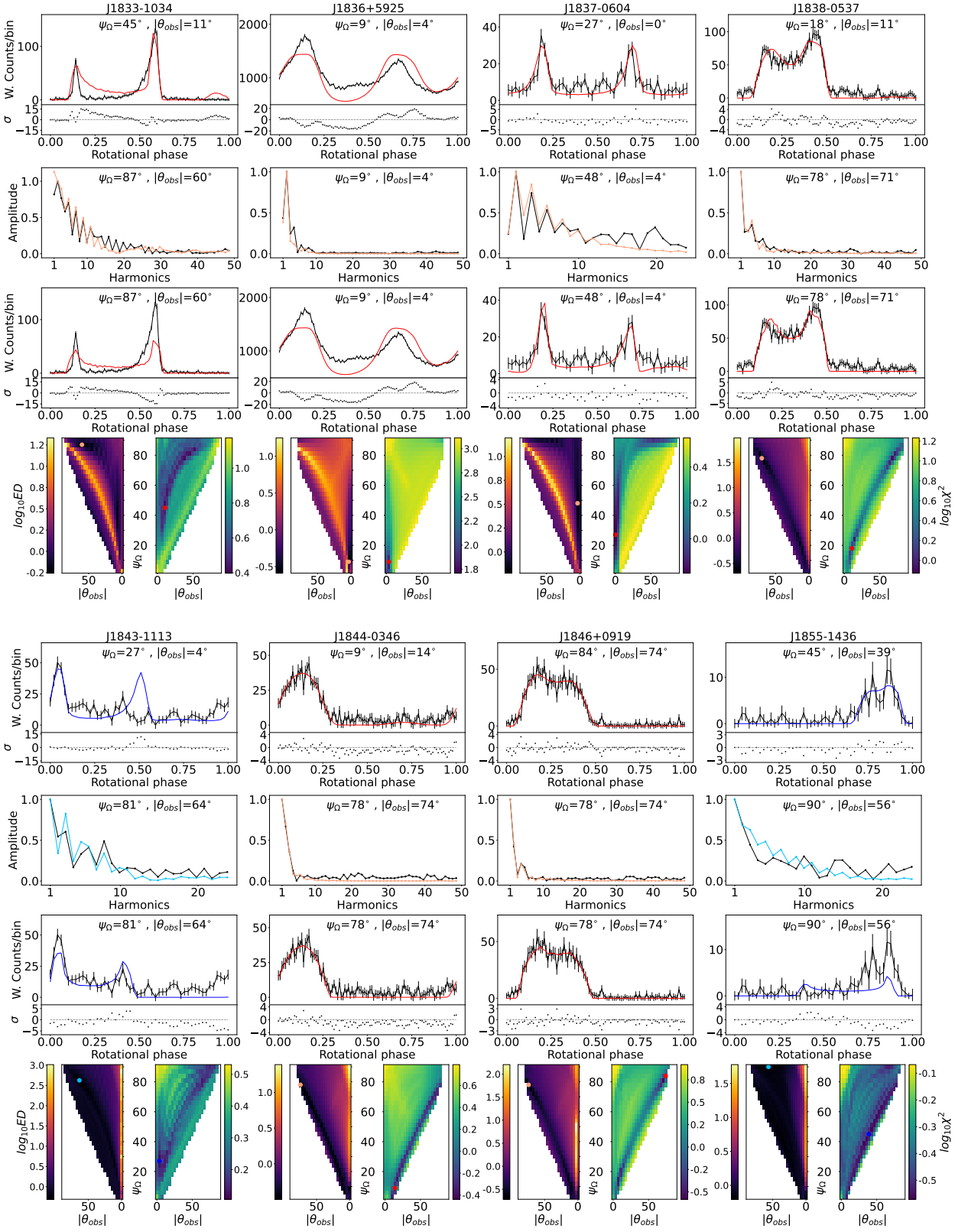


Figure F.1: - *continued*

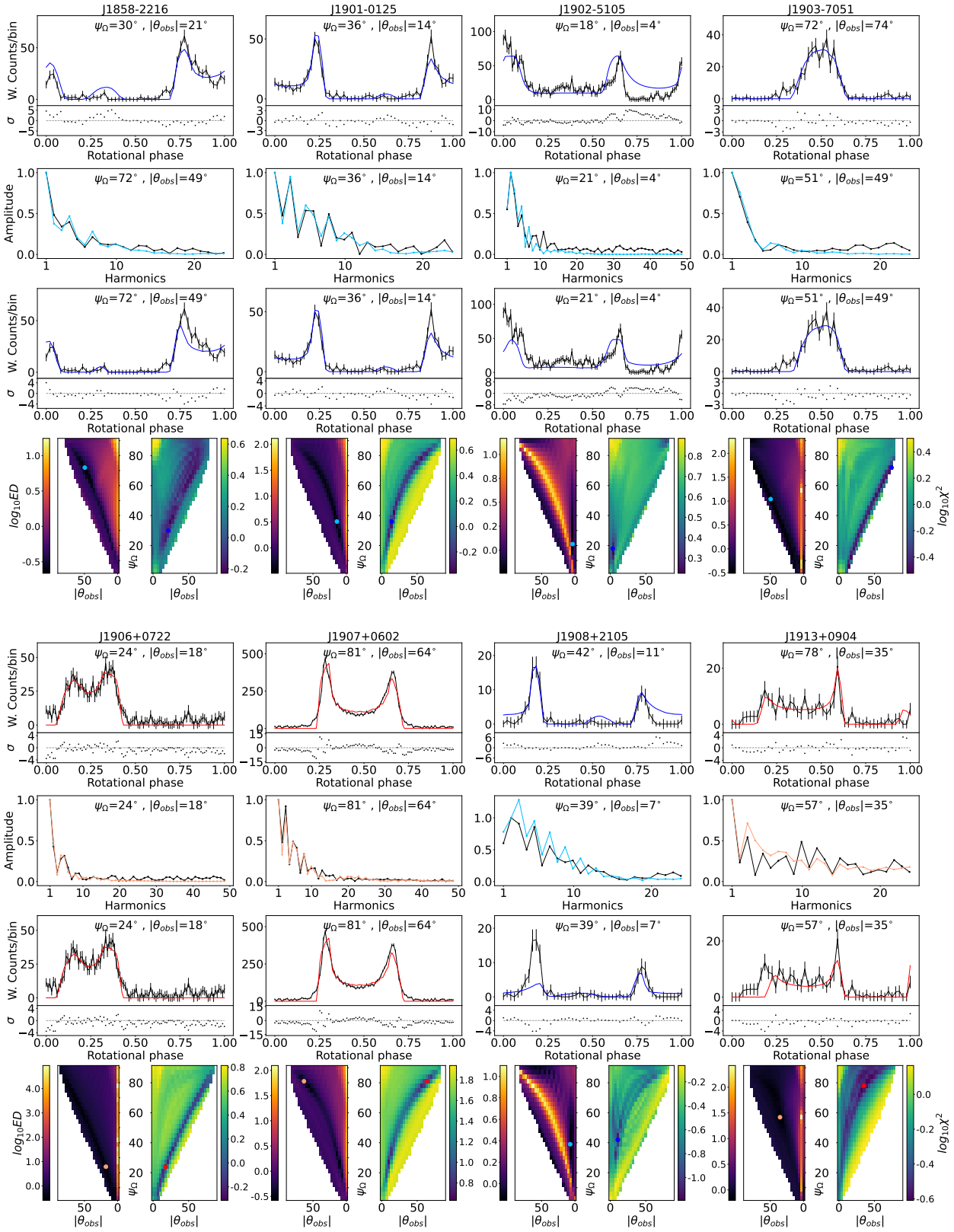


Figure F.1: - *continued*

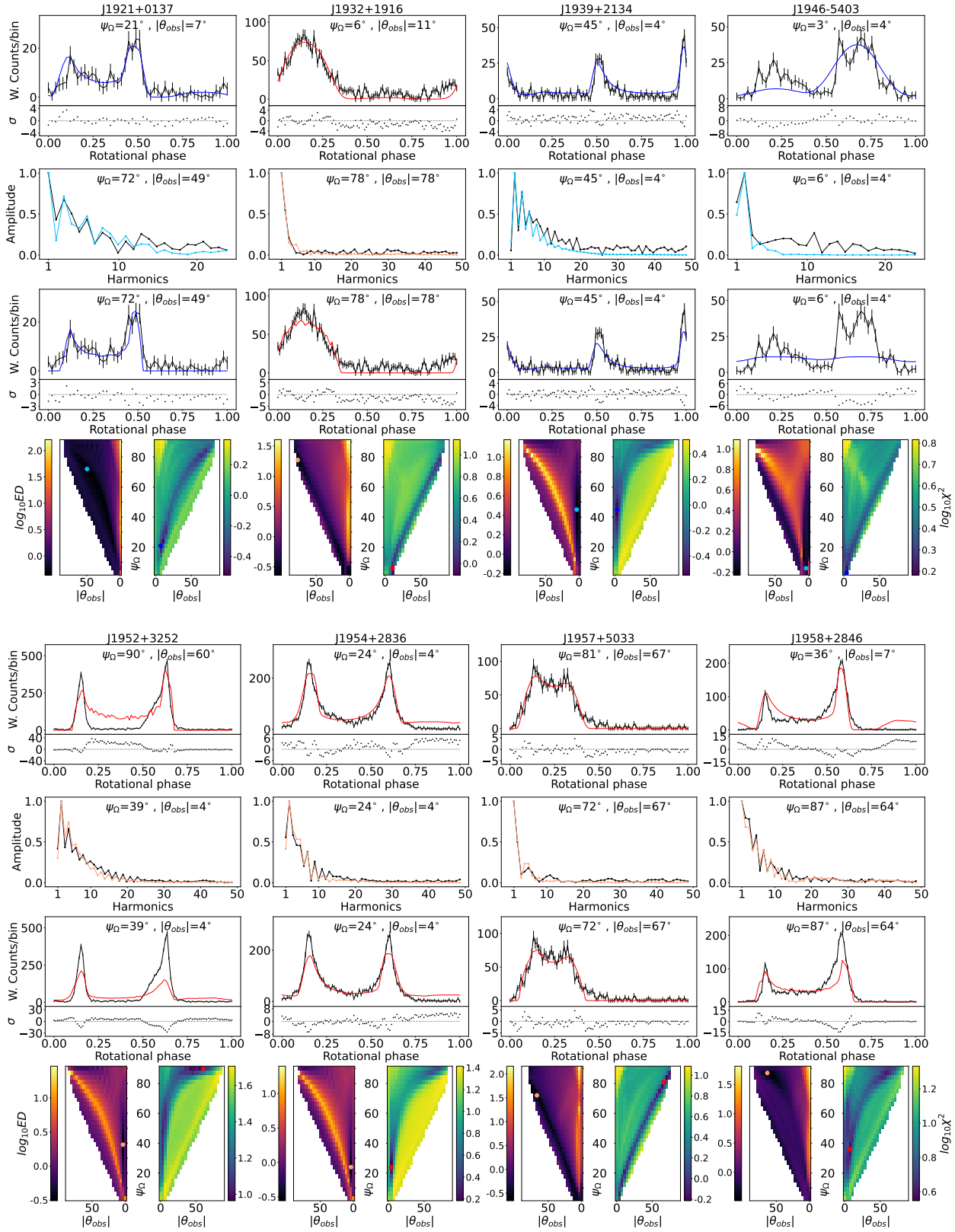


Figure F.1: - *continued*

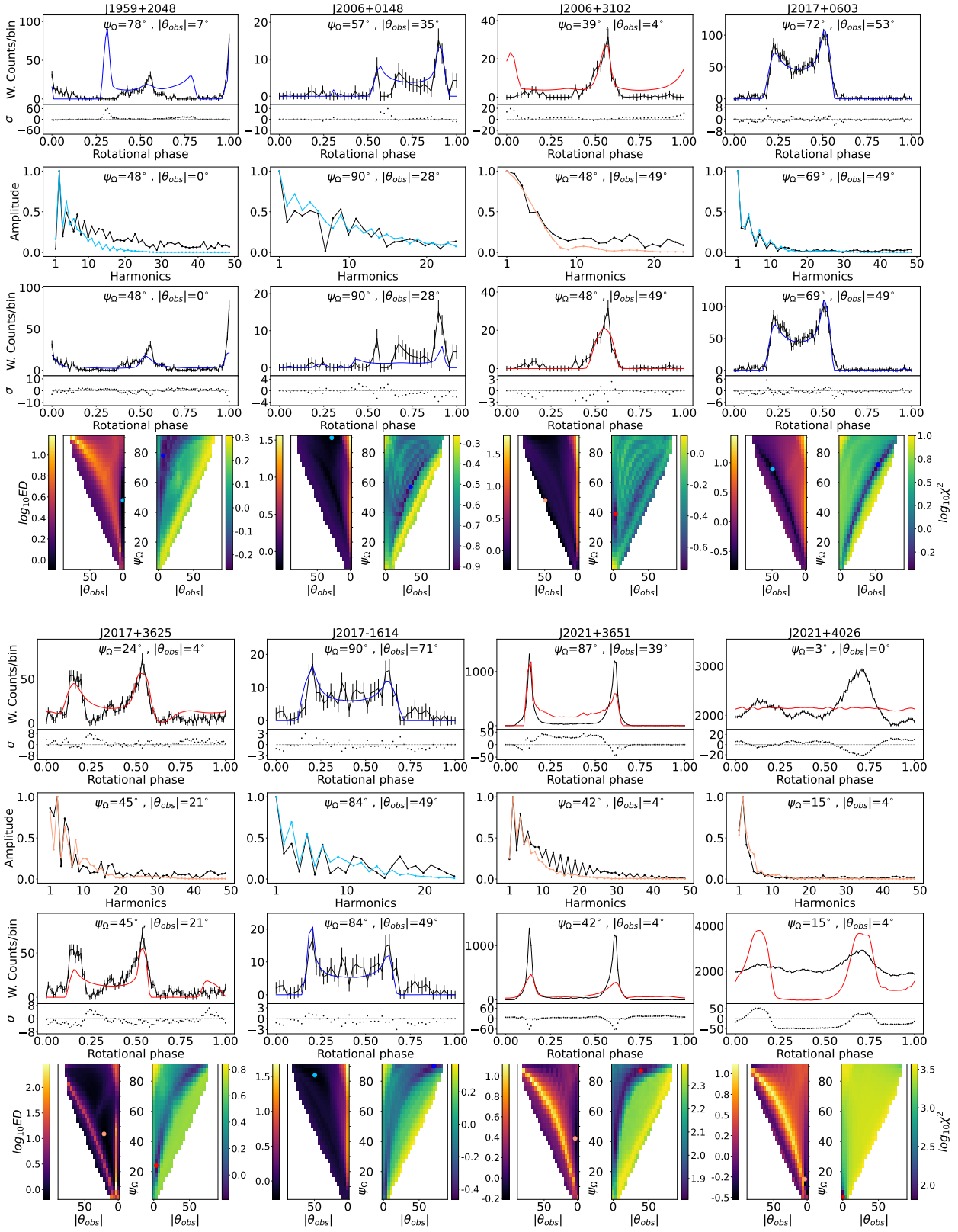


Figure F.1: - *continued*

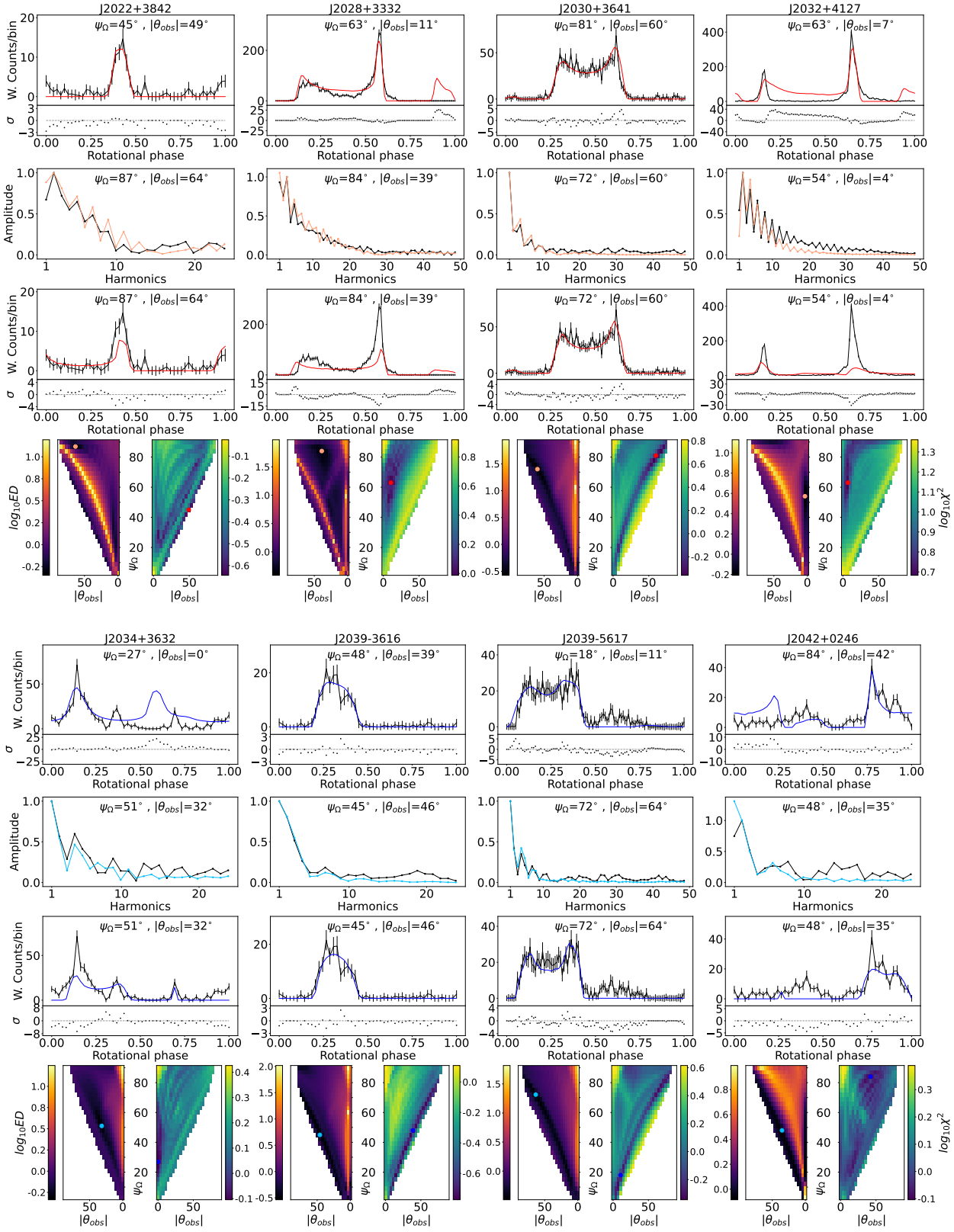


Figure F.1: - *continued*

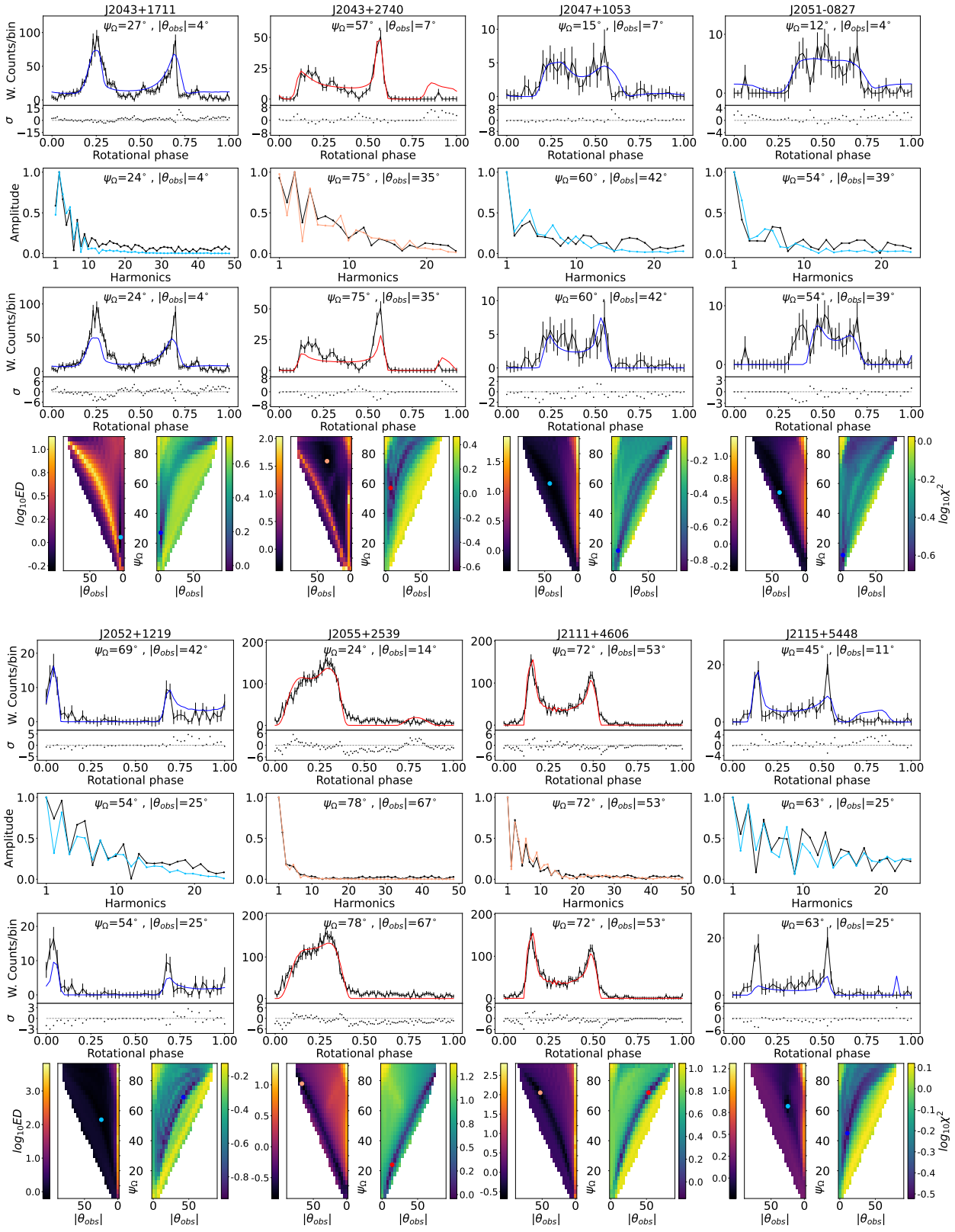


Figure F.1: - *continued*

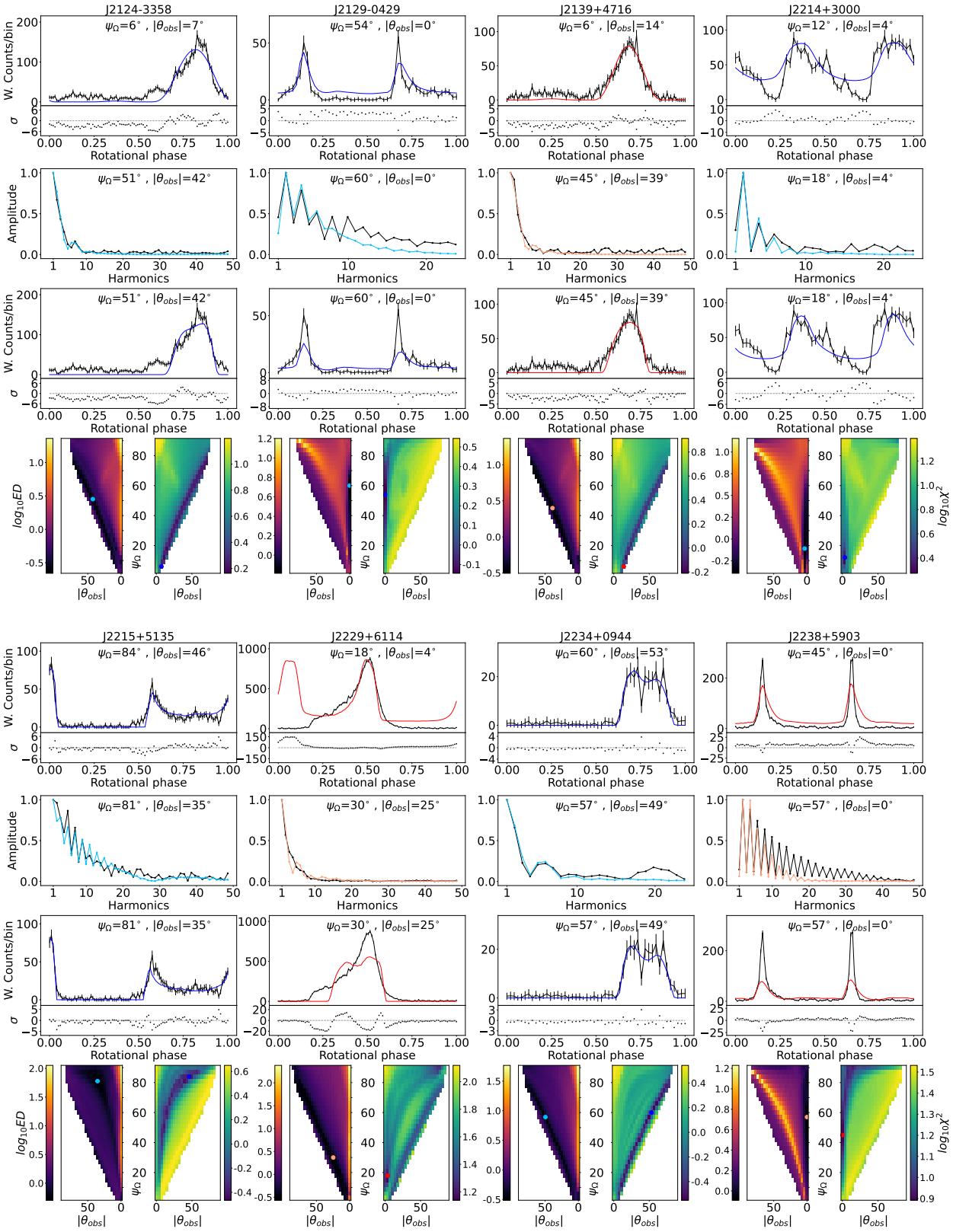


Figure F.1: - *continued*

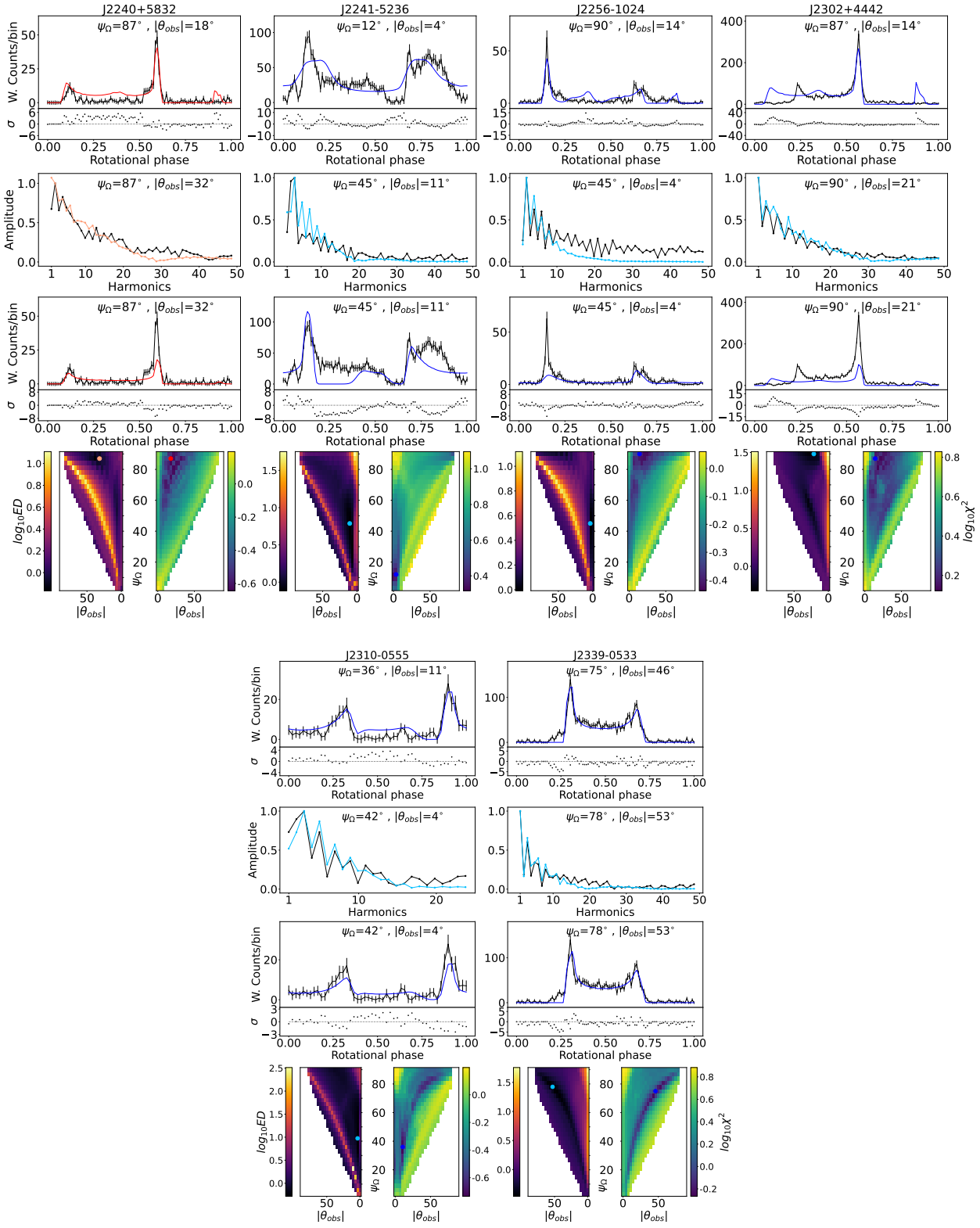


Figure F.1: - *continued*

Bibliography

B. P. Abbott, R. Abbott, T. D. Abbott, et al. GW170817: Observation of Gravitational Waves from a Binary Neutron Star Inspiral. *Phys. Rev. Lett.*, 119(16):161101, Oct. 2017. doi: 10.1103/PhysRevLett.119.161101.

A. A. Abdo, M. Ackermann, Ajello, et al. The First Fermi Large Area Telescope Catalog of Gamma-ray Pulsars. *ApJS*, 187(2):460–494, Apr. 2010a. doi: 10.1088/0067-0049/187/2/460.

A. A. Abdo, M. Ackermann, M. Ajello, et al. Fermi-LAT Observations of the Geminga Pulsar. *ApJ*, 720(1):272–283, Sept. 2010b. doi: 10.1088/0004-637X/720/1/272.

A. A. Abdo, M. Ackermann, M. Ajello, et al. The Vela Pulsar: Results from the First Year of Fermi LAT Observations. *ApJ*, 713(1):154–165, Apr. 2010c. doi: 10.1088/0004-637X/713/1/154.

A. A. Abdo, K. S. Wood, M. E. DeCesar, F. Gargano, F. Giordano, P. S. Ray, D. Parent, A. K. Harding, M. C. Miller, D. L. Wood, and M. T. Wolff. PSR J0007+7303 in the CTA1 Supernova Remnant: New Gamma-Ray Results from Two Years of Fermi Large Area Telescope Observations. *ApJ*, 744(2):146, Jan. 2012. doi: 10.1088/0004-637X/744/2/146.

A. A. Abdo, M. Ajello, Allafort, et al. The second Fermi-Large Area Telescope catalog of gamma-ray pulsars. *The Astrophysical Journal Supplement Series*, 208(2):17, Sep 2013. ISSN 1538-4365. doi: 10.1088/0067-0049/208/2/17. URL http://dx.doi.org/10.1088/0067-0049/208/2/17.

S. Abdollahi, F. Acero, L. Baldini, et al. Incremental Fermi Large Area Telescope Fourth Source Catalog. *ApJS*, 260(2):53, June 2022. doi: 10.3847/1538-4365/ac6751.

K. Abe, S. Abe, A. Abhishek, et al. A detailed study of the very high-energy Crab pulsar emission with the LST-1. *A&A*, 690:A167, Oct. 2024. doi: 10.1051/0004-6361/202450059.

V. A. Acciari, S. Ansoldi, L. A. Antonelli, et al. Search for Very High-energy Emission from the Millisecond Pulsar PSR J0218+4232. *ApJ*, 922(2):251, Dec. 2021. doi: 10.3847/1538-4357/ac20d7.

D. Agarwal, E. F. Lewis, D. R. Lorimer, M. A. McLaughlin, B. Cui, A. Turner, and N. McMann. The RRATalog: a Galactic census of rotating radio transients. *MNRAS*, Apr. 2026. doi: 10.1093/mnras/stag787.

L. G. Althaus, A. H. Córsico, J. Isern, and E. García-Berro. Evolutionary and pulsational properties of white dwarf stars. *A&A Rev.*, 18(4):471–566, Oct. 2010. doi: 10.1007/s00159-010-0033-1.

N. Andersson, K. Glampedakis, W. C. G. Ho, and C. M. Espinoza. Pulsar Glitches: The Crust is not Enough. *Phys. Rev. Lett.*, 109(24):241103, Dec. 2012. doi: 10.1103/PhysRevLett.109.241103.

S. Ansoldi, L. A. Antonelli, P. Antoranz, et al. Teraelectronvolt pulsed emission from the Crab Pulsar detected by MAGIC. *A&A*, 585:A133, Jan. 2016. doi: 10.1051/0004-6361/201526853.

D. Antonopoulou, B. Haskell, and C. M. Espinoza. Pulsar glitches: observations and physical interpretation. *Reports on Progress in Physics*, 85(12):126901, Dec. 2022. doi: 10.1088/1361-6633/ac9ced.

R. F. Archibald, E. V. Gotthelf, R. D. Ferdman, V. M. Kaspi, S. Guillot, F. A. Harrison, E. F. Keane, M. J. Pivovaroff, D. Stern, S. P. Tendulkar, and J. A. Tomsick. A High Braking Index for a Pulsar. *ApJ*, 819(1):L16, Mar. 2016a. doi: 10.3847/2041-8205/819/1/L16.

R. F. Archibald, V. M. Kaspi, S. P. Tendulkar, and P. Scholz. A Magnetar-like Outburst from a High-B Radio Pulsar. *ApJ*, 829(1):L21, Sept. 2016b. doi: 10.3847/2041-8205/829/1/L21.

J. Arons. Pair creation above pulsar polar caps : geometrical structure and energetics of slot gaps. *The Astrophysical Journal*, 266:215–241, Mar. 1983. doi: 10.1086/160771.

J. Arons and E. T. Scharlemann. Pair formation above pulsar polar caps: structure of the low altitude acceleration zone. *ApJ*, 231:854–879, Aug. 1979. doi: 10.1086/157250.

W. B. Atwood, A. A. Abdo, Ackermann, et al. The Large Area Telescope on the Fermi Gamma-Ray Space Telescope Mission. *ApJ*, 697(2):1071–1102, June 2009. doi: 10.1088/0004-637X/697/2/1071.

Y. Avni. Energy spectra of X-ray clusters of galaxies. *ApJ*, 210:642–646, Dec. 1976. doi: 10.1086/154870.

W. Baade and F. Zwicky. Remarks on Super-Novae and Cosmic Rays. *Physical Review*, 46 (1):76–77, July 1934. doi: 10.1103/PhysRev.46.76.2.

A. Bahramian and N. Degenaar. Low-Mass X-ray Binaries. In *Handbook of X-ray and Gamma-ray Astrophysics*, page 120. 2023. doi: 10.1007/978-981-16-4544-0_94-1.

X.-N. Bai and A. Spitkovsky. Modeling of Gamma-ray Pulsar Light Curves Using the Force-free Magnetic Field. *ApJ*, 715(2):1282–1301, June 2010. doi: 10.1088/0004-637X/715/2/1282.

W. Becker. X-Ray Emission from Pulsars and Neutron Stars. In W. Becker, editor, *Neutron Stars and Pulsars*, volume 357 of *Astrophysics and Space Science Library*, page 91, Jan. 2009. doi: 10.1007/978-3-540-76965-1.

M. Bejger and P. Haensel. Moments of inertia for neutron and strange stars: Limits derived for the Crab pulsar. *A&A*, 396:917–921, Dec. 2002. doi: 10.1051/0004-6361:20021241.

M. A. Belyaev. Dissipation, energy transfer, and spin-down luminosity in 2.5D PIC simulations of the pulsar magnetosphere. *MNRAS*, 449(3):2759–2767, May 2015. doi: 10.1093/mnras/stv468.

D. J. Berndt and J. Clifford. Using dynamic time warping to find patterns in time series. In *KDD Workshop*, 1994. URL https://api.semanticscholar.org/CorpusID:929893.

R. D. Blandford. in Lighthouses of the Universe: The Most Luminous Celestial Objects and Their Use for Cosmology, eds. M. Gilfanov, R. Sunyeav, & E. Churazov (Berlin Heidelberg: Springer). *ESO Astrophysics Symposia*, page 381, 2002. doi: 10.1007/10856495_59.

S. V. Bogovalov. On the physics of cold MHD winds from oblique rotators. *A&A*, 349: 1017–1026, Sept. 1999. doi: 10.48550/arXiv.astro-ph/9907051.

A. Borghese and F. Coti Zelati. The zoo of isolated neutron stars. In *Encyclopedia of Astrophysics, Volume 3*, volume 3, pages 145–159, Jan. 2026. doi: 10.1016/B978-0-443-21439-4.00095-X.

A. Borghese, N. Rea, F. Coti Zelati, A. Tiengo, R. Turolla, and S. Zane. Narrow phase-dependent features in X-ray dim isolated neutron stars: a new detection and upper limits. *MNRAS*, 468(3):2975–2983, July 2017. doi: 10.1093/mnras/stx632.

G. Brambilla, C. Kalapotharakos, A. K. Harding, and D. Kazanas. Testing Dissipative Magnetosphere Model Light Curves and Spectra with Fermi Pulsars. *ApJ*, 804(2):84, May 2015. doi: 10.1088/0004-637X/804/2/84.

G. Brambilla, C. Kalapotharakos, A. N. Timokhin, A. K. Harding, and D. Kazanas. Electron-Positron Pair Flow and Current Composition in the Pulsar Magnetosphere. *ApJ*, 858(2): 81, May 2018. doi: 10.3847/1538-4357/aab3e1.

A. Burrows. Colloquium: Perspectives on core-collapse supernova theory. *Reviews of Modern Physics*, 85(1):245–261, Jan. 2013. doi: 10.1103/RevModPhys.85.245.

G. Cao, X. Yang, and L. Zhang. The Modeling of Pulsar Magnetosphere and Radiation. *Universe*, 10(3):130, Mar. 2024. doi: 10.3390/universe10030130.

F. Carrasco, C. Palenzuela, and O. Reula. Pulsar magnetospheres in general relativity. *Phys. Rev. D*, 98(2):023010, July 2018. doi: 10.1103/PhysRevD.98.023010.

F. Carrasco, J. Pelle, O. Reula, D. Viganò, and C. Palenzuela. Relativistic force-free models of the thermal X-ray emission in millisecond pulsars observed by NICER. *MNRAS*, 520 (2):3151–3163, Apr. 2023. doi: 10.1093/mnras/stad333.

F. L. Carrasco and O. A. Reula. Novel scheme for simulating the force-free equations: Boundary conditions and the evolution of solutions towards stationarity. *Phys. Rev. D*, 96(6):063006, Sept. 2017. doi: 10.1103/PhysRevD.96.063006.

B. Cerutti and A. M. Beloborodov. Electrodynamics of Pulsar Magnetospheres. *Space Science Reviews*, 207(1-4):111–136, July 2017. doi: 10.1007/s11214-016-0315-7.

B. Cerutti, A. Philippov, K. Parfrey, and A. Spitkovsky. Particle acceleration in axisymmetric pulsar current sheets. *MNRAS*, 448(1):606–619, Mar. 2015. doi: 10.1093/mnras/stv042.

B. Cerutti, A. A. Philippov, and A. Spitkovsky. Modelling high-energy pulsar light curves from first principles. *MNRAS*, 457(3):2401–2414, Apr. 2016. doi: 10.1093/mnras/stw124.

B. Cerutti, A. A. Philippov, and G. Dubus. Dissipation of the striped pulsar wind and non-thermal particle acceleration: 3D PIC simulations. *A&A*, 642:A204, Oct. 2020. doi: 10.1051/0004-6361/202038618.

B. Cerutti, E. Figueiredo, and G. Dubus. Synthetic pulsar light curves from global kinetic simulations and comparison with the Fermi-LAT catalog. *A&A*, 695:A93, Mar. 2025. doi: 10.1051/0004-6361/202451948.

J. Chadwick. The Existence of a Neutron. *Proceedings of the Royal Society of London Series A*, 136(830):692–708, June 1932. doi: 10.1098/rspa.1932.0112.

A. Y. Chen and A. M. Beloborodov. Electrodynamics of Axisymmetric Pulsar Magnetosphere with Electron-Positron Discharge: A Numerical Experiment. *ApJL*, 795(1):L22, Nov. 2014. doi: 10.1088/2041-8205/795/1/L22.

A. Cheng, M. Ruderman, and P. Sutherland. Current flow in pulsar magnetospheres. *ApJ*, 203:209–212, Jan. 1976. doi: 10.1086/154068.

K. S. Cheng and J. L. Zhang. General Radiation Formulae for a Relativistic Charged Particle Moving in Curved Magnetic Field Lines: The Synchrocurvature Radiation Mechanism. *ApJ*, 463:271, May 1996. doi: 10.1086/177239.

K. S. Cheng, C. Ho, and M. Ruderman. Energetic Radiation from Rapidly Spinning Pulsars. I. Outer Magnetosphere Gaps. *The Astrophysical Journal*, 300:500, Jan. 1986a. doi: 10.1086/163829.

K. S. Cheng, C. Ho, and M. Ruderman. Energetic Radiation from Rapidly Spinning Pulsars. II. VELA and Crab. *ApJ*, 300:522, Jan. 1986b. doi: 10.1086/163830.

K. S. Cheng, M. Ruderman, and L. Zhang. A Three-dimensional Outer Magnetospheric Gap Model for Gamma-Ray Pulsars: Geometry, Pair Production, Emission Morphologies, and Phase-resolved Spectra. *ApJ*, 537(2):964–976, July 2000. doi: 10.1086/309051.

M. Chernyakova and D. Malyshev. Gamma-ray binaries. In *Multifrequency Behaviour of High Energy Cosmic Sources - XIII. 3-8 June 2019. Palermo*, page 45, Dec. 2020. doi: 10.22323/1.362.0045.

J. Chiang and R. W. Romani. Gamma Radiation from Pulsar Magnetospheric Gaps. *ApJ*, 400:629, Dec. 1992. doi: 10.1086/172024.

J. Chiang and R. W. Romani. An Outer Gap Model of High-Energy Emission from Rotation-powered Pulsars. *ApJ*, 436:754, Dec. 1994. doi: 10.1086/174949.

E. Churazov, M. Gilfanov, W. Forman, and C. Jones. Mapping the Gas Temperature Distribution in Extended X-Ray Sources and Spectral Analysis in the Case of Low Statistics: Application to ASCA Observations of Clusters of Galaxies. *ApJ*, 471:673, Nov. 1996. doi: 10.1086/177997.

I. Contopoulos, D. Kazanas, and C. Fendt. The Axisymmetric Pulsar Magnetosphere. *ApJ*, 511(1):351–358, Jan. 1999. doi: 10.1086/306652.

F. V. Coroniti. Magnetically Striped Relativistic Magnetohydrodynamic Winds: The Crab Nebula Revisited. *ApJ*, 349:538, Feb. 1990. doi: 10.1086/168340.

F. Coti Zelati, D. F. Torres, J. Li, and D. Viganò. Spectral characterization of the non-thermal X-ray emission of gamma-ray pulsars. *MNRAS*, 492(1):1025–1043, Feb. 2020. doi: 10.1093/mnras/stz3485.

J. K. Daugherty and A. K. Harding. Electromagnetic cascades in pulsars. *ApJ*, 252:337–347, Jan. 1982. doi: 10.1086/159561.

J. K. Daugherty and A. K. Harding. Polar CAP Models of Gamma-Ray Pulsars: Emission from Single Poles of Nearly Aligned Rotators. *ApJ*, 429:325, July 1994. doi: 10.1086/174321.

J. K. Daugherty and A. K. Harding. Gamma-Ray Pulsars: Emission from Extended Polar CAP Cascades. *The Astrophysical Journal*, 458:278, Feb. 1996. doi: 10.1086/176811.

A. J. Deutsch. The electromagnetic field of an idealized star in rigid rotation in vacuo. *Annales d'Astrophysique*, 18:1, Jan. 1955.

R. Diehl, H. Halloin, and Kretschmer. Radioactive ^{26}Al from massive stars in the Galaxy. *Nature*, 439(7072):45–47, Jan. 2006. doi: 10.1038/nature04364.

J. Dyks and B. Rudak. Two-Pole Caustic Model for High-Energy Light Curves of Pulsars. *ApJ*, 598(2):1201–1206, Dec. 2003. doi: 10.1086/379052.

C. M. Espinoza, A. G. Lyne, M. Kramer, R. N. Manchester, and V. M. Kaspi. The Braking Index of PSR J1734-3333 and the Magnetar Population. *ApJ*, 741(1):L13, Nov. 2011. doi: 10.1088/2041-8205/741/1/L13.

F. Fornasini, V. Antoniou, and G. Dubus. High-Mass X-ray Binaries. In *Handbook of X-ray and Gamma-ray Astrophysics*, page 143. 2023. doi: 10.1007/978-981-16-4544-0_95-1.

B. M. Gaensler and P. O. Slane. The Evolution and Structure of Pulsar Wind Nebulae. *ARA&A*, 44(1):17–47, Sept. 2006. doi: 10.1146/annurev.astro.44.051905.092528.

C. R. García and D. F. Torres. Quantitative Exploration of the Similarity of Gamma-Ray Pulsar Light Curves. *ApJ*, 982(2):L51, Apr. 2025. doi: 10.3847/2041-8213/adbf0f.

C. R. García, D. F. Torres, and A. Patruno. Visualizing the pulsar population using graph theory. *MNRAS*, 515(3):3883–3897, Sept. 2022. doi: 10.1093/mnras/stac1997.

F. P. Gavriil, M. E. Gonzalez, E. V. Gotthelf, V. M. Kaspi, M. A. Livingstone, and P. M. Woods. Magnetar-Like Emission from the Young Pulsar in Kes 75. *Science*, 319(5871): 1802, Mar. 2008. doi: 10.1126/science.1153465.

T. Gold. Rotating Neutron Stars as the Origin of the Pulsating Radio Sources. *Nature*, 218 (5143):731–732, May 1968. doi: 10.1038/218731a0.

P. Goldreich and W. H. Julian. Pulsar Electrodynamics. *The Astrophysical Journal*, 157: 869, Aug 1969. doi: 10.1086/150119.

V. Graber, M. Ronchi, C. Pardo-Araujo, and N. Rea. Isolated Pulsar Population Synthesis with Simulation-based Inference. *ApJ*, 968(1):16, June 2024. doi: 10.3847/1538-4357/ad3e78.

A. Gruzinov. Stability in Force-Free Electrodynamics. *arXiv e-prints*, art. astro-ph/9902288, Feb. 1999. doi: 10.48550/arXiv.astro-ph/9902288.

A. Gruzinov. Power of an Axisymmetric Pulsar. *Phys. Rev. Lett.*, 94(2):021101, Jan. 2005. doi: 10.1103/PhysRevLett.94.021101.

A. Gruzinov. Dissipative pulsar magnetospheres. *J. Cosmology Astropart. Phys.*, 2008(11): 002, Nov. 2008. doi: 10.1088/1475-7516/2008/11/002.

M. Gullón, J. A. Miralles, D. Viganò, and J. A. Pons. Population synthesis of isolated neutron stars with magneto-rotational evolution. *MNRAS*, 443(3):1891–1899, Sept. 2014. doi: 10.1093/mnras/stu1253.

H. E. S. S. Collaboration et al. Discovery of a radiation component from the Vela pulsar reaching 20 teraelectronvolts. *Nature Astronomy*, 7:1341–1350, Nov. 2023. doi: 10.1038/s41550-023-02052-3.

P. Haensel, A. Y. Potekhin, and D. G. Yakovlev. *Neutron Stars 1 : Equation of State and Structure*, volume 326. 2007.

H. Hakobyan, A. Philippov, and A. Spitkovsky. Effects of Synchrotron Cooling and Pair Production on Collisionless Relativistic Reconnection. *ApJ*, 877(1):53, May 2019. doi: 10.3847/1538-4357/ab191b.

H. Hakobyan, A. Philippov, and A. Spitkovsky. Magnetic Energy Dissipation and γ-Ray Emission in Energetic Pulsars. *ApJ*, 943(2):105, Feb. 2023. doi: 10.3847/1538-4357/acab05.

P. E. Hardee. Production and beaming of pulsar gamma -ray emission. *ApJ*, 216:873–880, Sept. 1977. doi: 10.1086/155532.

A. K. Harding. Pulsar gamma-rays : spectra, luminosities and efficiencies. *ApJ*, 245:267–273, Apr. 1981. doi: 10.1086/158807.

A. K. Harding. The neutron star zoo. *Frontiers of Physics*, 8(6):679–692, Dec. 2013. doi: 10.1007/s11467-013-0285-0.

A. K. Harding. The Emission Physics of Millisecond Pulsars. In S. Bhattacharyya, A. Papitto, and D. Bhattacharya, editors, *Astrophysics and Space Science Library*, volume 465 of *Astrophysics and Space Science Library*, pages 57–85, Jan. 2022. doi: 10.1007/978-3-030-85198-9_3.

A. K. Harding, E. Tademaru, and L. W. Esposito. A curvature - radiation - pair-production model for gamma -ray pulsars. *ApJ*, 225:226–236, Oct. 1978. doi: 10.1086/156486.

A. K. Harding, J. V. Stern, J. Dyks, and M. Frackowiak. High-Altitude Emission from Pulsar Slot Gaps: The Crab Pulsar. *ApJ*, 680(2):1378–1393, June 2008. doi: 10.1086/588037.

A. K. Harding, C. Kalapotharakos, M. Barnard, and C. Venter. Multi-TeV Emission from the Vela Pulsar. *ApJ*, 869(1):L18, Dec. 2018. doi: 10.3847/2041-8213/aaf3b2.

A. K. Harding, C. Venter, and C. Kalapotharakos. Very-high-energy Emission from Pulsars. *ApJ*, 923(2):194, Dec. 2021. doi: 10.3847/1538-4357/ac3084.

B. Haskell and A. Melatos. Models of pulsar glitches. *International Journal of Modern Physics D*, 24(3):1530008, Jan. 2015. doi: 10.1142/S0218271815300086.

A. Hewish, S. J. Bell, J. D. H. Pilkington, P. F. Scott, and R. A. Collins. Observation of a Rapidly Pulsating Radio Source. *Nature*, 217(5130):709–713, Feb. 1968. doi: 10.1038/217709a0.

K. Hirotani. Particle Accelerator in Pulsar Magnetospheres: Super-Goldreich-Julian Current with Ion Emission from the Neutron Star Surface. *ApJ*, 652(2):1475–1493, Dec. 2006. doi: 10.1086/508317.

K. Hirotani and S. Shibata. One-dimensional electric field structure of an outer gap accelerator - I. gamma-ray production resulting from curvature radiation. *MNRAS*, 308(1):54–66, Sept. 1999. doi: 10.1046/j.1365-8711.1999.02696.x.

G. Hobbs, D. R. Lorimer, A. G. Lyne, and M. Kramer. A statistical study of 233 pulsar proper motions. *MNRAS*, 360(3):974–992, July 2005. doi: 10.1111/j.1365-2966.2005.09087.x.

N. J. Holloway. P-N Junctions in Pulsar Magnetospheres ? *Nature Physical Science*, 246 (149):6–9, Nov. 1973. doi: 10.1038/physci246006a0.

R. A. Hulse and J. H. Taylor. Discovery of a pulsar in a binary system. *ApJ*, 195:L51–L53, Jan. 1975. doi: 10.1086/181708.

D. Íñiguez-Pascual, D. Viganò, and D. F. Torres. Synchro-curvature emitting regions in high-energy pulsar models. *MNRAS*, 516(2):2475–2485, Oct. 2022. doi: 10.1093/mnras/stac2275.

D. Íñiguez-Pascual, D. F. Torres, and D. Viganò. Synchro-curvature description of γ-ray light curves and spectra of pulsars: global properties. *MNRAS*, 530(2):1550–1562, May 2024. doi: 10.1093/mnras/stae933.

D. Íñiguez-Pascual, D. F. Torres, and D. Viganò. Synchro-curvature description of γ-ray light curves and spectra of pulsars: concurrent fitting. *MNRAS*, 541(2):806–820, Aug. 2025a. doi: 10.1093/mnras/staf1044.

D. Íñiguez-Pascual, D. Viganò, and D. F. Torres. The dispersion in pulsar γ-ray efficiency. *A&A*, 704:L14, Dec. 2025b. doi: 10.1051/0004-6361/202557622.

J. D. Jackson. *Classical Electrodynamics, 3rd Edition*. 1998.

T. J. Johnson, C. Venter, A. K. Harding, L. Guillemot, D. A. Smith, M. Kramer, Ö. Çelik, P. R. den Hartog, E. C. Ferrara, X. Hou, J. Lande, and P. S. Ray. Constraints on the Emission Geometries and Spin Evolution of Gamma-Ray Millisecond Pulsars. *ApJS*, 213 (1):6, July 2014. doi: 10.1088/0067-0049/213/1/6.

C. Kalapotharakos and I. Contopoulos. Three-dimensional numerical simulations of the pulsar magnetosphere: preliminary results. *A&A*, 496(2):495–502, Mar. 2009. doi: 10.1051/0004-6361:200810281.

C. Kalapotharakos, I. Contopoulos, and D. Kazanas. The extended pulsar magnetosphere. *MNRAS*, 420(4):2793–2798, Mar. 2012a. doi: 10.1111/j.1365-2966.2011.19884.x.

C. Kalapotharakos, D. Kazanas, A. Harding, and I. Contopoulos. Toward a Realistic Pulsar Magnetosphere. *ApJ*, 749(1):2, Apr. 2012b. doi: 10.1088/0004-637X/749/1/2.

C. Kalapotharakos, A. K. Harding, and D. Kazanas. Gamma-Ray Emission in Dissipative Pulsar Magnetospheres: From Theory to Fermi Observations. *ApJ*, 793(2):97, Oct. 2014. doi: 10.1088/0004-637X/793/2/97.

C. Kalapotharakos, G. Brambilla, A. Timokhin, A. K. Harding, and D. Kazanas. Three-dimensional Kinetic Pulsar Magnetosphere Models: Connecting to Gamma-Ray Observations. *ApJ*, 857(1):44, Apr. 2018. doi: 10.3847/1538-4357/aab550.

C. Kalapotharakos, Z. Wadiasingh, A. K. Harding, and D. Kazanas. The Gamma-Ray Pulsar Phenomenology in View of 3D Kinetic Global Magnetosphere Models. *ApJ*, 954(2):204, Sept. 2023. doi: 10.3847/1538-4357/ace972.

V. M. Kaspi and A. M. Beloborodov. Magnetars. *ARA&A*, 55(1):261–301, Aug. 2017. doi: 10.1146/annurev-astro-081915-023329.

V. M. Kaspi and M. Kramer. Radio Pulsars: The Neutron Star Population & Fundamental Physics. *arXiv e-prints*, art. arXiv:1602.07738, Feb. 2016. doi: 10.48550/arXiv.1602.07738.

V. M. Kaspi, A. G. Lyne, Manchester, et al. Discovery of a Young Radio Pulsar in a Relativistic Binary Orbit. *ApJ*, 543(1):321–327, Nov. 2000. doi: 10.1086/317103.

V. M. Kaspi, M. S. E. Roberts, and A. K. Harding. Isolated neutron stars. In W. H. G. Lewin and M. van der Klis, editors, *Compact stellar X-ray sources*, volume 39, pages 279–339. 2006. doi: 10.48550/arXiv.astro-ph/0402136.

S. R. Kelner, A. Y. Prosekin, and F. A. Aharonian. Synchro-Curvature Radiation of Charged Particles in the Strong Curved Magnetic Fields. *AJ*, 149(1):33, Jan. 2015. doi: 10.1088/0004-6256/149/1/33.

C. F. Kennel and F. V. Coroniti. Confinement of the Crab pulsar's wind by its supernova remnant. *ApJ*, 283:694–709, Aug. 1984. doi: 10.1086/162356.

R. Kippenhahn, A. Weigert, and A. Weiss. *Stellar Structure and Evolution*. 2013. doi: 10.1007/978-3-642-30304-3.

J. G. Kirk and O. Skjæraasen. Dissipation in Poynting-Flux-dominated Flows: The σ-Problem of the Crab Pulsar Wind. *ApJ*, 591(1):366–379, July 2003. doi: 10.1086/375215.

J. G. Kirk, O. Skjæraasen, and Y. A. Gallant. Pulsed radiation from neutron star winds. *A&A*, 388:L29–L32, June 2002. doi: 10.1051/0004-6361:20020599.

B. Kiziltan, A. Kottas, M. De Yoreo, and S. E. Thorsett. The neutron star mass distribution. *ApJ*, 778(1):66, nov 2013. doi: 10.1088/0004-637X/778/1/66. URL https://dx.doi.org/10.1088/0004-637X/778/1/66.

D. A. Kniffen, R. C. Hartman, D. J. Thompson, G. F. Bignami, and C. E. Fichtel. Gamma radiation from the Crab Nebula above 35 MeV. *Nature*, 251(5474):397–399, Oct. 1974. doi: 10.1038/251397a0.

S. S. Komissarov. Electrodynamics of black hole magnetospheres. *MNRAS*, 350(2):427–448, May 2004. doi: 10.1111/j.1365-2966.2004.07598.x.

L. Kuiper and W. Hermsen. The soft γ-ray pulsar population: a high-energy overview. *MNRAS*, 449(4):3827–3866, June 2015. doi: 10.1093/mnras/stv426.

M. Lemoine-Goumard, V. E. Zavlin, M.-H. Grondin, et al. Discovery of gamma- and X-ray pulsations from the young and energetic PSR J1357-6429 with Fermi and XMM-Newton. *A&A*, 533:A102, Sept. 2011. doi: 10.1051/0004-6361/201117413.

J. Li, A. Spitkovsky, and A. Tchekhovskoy. Resistive Solutions for Pulsar Magnetospheres. *ApJ*, 746(1):60, Feb. 2012. doi: 10.1088/0004-637X/746/1/60.

J. Li, D. F. Torres, E. de Oña Wilhelmi, N. Rea, and J. Martin. Gamma-ray Emission from PSR J0007+7303 Using Seven Years of Fermi Large Area Telescope Observations. *ApJ*, 831(1):19, Nov. 2016. doi: 10.3847/0004-637X/831/1/19.

J. Li, D. F. Torres, F. Coti Zelati, A. Papitto, M. Kerr, and N. Rea. Theoretically Motivated Search and Detection of Non-thermal Pulsations from PSRs J1747-2958, J2021+3651, and J1826-1256. *ApJ*, 868(2):L29, Dec. 2018a. doi: 10.3847/2041-8213/aae92b.

J. Li, D. F. Torres, T. T. Lin, M.-H. Grondin, M. Kerr, M. Lemoine-Goumard, and E. de Oña Wilhelmi. Observing and Modeling the Gamma-Ray Emission from Pulsar/Pulsar Wind Nebula Complex PSR J0205+6449/3C 58. *ApJ*, 858(2):84, May 2018b. doi: 10.3847/1538-4357/aabac9.

D. R. Lorimer and M. Kramer. *Handbook of Pulsar Astronomy*, volume 4. 2004.

A. G. Lyne and R. N. Manchester. The shape of pulsar radio beams. *MNRAS*, 234:477–508, Oct. 1988. doi: 10.1093/mnras/234.3.477.

A. G. Lyne, M. Burgay, M. Kramer, et al. A Double-Pulsar System: A Rare Laboratory for Relativistic Gravity and Plasma Physics. *Science*, 303(5661):1153–1157, Feb. 2004. doi: 10.1126/science.1094645.

Y. E. Lyubarskii. A model for the energetic emission from pulsars. *A&A*, 311:172–178, July 1996.

Y. E. Lyubarskii and S. A. Petrova. Synchrotron absorption in pulsar magnetospheres. *A&A*, 337:433–440, Sept. 1998.

Y. Lyubarsky and J. G. Kirk. Reconnection in a Striped Pulsar Wind. *ApJ*, 547(1):437–448, Jan. 2001. doi: 10.1086/318354.

MAGIC Collaboration. Observation of Pulsed γ-Rays Above 25 GeV from the Crab Pulsar with MAGIC. *Science*, 322(5905):1221, Nov. 2008. doi: 10.1126/science.1164718.

MAGIC Collaboration. Detection of the Geminga pulsar with MAGIC hints at a power-law tail emission beyond 15 GeV. *A&A*, 643:L14, Nov. 2020. doi: 10.1051/0004-6361/202039131.

R. N. Manchester, G. B. Hobbs, A. Teoh, and M. Hobbs. The Australia Telescope National Facility Pulsar Catalogue. *AJ*, 129(4):1993–2006, Apr. 2005. doi: 10.1086/428488.

M. Marelli, A. De Luca, and P. A. Caraveo. A Multiwavelength Study on the High-energy Behavior of the Fermi/LAT Pulsars. *ApJ*, 733(2):82, June 2011. doi: 10.1088/0004-637X/733/2/82.

J. G. Martinez, K. Stovall, P. C. C. Freire, J. S. Deneva, F. A. Jenet, M. A. McLaughlin, M. Bagchi, S. D. Bates, and A. Ridolfi. Pulsar J0453+1559: A Double Neutron Star System with a Large Mass Asymmetry. *ApJ*, 812(2):143, Oct. 2015. doi: 10.1088/0004-637X/812/2/143.

L. Mestel. Pulsar Magnetosphere. *Nature Physical Science*, 233(43):149–152, Oct. 1971. doi: 10.1038/physci233149a0.

L. Mestel and S. Shibata. The axisymmetric pulsar magnetosphere: a new model. *MNRAS*, 271:621–638, Dec. 1994. doi: 10.1093/mnras/271.3.621.

F. C. Michel. Rotating Magnetospheres: an Exact 3-D Solution. *ApJ*, 180:L133, Mar. 1973. doi: 10.1086/181169.

F. C. Michel. Magnetic Structure of Pulsar Winds. *ApJ*, 431:397, Aug. 1994. doi: 10.1086/174493.

F. C. Michel and H. Li. Electrodynamics of neutron stars. *Phys. Rep.*, 318(6):227–297, Sept. 1999. doi: 10.1016/S0370-1573(99)00002-2.

R. P. Mignani. Optical, ultraviolet, and infrared observations of isolated neutron stars. *Advances in Space Research*, 47(8):1281–1293, Apr. 2011. doi: 10.1016/j.asr.2009.12.011.

R. P. Mignani, P. A. Caraveo, and G. F. Bignami. Optical observations of pulsars: the ESO contribution. *The Messenger*, 99:22–26, Mar. 2000.

M. Morini. Inverse Compton gamma-rays from pulsars. I. The VELA pulsar. *MNRAS*, 202:495–510, Feb. 1983. doi: 10.1093/mnras/202.2.495.

A. G. Muslimov and A. K. Harding. Extended Acceleration in Slot Gaps and Pulsar High-Energy Emission. *ApJ*, 588(1):430–440, May 2003. doi: 10.1086/368162.

A. G. Muslimov and A. K. Harding. High-Altitude Particle Acceleration and Radiation in Pulsar Slot Gaps. *The Astrophysical Journal*, 606(2):1143–1153, May 2004. doi: 10.1086/383079.

A. G. Muslimov and A. I. Tsygan. General relativistic electric potential drops above pulsar polar caps. *MNRAS*, 255:61–70, Mar. 1992. doi: 10.1093/mnras/255.1.61.

J. A. Nelder and R. Mead. A Simplex Method for Function Minimization. *Comput. J.*, 7:308–313, 1965. doi: 10.1093/comjnl/7.4.308.

S. A. Olausen and V. M. Kaspi. The McGill Magnetar Catalog. *ApJS*, 212(1):6, May 2014. doi: 10.1088/0067-0049/212/1/6.

J. R. Oppenheimer and G. M. Volkoff. On Massive Neutron Cores. *Physical Review*, 55(4):374–381, Feb. 1939. doi: 10.1103/PhysRev.55.374.

J. P. Ostriker and J. E. Gunn. On the Nature of Pulsars. I. Theory. *ApJ*, 157:1395, Sept. 1969. doi: 10.1086/150160.

F. Özel and P. Freire. Masses, Radii, and the Equation of State of Neutron Stars. *ARA&A*, 54:401–440, Sept. 2016. doi: 10.1146/annurev-astro-081915-023322.

F. Pacini. Energy Emission from a Neutron Star. *Nature*, 216(5115):567–568, Nov. 1967. doi: 10.1038/216567a0.

F. Pacini. Rotating Neutron Stars, Pulsars and Supernova Remnants. *Nature*, 219(5150):145–146, July 1968. doi: 10.1038/219145a0.

A. Papitto and D. de Martino. Transitional Millisecond Pulsars. In S. Bhattacharyya, A. Papitto, and D. Bhattacharya, editors, *Astrophysics and Space Science Library*, volume 465 of *Astrophysics and Space Science Library*, pages 157–200, Jan. 2022. doi: 10.1007/978-3-030-85198-9_6.

C. Pardo-Araujo, M. Ronchi, V. Graber, and N. Rea. Radio pulsar population synthesis with consistent flux measurements using simulation-based inference. *A&A*, 696:A114, Apr. 2025. doi: 10.1051/0004-6361/202453314.

A. Parthasarathy, R. M. Shannon, S. Johnston, L. Lentati, M. Bailes, S. Dai, M. Kerr, R. N. Manchester, S. Osłowski, C. Sobey, W. van Straten, and P. Weltevrede. Timing of young radio pulsars - I. Timing noise, periodic modulation, and proper motion. *MNRAS*, 489 (3):3810–3826, Nov. 2019. doi: 10.1093/mnras/stz2383.

J. Pétri. The pulsar force-free magnetosphere linked to its striped wind: time-dependent pseudo-spectral simulations. *MNRAS*, 424(1):605–619, July 2012a. doi: 10.1111/j.1365-2966.2012.21238.x.

J. Pétri. High-energy emission from the pulsar striped wind: a synchrotron model for gamma-ray pulsars. *MNRAS*, 424(3):2023–2027, Aug. 2012b. doi: 10.1111/j.1365-2966.2012.21350.x.

J. Pétri. General-relativistic force-free pulsar magnetospheres. *MNRAS*, 455(4):3779–3805, Feb. 2016a. doi: 10.1093/mnras/stv2613.

J. Pétri. Theory of pulsar magnetosphere and wind. *Journal of Plasma Physics*, 82(5): 635820502, Oct. 2016b. doi: 10.1017/S0022377816000763.

J. Pétri. Electrodynamics and Radiation from Rotating Neutron Star Magnetospheres. *Universe*, 6(1):15, Jan. 2020. doi: 10.3390/universe6010015.

J. Pétri and J. G. Kirk. The Polarization of High-Energy Pulsar Radiation in the Striped Wind Model. *ApJ*, 627(1):L37–L40, July 2005. doi: 10.1086/431973.

A. Philippov, A. Tchekhovskoy, and J. G. Li. Time evolution of pulsar obliquity angle from 3D simulations of magnetospheres. *MNRAS*, 441(3):1879–1887, July 2014. doi: 10.1093/mnras/stu591.

A. A. Philippov and M. Kramer. Pulsar Magnetospheres and Their Radiation. *ARA&A*, 60: 495–558, Aug. 2022. doi: 10.1146/annurev-astro-052920-112338.

A. A. Philippov and A. Spitkovsky. Ab Initio Pulsar Magnetosphere: Three-dimensional Particle-in-cell Simulations of Axisymmetric Pulsars. *ApJL*, 785(2):L33, Apr. 2014. doi: 10.1088/2041-8205/785/2/L33.

A. A. Philippov and A. Spitkovsky. Ab-initio Pulsar Magnetosphere: Particle Acceleration in Oblique Rotators and High-energy Emission Modeling. *The Astrophysical Journal*, 855 (2):94, Mar. 2018. doi: 10.3847/1538-4357/aaabbc.

A. A. Philippov, B. Cerutti, A. Tchekhovskoy, and A. Spitkovsky. Ab Initio Pulsar Magnetosphere: The Role of General Relativity. *ApJL*, 815(2):L19, Dec. 2015a. doi: 10.1088/2041-8205/815/2/L19.

A. A. Philippov, A. Spitkovsky, and B. Cerutti. Ab Initio Pulsar Magnetosphere: Three-dimensional Particle-in-cell Simulations of Oblique Pulsars. *ApJ*, 801(1):L19, Mar. 2015b. doi: 10.1088/2041-8205/801/1/L19.

M. Pierbattista, I. A. Grenier, A. K. Harding, and P. L. Gonthier. Constraining γ-ray pulsar gap models with a simulated pulsar population. *A&A*, 545:A42, Sept. 2012. doi: 10.1051/0004-6361/201219135.

M. Pierbattista, A. K. Harding, I. A. Grenier, T. J. Johnson, P. A. Caraveo, M. Kerr, and P. L. Gonthier. Light-curve modelling constraints on the obliquities and aspect angles of the young Fermi pulsars. *A&A*, 575:A3, Mar. 2015. doi: 10.1051/0004-6361/201423815.

M. Pierbattista, A. K. Harding, P. L. Gonthier, and I. A. Grenier. Young and middle age pulsar light-curve morphology: Comparison of Fermi observations with γ-ray and radio emission geometries. *A&A*, 588:A137, Apr. 2016. doi: 10.1051/0004-6361/201527821.

J. A. Pons, D. Viganò, and U. Geppert. Pulsar timing irregularities and the imprint of magnetic field evolution. *A&A*, 547:A9, Nov. 2012. doi: 10.1051/0004-6361/201220091.

A. Y. Potekhin, J. A. Pons, and D. Page. Neutron Stars—Cooling and Transport. *Space Sci. Rev.*, 191(1-4):239–291, Oct. 2015. doi: 10.1007/s11214-015-0180-9.

W. H. Press, S. A. Teukolsky, W. T. Vetterling, and B. P. Flannery. *Numerical Recipes in C (2nd Ed.): The Art of Scientific Computing*. Cambridge University Press, USA, 1992. ISBN 0521431085.

V. Radhakrishnan and D. J. Cooke. Magnetic Poles and the Polarization Structure of Pulsar Radiation. *Astrophysical Letters*, 3:225, Jan. 1969.

J. M. Rankin. Toward an Empirical Theory of Pulsar Emission. VI. The Geometry of the Conal Emission Region. *ApJ*, 405:285, Mar. 1993. doi: 10.1086/172361.

N. Rea and D. De Grandis. Magnetars. In *Encyclopedia of Astrophysics, Volume 3*, volume 3, pages 205–222, Jan. 2026. doi: 10.1016/B978-0-443-21439-4.00096-1.

N. Rea, A. Borghese, P. Esposito, F. Coti Zelati, M. Bachetti, G. L. Israel, and A. De Luca. Magnetar-like Activity from the Central Compact Object in the SNR RCW103. *ApJ*, 828 (1):L13, Sept. 2016. doi: 10.3847/2041-8205/828/1/L13.

R. W. Romani. Gamma-Ray Pulsars: Radiation Processes in the Outer Magnetosphere. *The Astrophysical Journal*, 470:469, Oct. 1996. doi: 10.1086/177878.

R. W. Romani and K. P. Watters. Constraining Pulsar Magnetosphere Geometry with γ-ray Light Curves. *ApJ*, 714(1):810–824, May 2010. doi: 10.1088/0004-637X/714/1/810.

R. W. Romani and I. A. Yadigaroglu. Gamma-Ray Pulsars: Emission Zones and Viewing Geometries. *The Astrophysical Journal*, 438:314, Jan. 1995. doi: 10.1086/175076.

R. W. Romani, D. Kandel, and A. V. Filippenko. PSR J0952-0607: The Fastest and Heaviest Known Galactic Neutron Star. *ApJ*, 934(2):L17, Aug. 2022. doi: 10.3847/2041-8213/ac8007.

M. A. Ruderman and P. G. Sutherland. Theory of pulsars: polar gaps, sparks, and coherent microwave radiation. *ApJ*, 196:51–72, Feb. 1975. doi: 10.1086/153393.

P. Rudolf. Optimization methods for hydraulic machines design - -shape optimization of swirl turbine draft tube. 09 2006.

M. Ruiz, V. Paschalidis, and S. L. Shapiro. Pulsar spin-down luminosity: Simulations in general relativity. *Phys. Rev. D*, 89(8):084045, Apr. 2014. doi: 10.1103/PhysRevD.89.084045.

M. Salvati and E. Massaro. Gamma-ray emission from pulsars. *A&A*, 67:55–63, June 1978.

E. T. Scharlemann and R. V. Wagoner. Aligned Rotating Magnetospheres. General Analysis. *ApJ*, 182:951–960, June 1973. doi: 10.1086/152195.

D. A. Smith, L. Guillemot, F. Camilo, et al. Pulsar timing for the Fermi gamma-ray space telescope. *A&A*, 492(3):923–931, Dec. 2008. doi: 10.1051/0004-6361:200810285.

D. A. Smith, S. Abdollahi, Ajello, et al. The Third Fermi Large Area Telescope Catalog of Gamma-Ray Pulsars. *ApJ*, 958(2):191, Dec. 2023. doi: 10.3847/1538-4357/acee67.

F. G. Smith, D. H. P. Jones, J. S. B. Dick, and C. D. Pike. The optical polarization of the Crab pulsar. *MNRAS*, 233:305–319, July 1988. doi: 10.1093/mnras/233.2.305.

A. Soudais, B. Cerutti, and I. Contopoulos. Scaling up global kinetic models of pulsar magnetospheres using a hybrid force-free-PIC numerical approach. *A&A*, 690:A170, Oct. 2024. doi: 10.1051/0004-6361/202450238.

M. Spir-Jacob, A. Djannati-Ataï, L. Mohrmann, G. Giavitto, B. Khélifi, B. Rudak, C. Venter, and R. Zanin. Detection of sub-100 GeV gamma-ray pulsations from PSR B1706-44 with H.E.S.S. *arXiv e-prints*, art. arXiv:1908.06464, Aug. 2019. doi: 10.48550/arXiv.1908.06464.

A. Spitkovsky. Time-dependent Force-free Pulsar Magnetospheres: Axisymmetric and Oblique Rotators. *ApJL*, 648(1):L51–L54, Sept. 2006. doi: 10.1086/507518.

M. Springer. *The algebra of random variables*. Wiley series in probability and mathematical statistics. Wiley, New York [u.a.], 1979. ISBN 0471014060. URL https://www.ime.usp.br/~jmstern/wp-content/uploads/2020/11/Springer1979.pdf.

S. J. Sturner and C. D. Dermer. On the Spectra and Pulse Profiles of Gamma-Ray Pulsars. *ApJ*, 420:L79, Jan. 1994. doi: 10.1086/187167.

S. J. Sturner, C. D. Dermer, and F. C. Michel. Magnetic Compton-induced Pair Cascade Model for Gamma-Ray Pulsars. *ApJ*, 445:736, June 1995. doi: 10.1086/175736.

P. A. Sturrock. A Model of Pulsars. *The Astrophysical Journal*, 164:529, Mar. 1971. doi: 10.1086/150865.

A. Szary, B. Zhang, G. I. Melikidze, et al. Radio Efficiency of Pulsars. *ApJ*, 784(1):59, Mar. 2014. doi: 10.1088/0004-637X/784/1/59.

T. M. Tauris and R. N. Manchester. On the Evolution of Pulsar Beams. *MNRAS*, 298(3): 625–636, Aug. 1998. doi: 10.1046/j.1365-8711.1998.01369.x.

T. M. Tauris and E. P. J. van den Heuvel. *Physics of Binary Star Evolution. From Stars to X-ray Binaries and Gravitational Wave Sources*. 2023. doi: 10.48550/arXiv.2305.09388.

T. M. Tauris, M. Kramer, P. C. C. Freire, N. Wex, H.-T. Janka, N. Langer, P. Podsiadlowski, E. Bozzo, S. Chaty, M. U. Kruckow, E. P. J. van den Heuvel, J. Antoniadis, R. P. Breton, and D. J. Champion. Formation of Double Neutron Star Systems. *ApJ*, 846(2):170, Sept. 2017. doi: 10.3847/1538-4357/aa7e89.

J. H. Taylor and J. M. Weisberg. A new test of general relativity - Gravitational radiation and the binary pulsar PSR 1913+16. *ApJ*, 253:908–920, Feb. 1982. doi: 10.1086/159690.

J. H. Taylor, L. A. Fowler, and P. M. McCulloch. Measurements of general relativistic effects in the binary pulsar PSR1913 + 16. *Nature*, 277(5696):437–440, Feb. 1979. doi: 10.1038/277437a0.

C. Thompson and R. C. Duncan. Neutron Star Dynamos and the Origins of Pulsar Magnetism. *ApJ*, 408:194, May 1993. doi: 10.1086/172580.

D. J. Thompson. Gamma ray pulsars: Multiwavelength observations. *Astrophys. Space Sci. Libr.*, 304:149–168, 2004. doi: 10.1007/978-1-4020-2256-2_7.

D. J. Thompson, C. E. Fichtel, D. A. Kniffen, and H. B. Ogelman. SAS-2 high-energy gamma-ray observations of the Vela pulsar. *ApJ*, 200:L79–L82, Sept. 1975. doi: 10.1086/181902.

A. N. Timokhin. On the force-free magnetosphere of an aligned rotator. *MNRAS*, 368(3): 1055–1072, May 2006. doi: 10.1111/j.1365-2966.2006.10192.x.

A. N. Timokhin. Time-dependent pair cascades in magnetospheres of neutron stars - I. Dynamics of the polar cap cascade with no particle supply from the neutron star surface. *MNRAS*, 408(4):2092–2114, Nov. 2010. doi: 10.1111/j.1365-2966.2010.17286.x.

A. N. Timokhin and J. Arons. Current flow and pair creation at low altitude in rotation-powered pulsars' force-free magnetospheres: space charge limited flow. *MNRAS*, 429(1): 20–54, Feb. 2013. doi: 10.1093/mnras/sts298.

R. C. Tolman. Static Solutions of Einstein's Field Equations for Spheres of Fluid. *Physical Review*, 55(4):364–373, Feb. 1939. doi: 10.1103/PhysRev.55.364.

D. F. Torres. Order parameters for the high-energy spectra of pulsars. *Nature Astronomy*, 2:247–256, Feb 2018. doi: 10.1038/s41550-018-0384-5.

D. F. Torres, D. Viganò, F. Coti Zelati, and J. Li. Synchrocurvature modelling of the multifrequency non-thermal emission of pulsars. *MNRAS*, 489(4):5494–5512, Nov 2019. doi: 10.1093/mnras/stz2403.

R. Turolla. Isolated Neutron Stars: The Challenge of Simplicity. In W. Becker, editor, *Astrophysics and Space Science Library*, volume 357 of *Astrophysics and Space Science Library*, page 141, Jan. 2009. doi: 10.1007/978-3-540-76965-1_7.

C. Venter, A. K. Harding, and L. Guillemot. Probing Millisecond Pulsar Emission Geometry Using Light Curves from the Fermi/Large Area Telescope. *ApJ*, 707(1):800–822, Dec. 2009. doi: 10.1088/0004-637X/707/1/800.

VERITAS Collaboration. Detection of Pulsed Gamma Rays Above 100 GeV from the Crab Pulsar. *Science*, 334(6052):69, Oct. 2011. doi: 10.1126/science.1208192.

D. Viganò and D. F. Torres. A novel approach for the analysis of the geometry involved in determining light curves of pulsars. *MNRAS*, 490(1):1437–1450, Nov 2019. doi: 10.1093/mnras/stz2685.

D. Viganò, N. Rea, J. A. Pons, R. Perna, D. N. Aguilera, and J. A. Miralles. Unifying the observational diversity of isolated neutron stars via magneto-thermal evolution models. *MNRAS*, 434(1):123–141, Sept. 2013. doi: 10.1093/mnras/stt1008.

D. Viganò, D. F. Torres, K. Hirotani, and M. E. Pessah. Compact formulae, dynamics and radiation of charged particles under synchro-curvature losses. *MNRAS*, 447(2):1164–1172, Dec 2015a. ISSN 0035-8711. doi: 10.1093/mnras/stu2456. URL http://dx.doi.org/10.1093/mnras/stu2456.

D. Viganò, D. F. Torres, K. Hirotani, and M. E. Pessah. An assessment of the pulsar outer gap model – I. Assumptions, uncertainties, and implications on the gap size and the accelerating field. *MNRAS*, 447(3):2631–2648, Jan 2015b. ISSN 0035-8711. doi: 10.1093/mnras/stu2564. URL http://dx.doi.org/10.1093/mnras/stu2564.

D. Viganò, D. F. Torres, K. Hirotani, and M. E. Pessah. An assessment of the pulsar outer gap model – II. Implications for the predicted γ-ray spectra. *MNRAS*, 447(3):2649–2657, Jan 2015c. ISSN 0035-8711. doi: 10.1093/mnras/stu2565. URL http://dx.doi.org/10.1093/mnras/stu2565.

D. Viganò, D. F. Torres, and J. Martín. A systematic synchro-curvature modelling of pulsar γ-ray spectra unveils hidden trends. *MNRAS*, 453(3):2600–2622, Sep 2015d. ISSN 1365-2966. doi: 10.1093/mnras/stv1582. URL http://dx.doi.org/10.1093/mnras/stv1582.

G. A. Wade, C. Neiner, E. Alecian, et al. The MiMeS survey of magnetism in massive stars: introduction and overview. *MNRAS*, 456(1):2–22, Feb. 2016. doi: 10.1093/mnras/stv2568.

H. G. Wang, F. P. Pi, X. P. Zheng, C. L. Deng, S. Q. Wen, F. Ye, K. Y. Guan, Y. Liu, and L. Q. Xu. A Fan Beam Model for Radio Pulsars. I. Observational Evidence. *ApJ*, 789(1):73, July 2014. doi: 10.1088/0004-637X/789/1/73.

K. P. Watters, R. W. Romani, P. Weltevrede, and S. Johnston. An Atlas for Interpreting γ-Ray Pulsar Light Curves. *ApJ*, 695(2):1289–1301, Apr. 2009. doi: 10.1088/0004-637X/695/2/1289.

P. Weltevrede and S. Johnston. The population of pulsars with interpulses and the implications for beam evolution. *MNRAS*, 387(4):1755–1760, July 2008. doi: 10.1111/j.1365-2966.2008.13382.x.

Y. Xing and Z. Wang. Fermi Study of Gamma-ray Millisecond Pulsars: the Spectral Shape and Pulsed Emission from J0614-3329 up to 60 GeV. *ApJ*, 831(2):143, Nov. 2016. doi: 10.3847/0004-637X/831/2/143.

Y.-J. Xu, H.-L. Peng, S.-S. Weng, X. Zhang, and M.-Y. Ge. A New X-Ray Census of Rotation Powered Pulsars. *ApJ*, 981(2):100, Mar. 2025. doi: 10.3847/1538-4357/adaebc.

D. G. Yakovlev, A. D. Kaminker, O. Y. Gnedin, and P. Haensel. Neutrino emission from neutron stars. *Phys. Rep.*, 354(1-2):1–155, Nov. 2001. doi: 10.1016/S0370-1573(00)00131-9.

L. Zhang and K. S. Cheng. High-Energy Radiation from Rapidly Spinning Pulsars with Thick Outer Gaps. *ApJ*, 487(1):370–379, Sept. 1997. doi: 10.1086/304589.